THE UNIVERSITY *of* EDINBURGH

The State Of The Gas In Intense Lensed Starbursts

Richard George

Institute for Astronomy

School of Physics and Astronomy

Doctor of Philosophy

The University of Edinburgh

2015

Declaration

Except where otherwise stated, the research undertaken in this thesis was the unaided work of the author. Where the work was done in collaboration with others, a significant contribution was made by the author. No part of this thesis has be submitted for any other degree or professional qualification. The majority of the work in Chapter 3 and Chapter 4 has been published in the Monthly Notices of the Royal Astronomical Society as George et al. (2013) and George et al. (2014).

Richard George
June 2015

Lay summary

Today, the most massive galaxies are 'red and dead', consisting mostly of old stars, with little ongoing star formation. These titans, which are often the central body of clusters of galaxies, were not always so peaceful, with a history including assimilation of smaller galaxies, extreme star formation and hosting the most powerful phenomena in the Universe: supernovae, gamma-ray bursts and quasars. Such galaxies were some of the earliest to form, and since this time their evolution has been shaped by many factors, of which one is of particular interest here: mergers with other similarly massive galaxies in the distant past.

The huge disruptions of interstellar gas during these mergers trigger the most strongly star-forming events in the Universe, producing many stars massive enough to die spectacularly as supernovae. Despite the huge light output of these merger-induced starbursts, the dust produced in the death throes of the first wave of stars ironically hides this otherwise brightest stage of a galaxy's life. These events are not completely invisible however: the ultraviolet energy absorbed by the enshrouding dust grains is re-emitted as heat radiation in the far-infrared region of the electromagnetic spectrum, stretched towards microwave wavelengths by the expansion of the Universe during its several-billion-year travel time towards us.

The interstellar gas and dust of these primitive galaxies is critical to their observed properties and evolution; however detecting its signatures at the huge distances of these dusty galaxies is very challenging, requiring long-duration observations with large telescopes, and experiencing further complications arising from atmospheric absorption and/or emission, highly significant at the infrared wavelengths of their brightest emission. Space-based observations negate these atmospheric issues, but are restricted by mirror size and mass, a situation that leads to sources *blending* into one another.

The laws of gravitation, while constraining the mass of telescopes able to be placed in orbit, provide a positive effect that somewhat counteracts this blending. Most famously in the case of black holes, but occurring for all matter, the presence of mass bends spacetime, deflecting even the path of light. Fortuitously positioned foreground galaxies or clusters of galaxies can distort light from distant dusty star-forming galaxies, amplifying the brightness and stretching its appearance into large arcs, allowing us to observe their structure on smaller scales and in a fraction of the usual observation time.

Wide-area far-infrared surveys counter the scarcity of the most extreme cases of this *gravitational lensing*, and have allowed the assembly of a sample of bright yet intrinsically "normal" dusty star-forming galaxies which are much more representative of the population as a whole than the hyper-luminous objects otherwise visible at similar flux densities from these great distances.

This thesis presents and analyses new observations of interstellar gas in distant dusty star-forming galaxies using the uniquely-capable combination of strong gravitational lensing and the SPIRE spectrometer on board the *Herschel Space Observatory*.

Abstract

The most intensely star-forming galaxies lie at $z \sim 2$ and are thought to be the progenitors of the most massive galaxies today, yet study of this important population has been hampered by vast quantities of dust, making them almost invisible in the optical and ultraviolet (UV) regimes, and by the low sensitivity and angular resolution of many infrared (IR) facilities.

Chapter 2 describes the use of the flux and angular extent boost provided by strong gravitational lensing in the detailed study of individual high-redshift dusty star-forming galaxies (DSFGs). The low number density of such systems has been overcome by recent wide area far-infrared (FIR)–mm surveys, and a sample of candidate systems which are bright enough to study with single-dish FIR telescopes are assembled from these surveys. The chapter further describes spectra of these galaxies obtained using the the Spectral and Photometric Imaging REceiver (SPIRE; Griffin et al. 2010) Fourier transform spectrometer (FTS) on board the *Herschel Space Observatory* (Pilbratt et al. 2010), exploiting the increased flux densities to search for FIR atomic and ionic spectral lines: important coolants of warm gas surrounding star-formation regions.

Chapter 3 describes the first "blind" redshift obtained using *Herschel*, via the detection of [C II] 158 µm in one of our spectra. Confirmation of this redshift was provided by detection of CO lines with the Combined Array for Research in Millimeter-wave Astronomy (CARMA) and the Plateau de Bure Interferometer (PdBI), and along with multi-wavelength photometric follow-up, allowed a characterisation of the galaxy, indicating both a merger-driven starburst and an active galactic nucleus (AGN) within the system.

Chapter 4 describes the first detection of a massive outflow of molecular gas at high-redshift. Stacking five repeat spectra of the Cosmic Eyelash, one of the best-studied strongly lensed DSFGs, one of the massive star-forming clumps is shown to drive this outflow, albeit likely at a velocity lower than that required to become unbound from the hosting gravitational potential well.

Chapter 5 describes line measurements and spectral energy distribution (SED) fitting from the full set of spectra and *Herschel* PACS mini scan maps. The spectra are stacked to search for faint lines, and compared to a detailed interstellar medium (ISM) model to determine average physical properties of the star-forming gas. Photodissociation region (PDR) properties are found to be similar to those derived using other models, however a cosmic ray ionisation rate of 10^3 times that of the Milky Way, expected in galaxies of this type cannot reproduce the observed line ratios, in particular the low [O I] 63 µm flux.

Chapter 6 finally describes the conclusions drawn from the work presented in this thesis and how these data and analysis add to our knowledge and interpretation of high-redshift DSFGs.

Contents

List of Figures

List of Tables

Chapter 1

Introduction

Before the significance of FIR spectral observations of high-redshift DSFGs can be understood, the properties and cosmological context of this population must be discussed.

1.1 Cosmology

1.1.1 The Big Bang and the cosmic microwave background (CMB)

Olbers' paradox: that all lines of sight out into the Universe should end on the surface of a star and therefore the whole sky should be as bright as the sun; is now known to be simply a result of the expansion of a finite-age Universe. From Hubble's initial observational evidence of a non-static Universe (Hubble and Humason 1931), this theory has been subsequently developed to suggest an original instant of singularity known as the Big Bang, now supported by many observations. Combining measurements of the CMB power spectrum from *Planck* with CMB polarisation data from the *Wilkinson Microwave Anisotropy Probe* (*WMAP*), high-l data from the ground-based Atacama Cosmology Telescope (ACT; Swetz et al. 2011) and the South Pole Telescope (SPT; Carlstrom et al. 2011), and baryon acoustic oscillations (BAOs) measurements from 6df, the Sloan Digital Sky Survey (SDSS) and Baryon Oscillation Spectroscopic Survey (BOSS; Dawson et al. 2013) currently gives the most accurate values of cosmological parameters and place the time of the Big Bang at 13.8 Gyr before present (Planck Collaboration et al. 2014b). A graphical depiction of the history of the Universe is shown in Figure 1.1.

Today the most commonly-accepted theory of the early Universe is one involving a period of extreme expansion known as *inflation* (Guth 1981; Linde 1982), beginning $\sim 10^{-36}$ s after the Big Bang, during which the radius of the observable Universe increased by a factor of at least 10^{26} (Liddle and Lyth 2000) in $\sim 10^{-32}$ s. The mechanism required to achieve this is thought to involve random quantum fluctuations inducing the phase transition of a scalar field to a lower energy state, releasing that potential energy in the form of radiation and matter (particles).

With the transition from the quark epoch to the hadron epoch, the continual decrease in temperature finally enabled individual quarks to become bound together into baryons and

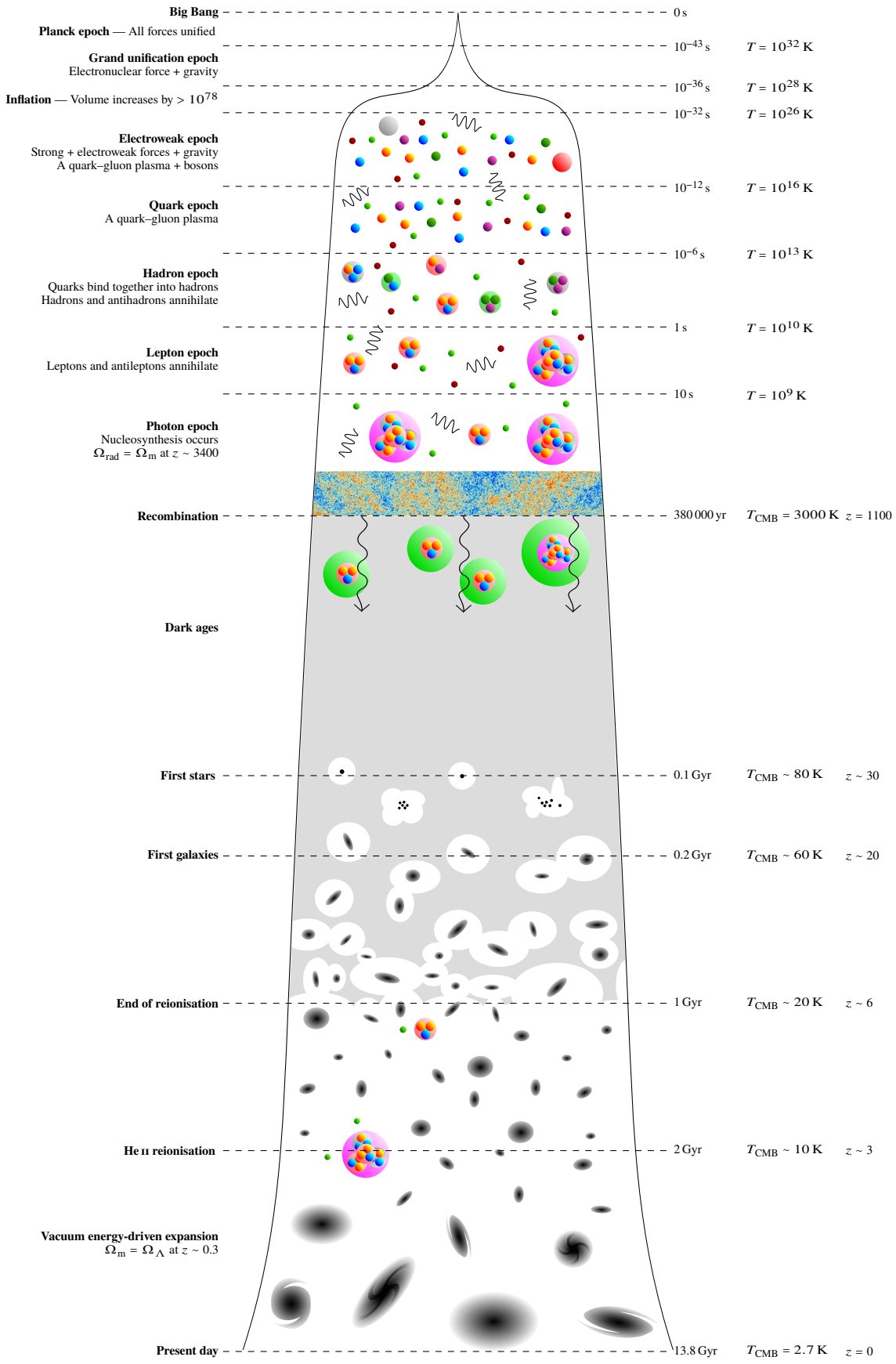

Figure 1.1. The major cosmological events occurring through the history of the Universe. Note that particularly in the early (pre-CMB) Universe, the times and temperatures at epoch boundaries is very uncertain.

mesons. Matter-antimatter annihilation occurred once hadron–antihadron pairs could no longer be produced in thermal equilibrium, leaving a relic population of hadrons likely due to some currently indecisively determined symmetry-violating particle interactions (for a review see Riotto and Trodden 1999). After similar lepton–antilepton annihilation during the subsequent lepton epoch, nucleosynthesis (binding of nucleons into helium and lithium nuclei) ensued during the first few minutes of the photon epoch. Until nuclear fusion within the first stars, these elements were the only ones in existence, and primordial gas of this composition (74 % H, 25 % He, 3×10^{-7} % Li by mass; Coc et al. 2004) is still the dominant repository of baryons in the Universe.

As the average temperature of the expanding Universe decreased below 3000 K, the rate of ionisation of any present atomic hydrogen finally became equal to the rate of combination of electron and proton to form atomic hydrogen. At this point, approximately 380 000 yr after the Big Bang (Planck Collaboration et al. 2014b), one of the most dramatic physical changes in the history of the Universe occurred, with the chemical state of matter changing from an optically thick plasma to an optically thin neutral gas. This event has become known as *recombination*, however since at no point previously had the Universe been composed of primarily neutral particles, a better name is *combination*. The vast reservoir of photons previously scattering off charged particles, now unable to maintain the ionised fraction of hydrogen, were released and have since travelled across the optically thin Universe. Observing these photons describes their *surface of last scattering*, showing temperature variations at the 0.001 % level (Planck Collaboration et al. 2014a), a fingerprint of seed perturbations in the density of the Universe. The large angular scale of these fluctuations is amongst the strongest evidence for inflation, which would have allowed a smaller Universe pre-expansion, and hence diffusion of energy from over- to under-densities, smoothing on small scales.

A commonly used measure of the expansion of the universe is redshift, denoted by the letter z, and defined as the ratio of the difference between the observed and emitted wavelengths from a moving source, to the emitted wavelength, due to the Doppler effect

$$z = \frac{\lambda_{\mathrm{obs}} - \lambda_{\mathrm{emit}}}{\lambda_{\mathrm{emit}}} = \frac{\lambda_{\mathrm{obs}}}{\lambda_{\mathrm{emit}}} - 1 = \frac{\nu_{\mathrm{emit}}}{\nu_{\mathrm{obs}}} - 1. \tag{1.1}$$

For remote objects: where peculiar velocities are negligible in comparison to the contribution due to expansion of the Universe, or in lieu of independent measurements; redshift is typically used to describe the intervening distance and hence light-travel time.

1.1.2 Formation of baryonic systems in dark-matter haloes

Stars in the outskirts of disc galaxies orbit the centre of the galaxy more rapidly than expected given the observed stellar mass enclosed within that radius (Persic, Salucci, and Stel 1996, and references within). As further evidence mounted, including measurements of the velocity dispersion of elliptical galaxies and of CMB fluctuations, a theory came to be commonly accepted of a source of matter effectively invisible to electromagnetic radiation and only discernible by its

gravitational effect on nearby baryonic material – *dark-matter*.

Comprising a large fraction of the energy density of the Universe since early times, dark-matter has had a dominant effect on the growth and distribution of structure throughout the Universe, traced today by galaxies and clouds of neutral gas along quasar sight-lines (Rauch 1998). The most direct evidence of dark-matter however is due to gravitational lensing, and in particular the Bullet Cluster and MACS J0025.4-1222, systems thought to represent the first passage of two interacting galaxy clusters, in which the x-ray-emitting intra-cluster gas of each component displays an offset to the lensing-determined dark-matter (Bradač et al. 2008). Measurements of the power spectrum of the CMB have provided the most precise estimates of the energy fraction in dark-matter: data from *Planck* + *WMAP* polarisation + ACT + SPT + BAO suggest $\Omega_{\rm dm} = 0.2582 \pm 0.0056$ (Planck Collaboration et al. 2014b).

Baryons are gravitationally attracted to dark-matter overdensities and are therefore good tracers of the large-scale dark-matter structure. The baryonic content of the Universe exists in several different phases. At all epochs most of the baryonic content exists in the intergalactic medium (IGM): even by $z = 0$ only ~15 % is found within galaxies (Salucci and Persic 1999; Fukugita and Peebles 2004), the intracluster medium (ICM) (Fukugita and Peebles 2004) and circumgalactic medium (CGM) (Shull, Smith, and Danforth 2012) together. Within the IGM, the fraction extant in each physical phase has varied with redshift. Neutral gas has contained no more than ~3 % since $z = 4$ (Noterdaeme et al. 2009), even less than is currently contained within stars (Cole et al. 2001). Measurements towards distant quasars of the low opacity of the IGM to photons blueward of Lyman-alpha (Lyα) indicates a warm (10^4 K) photoionised component. This is dominant at high redshift, containing $\gtrsim$90 % of the baryon budget of the Universe at $z \sim 3$ (Rauch et al. 1997; Prochaska and Tumlinson 2009), but declining to 30 % by $z = 0$ (Danforth and Shull 2008). The warm-hot IGM (WHIM), at $T = 10^5 - 10^7$ K is probably shock excited and may may be detected via broad Lyα absorption features (Lehner et al. 2007; Danforth, Stocke, and Shull 2010), and absorption lines of O VI (Smith et al. 2011; Tilton et al. 2012). Cosmological simulations (Cen and Ostriker 1999; Davé et al. 2001; Smith et al. 2011) have predicted that the WHIM also contains the additional large proportion of baryons currently not reliably detected (Yao et al. 2012). Detections of weak X-ray absorption features from even more highly ionised metal species (O VIII, Ne IX and others; Cen 2012; Shull, Smith, and Danforth 2012) may in the future confirm that this phase contains up to 60 % of all baryons (Shull, Smith, and Danforth 2012).

The dark-matter and baryon distribution throughout the Universe is not homogeneous, and changes with time, influencing all other matter. An understanding of this dominant matter component is therefore essential for studies of galaxy formation and evolution.

1.1.2.1 Dark matter collapse

With the primary force able to act on dark-matter – gravity – exclusively attractive, overdensities will enlarge with time. From a theorised initial uniform distribution with Gaussian random

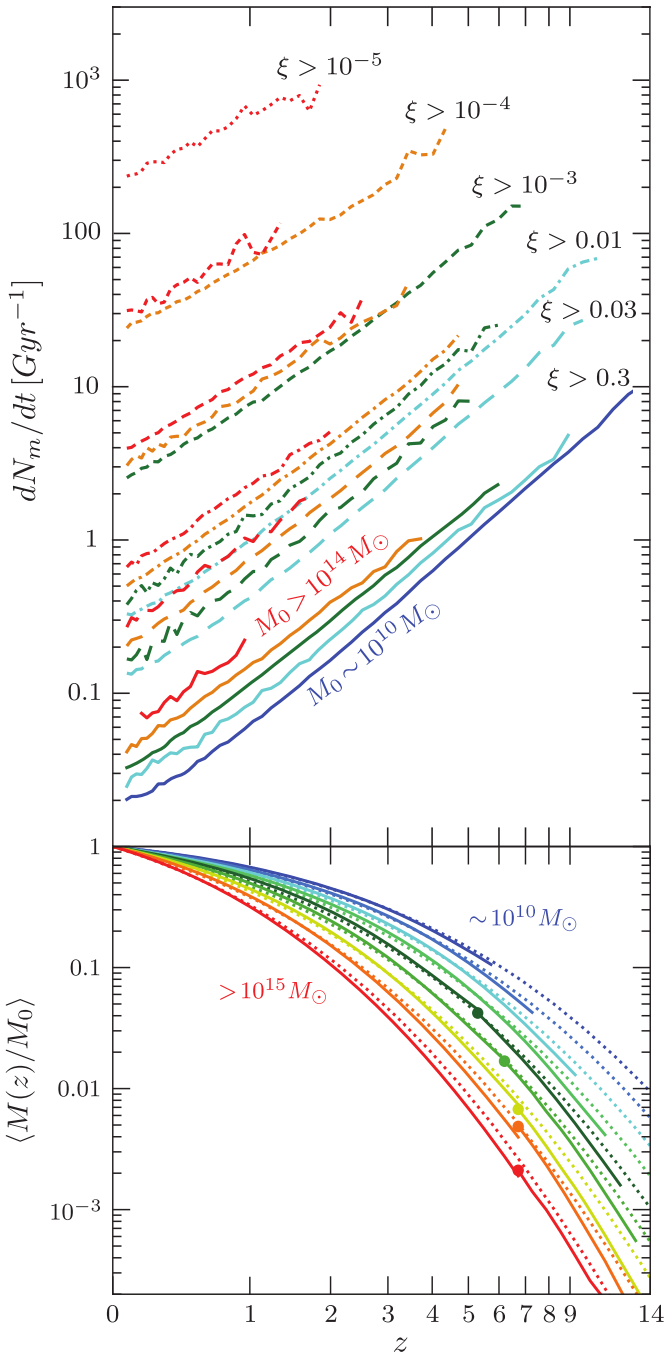

Figure 1.2. *Upper*: Rate of mergers of different larger to smaller component mass ratio ξ as a function of redshift from the Millennium I and II simulations.
Lower: Mass growth of haloes as a function of redshift.
Adapted from Fakhouri, Ma, and Boylan-Kolchin (2010).

seed perturbations (Komatsu et al. 2003, and references therein), a complex web of dark-matter filaments has been shown to emerge in cosmological simulations (e.g. Springel et al. 2005) and exist at our current and past epochs in observational data (e.g. Gott et al. 2005): funnelling both dark-matter and gravitationally-bound baryons towards those larger overdensities at knots and intersections of the web. Positive feedback accelerates this process, with the largest haloes over 10^{15} $M_\odot$ at the present day, and huge underdense voids opening in other locations.

At $z \lesssim 15$ the more massive haloes host galaxies and associated smaller satellites. The distribution of dark-matter density with radius in haloes is therefore of interest. While early dark-matter-only simulations produced important results, including the commonly-used NFW profile (Navarro, Frenk, and White 1997), the true form is non-trivial, depending on the total (dark-matter + baryonic) matter distribution, which in turn depends on the gravitational potential at earlier times, and any energy/momentum input to the baryonic component during that interval.

The free-streaming length of a dark-matter particle determines the scale of structure formed, and compared against the size of observed protogalaxies can be used to define an effective temperature, where *cold dark-matter (CDM)* particles have small free-streaming lengths. Some component of unknown size almost certainly consists of baryonic CDM in the form of massive compact halo objects (MACHOs) (Tisserand et al. 2007): cool white dwarf stars, neutron stars and black holes; these could represent a significant fraction of dark-matter mass in inner galactic regions. The composition of the dominant dark-matter particle is still unknown however and the exact effective temperature remains a contentious issue. Sterile neutrinos (a species that may only interact via gravity) are a *warm dark-matter (WDM)* candidate, but warm and hot dark-matter will smooth out small-scale structure. CDM candidates include axions and weakly-interacting massive particles (WIMPs), which are the currently favoured particles and include a lightest supersymmetric particle (LSP) (Bertone, Hooper, and Silk 2005).

Shown in Figure 1.2 are merger and mass growth rates as a function of halo mass and redshift from simulations. The visible increase in major merger rate with halo mass is at first glance unintuitive as the global number density of massive haloes is much lower than of those with lower masses (Jenkins et al. 2001). Small haloes have survived with low masses to the present day (necessarily experiencing little growth and without being merged into a larger halo) through being preferentially located in voids or other low density environments, in which mass accretion and merger rates are and have remained low. Merger rates are particularly important to understand as the mass growth of dark-matter haloes (at least at the high mass end) is dominated by mergers rather than accretion (Fakhouri, Ma, and Boylan-Kolchin 2010), causing similar mergers between the galaxies contained inside the haloes.

1.1.2.2 Galaxies in a cosmological context

While the first stars may well have formed in isolation, as halo sizes increased later stars will have formed in small associations, larger hundred-pc scale clusters, and eventually within the first galaxies.

A galaxy is a gravitationally-bound system of dark-matter, stars, interstellar media and other subdominant components such as stellar remnants and planetary systems. They now exhibit a vast range of morphologies and sizes, ranging from $\sim 10^{14}$ stars in the most massive brightest cluster galaxies (BCGs) to $<10^{6}$, this diversity arising from the specific events of their lives to this point. The primary classes of galaxy in existence have varied through each epoch of the Universe: mergers, starbursts and AGN producing rapid changes on top of gradual evolution

from small and active to large and passive.

This first generation of galaxies have yet to be observed, but new and upcoming major facilities such as the Atacama Large Millimeter Array (ALMA), the James Webb Space Telescope (JWST), the Square Kilometre Array (SKA) and the European Extremely Large Telescope (E-ELT) will spearhead search efforts. Several galaxies at $z \sim 10$ have been observed (e.g. Bouwens et al. 2014; Oesch et al. 2014), however none of these have been spectroscopically confirmed. The first galaxies are predicted to lie at $z \sim 15-20$ (e.g. Bromm and Larson 2004), but being located within small haloes were likely susceptible to dissociation from supernovae (SNe).

Infalling dark-matter, primarily along the narrow discrete filaments (Stewart et al. 2011) feeding each large halo, pulls with it a stream of primordial intergalactic gas. Throughout the early life of a massive galaxy, this gas replenishes that converted to stars, fuelling the secular growth now thought by many to dominate the stellar population of most galaxies. Moreover, in a battle against the expansion of the Universe, the continual evolution of large-scale dark-matter structure under gravity can overcome the increasing separation of galaxies on short scales, leading to mergers of dark-matter haloes and the creation of large gravitationally-bound groups and clusters.

As with their enclosing dark-matter haloes, with a high enough reduction in their angular momentum galaxies may merge, and indeed much of the cosmic evolution of galaxies is driven via mergers. While stars are essentially collisionless point-masses and in that regard may act like dark-matter, the interstellar gas also present is strongly affected by merger events, becoming heated and compressed and star formation is triggered. A distinction can therefore be made between "wet" and "dry" mergers: those in which both galaxies contain significant gas reserves, and those in which there is little gas. Of course most events will lie between these extrema, effecting some star formation and contributing existing stars.

A major merger is classified as one involving mass ratios smaller than around 1:3. As first-passages of even minor mergers are often marked by extended tidal tails (Martínez-Delgado et al. 2010), both components of a major merger usually exhibit significant morphological disturbance or more even extreme asymmetries in their light distribution. A major merger lasts for only ~0.7 Gyr, and towards final coalescence of the galactic cores, the star formation rate peaks for around 100 Myr as an intense nuclear starburst (e.g. Narayanan et al. 2010), fuelled by gas torqued inwards by angular momentum transfer. Following a major-merger induced starburst, many observations and simulations predict a transition of the combined system to an early-type galaxy (e.g. Bernardi et al. 2010; Bournaud et al. 2011), and indeed an event of this nature may be required for the formation of all massive ellipticals (van der Wel et al. 2009). Implications of major mergers for DSFGs, a population within which these events seem to be prevalent, are discussed in Section 1.3.

Minor mergers have a higher occurrence rate than more equal-mass events and so while a galaxy may experience little effect from each minor merger individually, its stellar mass buildup can become dominated by these events combined, particularly for the case of more massive $M_* > 10^{11}\,\mathrm{h}^{-1}\,\mathrm{M}_\odot$ galaxies (Guo and White 2008; Cattaneo et al. 2011). Size evolution is

also expected to be governed by minor mergers (McLure et al. 2013), with over half resulting from mergers of ratio 1:10 or lower (López-Sanjuan et al. 2012). Some fraction of the minor mergers experienced by the most massive galaxies will involve the accretion of satellites formed or becoming bound for extended time periods within the larger dark-matter halo of the central object. Such satellites are located in small subhaloes, the shallow potential wells resulting in easy removal of gas (which will accrete onto the central galaxy) by SNe and ram pressure/dynamical friction, and an eventual cessation of star-formation. The satellites, now with small ($\sim 10^7$ $M_\odot$) ageing stellar populations and high mass-to-light ratios will experience tidal stripping of stars, and after enough angular momentum loss will themselves eventually merge with the central object. Star formation within many ellipticals has been re-ignited since $z \sim 0.2$ by such events (Thomas et al. 2010).

Particularly at high-redshift, where spectroscopy and imaging at high enough resolution to detect morphological evidence of mergers is expensive, cosmological simulations provide more easily obtainable (and possibly more reliable) results. While dark-matter-only simulations have produced results that are well understood and consistent, the details of baryonic physics, particularly on scales smaller than the simulation resolution, "subgrid physics", are much more complex and no simulation has so far reproduced all observations *ab initio*. Current challenges include reproducing the metallicities (Schaye et al. 2015) and stellar ages of low-mass galaxies (Vogelsberger et al. 2014), partly due to overly-efficient cooling resulting from this higher metallicity, the nature and strength of AGN feedback (Genel et al. 2014), radiation transport and magnetic fields (Schaye et al. 2015). Despite this, modern simulations have provided new insights and predictions otherwise unobtainable.

The variety and nature of galaxies at low and high redshift is discussed in greater detail in Section 1.3. Many of the most important internal processes and observational targets of galaxies however arise within the ISM, and it is therefore instructive to first explore this critical component of a galaxy.

1.2 The interstellar medium (ISM)

In our local environment, only 3×10^{-10} of space is occupied by stars and planetary systems (Tielens 2005): the remainder holds the ISM. The ISM of a galaxy is a tenuous mixture of atomic, ionic and molecular hydrogen, helium, and a sprinkling of heavier elements, existing in several distinct phases embedded within one another.

This often-overlooked component of a galaxy is the source of all stars and a repository of the scattered ashes of most, and an understanding of the ISM is critical for our understanding of the variety and evolution of galaxies, explored in the next section.

1.2.1 Spectral emission lines

The broad continuum black-body emission from stars in the UV, optical and near-infrared (NIR), dust in the mid-infrared (MIR) and FIR, and synchrotron emission in the radio dominates the electromagnetic output of galaxies, but at higher spectral resolutions narrow bright and dark lines become visible. It is difficult to observe the stellar continuum from high-redshift DSFGs due to dust extinction, but the unique set of lines for each chemical species can be used as a fingerprint, and line profiles, ratios and spatially resolved emission can reveal the physical state of the ISM and indicate the intensity, distribution and mechanics of star-formation within these systems, and as such study of these spectral lines is of great interest.

1.2.1.1 Primary emission lines from galaxies

Several of the brightest and most important spectral emission lines are described below.

Lyα:
Lyman alpha is the $n = 2 \rightarrow 1$ transition of H, producing a photon of wavelength 121.6 nm. As the most easily-excited transition of the most abundant element in the ISM (yet still requiring 10.5 eV $\sim$ 120 000 K), Lyα is often the brightest emission line from any galaxy, in particular from low-mass high-redshift star-forming galaxies. The Lyα cross section for interactions is $\sim 10^6$ times the average cross section for ionising photons in the Lyman continuum, so its optical depth is 10^6 (compared to $\sim$1 for other ionising photons). At a density of 10^3 cm^{-3}, a median Lyα photon will therefore perform a random walk between scattering interactions with neutral H atoms, travelling <100 au in total before being absorbed by a dust grain, and as a result is an important source of dust heating in H II regions. Within PDRs, Lyα emission from collisionally excited hydrogen atoms is one of the primary thermostat lines, limiting gas to $\sim$10 000 K across a range of input energy fluxes too high to be regulated by FIR cooling lines. Lyα may also be seen in absorption towards distant quasars, as Lyman continuum photons are redshifted to this frequency at the positions of neutral clouds tracing minor overdensities along the line of sight, producing a feature known as the Lyα forest.

[C II] $^2P_{3/2} \rightarrow ^2 P_{1/2}$ 157.7409 µm:
C II is the dominant ionisation state of this comparatively common element throughout much of the ISM. Despite being a magnetic dipole transition and hence *forbidden*, with a rate 10^{14} times lower than that of Lyα, [C II] 158 µm is typically the strongest FIR emission line ($T_{\rm ul}$ = 92 K), providing 0.1 – 1 % of the measured FIR flux (Stacey et al. 1991). The optical depth of this transition depends on the size of emitting regions, however it is typically below unity. Unlike neutral or higher-ionisation lines (e.g. [O I], [N II]; see Section 1.2.3.1), production conditions can be found in both H II regions and PDRs, complicating analysis when only a galaxy-integrated flux is available. This line is usually collisionally excited either by electrons in H II regions ($n_{\rm crit} \sim 10$ cm^{-3}), or by atomic or molecular hydrogen in more neutral regions which are too diffuse to be bright in CO ($n_{\rm crit} \sim 3 \times 10^3$ cm^{-3}). Figure 1.5 indicates the use of this line as a diagnostic of the physical conditions within PDRs, of which it is one of the most useful tracers,

particularly in cooler and more rarefied examples. The high efficiency of this and other FIR cooling lines can maintain gas at ~100 K across a range of energy input fluxes. Should the heating rate overcome this cooling ability however, the gas temperature will increase until balanced by transitions between low electronic levels in trace metal species and Lyα at 5000 – 10 000 K, creating a dichotomy across much of the ISM. Despite its relative brightness, its location in the FIR has in the past restricted observations of this line, particularly for extragalactic sources. With ALMA recently operational however, this line has become one of the primary diagnostic targets at high-redshift (e.g. Swinbank et al. 2012; Wagg et al. 2012; Ota et al. 2014; Riechers et al. 2014b). New detections of [C II] at redshifts corresponding to the peak of star-formation are presented in later chapters of this thesis, and analysed against these ALMA findings amongst others.

CO:

CO is the second most common molecule in the ISM, with an abundance of $\sim 10^{-4} - 10^{-5}$ of that of H_2. The nuclei are bound by a covalent triple bond, however four of the six shared electrons are donated by the oxygen atom, leaving a net small positive charge, and an equivalent negative charge on the carbon atom. The resultant dipole moment is small (0.122 Debye), but as the dominant molecular species H_2 has identical nuclei and can only emit weakly via forbidden quadrupole rotational and ro-vibrational transitions starting in the MIR (see Figure 1.6), CO emission has therefore become a primary target for observations of galactic and extragalactic interstellar molecular gas. Being excited at typical giant molecular cloud (GMC) temperatures and densities (5.5 K and 1.1×10^3 cm^{-3} for $J = 1 \rightarrow 0$), the mm–FIR rotational transitions are the most commonly observed. Higher J transitions are excited at higher densities or temperatures (e.g. 1.3×10^5 cm^{-3} for $J = 6 \rightarrow 5$; see Figure 1.6 for details of this and a comparison to other molecular lines), and are reasonable tracers of the regions of brightest FIR emission. The high column densities present in molecular clouds lead to optical depths greater than unity, particularly among the lower J transitions which trace more extended, diffuse gas than the higher energy transitions (e.g. $J = 6 \rightarrow 5$). In addition to limiting the use of ^{12}CO radiation for estimates of cloud mass, different spectral line energy distributions (SLEDs) will be determined depending on the depth and hence temperature at which these photons can escape. Several factors complicate the use of CO lines as diagnostic tools however: cosmic rays and shocks (e.g. Papadopoulos et al. 2012b), X-rays (e.g. van der Werf et al. 2010) and even high dust optical depths (Papadopoulos et al. 2010) can dominate the intensities of certain CO lines, often resulting in a SLED similar to that produced by stellar radiation excitation. At higher densities, isotopologues such as ^{13}CO can provide significant emission due to its optically thin nature, despite a lower abundance $\left({}^{13}\mathrm{CO}/{}^{12}\mathrm{CO} = 1/65 \text{ in the ISM; Tielens 2005} \right)$, even reaching similar observed line intensities to ^{12}CO in some instances. These isotopologues can thus probe a much larger volume and provide better mass estimates where bright enough to detect (e.g. Danielson et al. 2013).

Polycyclic aromatic hydrocarbon (PAH):

As well as features characteristic of single- and few-nucleus species, those of aromatic species

are also present in spectra of the ISM, indicating that large carbon-based molecules in addition to classical grains constitute the dust component. Systems of fused aromatic (benzene) rings, PAHs are the likely perpetrators, typically with sizes <1 nm and containing ~50 carbon atoms. Interestingly, the existence of these molecules gives space a noticeable *smell* (ISS Science Officer Don Pettit 2003).

These atoms form covalent bonds with three others in a plane, while the remaining electrons lie in a delocalised cloud above and below this plane, as the electronic orbitals of neighbouring atoms overlap. A UV photon may be absorbed causing electronic excitation, which is transferred to vibrational excitation of the molecule. Radiation of this energy though IR fluorescence is responsible for their contribution to interstellar spectra, primarily a series of broad emission lines in the MIR (Leger and Puget 1984). Both dust and stellar emission is relatively weak in this frequency regime and star formation can provide the energy output required to heat these molecules without significant destruction, allowing PAH emission to dominate the radiated power in the MIR. Only in quasi-stellar objects (QSOs) with very hot dust and a high flux of photons capable of dissociating PAHs is this situation different. PAHs are important for balancing ionisation rates within the ISM, so an understanding of these are necessary for interpreting measured line ratios from other interstellar species.

1.2.1.2 Other far-infrared spectral lines

Several other rest-frame FIR emission lines are also relatively bright and present useful diagnostics of the ISM in source galaxies. Figure 1.3 shows the $n_{\rm crit}$ and ranges of ionisation energies within which these lines may be produced.

[O I] $^3P_1 \rightarrow ^3 P_2$ 63.184 µm

This is one of the strongest PDR cooling lines, which with a hydrogen collision critical density of 9.7×10^5 cm^{-3} and transition energy of 228 K dominates over [C II] at higher temperatures and densities — see Figure 1.5. Unlike [C II], little flux is contributed by H II regions making this a "cleaner" tracer of PDRs, however with a typical optical depth of 1 – 3 (Tielens 2005), exact conversions of line flux to gas conditions are difficult. This line also is strong relative to [C II] when arising from shockheated (rather than photoheated) gas, particularly within high column density regions where most carbon exists within CO. As the brightest two FIR lines, ($L_{\rm [C\,II]\,158\,\mu m}$ + $L_{\rm [O\,I]\,63\,\mu m}$) / FIR therefore provides a measure of photoelectric heating efficiency.

[O I] $^3P_0 \rightarrow ^3 P_1$ 145.525 µm

This faint line can be used along with [O I] 63 µm to determine the ionisation-independent temperature and density, having a lower critical density of 1.5×10^5 cm$^-3$ and transition energy of 98 K, similar to that of [C II].

[O III] $^3P_1 \rightarrow ^3 P_0$ 88.356 µm

The requirement of 35 eV photons to reach this ionisation state restricts this species to H II regions. Unlike its bright 500 nm counterpart, the low excitation energy of 160 K however desensitises this transition to temperature, as such the observed flux is governed primarily by the ionisation

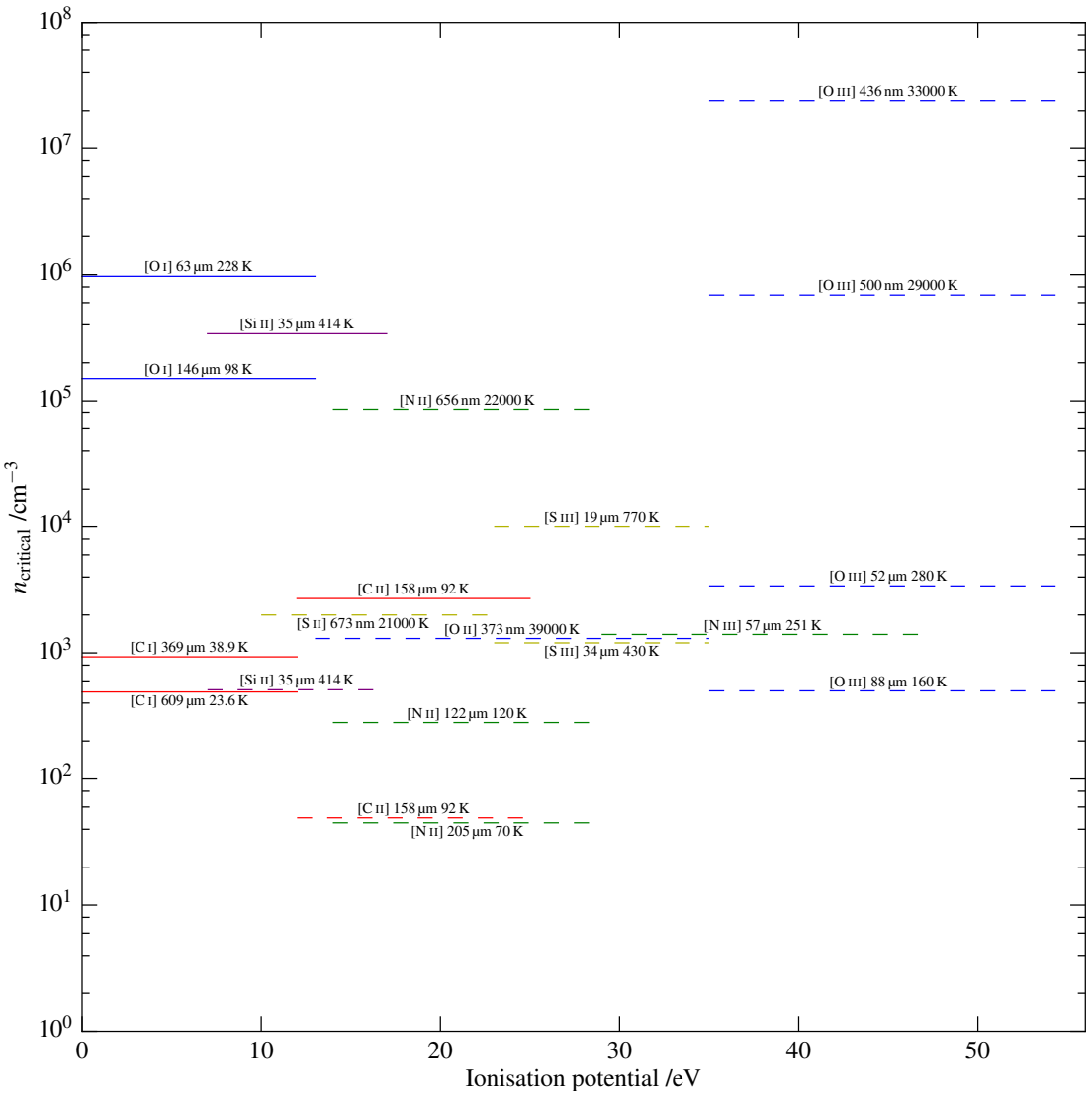

Figure 1.3. Critical densities and collisional excitation temperatures of several important PDR and H II region spectral emission lines. Coloured lines show the range of ionisation energies in which the chemical species may be found, elements distinguished by colour. Solid lines indicate number density ns within a 100 K PDR, where the chemical species are primarily excited by collisions with neutral hydrogen. Dashed lines indicate critical densities a within a 10 000 K H II region, where collisional excitation by electrons is dominant. Data from Tielens (2005).

structure.

[N II] $^3P_2 \rightarrow ^3 P_1$ 121.898 µm

[N II] has a critical density similar to [O III] but a lower ionisation potential, making the ratio of these lines a useful tracer of the H II region ionisation parameter U (defined in Section 1.2.3.1, also see Ferkinhoff et al. 2011).

OH $^2\Pi_{3/2}$ $J = \frac{3}{2} \rightarrow \frac{5}{2}$ 119.3 µm

While not an atom/ion like the producers of most FIR lines, the OH radical exhibits several FIR transitions and a dipole moment of 1.668 Debye which is around 15 times that of CO. Its usefulness is however restricted by the very large density required for thermalisation, and so

while emission from photoexcitation is possible, this ground-state transition (actually lambda-doubled into 119.233 and 119.441 μm lines) is more readily seen as a strong absorption feature. See Chapter 4 for more details, particularly for its use as a tracer of star-formation/AGN-driven outflowing molecular gas. The 79 μm cross ladder transition (between the two total angular momentum states $\Pi_{1/2}$ and $\Pi_{3/2}$) may however receive more attention in the future as the Space Infrared telescope for Cosmology and Astrophysics (SPICA; Swinyard et al. 2009) will cover this line across a range of redshifts hosting high-redshift DSFGs.

1.2.2 Dust

By mass, approximately 1 % of the ISM is in the form of dust (e.g. Spitzer 1978; Dunne, Eales, and Edmunds 2003; Sandstrom et al. 2013). The dominant ISM components (H and He) are light however, and so dust may contain a large fraction of the metals within the ISM. Despite very low number densities (1×10^{-10} H atom^{-1} for 10 nm grains (Weingartner and Draine 2001)), dust grains play several highly significant roles in the ISM and for the evolution and observed properties of stars and galaxies.

Grains sizes range from $10^{-4} - 1$ μm (Weingartner and Draine 2001). In addition to this size range, dust grains do not have identical compositions, the principal types being silicate- and carbon-based. The size and composition of a grain affects the conditions required for formation, typically within SNe (Rho et al. 2008; Dunne et al. 2009; Barlow et al. 2010) or asymptotic giant branch (AGB) ejecta (Gehrz 1989; Ferrarotti and Gail 2006; Sargent et al. 2010a). The ratio of carbonaceous to silicate grains may change with time after a starburst as carbon-based grains are typically larger and more able to withstand the formation conditions in SNe, with the silicate grain fraction increasing later with the occurrence of AGB stars (Draine 2003). Destruction of grains can occur through sputtering, high-velocity collisions or sublimation (Jones et al. 1994), and a once a galaxy transitions to an elliptical, a lifetime of only several $\times 10^7$ yr is predicted (Clemens et al. 2010).

Below ~200 K, grain surfaces are often covered with mantles of H_2O or NH_3 ices. These surfaces are an important site of interstellar chemical reactions, in particular hosting the dominant formation mechanism of H_2 at non-zero metallicity. Dust is thus required for the formation of stars in the local Universe.

Dust absorbs incident UV and optical radiation, making galaxies more difficult to observe, and changing estimates of properties derived from UV and optical observations such as stellar mass, star formation rate (SFR), time since a star-formation episode and UV spectral slope β. A further effect is differential extinction — while most stellar continuum emission experiences attenuation from the diffuse ISM with an $A_\lambda \propto \lambda^{-0.7}$ frequency dependence, with older cooler stars experiencing less light scattering and absorption than younger stars, the dense birth clouds surrounding massive stars block most continuum radiation and cause the remaining transmission (mostly spectral lines) to experience a screen-like and greater level of extinction with a different frequency dependence of $A_\lambda \propto \lambda^{-1.3}$ (Charlot and Fall 2000; Wild et al. 2007; da Cunha,

Charlot, and Elbaz 2008).

The absorbed energy is emitted as thermal radiation in the FIR. This dust emission peaks at around 100 µm and resembles that of a black body, the spectrum of which depends only on temperature:

$$B_{\nu_{\text{rest}}}(T_{\text{rest}}) = \frac{2h\nu^3}{{c_0}^2} \frac{1}{e^{\frac{h\nu_{\text{rest}}}{k_B T_{\text{rest}}}} - 1}. \tag{1.2}$$

Measured spectra are better fit by a *grey* body function: a black body with some non-unity emissivity ε: this property is a measure of the ability of a material to absorb and emit electromagnetic radiation. The value will vary with frequency, and is often parametrised as

$$\varepsilon \propto \nu^{\beta}, \tag{1.3}$$

where β is the dust mass temperature index (not to be confused with the similarly-denoted UV spectral slope), for which a value of 1.5 is often used, however an average Galactic value 1.8 ± 0.1 is found by *Planck* (Planck Collaboration et al. 2011b). Theoretically it should relate to the fractal dimensionality of the dust D as $\beta = D - 1$ and so should lie between 1 and 2 (Yang and Phillips 2007), however the exact value will have a more complex dependence on the physical characteristics of the emitting grains including composition and details of any ice mantle. An inverse correlation between β and temperature has been noted in the laboratory (Mennella et al. 1998), and also in astronomical observations, with lower β values observed in star-forming galaxies and circumstellar envelopes (Knapp, Sandell, and Robson 1993; Dunne et al. 2000; Yang and Phillips 2007). Primarily a function of UV radiation intensity, dust temperatures exhibit little variation with radiation hardness, but do depend on the individual grain size and structure. Very small grains cannot be thermalised and experience large variations in their temperature upon absorption of a UV photon. A power-law spectrum is observed from these grains as they can be significantly smaller than the wavelength of emission.

An alternative to this simple dependence of the emissivity on frequency is to note that the dust optical depth is not constant across the emission peak: radiation on the Rayleigh-Jeans side is essentially optically thin, while that emitted by hotter grains has $\tau > 1$. The optical depth can hence be expressed (Kovács et al. 2010) as

$$\tau_{\nu} \propto \kappa_0 \left(\frac{\nu}{\nu_0} \right)^{\beta}, \tag{1.4}$$

where κ_0 is a normalisation constant known as the dust mass absorption coefficient: the characteristic photon cross section to mass ratio of particles at some measured frequency ν_0; experimentally determined to be $\sim(0.10 \pm 0.05)\,\text{m}^2\,\text{kg}^{-1}$ at 850 µm (Bianchi, Davies, and Alton 1999; James et al. 2002; Dunne, Eales, and Edmunds 2003), with an uncertainty based on the uncertainty in β and range of published estimates. The emissivity can then be related to the optical depth as $\varepsilon = 1 - e^{-\tau}$, leading to the extrema: if $\tau \gg 1$ then $\varepsilon \to 1$; if $\tau \ll 1$ then $\varepsilon \to \tau$.

A further source of interstellar IR emission often classified with dust are PAHs. These are

described in Section 1.2.1.1.

1.2.3 The phases of the interstellar medium

The phases of the ISM are usually described in terms of the chemical state of hydrogen.

Molecular hydrogen, H_2, forms on the surface of dust grains and if sufficiently shielded can form large dense clouds known as giant molecular clouds (GMCs). These clouds are the birth sites of stars, and the formation of a massive ($M \gtrsim 10\,M_\odot$) star within a GMCs causes a dramatic physical change in its local environment. The intense flux of high-energy photons emitted by the star dissociates and ionises the surrounding molecules, forming an H II region, named after the dominant chemical species. Bounding this, on the surface of denser molecular regions exists a PDR, a transition zone between fully ionised and fully molecular gas, in which the physical processes are still primarily powered by the incident UV photons, but the ionisation and recombination times are now more equal, allowing atomic states to exist.

These are not the only phases within the ISM however. The neutral atomic component dominates the mass fraction, existing primarily as either of two temperatures ~100 and 8000 K, regulated by FIR fine-structure lines, in particular [C II] and optical/UV lines, in particular Lyα, respectively which act to counter heating sources (Tielens 2005). Dispersion of pulsar signals has indicated a warm (8000 K) ionised phase of the ISM, in essence a diffuse ($\sim 10^5$ m^{-3}) large-scale H II region. As with their denser, more localised cousins, the dominant input energy flux is radiation from O and B stars. In addition, SNe and stellar winds from massive stars release huge amounts of mechanical energy, opening bubbles in the surrounding ISM of very low density (~3000 m^{-3}) and high temperature (10^6 K). OB associations can form super-bubbles, and eventually vent this hot intercloud medium (HIM) into the halo, eventually *raining* back onto the disc, $\sim 5\,M_\odot$ yr^{-1} transitions each way.

A convenient unit of measurement for dealing with the variety of conditions encountered is optical depth: a PDR lies at $0.5 < \tau_V < 3$, and the densest cores within a GMC can reach $\tau_V > 30$. A depiction of this showing important chemical species extant at each optical depth is given in Figure 1.4. Optical depth is largely determined by grain number densities and properties. Dust can both absorb and scatter photons, the wavelength dependence of the emissivity leads to interstellar reddening, with the more numerous smaller grains affecting redder photons less. The strong spectral line emission of H II regions, PDRs and GMCs is particularly useful for highly optically-obscured systems such as DSFGs, in which the direct stellar emission may be too faint to derive useful properties. While contributing little to the total ISM mass, dust dominates the total ISM luminosity, with significant additions from transition line emission (particularly Hα and forbidden lines of heavier elements). More detail is given on these environments below.

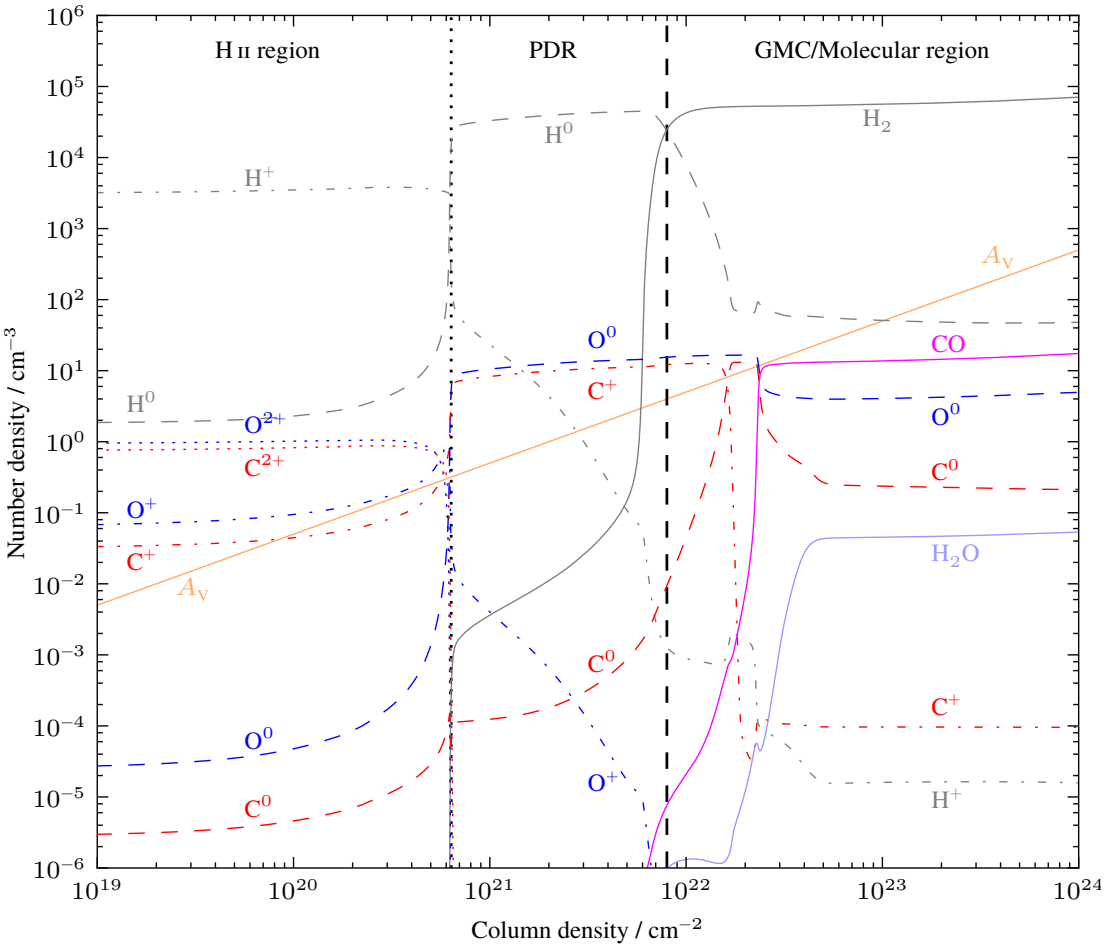

Figure 1.4. The primary features and chemical species present during the transition from a H II region (left hand side) via a PDR to a GMC (right hand side). The exact values of column density/extinction/optical depth ($A_V \sim 1.086\tau_V$) at which the dominant chemical species transitions occur depends on the gas density, flux of ionising photons, dust properties and other parameters. Model based on that of Abel et al. (2005), see Section 5.3.3 for further details.

1.2.3.1 H II regions

H II regions are pockets within the ISM within which hydrogen is predominantly ionised, typically surrounding individual or complexes of massive stars. The ionisation may be described by an "ionisation parameter" $U = \frac{\phi_H}{n_H c}$, where ϕ_H is the flux of photons capable of ionising hydrogen. Typically $10^{-4} < U < 10^{-1}$ (Veilleux and Osterbrock 1987).

The boundary of an H II region is sharp, transitioning from almost fully ionised to almost fully neutral in ~0.1 pc, across the surface where the hydrogen ionisation time equals the recombination time. For an isolated star, this is also known as the Strömgren radius, and while possessing a dependence on gas density, typically exists at over 1 pc for the hottest O stars. Approaching this boundary, the radiation field becomes harder due to the preferential excitation of H I by lower-energy photons. This hardening has the effect of raising the electron temperature by several thousand K, allowing emission from UV lines such as [O II] 373 nm. Despite a typical neutral hydrogen fraction of $\sim 10^{-3}$, radiative recombination takes ~100 yr, as the recombination

coefficient varies inversely with electron temperature.

Much of the cooling of H II regions is through emission lines of ionised trace metal species. Close to hot O stars there is often emission from highly ionised species such as He III, O IV and N IV, but across the bulk of H II region conditions, O III, O II and N II lines are more common. Up to 50 % of [C II] flux can also arise from these environments, complicating efforts to estimate gas conditions and masses from this strong FIR transition. Figure 1.3 displays several of the key H II region cooling lines. Strong Balmer lines (Hα and Hβ) are also seen from H II regions, and a comparison of these line strengths to emission lines of higher-ionisation metal species at similar wavelengths can provide a powerful diagnostic: the Baldwin-Phillips-Terlevich (BPT; Baldwin, Phillips, and Terlevich 1981) diagram. For further details see Kewley et al. (2013).

1.2.3.2 Photodissociation regions (PDRs)

A PDR (or photon-dominated region) is any volume of the ISM with a significant neutral hydrogen fraction and whose chemistry is dominated by incident UV photons. A more practical definition also includes the low optical depth regions of molecular clouds, in which FUV photons still play an important role. The primary hydrogen ionisation state varies with gas density and flux of ionising photons, with a neutral fraction of 0.05 – 0.1 in the densest environments (van der Werf, Goss, and O'Dell 2013), but a larger value in lower density regions, in which the PDR will also have a larger physical extent. This description covers most of a galaxy's ISM (Kaufman et al. 1999) and a wide range of chemical species, densities, temperatures and optical depths, see Figure 1.5.

Photons provide almost all of the heating of a PDR, the incident FUV radiation field G_0 being defined as

$$G_0 = \frac{\int_{13.6\,\mathrm{eV}=92.1\,\mathrm{nm}}^{6\,\mathrm{eV}=206.7\,\mathrm{nm}} I_\lambda \,\mathrm{d}\lambda}{1.6 \times 10^{-6}\,\mathrm{W\,m^{-2}}} \tag{1.5}$$

measured in units of the Habing field (Habing 1968): the local value of this quantity. These photons are primarily absorbed by dust grains, which re-radiate most energy away in the IR, however the high measured fraction of a galaxy's luminosity emitted through PDR spectral lines (up to ~1 %; Stacey et al. 1991) requires an efficient mechanism to convert UV photon energy to gas heating. In lower density environments, this is though to occur through interaction with electrons photoelectrically emitted from dust grain surfaces. At higher densities, collisions with H_2 which has become vibrationally excited by absorption of a UV photon become an important source (Tielens and Hollenbach 1985).

The strongest emission line from PDRs is often [C II] 158 μm, however at higher temperatures or densities emission from O I, C I, CO and other species can be significant. Displayed in Figure 1.3 are the critical densities, transition energies and ionisation potentials of several key PDR cooling lines. In local ultra-luminous infrared galaxies (ULIRGs), small nuclear starbursts exhibit higher gas densities and optical depths than in the more extended, lower intensity star-formation regions of high-redshift DSFGs, in which larger volumes of the ISM are illuminated. This results in

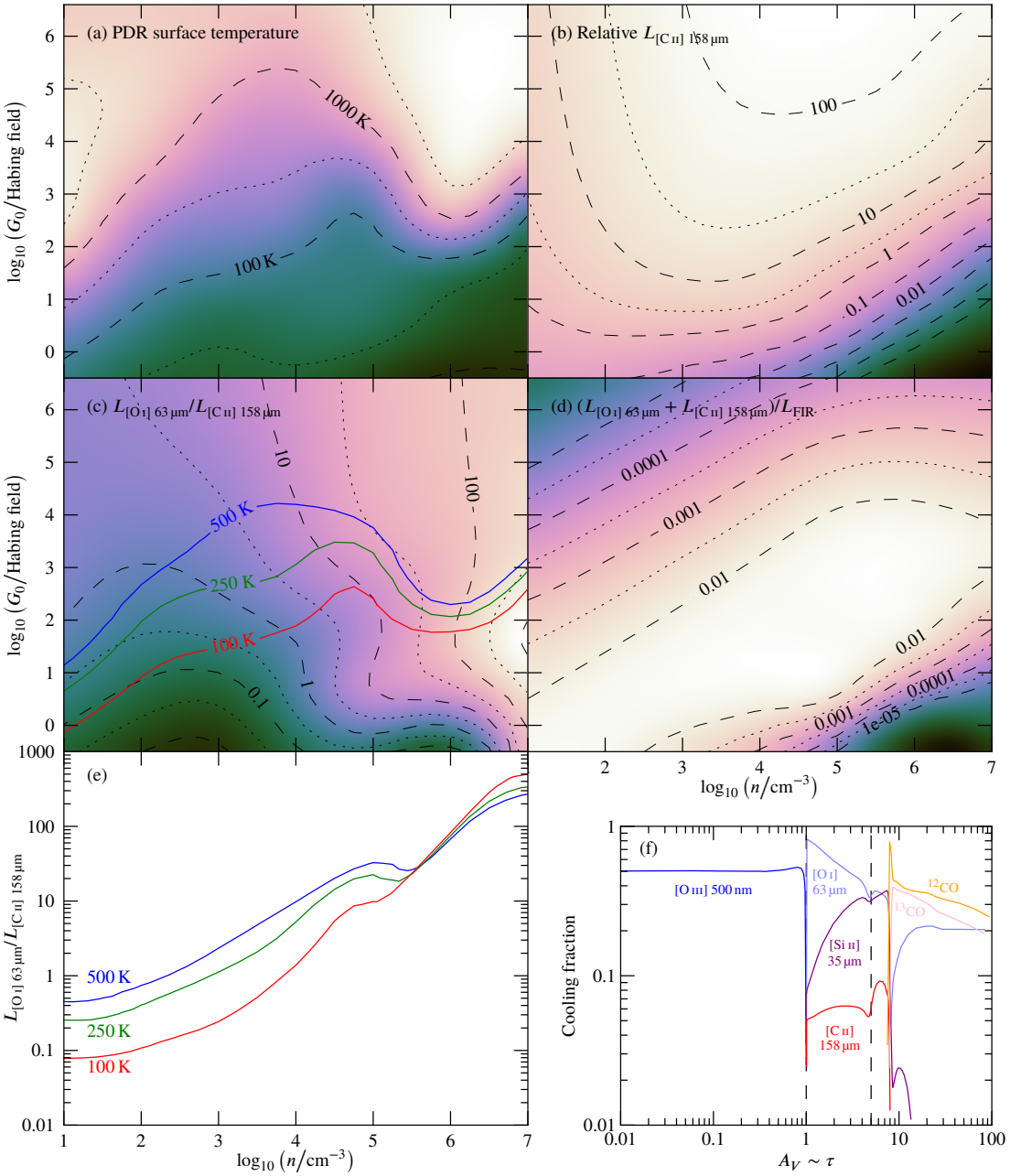

Figure 1.5. PDR models primarily from Kaufman et al. (1999), showing the ability of the brightest FIR lines to trace physical conditions within emission regions. n indicates the PDR density, and G_0 indicates the incident far-ultraviolet (FUV) radiation field in units of the Habing field (the Solar neighbourhood value is ~1.4 Habing fields).
(a): PDR surface temperature, primarily increases with incident radiation strength.
(b): relative intensity of [C II] emission, again increasing with G_0, and decreasing at $n > n_{crit} \sim 3 \times 10^3\,cm^{-3}$.
(c): [O I] – [C II] intensity ratio, varying due to the higher critical density and temperature of the [O I] line. Overplotted are three constant-temperature curves from panel (a).
(d): FIR spectral line – FIR dust continuum ratio, which is low when the PDR is highly ionised or very cool.
(e): The [O I] – [C II] line ratio as a function of density along the three constant-temperature curves in panel (c).
(f): Cooling fraction provided by strong lines within H II regions and PDRs. The ISM in this model is denser (e.g. $n_{PDR} > 10^5\,cm^{-3}$) than is found in many high-redshift DSFGs ($n_{PDR} \sim 10^3\,cm^{-3}$; e.g. Valtchanov et al. 2011; Danielson et al. 2013), which will exhibit stronger [C II] emission (see panel (e)). The vertical dashed lines indicate the H II/H I transition and the 50 % H_2 depth. Adapted from Abel et al. (2005) Fig. 12.

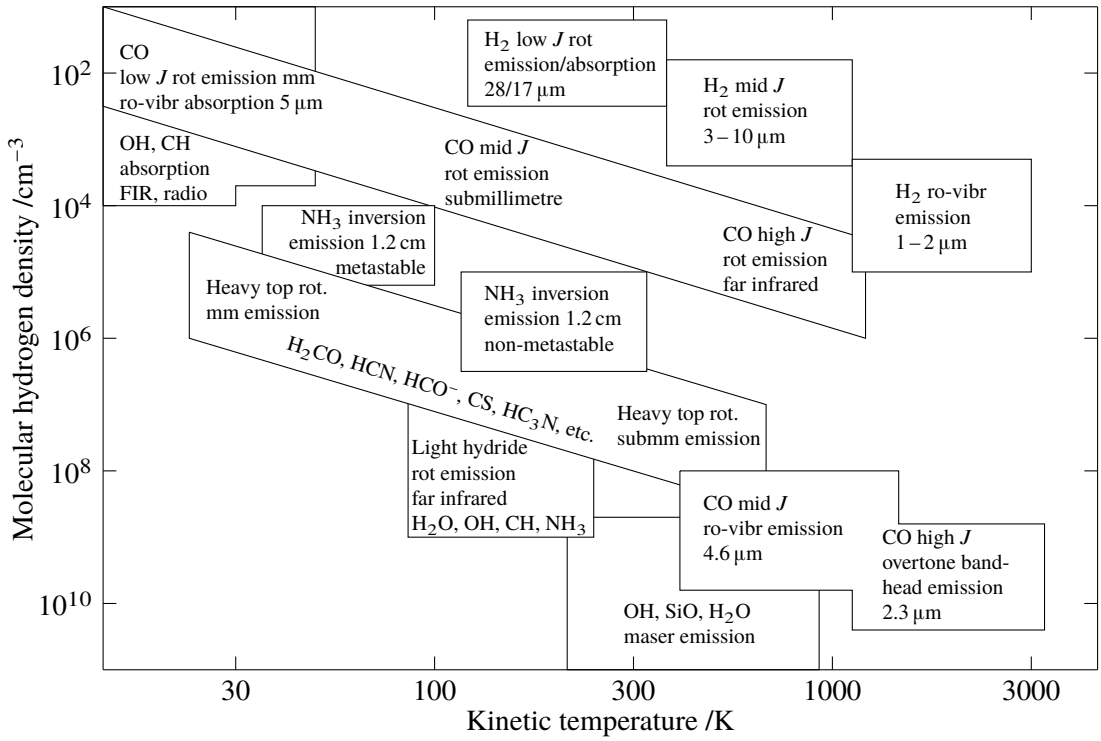

Figure 1.6. Molecular lines emission from GMCs as a function of temperature and density. Reproduced from Lada and Kylafis (1991) p155 (figure author R. Genzel).

stronger emission in carbon lines at higher z than from nearby starbursts due to the low critical densities and temperatures of those transitions. This can be more readily seen in the PDR model displayed in Figure 1.5. Emission lines strengths also depend upon the 'clumpiness' of a cloud, with photons not able to penetrate as far into a more uniform gas region

1.2.3.3 Giant molecular clouds (GMCs)

A medium is prone to develop turbulence when its Reynolds number Re $\geq$ 4000. The ISM typically has a Reynolds number of $10^6 - 10^8$ (Tielens 2005), thus over-densities are likely to occur, collapsing into giant clouds if the incident radiation field is low enough. Future sites of star-formation within the Milky Way, GMCs are gravitationally bound and have typical temperature 10 K, mass 4×10^5 $M_\odot$, size 40 pc and density 200 cm^{-3} (Tielens 2005). Molecular clouds can form quickly (after ~10 Myr) from turbulence in atomic regions, with star-formation beginning ~2 Myr later (Clark et al. 2012). Efficient sustained star-formation within GMCs is restricted by turbulence (5 km s^{-1} is a typical CO linewidth), which is prevented from decaying on timescales of ~1 crossing time (Ostriker, Stone, and Gammie 2001) by stellar feedback.

Following the universal elemental abundances, the dominant constituent of GMCs is hydrogen, however as indicated by the name, it exists primarily as the molecule H_2. This is thought to form on the surface of dust grains, due to no known gas-phase mechanism of the required efficiency. Due to its identical nuclear charges, H_2 does not have a permanent electric dipole, and can radiate only weakly via forbidden quadrupole transitions if subjected to shocks, non-ionising

UV radiation or at high (2000 K) temperatures. At ~10 K, the rate of energy loss through IR emission is very low so the primary coolants of GMCs are emission lines from trace molecular species containing metal nuclei, in particular via rotational transitions which are excited at low temperatures. The primary coolant of low-density molecular clouds is the rotational transition ladder of ^{12}CO, see Section 1.2.1.1 for more information. HCN/HNC, O_2 and H_2O dominate the gas cooling at even higher densities (see Figure 1.6), however as the temperature increases, some of these molecules can become pumped by IR radiation and their efficiency as a coolant will drop off (van der Werf et al. 2011). Due to the differing ranges of physical conditions in which each species and state can exist, determined properties will be dependent on the observed transition, for example gas densities derived from CO may be 20× those derived from H_2 (van der Werf et al. 1996), care must therefore be taken in analysis from single tracers.

As most incident UV radiation is absorbed within the PDR that forms on the surface of a GMC, other energy sources are thought to dominate the excitation at higher optical depths ($\tau \gtrsim 3$). While too few in number to provide a large effect relative to radiation throughout the rarefied bulk of the ISM, cosmic rays as high energy particles can penetrate into dense regions and dominate the chemistry of pre-star-forming clouds. Turbulence is the main mechanical heating mechanism however, contributing a factor ~4 times the heating of cosmic rays (Pan and Padoan 2009), and is dominant within hotter regions: in some galaxies $L_{\mathrm{mechanical}} \approx L_{\mathrm{IR}}$. Energy is input by SNe and other sources at large length scales and transferred to gas heating via viscous dissipation down across a range of scales to <1 pc.

1.2.4 Star formation and stellar feedback

1.2.4.1 Star formation

Stars form in the densest regions of GMCs. Compared to more recent populations, substantial differences exist in the birth conditions and stellar properties of the first generation of stars (Population III) which will not be discussed further here.

Within cool clouds of molecular gas, filamentary overdensities form as a result of large-scale magnetohydrodynamic (MHD) turbulence (Shu, Adams, and Lizano 1987), gravity enhancing the collapse and able to overcome pressure support, allowing these filaments and hubs to reach $A_V > 100$, see Myers (2009a) for more details of these structures. Should the Jeans mass (Jeans 1902) be exceeded within any volume, collapse will begin, with further fragmentation during this process creating individual protostellar cores. The distribution of core masses (the core mass function (CMF)) will depend strongly upon temperature, the increase of which with density is regulated by emission of spectral cooling lines, the efficiency of which in turn is affected by optical depth and metallicity. Several theories and models predict hotter gas may fragment less as it collapses, forming more massive cores, however any change to the global initial mass function (IMF) as a result is unknown and controversial.

Fed by its circumstellar disc, a protostar will increase in mass while simultaneously radiating

thermally, allowing continued contraction and eventually a distribution of protostar masses similar to the IMF can be found (Myers 2009b). Deuterium fusion can be achieved at lower energies than are required for hydrogen, however the low energy released merely slows the collapse temporarily and is unable to clear the local environment of accreting material. Before the central pressure and temperature reach those required for a self-sustaining rate of 4H → He fusion and hydrostatic equilibrium is established, the protostar (now a T Tauri or Herbig Ae/Be star) follows the Hayashi track, continuing to grow via magnetically-controlled accretion and clearing its surroundings though bipolar jets.

After accretion, the distribution of "final" stellar masses will be different to that of the CMF, and is termed the initial mass function (IMF). Most individual stars can only be resolved within the Milky Way and Magellanic clouds, with the lowest mass stars often only identifiable in IR imaging. As such, the form of the IMF ($n(M) = NM^{\gamma}$ where $\gamma = -3.5$; Salpeter 1955, or similar more modern parametrisations e.g. Kroupa 2001; Chabrier 2003) can only be theorised in other environments, typically through observations of star-formation in a multitude of physical conditions throughout the Milky Way, through hydrodynamic and radiative transfer cloud collapse simulations (e.g. Padoan and Nordlund 2002; Bate and Bonnell 2005; Bate 2009) and via population synthesis modelling. The high luminosity ratio of massive to low-mass stars, the short lifespan of the most massive, and the location of formation sites within dense GMCs contribute to the difficulty of simultaneous observations of a complete range of formed stellar masses. While most studies indicate a near-universal IMF (Bastian, Covey, and Meyer 2010, and references therein), it is generally agreed upon that it varies for very low metallicities, and several authors have postulated variations in less extreme conditions (e.g. Briceño et al. 2002; Davé 2008; van Dokkum and Conroy 2010; Treu et al. 2010). IMF modifications have also been proposed (Baugh et al. 2005) to explain submillimetre galaxies (SMGs; Smail, Ivison, and Blain 1997; Hughes et al. 1998), the most intensely star-forming objects in the Universe.

A further contribution to the IMF is multiplicity. Most massive stars may be formed as near-equal mass binaries (Zinnecker and Yorke 2007; Mason et al. 2009), while the lowest mass may have a binary fraction of only ~10 % (Burgasser 2007). Multiplicity has some large effects on stellar evolution including transfer of matter and angular momentum, likely leading to type 1a SNe and enhanced rotation of one member, increasing mixing and being a potential requirement for gamma-ray bursts (GRBs) (MacFadyen and Woosley 1999),

Shown in Figure 1.7 is the evolution with time of a the SED produced by an ageing SSP. Within a real galaxy, dust absorption will change the SED shapes, particularly at times shortly after the starburst.

1.2.4.2 Stellar feedback and superwinds

As powerful liberators of energy from baryonic matter, stars should be expected to impact their surrounding environment, and indeed this *stellar feedback* occurs in several forms, with the most massive stars able to produce $L_{\rm bol} > 10^6\,{\rm L}_{\odot}$ dominating the effect. The most immediately

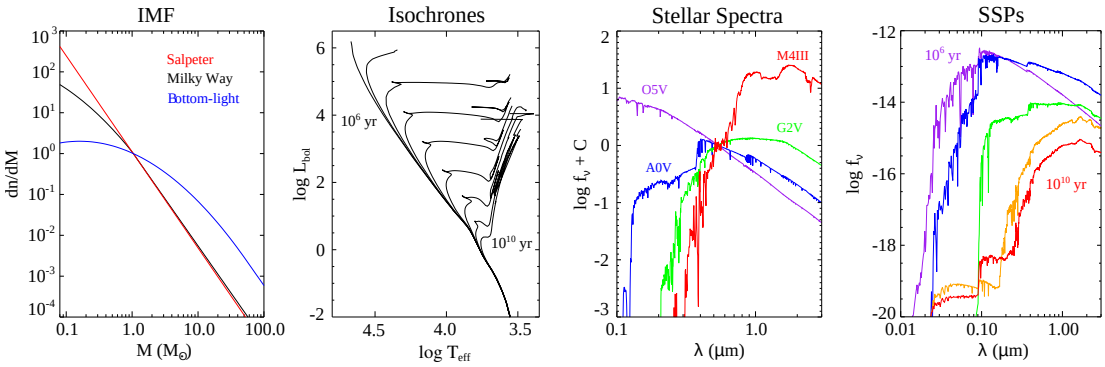

Figure 1.7. Several factors contributing to stellar emission. Knowledge of the IMF, stellar evolution and stellar SEDs is all required to understand the evolution of the emission of a single stellar population (SSP) (right hand plot), the basis of many galaxy SED models. Adapted from Conroy (2013).

obvious form of energy output from stars is electromagnetic radiation, however cosmic rays, winds and SNe are other important feedback methods, and indirectly stars power turbulence and magnetic fields within the ISM. As almost perfect black bodies, stars emit across a wide range of frequencies dependent on their surface temperature. Being both more voluminous and hotter than stars such as our Sun, O and B stars dominate the light output of any young stellar population, and the prodigious amounts of hydrogen-ionising radiation emitted create large surrounding H II regions.

The most dramatic and shortest duration form of feedback is that provided by SNe. These huge explosions can inject 10^{44} J ($\sim 10^{10}\,L_\odot$ yr) of energy into the ISM (around 100 times more is released as neutrinos), and if occurring within the smallest dark-matter haloes, can drive gas out entirely (Strickland and Heckman 2009). Often included as a contribution to SNe in simulations, due to the primary contributors being the same short-lived massive stars that expire as SNe, radiation pressure is now being recognised as an important ingredient requiring (computationally expensive) separate treatment (Murray, Ménard, and Thompson 2011). Stellar winds are produced by massive stars in several phases of their life, particularly being necessary to expose the hotter inner region as a Wolf-Rayet star, and as a prerequisite for type Ib and Ic SNe, and also by AGB stars. This form of feedback greatly enriches the metal content of the ISM, particularly in the case of AGB which are important dust factories, however its effects are more localised than those of radiation or SNe (Murray, Quataert, and Thompson 2005). Cosmic rays are high energy charged particles such as electrons and protons which while having little effect throughout most of the ISM, can dominate the chemistry of GMCs due to their penetrative abilities (Uhlig et al. 2012), see Section 1.2.3.3 for more details.

Feedback will disrupt GMCs on timescales shorter than the lifetime of a massive star such that radiation pressure rather than SN shocks is the primary disruptive mechanism (Murray, Quataert, and Thompson 2010). This allows a conversion of only 10 – 15 % of proto-stellar cores to stars, which combined with the efficiency of core formation, enables conversion of 3 – 6 % of gas mass to stars in the Milky Way (Jørgensen et al. 2007; Murray, Quataert, and Thompson 2010). In more massive and higher surface density clumps/GMCs, such as in the densest regions of

ULIRGs, the star-formation efficiency increases to ~40 %.

This cloud dispersion will pause star-formation, however at high ISM column densities dust absorption and gas self shielding cause the heating rate to drop below that of cooling, and formation of further molecular clouds is possible. Complete removal from the ISM rather than simple dispersion and heating of the gas is therefore required for the decline of star-formation at the end of a starburst. Much of the removal will occur through conversion into stars, but as described above this is a slow and inefficient process. The combined energy and momentum feedback of these SNe and stellar winds, in addition to radiation pressure and cosmic rays during the stars' lifetimes will apply pressure to the surrounding ISM and drive an outward flow of material. Large-scale star-formation in starbursting galaxies can therefore lead to a galaxy-scale superwind, with a velocity as high as 700 km s^{-1} (Martin 2005). In all but the smallest dark-matter haloes however, this velocity may be insufficient for the material to escape the global potential well, leading to a 'fountain': material subsequently falls back, leading to star-formation over a time-scale much greater than that of the original burst (Hopkins et al. 2013a).

While the majority of superwinds observed locally are primarily powered by star-formation, those generated in late-stage mergers are typically driven by the vast power output of AGN (Veilleux et al. 2013), and these may be required for complete expulsion of gas to the surrounding medium, since some seem able to drive outflow velocities of over 1000 km s^{-1} (Rupke, Veilleux, and Sanders 2005; Spoon et al. 2013). Locally, outflowing gas from both forms of source is observed, e.g. the starburst of M 82 (Bland and Tully 1988; Walter, Weiss, and Scoville 2002) and the AGN of Mrk 231 (Hamilton and Keel 1987; Rupke, Veilleux, and Sanders 2005).

As with the ISM from which it originates, a superwind is expected to comprise multiple gas phases moving with different velocities. Whilst observations of X-ray and UV absorption lines have indicated ionised and neutral atomic components (e.g. Martin 2005; Martin et al. 2012; Kornei et al. 2012), the presence of molecular gas may also be required (depending on the time-scale for material to cycle from atomic to molecular) if future star-formation is to be reduced.

The most abundant non-H_2 molecule, CO, is a common molecular gas tracer. Strong and broad emission lines can mask outflow signatures, however sensitive interferometric observations have revealed broad emission wings in several local ULIRGs and QSOs (Sakamoto et al. 2009; Feruglio et al. 2010; Cicone et al. 2014). Another common molecule, OH, is particularly well suited for tracing molecular gas in galactic winds. It possesses a dipole moment ~15× that of CO. Due to the high densities required to thermalise OH rotational transitions (~10^9 cm^{-3}; Storey, Watson, and Townes 1981), the strongest OH line is typically the ground-state absorption ^{16}OH $^2\Pi_{3/2}$ $J = \frac{3}{2} \rightarrow \frac{5}{2}$, split by lambda-doubling into rest-frame 119.233 and 119.441 µm transitions. Back-lit molecular gas provides a prime opportunity to observe these transitions, with a blueshift expected from the radial movement of an outflow. Such observations (e.g. Fischer et al. 2010; Sturm et al. 2011; Spoon et al. 2013; Veilleux et al. 2013) indicate a correlation between AGN luminosity and maximum outflow velocity and show that outflows are prevalent among local ULIRGs. When a wider range of OH transitions are observed, detailed excitation

and physical models can be derived, indicating for example dust temperature (T_d) ~ 100 K and N_{col} ~ 10^{17} cm^{-2} within the Arp 220 outflow (González-Alfonso et al. 2012),

Stellar feedback and outflows are likely to be strongest within the galaxies experiencing the highest rates of star formation. This population, their properties, and evolution is discussed in the next section.

1.3 Dusty Star Forming Galaxies (DSFGs)

Most galaxies form stars within regions of dense molecular gas as discussed in the previous sections, at a relatively slow but consistent rate, gradually adding to their stellar mass. The *main sequence* is an observed correlation between the SFR and stellar mass of these "normal" star-forming galaxies, such that more massive galaxies have higher SFRs, with a form SFR $\propto f(t)\, {M_*}^{1+\beta}$ (Brinchmann et al. 2004; Daddi et al. 2007; Elbaz et al. 2007; Noeske et al. 2007). This correlation holds over many orders of magnitude in both parameters and to high redshift, from small irregular galaxies at the low-mass end to large spirals and lenticulars at the high-mass end, see Figure 1.8. While the existence of the main sequence is fairly certain, the slope and width reported differ between studies (e.g. Noeske et al. 2007; Karim et al. 2011; Reddy et al. 2012), although the value of β likely lies around -0.1.

As the SFR of a galaxy reduces, it drops below the main sequence to the region occupied by passive galaxies, with by definition low SFRs for their stellar mass. Large ellipticals and dwarf spheroidals lie towards the high and low mass ends respectively.

These passive galaxies are however not the only systems to lie off the main sequence, with examples found far above the relation, ironically their high brightness making them historically difficult to detect. The majority of observations today as well as all performed before the advent of cryogenic cooling, occur in the UV–NIR regime of the EM spectrum. The first MIR observations of extragalactic sources (e.g. Kleinmann and Low 1970; Rieke and Low 1972) however indicated strong emission further into the infrared. Throughout the 1970s this was shown to be a common property (e.g. Harper and Low 1973; Neugebauer et al. 1976; Rieke and Lebofsky 1978; Telesco and Harper 1980), with theoretical models suggesting this feature could be best understood as thermal emission from dust grains (Rees et al. 1969) heated by massive young stars. The population of IR-bright galaxies is described below. Firstly the nearby objects visible in those early surveys are discussed, followed by their high-redshift counterparts now of great interest for our understanding of galactic evolution, and which are the focus of this thesis.

1.3.1 Low-redshift DSFGs

The abundance of extragalactic objects exhibiting strong dust emission was revealed by the *InfraRed Astronomy Satellite* (*IRAS*; Neugebauer et al. 1984), with the first (almost) full-sky maps discovering ~250 000, most of which possessed infrared luminosities in excess of 10^{11} L$_\odot$. These luminous infrared galaxies (LIRGs), as objects of this class ($L_{IR} > 10^{11}$ L$_\odot$) have since

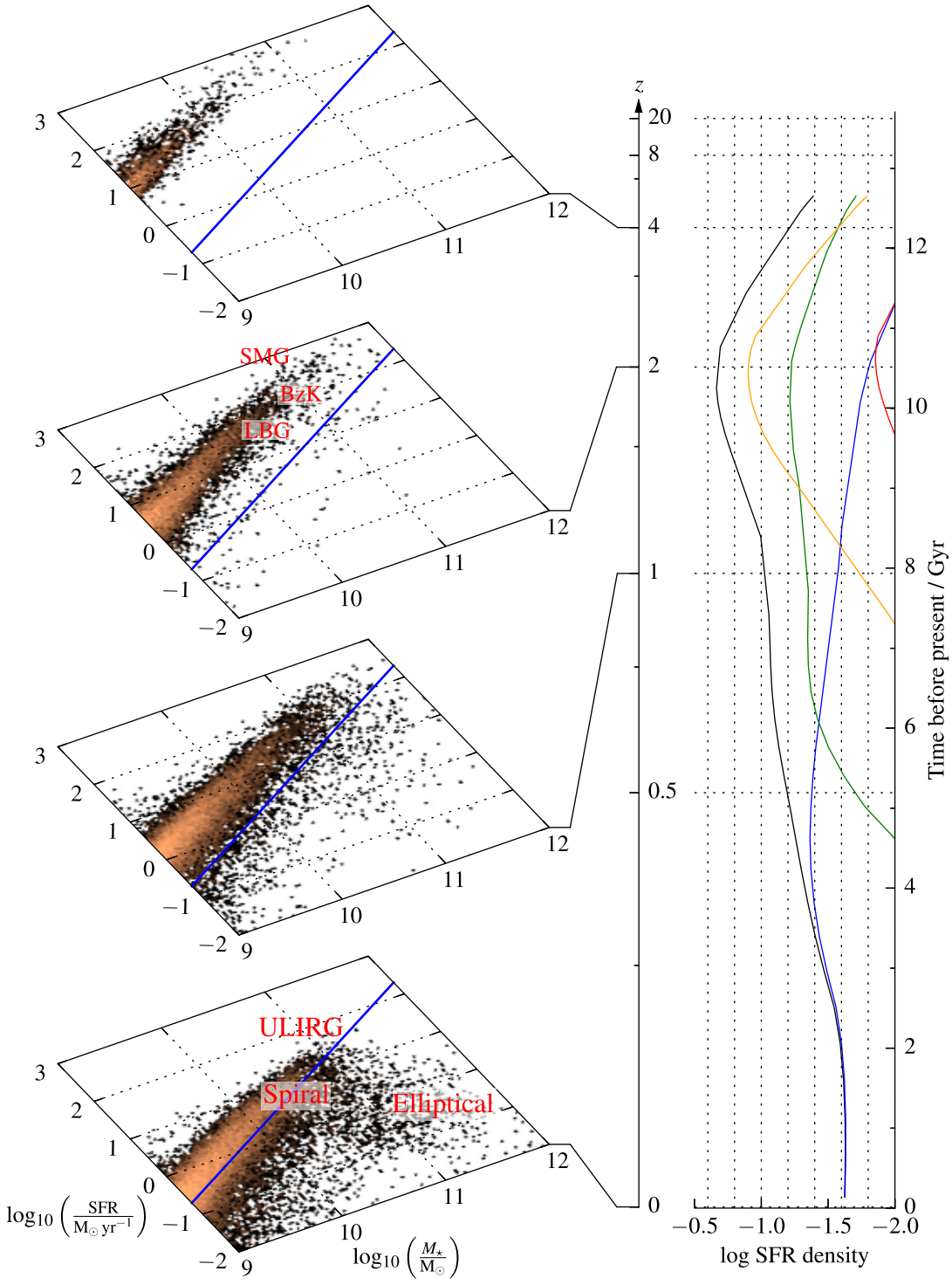

Figure 1.8. The evolution of the star-forming main sequence with redshift, and the galaxy populations found at various locations in the SFR–stellar mass parameter space. Images displayed on each plane are taken from Sparre et al. (2015), data produced by the Illustris simulation.
Right: The total star formation rate density (SFRD) and L_{IR}-separated contributions from Figure 1.10, see that figure for details of colours.

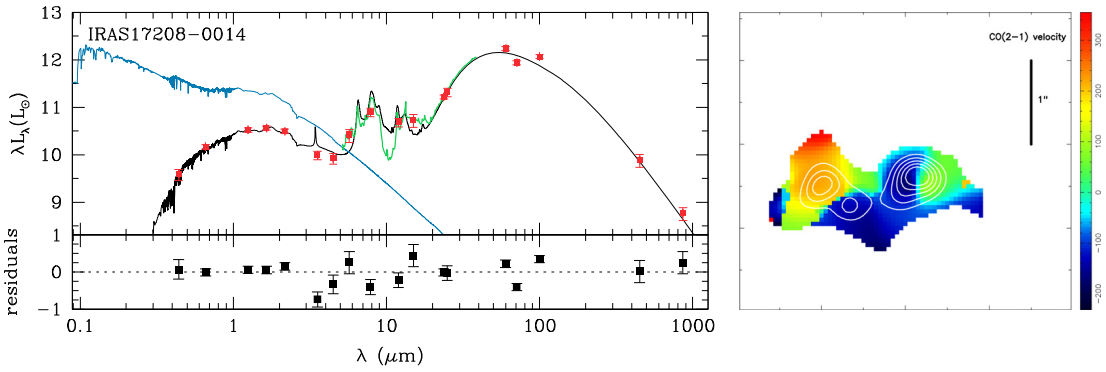

Figure 1.9. *Left*: SED fit for a typical ULIRG. The black line shows the best-fitting SED, exhibiting strong dust dust attenuation and emission. Shown in blue is the corresponding unattenuated stellar emission and in green the *Spitzer Space Telescope*/Infrared Spectrograph (IRS) spectrum around the MIR PAH features. Taken from da Cunha et al. (2010).
Right: CO $J = 2 \rightarrow 1$ velocity map of Arp 220, overlaid with flux contours in white, indicating counter-rotating molecular gas discs of $\sim 10^9\,\mathrm{M}_\odot$ (Sakamoto et al. 2008). This object is the nearest ULIRG at $z \sim 0.018$ (77 Mpc). The high FIR flux powered by star-formation within these discs, and the detailed observations enabled by its proximity result in it being a standard comparison for more distant IR-bright galaxies, in particular its well-sampled SED. Taken from Engel et al. (2011).

become known, locally are primarily spiral galaxies exhibiting SFRs of $\sim 25\,\mathrm{M}_\odot\,\mathrm{yr}^{-1}$ (Meier et al. 2010), in comparison to $\sim 2\,\mathrm{M}_\odot\,\mathrm{yr}^{-1}$ within the Milky Way. Many Seyfert galaxies also satisfy the criterion, hot dust around an AGN emitting strongly in the infrared (e.g. NGC 1068; Jaffe et al. 2004). The archetypal starburst galaxy: M 82, the Cigar Galaxy; is widely used for comparison with distant starbursting galaxies. This object falls a little below the LIRG classification, however its most recent starburst results from tidal interaction with its larger neighbour M 81 several $\times 10^2$ Myr ago and as the output from this starburst is dying down, soon after the event this galaxy likely classified as a LIRG (Barker, de Grijs, and Cerviño 2008).

Nearby bright spiral galaxies were not the only objects found to be IR-bright. Several sources had no counterparts in existing optical catalogues, suggesting extraordinary levels of dust extinction required to produce the observed luminosity ratios of $L_\mathrm{IR}/L_\mathrm{B} \gtrsim 50$. Ground-based follow-up identified a population of faint $z = 0.1 - 0.2$ galaxies, and combining these redshifts with the *IRAS* fluxes indicated $L_\mathrm{IR} > 10^{12}\,\mathrm{L}_\odot$ and hence SFR $\gtrsim 150\,\mathrm{M}_\odot\,\mathrm{yr}^{-1}$, using the conversion of Murphy et al. (2011b). With such high SFRs, these galaxies lie an order of magnitude above the main sequence. The striking difference in physical properties of these ultra-luminous infrared galaxy (ULIRG): the most bolometrically luminous non-QSO objects at similar stellar mass in the local universe; to "normal" galaxies prompted extensive follow-up.

Morphological indications from both IR and optical imaging suggest a high incidence of late-stage major mergers around the time of final coalescence (Sanders and Mirabel 1996, and references therein; also Figure 1.9), and some fraction of ULIRGs may even consist of multiple merging components (Borne et al. 2000). It is uncertain yet whether this mechanism is responsible for systems observed to lie above the main sequence at all redshifts. The individual merging galaxies are fairly typical discs, with ULIRG stellar mass tending to be $10^{10} - 10^{11}\,\mathrm{M}_\odot$ (da Cunha et al. 2010; Rodríguez Zaurín, Tadhunter, and González Delgado 2010), comparable to that of the

Milky Way ($6.4 \times 10^{10}\,M_\odot$; McMillan 2011). As the small molecular discs both gravitate to the centre, the gas pressure increases, with the densities reaching $n \gtrsim 10^3 - 10^4\,\mathrm{cm}^{-3}$ (Solomon et al. 1997), similar to those in Galactic GMCs, powering a much higher total SFR than in the pre-merger components of a few $\times\, 100\,M_\odot\,\mathrm{yr}^{-1}$, and the volume over which this occurs is smaller and more centrally concentrated than within an average spiral galaxy. Luminosity $\propto \nu S_\nu$, so the higher dust temperatures exhibited by ULIRGs in comparison to "normal" spirals dramatically increase their IR output, with any older passive stellar populations (which typically control the cool dust component) contributing very little to the total. The left panel of Figure 1.9 shows an SED from a typical ULIRG, demonstrating the extreme dust absorption towards an ongoing nuclear starburst common in this population.

AGN are also common within ULIRGs, and AGN-identified objects comprise a large fraction of the most luminous systems (Kartaltepe et al. 2010). Mrk 231 is the most luminous ($L_{\mathrm{IR}} = 3.2 \times 10^{12}\,L_\odot$) local ($z = 0.04$) ULIRG, and while it possesses a ~200 Myr old starburst, ~70 % of the bolometric output is powered by an AGN (Davies et al. 2007), which is in fact the nearest quasar. The central supermassive black hole (SMBH) resides in a rotating molecular disc (Downes and Solomon 1998), the inner material of which is blown outwards at speeds of over $1000\,\mathrm{km\,s}^{-1}$ (Fischer et al. 2010; González-Alfonso et al. 2014). Molecular outflows appear to be common within this population (Spoon et al. 2013; Veilleux et al. 2013), with higher speeds ($v \gtrsim 1000\,\mathrm{km\,s}^{-1}$) likely provided by AGN and lower ($v \lesssim 700\,\mathrm{km\,s}^{-1}$) by star formation. This outflowing gas may reduce or even halt an ongoing starburst. An evolutionary picture particularly favoured in the past but increasingly appearing too limited suggests that these ULIRGs are a necessary phase in the transition from late- to early-type galaxies, with a merger triggering a nuclear starburst, initiating an AGN which blows out or heats star-forming gas and halting the starburst, after which the central SMBH becomes visible as a QSO and eventually shuts off leaving a passive elliptical galaxy (Sanders et al. 1988), see Section 1.3.5.2 for more details.

1.3.2 Cosmic background

The cosmic background is the combined emission of galaxies and the CMB contributing to the flux measured by a telescope; due to the much larger volume at high redshift, much of the extragalactic background light (EBL) arises there, so an understanding of the cosmic background can provide constraints upon the number density and luminosity of high-redshift sources. At optical and NIR wavelengths, the primary contributors to the EBL can often be resolved, however determining the individual distant (and often small) galaxies contributing is more of a problem in the IR due to the large point spread functions (PSFs) typically involved.

Absolute photometry measurements from the Diffuse Infrared Background Experiment (DIRBE) and the Far Infrared Absolute Spectrophotometer (FIRAS) on board the *COsmic Background Explorer* (*COBE*) (Puget et al. 1996; Dwek et al. 1998; Fixsen et al. 1998) have constrained the total cosmic infrared background (CIB), however the contribution from individual galaxy

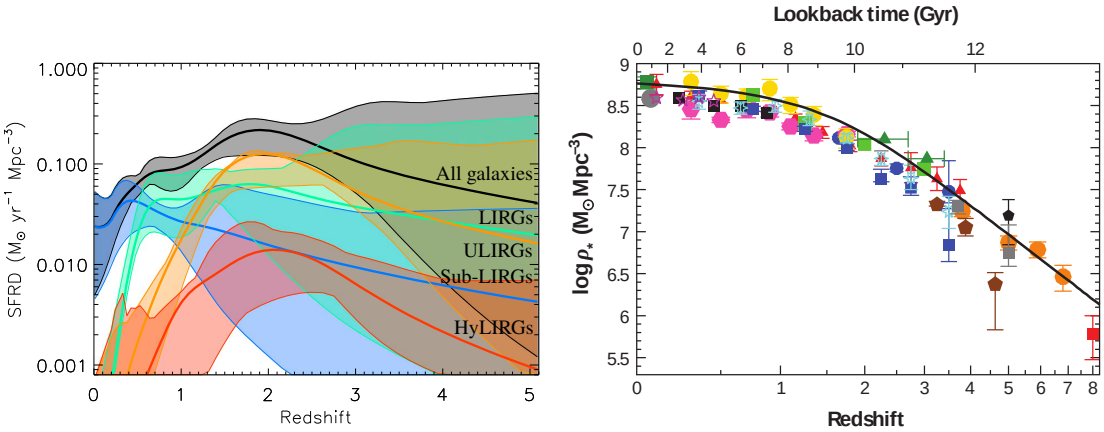

Figure 1.10. *Left*: Contributions to the SFRD of the Universe since $z = 5$ from several populations of galaxies classified by their IR luminosity. Adapted from Le Borgne et al. (2009).
Right: The integral over time of the quantity displayed in the left-hand figure, representing the build up of stellar mass in the Universe. The specific star formation rate density (SSFRD) is a related quantity that can be determined by division of the SFRD by stellar mass, indicating a shallow decline over $2 < z < 7$ and a more rapid decline since $z \sim 2$. Taken from Madau and Dickinson (2014), see references therein for details of the datasets displayed.

populations is still not completely determined. This measured CIB is ~50 % of the total EBL budget, however as the average IR output from $z = 0$ galaxies is ~1/3 of the optical light, IR emission may be very important at higher redshifts. The CIB appears to peak at around $\nu I_\nu = 14\,\mathrm{nW\,m^{-2}\,sr^{-1}}$, or $I_\nu \sim 0.6\,\mathrm{MJy\,sr^{-1}}$ at 100 – 160 µm. A *Herschel*/PACS beam covering this wavelength has a 12 – 14 arcsec full width at half maximum (FWHM), and hence a beam size $\Omega = \frac{\pi\theta^2}{4\ln(2)} \sim 4 \times 10^{-9}$ sr, so the CIB has a value of 2 – 3 mJy per beam, compared to a confusion noise level of 0.3 – 0.9 mJy in the deepest the PACS Evolutionary Probe (PEP; Lutz et al. 2011) field (Berta et al. 2011), allowing ~2/3 of the extragalactic background flux to be resolved. The redshift of the dominant population contributing to the CIB increases with observation wavelength (Viero et al. 2013), and while the exact redshift distribution in any band still has variations between studies (e.g. Devlin et al. 2009), broad trends have emerged such as that the EBL at $\lambda < 160$ µm is primarily provided by $z < 1$ galaxies (Berta et al. 2011). Most of these galaxies are thought to be relatively small ($10^{9.5} – 10^{11}\,M_\odot$) and moderately star-forming. The contribution of AGN to the CIB is expected to be 5 – 20 % (Matute et al. 2006; Jauzac et al. 2011).

The EBL is intimately related to the global SFRD through the history of the universe: an observation of any point in the sky measures the integrated flux in that band from all sources along that sightline back through the history of the Universe. The average SFRD of the Universe (in $M_\odot\,yr^{-1}\,Mpc^{-3}$) built up over the first few Gyr, peaked at $z \sim 2$, and has decreased slowly since (see Figure 1.10).

One effect of a much higher SFR in the past is that optical and NIR observations become increasingly insufficient to determine reliable estimates of the SFRD. MIR–submm measurements must therefore be added to capture obscured star-formation, particularly around the SFRD peak where LIRGs and ULIRGs dominate the total rate (e.g. Le Borgne et al. 2009, ; see Figure 1.10).

Should dust corrections be applied directly to measured UV fluxes, care must be taken to ensure suitable calibrations are used — those based on local starbursts (which exhibit higher visual extinctions than many high-redshift starbursts may overestimate the total star-formation (Buat et al. 2010). Additionally, the star-formation and dust attenuation evolutions may not be coincident, with the dust maximum occurring ~2.5 Gyr later than the peak SFR (Cucciati et al. 2012). The contribution of off-"main sequence" galaxies with even higher SFRs such as submillimetre galaxies (SMGs) depends on starburst duration (González et al. 2011), but may only account for 10 % of the SFRD at $z = 2$ (Rodighiero et al. 2011). X-rays may also be used to trace obscured star-formation, however their use at high-redshift declines due to likely changes in the ratio of high-to-low mass X-ray binaries (Fragos et al. 2013).

SFR correlates strongly with interstellar gas mass, and in particular with molecular gas surface density. At high redshift, where gas infall rates and mass fractions were much greater, SFRs in "normal" galaxies were therefore correspondingly higher. The Milky Way currently forms stars at a rate of ~2 $M_\odot$ yr^{-1} (Robitaille and Whitney 2010; Chomiuk and Povich 2011), however for a star-forming galaxy of equal mass, at $z = 2$ the SFR is ~30 times larger (Daddi et al. 2007). The entire main sequence therefore appears to become increasingly offset at higher redshifts, as visible in Figure 1.8. Increasing stellar masses and decreasing gas supplies also change the specific star formation rate (SSFR), the global value of which has decreased since $z = 7$ (Madau and Dickinson 2014, and references within). This stellar mass build up is shown in Figure 1.10, with the 50 % point of stellar mass buildup occurring at $z \sim 1$ (Pérez-González et al. 2008). Lower mass galaxies experience strong bursts of star-formation later than more massive galaxies (e.g. Pérez-González et al. 2008; Kajisawa et al. 2010), a process known as *downsizing*. This is evident with the most massive local galaxies, systems that formed the majority of their stars at $z \geq 1$ (Thomas et al. 2005). A simple explanation for this appears to be that the most efficient star-formation (as a fraction of the rate of baryon accretion from the IGM) occurs at $M_{\rm halo} \sim 10^{12}$ $M_\odot$ at all redshifts (Behroozi, Wechsler, and Conroy 2013), equivalent to $M_* \sim 10^{10} - 10^{10.5}$ $M_\odot$. At $z \sim 5$ these are very large galaxies but relatively small at $z = 0$.

1.3.3 Identification of high-redshift DSFGs

The redshift, dust mass and globally-averaged dust temperature of a DSFG strongly affect its identification, and hence its classification. This section describes the initial discovery of SMGs, more recent surveys and instruments detecting high-redshift DSFGs, and techniques used to cross-match these objects across other wavebands.

1.3.3.1 Submillimetre galaxies (SMGs)

Pre-SCUBA, a few optically-bright *IRAS*-detected galaxies were spectroscopically confirmed to lie at high-redshift through observations of rest-frame UV and optical emission lines (e.g. Rowan-Robinson et al. 1991; Irwin et al. 1998).

Thermal emission from the atmosphere restricts ground-based observations of the peak of dust

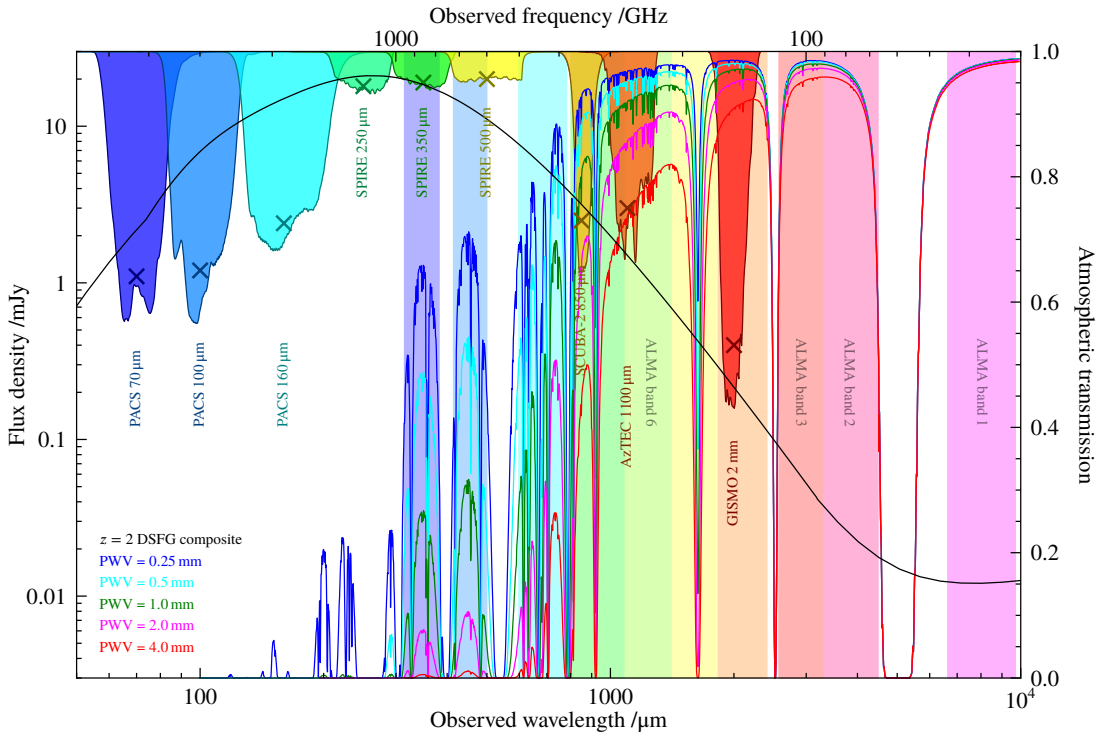

Figure 1.11. Atmospheric transmission and depths attainable in deep imaging using several important FIR–mm photometric bands. The blue, cyan, green, magenta and red lines display the atmospheric transmission at a selection of precipitable water vapour (PWV) levels. Data taken from the the Caltech Submillimeter Observatory (CSO) Atmospheric Transmission Interactive Plotter. For comparison, on Llano de Chajnantor (location of ALMA), 60 % of nights have PWV < 1 mm, and 10 % have PWV < 0.4 mm. The black curve displays the composite DSFG SED from Swinbank et al. (2014) shown at $z = 2$, and crosses display the 3σ obtainable depths using the PACS, SPIRE, the Submillimetre Common-User Bolometer Array 2, (SCUBA-2; Holland et al. 2013), AzTEC (Wilson et al. 2008) and Goddard IRAM Superconducting 2 Millimeter Observer (GISMO; Staguhn et al. 2008) instruments.

emission in most galaxies, however *windows* of high atmospheric transmission begin to appear at longer wavelengths (see Figure 1.11). Single-pixel bolometers operating at these frequencies (e.g. UKT14 on the James Clerk Maxwell Telescope (JCMT); Duncan et al. 1990) were used to follow up the known high-redshift IR-bright galaxies (e.g. Brown and Vanden Bout 1991; Clements et al. 1992; Isaak et al. 1994; Hughes, Dunlop, and Rawlings 1997), confirming a thermal (as opposed to a self-absorbed synchrotron) origin of the FIR emission. The total number of these objects known was small, and the sample was necessarily biased to the brightest DSFGs, in particular selecting strongly gravitationally lensed AGN (e.g. Broadhurst and Lehar 1995).

The Submillimetre Common-User Bolometer Array (SCUBA; Holland et al. 1999) on JCMT on Mauna Kea revolutionised this field, in particular the 37 element 850 μm array. Not only was this much more sensitive than previous instruments, but with a 2.5′ field of view, mapping of significant areas of sky became possible. Early deep imaging revealed a population of objects bright at submm wavelengths ($S_{850\,\mu\mathrm{m}} > 5$ mJy; e.g. Smail, Ivison, and Blain 1997; Hughes et al. 1998; Barger et al. 1998 — see Blain et al. 2002 for an overview of these early detections).

These discoveries did not immediately lead to a comprehensive multiwavelength understanding however: with only one $S_{850\,\mu\mathrm{m}} \geqslant 5$ mJy source per several square arcminutes, of order one per

night was found, providing some difficulty to building up a statistically significant sample, and these objects were difficult to single out in the rest frame UV and optical, a point explored more in Section 1.3.4.1.

As described in Section 1.2.2, thermal dust emission approximates a black body, scaled by an emissivity factor. Using the optical depth-based definition from that section

$$S_\nu \propto \frac{\nu^3}{\exp\left(\frac{h\nu}{k_\mathrm{B}T}\right) - 1}\left(1 - \exp\left[-C\kappa_0\left(\frac{\nu}{\nu_0}\right)^\beta\right]\right), \tag{1.6}$$

where C is some source-dependent scaling factor. At low frequencies: the long-wavelength side of the dust peak; a Taylor expansion $\mathrm{e}^x = 1 + \frac{x^1}{1!} + \frac{x^2}{2!} + \ldots$ can be used to retrieve the Rayleigh-Jeans law equivalent for grey bodies:

$$\exp\left(\frac{h\nu}{k_\mathrm{B}T}\right) \approx 1 + \frac{h\nu}{k_\mathrm{B}T} \quad \text{and} \quad \exp\left(C\kappa_0\left(\frac{\nu}{\nu_0}\right)^\beta\right) \approx 1 - C\kappa_0\left(\frac{\nu}{\nu_0}\right)^\beta, \tag{1.7}$$

leading to

$$S_\nu \propto \frac{\frac{C\kappa_0}{\nu_0^\beta}\nu^3\nu^\beta}{\frac{h\nu}{k_\mathrm{B}T}} \propto \nu^{2+\beta}. \tag{1.8}$$

β is positive, so this situation produces a *negative k-correction*: when a higher redshift object is viewed, the dust emission peak is redshifted closer to the frequency of observation, reducing the effect of flux density decrease with distance.

For high-redshift $1 \lesssim z \lesssim 8$ (lookback time 7 – 13 Gyr) galaxies with substantial quantities of cool dust, this results in a striking effect (see Figure 1.12): when viewing a source at redshift z, the frequency observed ν_obs corresponds to an emitted frequency $\nu_\mathrm{emit} = (1+z)\,\nu_\mathrm{obs}$, however due to distance the flux decreases by a factor $\propto D_\mathrm{L}^2 \approx (1+z)^4$. Typically $\beta = 1.5$–2 (see Section 1.2.2), so on the long-wavelength side of the dust peak these two effects almost perfectly counter one another:

$$S_\mathrm{obs} \propto (1+z)^{2+\beta-4} \sim \text{constant}. \tag{1.9}$$

An additional problem for deriving photometric redshifts is the redshift–T_d degeneracy. Even when a source is well-sampled in the FIR-submm (estimating an observed dust emission peak wavelength of ~270 µm for example), a $T_\mathrm{d} = 50\,\mathrm{K}$ $z = 2$ galaxy with $\lambda_\mathrm{peak;rest} = 90\,\mu\mathrm{m}$ is difficult to distinguish from a $z = 1.5$ $T_\mathrm{d} = 40\,\mathrm{K}$ $\lambda_\mathrm{peak;rest} = 107\,\mu\mathrm{m}$ galaxy. This degeneracy persists up to ~60 K (Blain, Barnard, and Chapman 2003).

The wide range of redshifts at which DSFGs are therefore visible by SCUBA makes determination of exact luminosities and other intrinsic properties from this single data point difficult. Regardless of their precise redshift, these galaxies appeared to possess many similarities to local ULIRGs, in particular high SFRs and dust masses. Like local ULIRGs, a similarly luminous optical companion could not be found, again suggesting high levels of dust extinction, and questions of the nature of SMGs and their relationship to local ULIRGs are studied to this day, see Casey,

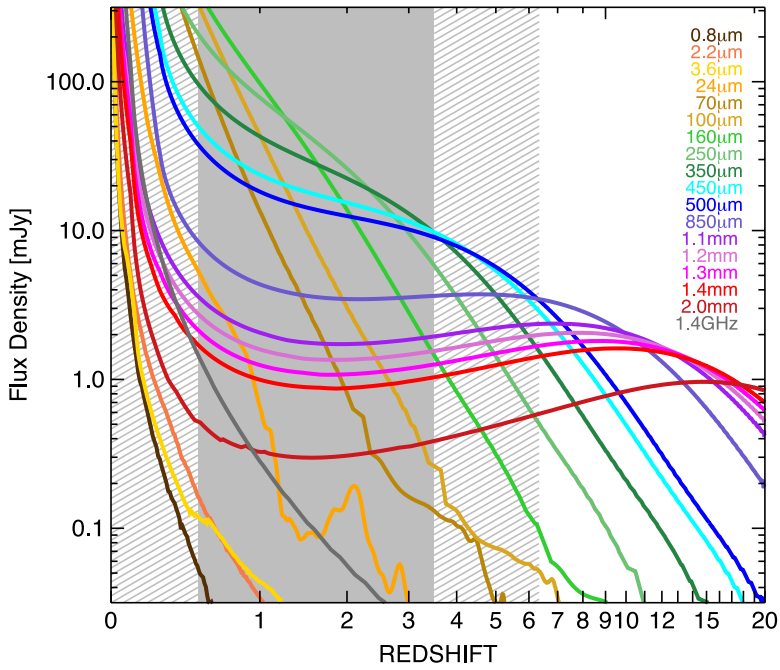

Figure 1.12. Observed flux densities for a $z = 2$ $10^{12.5}$ $L_\odot$ DSFG template from Pope et al. (2008). Of particular note is the flatness of the 850 μm flux density between $z \sim 1$ and $z \sim 7$. The grey shaded area shows the redshift range over which SMG follow-up has been particularly successful, the redshift distribution of this population likely stretches to higher values however. Taken from Casey, Narayanan, and Cooray (2014).

Narayanan, and Cooray (2014) for a recent review.

1.3.3.2 Other selections of DSFGs

Besides the original SCUBA SMG definition, several other selection criteria are commonly used to obtain samples of high-redshift DSFGs. Measurements of number density as a function of wavelength and flux density are given in Figure 1.13, however the exact method of selection (including the the waveband, angular resolution and depth) will bias the properties of the observed population, details of which is discussed below.

Millimetre-wavelength facilities preferentially select DSFGs galaxies with redshifts higher than those of SMGs, or those with larger masses of cool (10 – 30 K) dust. The South Pole Telescope (SPT; Carlstrom et al. 2011) is a 10 m telescope located at the geographic South Pole primarily used for cosmology. While the sensitivity is too low to detect the bulk of high-redshift DSFGs, an 87 deg^2 survey at 1.4 and 2 mm (Vieira et al. 2010) has been useful for constraining the bright-end of the mm luminosity function, particularly $z > 3$ strongly gravitationally lensed DSFGs (see Chapter 2 for more details of this population). Other millimetre-wavelength facilities include AzTEC, the MAx-planck Millimeter BOlometer (MAMBO) on the Institut de Radioastronomie Millimétrique (IRAM) 30 m telescope, ACT and Bolocam on CSO.

The highest flux densities from dust emission across the most common redshift range for high-redshift DSFGs lie in the FIR, making this regime in theory exceedingly useful for the

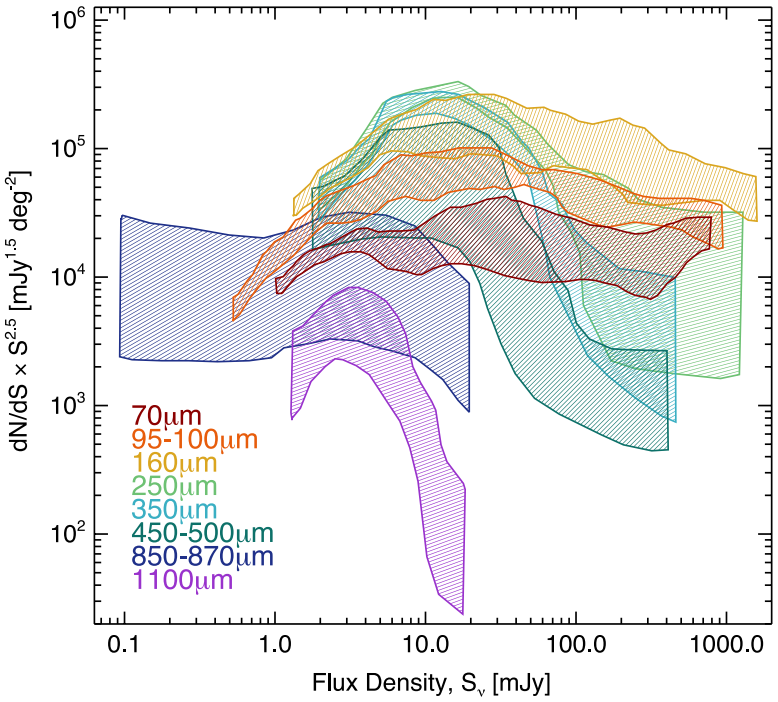

Figure 1.13. Shaded areas represent differential number counts at FIR–mm wavelengths plotted in Euclidean units to enhance details otherwise masked by the large dynamic range covered. Taken from Casey, Narayanan, and Cooray (2014).

discovery of such objects, however the requirement for very low atmospheric water limits ground-based observations, for example with SHARC-II or SCUBA-2 at 450 μm, to tens of days per year. Airborne facilities, such as the Balloon-bourne Large Aperture Submillimeter Telescope (BLAST; Pascale et al. 2008), operating at an altitude of ~39 km, and importantly those space-based are able to bypass this, but are themselves necessarily constrained to small aperture sizes and as such most galaxies observed are below the confusion limit. See Lutz (2014) for a recent review of FIR surveys.

Herschel was the fourth European Space Agency (ESA) "Horizon 2000" cornerstone mission, launched on 2009-05-13. The core dataset analysed in this thesis was obtained by *Herschel*. Three science instruments were housed above the 2367 litre superfluid helium cryostat, cooled by the liquid in that tank and gas escaping from it, and the mission was officially retired after depletion of this cryogen on 2013-04-29. The SPIRE instrument contained both a three band (250, 350 and 500 μm) photometer and an imaging FTS covering 194 – 671 μm. Similar to SPIRE, PACS contained both a spectrometer (55 – 210 μm), and a three band (70, 100 and 160 μm) photometer. See Figure 1.11 for an illustration of the photometer bandpasses.

The *Herschel* Astrophysical Terahertz Large Area Survey, (*H*-ATLAS; Eales et al. 2010) was the largest open time project undertaken by *Herschel*, surveying six fields of total 570 deg^2 with five bands: 100, 160, 250, 350 and 500 μm, over 600 h. Parallel imaging mode (PACS and SPIRE simultaneously) was used, with the fastest scan rate 60 arcsec s^{-1}. While SPIRE imaging with its large beam sizes of 18.2, 24.9 and 36.3 arcsec for the three bands is quickly limited by confusion, total noise in the three SPIRE bands was better than pre-launch estimates, at 5σ levels

of 33 – 45 mJy (Clements et al. 2010). The PACS data however was significantly shallower than planned with 5σ point-source sensitivities of 120 – 240 mJy (Ibar et al. 2010b). Data reduction to produce the final SPIRE maps and catalogues is presented in Pascale et al. (2011) and Rigby et al. (2011). The majority of galaxies studied in this thesis were selected from this *H*-ATLAS SPIRE imaging.

The *Herschel* Multi-tiered Extragalactic Survey (*Her*MES; Oliver et al. 2012) was another programme of comparable size to *H*-ATLAS, consisting of a series of observations of clusters and deep fields, with varying area coverage and depth. SPIRE 250, 350 and 500 µm imaging was taken of each field, with 100 and 160 µm PACS imaging of most. HeLMS, an additional 270 deg^2 SPIRE-only field of which ~55 deg^2 overlap SDSS Stripe 82 was added later to study bright-end counts and cosmic structure. Several *Her*MES sources are included in the galaxy sample studied in later chapters.

A simple flux cut at 24 µm primarily selects $z < 1$ galaxies (Le Floc'h et al. 2005), however combining this *Spitzer* imaging with with optical and NIR measurements can produce a sample of high-redshift DSFGs. Objects exhibiting criteria of $R - K > 4.5$ and $S_{24\,\mu\mathrm{m}}/S_{\mathrm{R}} > 1000$ are known as dust obscured galaxies (DOGs) (Dey et al. 2008; Fiore et al. 2008), and may trace a population with a lower intensity of SFR than for example SMGs, exhibiting more visible light luminosity. These galaxies still possess high column densities of $N_{\mathrm{H}} > 10^{24}$ cm^2 and optical depths of $A_{\mathrm{V}} > 30 - 300$ (Fiore et al. 2008), however <10 % appear to be ongoing major mergers (Schawinski et al. 2012). Questions remains over whether DOGs represent a distinct population, or a post-starburst/SMG stage, where an AGN is starting to blow out material and reduce the level of star formation, see Section 1.3.5.2.

1.3.4 Intrinsic Properties of high-redshift DSFGs

1.3.4.1 Spectral energy distribution (SED) and multiwavelength properties

The large numbers of high-redshift DSFGs now detected by surveys with *Herschel*, JCMT, the Atacama Pathfinder EXperiment (APEX; Güsten et al. 2006) and other facilities provide a wide range of examples of one of the most important galaxy populations, however multi-wavelength coverage is necessary to understand the physical properties, history and likely future evolution of these objects. Additionally, as described in Section 1.3.3.1, a redshift cannot be readily estimated from a submm flux alone, therefore multi-wavelength observations of some form are required to determine a galaxy's intrinsic luminosity, dust mass, SFR and other properties. The SED of a typical high-redshift DSFG is shown in Figure 1.14.

FIR–mm:
Current single-dish observatories operating at wavelengths longward of the FIR (those typically used for the wide-area discovery surveys) have relatively poor angular resolution: 15″ for SCUBA at 850 µm and 25″ for SPIRE at 350 µm for example, which at typical SMG redshifts are equivalent to ≳100 kpc. Moreover, while DSFGs may be bright across the FIR–mm, in

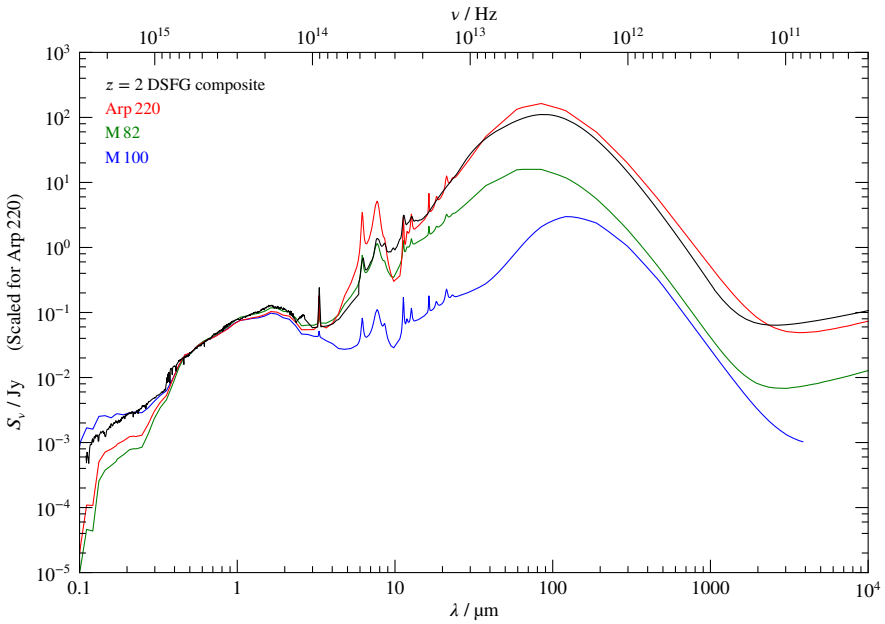

Figure 1.14. Rest frame SEDs of star-forming galaxies normalised in the V band.
Black: composite high-redshift DSFG SED from Swinbank et al. (2014).
Other SEDs are taken from Silva et al. (1998). Arp 220 (*red*) is a $z = 0$ ULIRGs, M 82 (*green*) is a starburst galaxy, and M 100 (*blue*) is a "normal" spiral galaxy.

other wavebands they are often unremarkable. To alleviate uncertainties in matching between different wavebands and reduce sample bias by requiring high fluxes in multiple bands, higher angular resolution observations at a similar frequency can provide a precise position, for example 870 μm ALMA imaging has been obtained of sources discovered at 870 μm in the LABOCA ECDFS Submillimeter Survey (LESS; Weiß et al. 2009b) (Hodge et al. 2013) and at 850 μm in the SCUBA-2 Cosmology Legacy Survey (Simpson et al. 2015). This method additionally provides constraints on multiplicity, finding a significant fraction of multiple sources, in particular finding no source brighter than ~10 mJy, and other maps where no source was found, indicating several faint sources blending to form a single-dish detection, see Section 1.3.4.3 for more details. Even in other FIR–mm bands, high-redshift DSFGs may not be detected given their redshift and instrument sensitivity. 34 out of the 99 ALMA-detected LESS sources were not visible individually in *Herschel*/SPIRE maps (Swinbank et al. 2014), likely suggesting a very high redshift.

Radio:

A tight correlation between the FIR luminosity and radio luminosity density of star-forming regions was found by Helou, Soifer, and Rowan-Robinson (1985). This far-infrared–radio correlation (FIRRC) has since been shown to be nearly universal within low redshift "normal" disc and starburst galaxies (Yun and Carilli 2002; Murphy et al. 2008) and even in the extreme starbursts of SMGs, where it allows observations at radio wavelengths (e.g. Ivison et al. 1998; Smail et al. 2000), where there is a lower number density of sources (~2.5 arcmin^{-2} objects of 1.4 GHz > 50 μJy flux density; Ivison et al. 2002) by interferometers with high angular resolution, alleviating uncertainty in position and identification of counterparts at other wavelengths, such

as the optical/NIR, albeit at a large cost in telescope time and hence under the restriction that sufficiently deep radio maps are currently less abundant than for example corresponding 24 μm coverage (see later).

This correlation originates through SNe, which should trace the SFR, and in particular the rate of formation of massive stars: those that dominate the flux powering the FIR emission. Electrons produced in SNe are decelerated in the magnetic field of the galaxy, emitting synchrotron radiation, the strength of which should therefore be related to that of the FIR.

This synchrotron emission dominates the radio SED and has a functional form $S_\nu \propto \nu^\alpha$, where $\alpha \sim -0.75$, indicating a positive k-correction and a quick drop-off of radio flux density with redshift. While $z \gtrsim 3$ DSFGs may be readily detected at 850 μm, radio counterparts become increasingly difficult to find and a substantial fraction may not be detected even in very deep radio data ($\sim 1/3$ have $S_{1.4\,\mathrm{GHz}} < 30\,\mu$Jy Chapman et al. 2003). A further contribution to this may involve the loss of electron energy to inverse Compton scattering off CMB photons, which increase in strength at very high redshifts (Schleicher and Beck 2013).

An AGN can also contribute to and in some cases dominate the radio flux of DSFGs. These are discussed further in Section 1.3.4.4.

MIR:

The MIR regime of high-redshift DSFGs can be dominated by AGN-heated hot dust continuum and PAH features that can provide bright detections in certain redshift windows (see Section 1.2.1.1). MIR imaging has typically somewhat higher angular resolution than JCMT or *Herschel*, and data from the Multiband Imaging Photometer for *Spitzer* (MIPS) (5.6 arcsec FWHM at 24 μm) or the Infrared Array Camera (IRAC) (3.6 – 8 μm bands) on *Spitzer* exists in many deep fields. These maps have been used to identify submm sources at this wavelength (e.g. Egami et al. 2004; Ivison et al. 2004; Pope et al. 2006; Dye et al. 2008), finding a median flux density at 24 μm of ~0.2 mJy, however the positive spectral slope shortward of the dust peak (such that such detections are biased toward lower-z objects), the variation of MIR to FIR flux densities (often due to AGN) and PAH absorption constrain the efficacy of this method, particularly at $z > 2$ (Pope et al. 2008; Menéndez-Delmestre et al. 2009). The occurrence and contribution of AGN within this population is discussed in Section 1.3.4.4. A more recent technique "*Her*MES XID" (Roseboom et al. 2010) has been used to cross-match confusion-limited *Herschel* SPIRE maps with *Spitzer* MIPS data. At shorter wavelengths, utilising IRAC colours along with positional likelihood ratios can successfully recover a large fraction of counterparts (Alberts et al. 2013).

UV/Optical/NIR:

Strong and varied optical extinction is exhibited by DSFGs, many of which show $S_{\mathrm{IR}}/S_{\mathrm{optical}} > 1000$, a median $R_{\mathrm{AB}} = 24.6$ being measured by Chapman et al. (2005) for example, with no detection of continuum after several hours of integration on an 8 m class telescope for a substantial fraction of sources. Not only are high-redshift DSFGs therefore sufficiently faint in many wavebands to require dedicated followup observations, but at these flux densities, there is

a high number density of unrelated galaxies — tens of potential counterparts may be visible within one FIR beam and identification of the correct counterpart source is not straightforward. The large redshift range observable at 850 µm due to the k-correction also plays a role here, with more distant members being significantly optically fainter than other nearby but unrelated $z = 1 - 2$ galaxies. The large amount of information available from observations in the optical, in particular the ability to determine a spectroscopic redshift, makes overcoming such issues important however.

The most certain method for determining the counterpart is to use the position from a deep 24 µm or radio map as a prior, however the area coverage of those data is substantially lower than available in the optical or NIR. To determine directly from the FIR position which optical source is most likely responsible for the FIR emission requires statistical techniques, often a likelihood ratio (e.g. Sutherland and Saunders 1992; Chapin et al. 2011) or a "p-value" (e.g. Downes et al. 1986; Ivison et al. 2002).

1.3.4.2 Dust emission and star formation rate (SFR)

Several properties of the dust and UV radiation production within a galaxy can be deduced by modelling the FIR dust emission peak of the SED.

A single-temperature grey body function can be used as a first approximation to the dominant cool dust component, and in the SCUBA era with only a single data point this was sufficient; however with the copious multi-wavelength data now available, more complex temperature distributions must be considered. A second grey-body distribution may be added to the model, accounting for emission from a lower mass (for example 1 %) of warm 60 – 100 µm dust. Other analytic approximations can extend the model more sensibly down to shorter wavelengths (e.g. Casey et al. 2012). A more physically-motivated analytic description however is a power-law distribution of dust temperatures $\frac{\mathrm{d}M_\mathrm{d}(T)}{\mathrm{d}T} \propto T^{-\gamma}$ with a low-temperature cutoff at some value T_c (Kovács et al. 2010; see Chapter 3 for further details). A similar power law distribution of radiation fields U: $\frac{\mathrm{d}M}{\mathrm{d}U} \propto U^{-\alpha}$, where α is the Wien-side spectral index (Dale et al. 2001; Dale and Helou 2002), is approximately equivalent ($\gamma \approx 4 + \alpha + \beta$) assuming radiative dust heating. A value $\gamma = 7.2$, appropriate value for local starbursts, is often found satisfactory even at high-redshift (e.g. Magnelli et al. 2012).

Numerical models may also be used to fit galaxy SEDs, for example those based on radiative transfer models (e.g. Silva et al. 1998; Dopita et al. 2005), empirical templates (e.g. Chary and Elbaz 2001; Rieke et al. 2009), or energy balance techniques (e.g. da Cunha, Charlot, and Elbaz 2008). The last of these is now commonly used to model high-redshift DSFGs (e.g. Negrello et al. 2014), although deep optical/NIR imaging is required to constrain the direct stellar emission, which requires determining a precise position and optical counterpart.

Modelling the FIR–mm region of the spectrum indicates a typical dust temperature of 20 – 40 K for star-formation dominated sources (e.g. Amblard et al. 2010; Symeonidis et al. 2013), increasing with L_IR (Magnelli et al. 2012; see Figure 1.15) and possibly stellar mass (Bourne

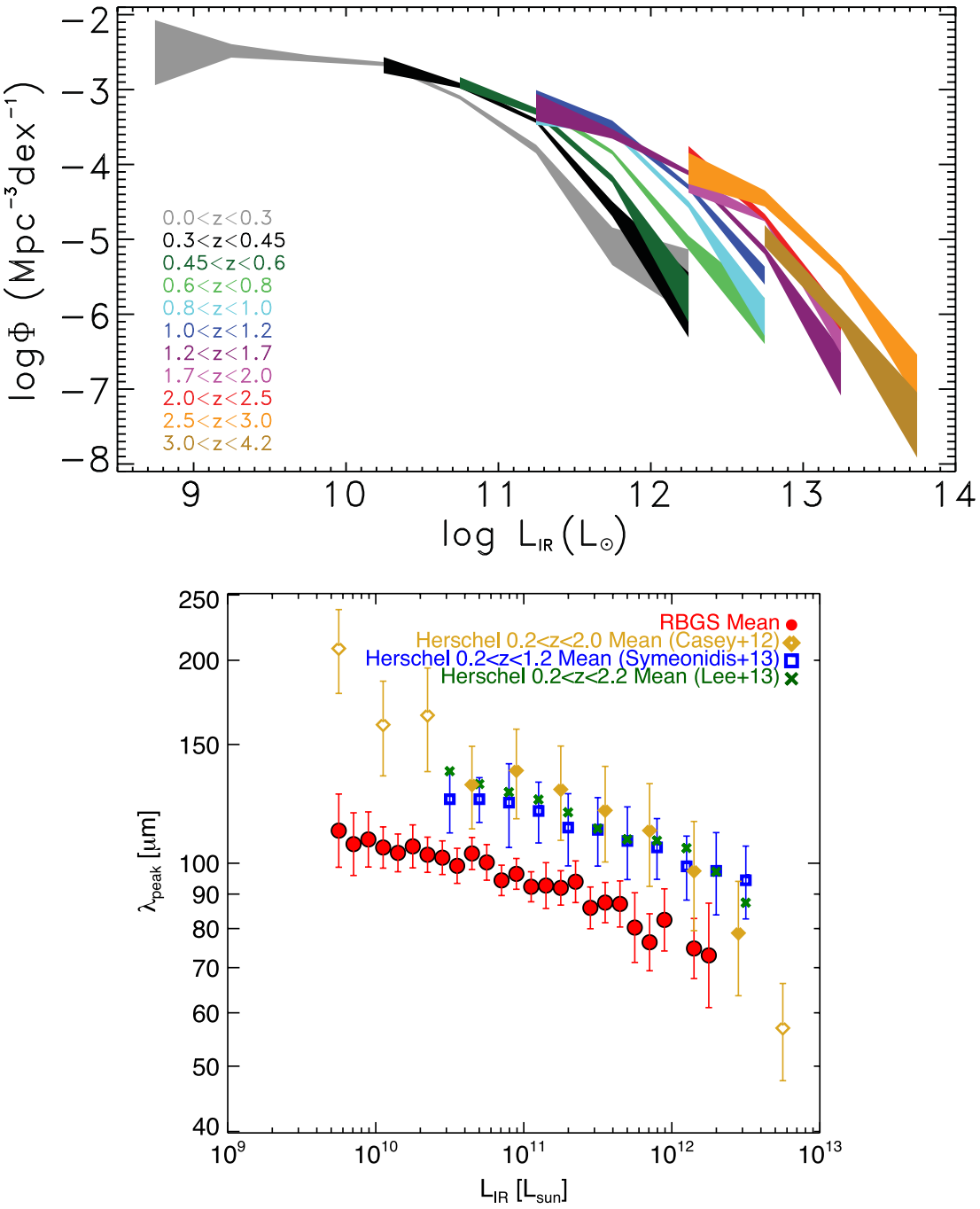

Figure 1.15. *Left:* The IR luminosity function as a function of redshift, derived from data from the PEP fields, showing an increase in L^*_{IR} and a decrease in Φ_{IR} with redshift, up to $z \sim 3$, above which the number of galaxies very bright in the infrared may decrease. Taken from Gruppioni et al. (2013).
Right: Variation of the wavelength of the dust emission peak as a function of luminosity and redshift. Yellow, green and blue points are from high-redshift *Herschel* SPIRE selected samples, which appear to be offset to cooler dust temperatures from the *IRAS* Revised Bright Galaxy Sample (RBGS; Sanders et al. 2003) (red points). Taken from Casey, Narayanan, and Cooray (2014), see that work for data references.

et al. 2012). These values are weighted averages across the usually unresolved galaxies, and so while useful for comparison between DSFGs (modelled with the same method), care must be taken in using them to determine anything about the true physical properties of the galaxy. Dust masses can range up to several $\times 10^9\,\mathrm{M}_\odot$, however a median value is likely $\sim 4 \times 10^8\,\mathrm{M}_\odot$ (Magnelli et al. 2012; Swinbank et al. 2014). The optical depth to dust emission increases with frequency as $\tau \propto \nu^\beta$, partly due to dust grain properties and partly due to hotter material being found closer to the heating source deep inside the dusty clouds. Systems with a greater dust mass (and hence higher average optical depth) therefore typically exhibit their maximum output flux density at longer wavelengths (Scoville 2013), however this is opposed by an increase in L_{IR} and SFR, which may correlate with ISM (and dust) mass, see Figure 1.14.

The conversion from a measured infrared luminosity to a star formation rate is not trivial, requiring the assumption of an IMF, optical depth, and contributions from older stellar populations and AGN among other complications. At high redshift, our ability to untangle these effects is reduced and a simple scaling factor or other few-free-parameter function is normally used, for example the calibration presented in Murphy et al. (2011b) is recommended in the review by Kennicutt and Evans (2012), a reformulation of which is

$$\frac{\mathrm{SFR}_{\mathrm{IR}}}{\mathrm{M}_\odot\,\mathrm{yr}^{-1}} = \frac{L_{\mathrm{IR}}}{6.7 \times 10^9\,\mathrm{L}_\odot}. \tag{1.10}$$

A few other factors complicate the issue of conversion only from IR measurements to SFRs, which further enhance the improvements obtained through using a more complex SED model such as that of da Cunha, Charlot, and Elbaz (2008): The IR-to-UV output of a galaxy at some particular SFR may change with redshift (Burgarella et al. 2013), and galaxies with significant SFRs and dust masses such as this population possibly exhibit a flux density excess at $\lambda > 500\,\mu\mathrm{m}$ due to magnetic or spinning dust grains (Draine 2003).

With $L_{\mathrm{IR}} = 10^{12}\,\mathrm{L}_\odot$ naïvely equivalent to $100-150\,\mathrm{M}_\odot\,\mathrm{yr}^{-1}$, an average $100-250\,\mathrm{M}_\odot\,\mathrm{yr}^{-1}$ is found for local ULIRGs (da Cunha et al. 2010). SFRs derived from the infrared luminosity of classical SMGs tend to average $\sim 500\,\mathrm{M}_\odot\mathrm{yr}^{-1}$ (Magnelli et al. 2012; Swinbank et al. 2014), however with many being resolved into multiple components by ALMA a median $\sim 330\,\mathrm{M}_\odot\mathrm{yr}^{-1}$ is found for the whole population (Swinbank et al. 2014). As with low redshift ULIRGs, these SFRs lie around 10 times higher than "normal" star-forming galaxies with a similar molecular gas mass; at these redshifts the BzK galaxies (e.g. Daddi et al. 2010b; Rodighiero et al. 2014). The separation of this starburst population from the M_*-SFR "main sequence" of star-forming galaxies provides evidence that as at , a different mechanism may be required to generate efficient star-formation, however nature of this mechanism may not be the same.

An alternative method of estimating the SFR without multiplicity uncertainties is via interferometric observations of free-free emission from H II regions around massive stars, with values $400-600\,\mathrm{M}_\odot\,\mathrm{yr}^{-1}$ (Thomson et al. 2012) in good agreement with other methods. The most extreme examples of high-redshifts DSFGs can have SFRs of $>2000\,\mathrm{M}_\odot\,\mathrm{yr}^{-1}$ (e.g. Riechers et al. 2013; Ivison et al. 2013), and will likely form enough stellar mass to become the central

objects of the most massive clusters today. These hyper-luminous infrared galaxies (HyLIRGs) can even approach the conditions of a "maximum" starburst (Elmegreen 1999), where the rate becomes Eddington limited.

1.3.4.3 Mass, size and kinematics

As with any galaxy, the mass of a DSFG is composed of several components: stars and stellar remnants, gas, dark-matter and the central black hole. Each of these can be estimated individually, and in the case of interstellar gas, no one tracer captures the mass of all phases, although in these systems the majority of gas is suspected to be molecular (e.g. Carilli and Walter 2013). One class of measurements: those providing kinematic information, can provide a total mass enclosed within the radius of measurement. Measurements of each of these in high-redshift DSFGs are now described, along with measurements of the size and kinematics.

High dust attenuation, intense ongoing starbursts and difficulty in locating optical counterparts hamper efforts to determine stellar masses, the bulk of which are contained within sub-solar-mass stars >1 Gyr old and brightest in the optical–NIR. Two studies utilising the same dataset epitomise the uncertainties involved, with Hainline et al. (2011) finding a median SMG stellar mass $3.5 \times 10^{11}\,\mathrm{M}_\odot$, and a re-analysis finding $7 \times 10^{10}\,\mathrm{M}_\odot$, a factor ~5 lower (Michałowski, Hjorth, and Watson 2010). Other estimates tend to lie around the more massive of these values (Borys et al. 2005; Dye et al. 2008), however a factor of a few uncertainty is likely due to assumptions made including the star formation history (SFH) and population synthesis models used (Michałowski et al. 2012). Another large source of uncertainty is the IMF: a stellar mass determined using a Salpeter (1955) IMF will be a factor of ~1.8 larger than if a Kroupa (2001) or Chabrier (2003) IMF were to be used.

Molecular gas is likely one of the most massive components of high-redshift DSFGs (Krumholz, McKee, and Tumlinson 2009), usually traced by CO emission (see Section 1.2.1.1). A CO line luminosity can be expressed in several forms. The first is simply from the line flux, and useful for comparison against the infrared luminosity and the luminosity of other spectral lines,

$$\frac{L_\mathrm{CO}}{\mathrm{L}_\odot} = 3.1110 \times 10^{19} \left(\frac{D_\mathrm{L}}{\mathrm{Mpc}}\right)^2 \left(\frac{F_\mathrm{CO}}{\mathrm{W\,m^{-2}}}\right) \tag{1.11}$$

$$= 1.0377 \times 10^{-3}\,(1+z)^{-1} \left(\frac{D_\mathrm{L}}{\mathrm{Mpc}}\right)^2 \left(\frac{\nu_\mathrm{rf}}{\mathrm{GHz}}\right) \left(\frac{\int S_\nu \mathrm{d}v}{\mathrm{Jy\,km\,s^{-1}}}\right). \tag{1.12}$$

An alternative formulation is the area and velocity integrated source brightness temperature

$$L'_\mathrm{CO} = \int_V \int_A T_\mathrm{b}\,\mathrm{d}a\,\mathrm{d}v \tag{1.13}$$

$$\frac{L'_\mathrm{CO}}{\mathrm{K\,km\,s^{-1}\,pc^2}} = 3.2548 \times 10^7\,(1+z)^{-1} \left(\frac{D_\mathrm{L}}{\mathrm{Mpc}}\right)^2 \left(\frac{\nu_\mathrm{rf}}{\mathrm{GHz}}\right)^{-2} \left(\frac{\int S_\nu \mathrm{d}v}{\mathrm{Jy\,km\,s^{-1}}}\right) \tag{1.14}$$

$$= 3.1365 \times 10^{10} \left(\frac{\nu_\mathrm{rf}}{\mathrm{GHz}}\right)^{-3} \left(\frac{L_\mathrm{CO}}{\mathrm{L}_\odot}\right). \tag{1.15}$$

This latter definition is often used to determine the mass of the molecular gas component through a linear conversion between CO $J = 1 \rightarrow 0$ luminosity and H_2(+ He) mass:

$$\frac{M_{H_2+He}}{M_\odot} = \frac{\alpha_{CO}}{M_\odot (K\ km\ s^{-1}\ pc^2)^{-1}} \left(\frac{L'_{CO\ 1\rightarrow0}}{K\ km\ s^{-1}\ pc^2} \right) \tag{1.16}$$

$$= 20478 \frac{\alpha_{CO}}{M_\odot (K\ km\ s^{-1}\ pc^2)^{-1}} \left(\frac{L_{CO\ 1\rightarrow0}}{L_\odot} \right). \tag{1.17}$$

Assuming virialised clouds, the value of the conversion factor α_{CO} is dependent upon both gas density and brightness temperature $\frac{M_{gas}}{L'_{CO\ 1\rightarrow0}} = \alpha_{CO} \propto \frac{n_{H_2}^{2/2}}{T_b}$ (e.g. Solomon et al. 1987). Despite the positive dependence upon density, the increased brightness temperatures experienced within dense star forming environments typically cause the factor to decrease in value in those regions. The conversion factor also increases at lower metallicity, where reduced dust allows for greater UV penetration into molecular clouds and dissociation of CO, which therefore will only exist in the deepest regions. See the review of Bolatto, Wolfire, and Leroy (2013) for further discussion of the conversion factor. The choice of value to use for high-redshift DSFGs is therefore uncertain, with various authors opting for the Milky Way value: $4.2\,M_\odot(K\ km\ s^{-1}\ pc^2)^{-1}$; a value appropriate for local ULIRGs: $0.8\,M_\odot(K\ km\ s^{-1}\ pc^2)^{-1}$; or somewhere between.

As α_{CO} only converts between $J = 1 \rightarrow 0$ and M_{gas}, measurements of other CO lines will require first an estimate of the $J = 1 \rightarrow 0$ luminosity. The most rigorous method is to use radiative transfer equations to fit a model of the cloud emission to multiple measured CO line fluxes, and estimate the $J = 1 \rightarrow 0$ luminosity from this model. The large velocity gradient (LVG) approximation offers a simple solution to these equations, assuming for example a collapsing spherical cloud with uniform density and kinetic temperature, in which the thermal velocity is much smaller than the collapse velocity. In this case the line intensity from any point in the cloud only depends upon the local source function and escape probability, such that in which each velocity channel in the observed line can be mapped to a single cloud position with a distinct radial velocity. In the typical situation for high-redshift DSFGs where only a single CO line: for example $J = 3 \rightarrow 2$; has been measured, empirical line ratio measurements or an assumption of the CO SLED must be used instead. Assuming both CO lines have similar emission areas and velocities, $L'_{CO} \eqsim T_b$, so the observed brightness temperature ratio is

$$r_{3\rightarrow2/1\rightarrow0} = \frac{T_{b;3-2}}{T_{b;1-0}} = \frac{L'_{CO\ 3\rightarrow2}}{L'_{CO\ 1\rightarrow0}} = \left(\frac{\nu_{1-0}}{\nu_{3-2}} \right)^3 \frac{F_{3-2}}{F_{1-0}}, \tag{1.18}$$

where CO fluxes are in W m^{-2}: the frequency ratio exponent is 2 if fluxes are in Jy km s^{-1}. Studies of the CO line brightness temperature ratios indicate $r_{3\rightarrow2/1\rightarrow0} \sim 0.5$, decreasing with frequency to $r_{7\rightarrow6/1\rightarrow0} \sim 0.2$ (Ivison et al. 2011; Bothwell et al. 2013). The values found are lower than those in local ULIRGs and star-forming regions within the Milky Way. While the higher J lines are emitted almost exclusively from dense, warm star-forming gas, $J = 1 \rightarrow 0$ can trace the large reservoir of extended, diffuse, cool gas, and its brightness temperature may vary greatly in comparison to other transitions. The CO lines may also be optically thick, complicating analysis

of the conditions and adding uncertainty to a conversion to a $J = 1 \rightarrow 0$ luminosity. Transitions above $J = 7 \rightarrow 6$ or so are likely to be sub-thermally populated and optically thin whatever the conditions, and may therefore become important targets in the future for probing the most dense regions. See Papadopoulos et al. (2012a) for a discussion of the dependence of the conversion factor on the observed transition and physical parameters within galaxies, in particular dynamical considerations.

Accepting the uncertainty in α_{CO} and any conversion from a non-$J = 1 \rightarrow 0$ flux, derived gas masses typically lie around $10^{10} - 10^{11}\,M_\odot$ (e.g. Frayer et al. 1998; Greve et al. 2005; Tacconi et al. 2006), with a large sample suggesting a median of $\sim 5 \times 10^{10}\,M_\odot$ (Bothwell et al. 2013). These values are ~3 times higher than are found in local ULIRGs (Solomon et al. 1997). The fraction of baryons in the ISM is also much higher in these systems than in galaxies today (see Figure 1.16), however this appears to be a simple evolution with redshift of the galaxy population as a whole rather than a particular property of DSFGs (Geach et al. 2011).

The mass of the atomic phase of the ISM is harder to determine, but is predicted to be subdominant to molecular gas at $\Sigma_{\mathrm{H\,I}} \gtrsim 10\,M_\odot \mathrm{pc}^{-2}$ (Krumholz, McKee, and Tumlinson 2009). Low ionisation PDR lines could be used, for example [O I] and [C II], however these are only excited at higher densities and incident fluxes respectively, and so will not trace all of the atomic gas and suffer contributions from H II regions and GMCs. The SKA or a successor may be able to observe [H I] 21 cm emission, however a conclusive measurement is not likely to be obtained in the near future.

A derived dust mass (median $\sim 4 \times 10^8\,M_\odot$, see Section 1.3.4.2) may be able to estimate the ISM mass (Scoville et al. 2014), however assumptions used are usually calibrated within the Milky Way or other low-redshift galaxies, and may not apply exactly in the high-redshift, high ISM mass environments of SMGs, where optical depths may be larger. The gas-to-dust mass ratio is one of these assumptions. It may hold relatively constant with metallicity (at least in the regions of strongest dust emission; Draine et al. 2007), or may vary (Sandstrom et al. 2013) with a large scatter (Rémy-Ruyer et al. 2014), being also metallicity calibration dependent. More complete datasets including CO and [H I] 21 cm observations indicate ~25 % variation in the masses estimated between dust and gas ISM estimates (Eales et al. 2012).

The Toomre Q-parameter (Toomre 1964) characterises the stability of a symmetric rotating thin gas disc against gravitational fragmentation, and is dependent upon the velocity dispersion, epicyclic frequency and surface mass density. Even "normal" star-forming galaxies at high-redshift are known to be gas rich with higher gas densities than found in their local counterparts (e.g. Daddi et al. 2010a; Tacconi et al. 2010). Systems with similar conditions in which the criterion $Q < 1$ is satisfied are liable to fragment into clumps of size a few hundred to one thousand pc (Genzel et al. 2011; Swinbank et al. 2011), giving the galaxy a more irregular appearance, however the overall morphology and dynamics likely remains (for an isolated galaxy) that of a disc not far removed from $z = 0$ spirals (van Starkenburg et al. 2008). These massive ($\sim 10^9\,M_\odot$; Swinbank et al. 2011) clumps likely survive for ~500 Myr (Genzel et al.

2011), before dynamical friction causes clumps to coalesce in the galactic centre, and help form a bulge. During this migration, older stars will be tidally stripped, leaving a young population throughout its life, fuelled by gas accreted on the journey to replace that lost (~50 % of its initial gas) through outflows (Bournaud et al. 2014).

A DSFG as with any galaxy exists within a dark-matter halo. Some fraction of this will be within the radius of the galaxy and contribute to the kinematics. This is difficult to measure directly, and is usually estimated as the "left over" mass after subtracting stellar and gas masses from the dynamical mass, however there are large uncertainties involved with any such measurements such that in many cases the stellar+gas mass is consistent with the dynamical mass with no dark-matter contribution required (e.g. Engel et al. 2010). Alternatively, dark-matter masses may be estimated via comparisons to cosmological simulations, although any mass of galaxy will be found within a range of dark-matter halo sizes within such a simulation. Hickox et al. (2012) estimate a dark-matter halo mass of $\sim 6 \times 10^{12}\,\mathrm{M}_{\odot}$, consistent with the range found by Narayanan et al. (2010). Only some small fraction of this halo mass may be within the radius of dust/CO emission however. Gravitational lensing can also theoretically be used to measure the halo mass directly. Most galaxies however only weakly lens background objects, an effect usually only measurable statistically over large samples of foreground galaxies or clusters.

Dynamical masses are usually derived from CO line widths, however the irregular morphologies and kinematics of high-redshift DSFGs (see later) can contribute to the uncertainty of these estimates. Low-J CO lines trace extended molecular gas, in particular $J = 1 \rightarrow 0$, observations of which indicate a dynamical mass $2 \times 10^{11}\,\mathrm{M}_{\odot}$ (Ivison et al. 2011), larger than estimates from higher frequency transitions (e.g. $6 \times 10^{10}\,\mathrm{M}_{\odot}$; Tacconi et al. 2006).

Within local ULIRGs, a concentrated ~1 kpc nuclear region generates most of their luminosity. Despite the relative compactness of many high-redshift galaxies in comparison to local spirals, star-formation within high-redshift DSFGs appears to be more extended than in their $z \sim 0$ counterparts. The exact measured size (usually a half-light radius or FWHM) will however depend on the observed waveband. The most common measurements are from CO using interferometers, $J = 4 \rightarrow 3$ and $J = 3 \rightarrow 2$ observations indicating sizes of ~4 kpc (Tacconi et al. 2006; Engel et al. 2010; Bothwell et al. 2010), while $J = 1 \rightarrow 0$ indicates larger values of ~7 kpc (Ivison et al. 2011). Sizes from NIR imaging may also be band dependent, with studies indicating from 2.3 kpc in I (Swinbank et al. 2010a), to 4 kpc in the K band (Targett et al. 2013). Sizes from dust continuum emission also appear to have significant variation between study with ALMA imaging of samples of SMGs suggesting a median half-light diameter of ~2 kpc (Ikarashi et al. 2014; Simpson et al. 2015), while demagnified sizes of a strongly gravitationally lensed sample are smaller, at ~1 kpc (Bussmann et al. 2013), however the brightest lensed system will preferentially be more compact. A study of the most luminous SMGs indicates sizes of 5 – 8 kpc (Younger et al. 2008), although these systems as the most luminous are selected not to be typical and may be outliers or the most massive extended mergers. Radio sizes appear to be similar to those of the more excited CO lines (Biggs and Ivison 2008), consistent with an origin from star-formation.

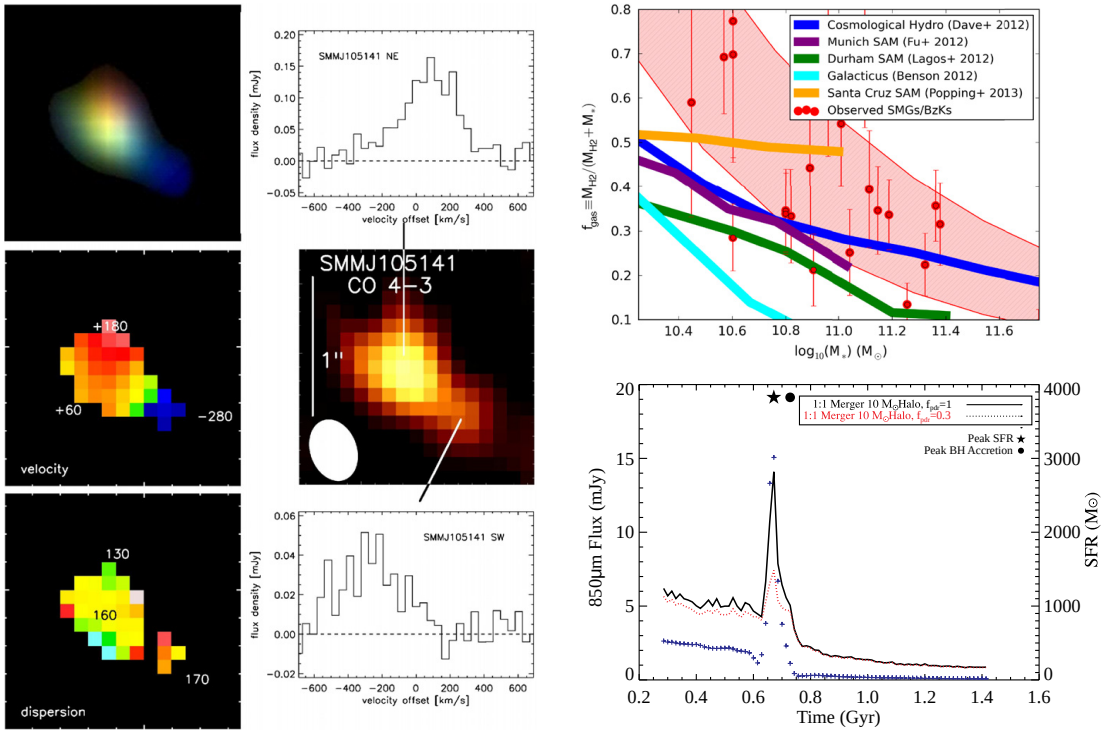

Figure 1.16. *Left half:* Kinematically resolved CO line imaging obtained by PdBI in the extended A configuration, displaying two merging galaxies separated by ~400 km s^{-1}. Taken from Engel et al. (2010).
Upper right: Fraction of mass of molecular gas and stars combined in molecular gas as a function of stellar mass for several simulations and observations of high-redshift star-forming galaxies. Taken from Casey, Narayanan, and Cooray (2014), see that work for details of the observations represented.
Lower right: The solid black and red dotted lines show 850 μm flux density as a function of time across a major merger event for two birth cloud covering fractions. Blue crosses show SFR (right hand axis), with the large solid black star and circle showing the peak SFR and black hole accretion rate respectively. Taken from Narayanan et al. (2010).

As in local ULIRGs, the highest SFR during a merger should occur around the time of final coalescence, producing a starburst more concentrated towards the nucleus than from a isolated disc, however before this point, asymmetric morphologically-extended star-formation should be visible and indicative of the merger. Many interferometric radio and CO line observations have found indications of a high incidence of major mergers within this population (e.g. Ivison et al. 1998, 2000, 2002, 2007, 2010b; Chapman et al. 2004; Tacconi et al. 2006, 2008; Engel et al. 2010, also see Figure 1.16), and such events are also observable by NIR integral field spectroscopy (Alaghband-Zadeh et al. 2012, and references therein). Isolated clumpy star-forming discs likely make up a significant fraction of the remainder of high-redshift DSFGs, appearing to dominate in some studies of NIR morphology (Targett et al. 2011, 2013), however this may simply be a result of cosmic variance or strong dust extinction toward the IR-brightest morphologically-disturbed regions.

Likely connected to the major merger incidence rate is multiplicity among high-redshift DSFGs. The most luminous systems may consist of multiple well-separated galaxies (e.g. Ivison et al. 2013), however a non-negligible fraction of moderate high-redshift DSFGs will also be blends. 35 % of the LESS sample were found to be resolved into multiple SMGs (Hodge et al. 2013),

consistent with similar SMA measurements (Barger et al. 2012). Additionally, 17 out of 88 good 0.4 mJy beam^{-1} r.m.s. ALMA maps contained no detected sources, suggesting even stronger multiplicity at the faint end where individual components do not satisfy the SMG criterion, a theory supported by simulations (Hayward et al. 2011, 2013).

Summarising the above points, high-redshift DSFGs are a varied population, however a typical system is likely composed of a merger of $\sim 10^{11}\,M_\odot$ galaxies, half of the mass of which is in gas, spread over an area of ~4 kpc, with a more compact ~1 kpc star-forming core.

1.3.4.4 AGN within DSFGs

Many local ULIRGs exhibit significant bolometric luminosity contributions from AGN; it should not be unlikely therefore to find AGN within their high-redshift counterparts. Using six high-redshift DSFGs exhibiting broad Hα or Hβ emission, and the virial black hole mass estimator of Greene and Ho (2005), Alexander et al. (2008) estimate the average SMBH mass within high-redshift DSFGs to be $M_{\rm SMBH} \sim 10^{7.8}\,M_\odot$. The effect on each system however depends on both of the black hole mass and mass infall rate, a comparison to the SFR providing an indication of the magnitude of influence.

Mass falling down the gravitational potential well of a SMBH will not immediately cross the event horizon, instead forming an accretion disc and shedding energy and angular momentum via viscous dissipation. The energy released is radiated in the UV and optical, and a hot corona above the disc emits X-rays. The rotational velocity of the SMBH is likely an important factor in the luminosity of an AGN, with the theoretical maximum energy recoverable from infalling matter reaching 42 % for rapid rotation, in comparison to 6 % for zero rotation, due to the last stable orbit being deeper within the potential well (e.g. Aliev and Özdemir 2002). This highly efficient energy liberation mechanism (compared to ~0.7 % for fusion within stars) can allow an AGN to dominate the power output of its galaxy, and with the high gas fractions and SFRs driving gas movement in high-redshift DSFGs, AGN are likely to be important in this population. AGN accreting material in this way are known to be in quasar or radiative mode. Below a mass infall rate of $\sim 0.01\,\dot{M}_{\rm Edd}$, the accreting material becomes very tenuous, and an alternative accretion mechanism results in radio-producing jets, and such AGN are known to be in radio, jet, maintenance or mechanical mode.. As suggested above, AGN are often detectable through emission in various wavebands: radiation from the accretion disc heats surrounding dust and can even be visible as X-rays, and radio emission may also be seen depending on the accretion rate, however with two distinct modes of feedback, there may be relatively little correlation between the radio output and dust-heating ability of an AGN.

Radiation from the hot accretion discs found around active SMBHs heat dust within the obscuring structure to several hundred kelvin. Underlying any PAH features, the MIR continuum is often fit by a power law, (e.g. Clavel et al. 2000; Menéndez-Delmestre et al. 2007) the slope of which will be modified by emission from this hot dust. Should the obscuration be high enough, the thermal emission will be reprocessed moving outwards until the optical depth becomes low enough for

photons to escape, which produce a luminosity contribution in the form of a $T \sim 100$ K grey-body, which is added to galactic SED fits, leaving a steep MIR slope with a gradient similar to that produced by star-formation alone. With a lower obscuration, potentially via a more face-on orientation or at a a later stage of evolution, higher dust temperatures can be observed in the MIR, resulting in a flatter slope and higher flux densities at shorter wavelengths than are generated by star-formation. This requirement of MIR imaging has however limited (particularly since the depletion of cryogen in *Spitzer*) our understanding of the occurrence rate within, and effect of AGN on, DSFGs.

In the MIR, on average AGN contribute at most 30 % of the MIR luminosity and only ~20 % of sources are dominated by AGN in this regime (Pope et al. 2008; Menéndez-Delmestre et al. 2009). At longer FIR–submm wavelengths, the effect from AGN is lessened (e.g Knudsen, van der Werf, and Jaffe 2003; Alexander et al. 2005), and will represent no more than a few percent of flux densities in this regime. The absolute AGN luminosities for low- and high-redshift DSFGs are similar, however the fractional contribution to bolometric luminosity in the latter is slightly lower at ~30 % (e.g. Alexander et al. 2008; Pope et al. 2008; Menéndez-Delmestre et al. 2009), compared to 35 – 40 % (Veilleux et al. 2009) for the lower redshift population due to the difference in SFR.

The radio spectral slope may differ from the standard $\alpha \sim -0.7$ if a galaxy is host to a radio-loud AGN. With at least two radio data points required to determine this, a less expensive method is to measure deviations of the FIRRC away from the observed $q_{\rm IR} \sim 2.4$ due to star-formation. Radio-loud AGN exhibiting low values of $q_{\rm IR}$ are more common at $z \sim 2$ (Wall et al. 2005) and correlate, possibly unsurprisingly, more strongly with 24 µm-selected samples (Ivison et al. 2010a) than with FIR-selected high-redshift DSFGs (Ivison et al. 2010d).

The most common method of searching for and studying AGN within high-redshift DSFGs is via their X-ray emission. The need to discriminate between emission from AGN and high mass x-ray binaries (HMXBs) however limits us to small sample sizes. Arising from the accretion disc close to the SMBH, the lower energy X-rays are absorbed by dust along with UV and optical emission from the accretion disc, however due to their increased energy, hard X-rays experience a lower optical depth and detection of these is a fairly conclusive indicator of an AGN rather than star-formation. In the most obscured systems, the obscuring material may be Compton-thick and no X-ray emission may be detected, for example in the very dense source GN20 (Riechers et al. 2014a). Selecting above a limit $L_{\rm X} \gtrsim 2 \times 10^9\,{\rm L}_\odot$, studies of the fraction of high-redshift DSFGs exhibiting indications of AGN find values between ~40 % (Alexander et al. 2005) and <20 % (Wang et al. 2013). The latter study find an average $L_{\rm X} \gtrsim 2.6 \times 10^8\,{\rm L}_\odot$, consistent with just star-formation for the population as a whole, utilising ALMA imaging to reduce uncertainty in correlating FIR and X-ray detections.

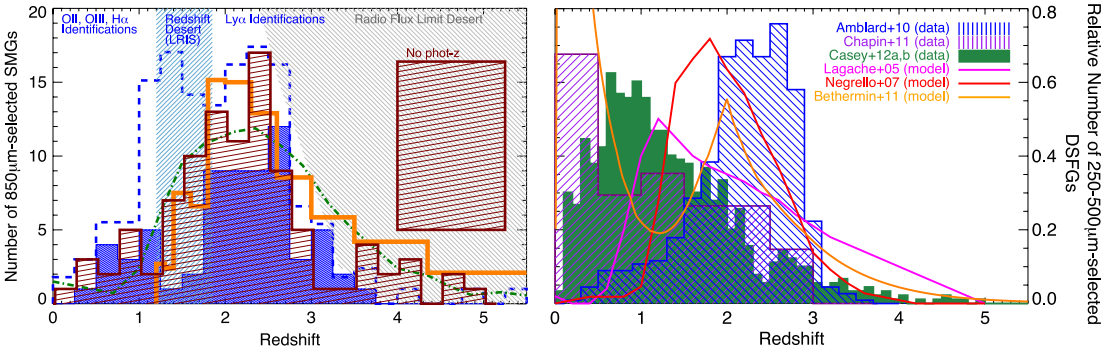

Figure 1.17. Predictions and observed measurements of FIR–submm source redshift distributions.
Left: 850 μm-selected DSFGs redshift distributions. The Chapman et al. (2005) redshift distribution is displayed with solid blue fill, also indicated are the LRIS redshift desert and radio flux limit cut-off. The dashed blue line shows an update to this distribution, with additions by Banerji et al. (2011) to fill the LRIS redshift desert and several high-redshift SMGs. The green dashed curve displays the Lewis, Chapman, and Helou (2005) model. The red line filled and orange histograms display photometric redshifts from the LESS sample from Wardlow et al. (2011) and Simpson et al. (2014) respectively, the large red line filled rectangle displays the fraction of sources in this sample with no redshift estimate.
Right: 250 – 500 μm-selected DSFGs redshift distributions. The blue line filled histogram displays the Amblard et al. (2010) statistical fits to 350 μm *H*-ATLAS sources, the purple line filled histogram displays the 250 – 500 μm BLAST redshift distribution of Chapin et al. (2011), and the green filled histogram displays the 250 – 500 μm *Herschel* redshift distribution of Casey et al. (2012). The phenomenological model distributions of Lagache, Puget, and Dole (2005), Negrello et al. (2007), and Béthermin et al. (2011) are shown in magenta, red and orange respectively, see Chapter 2 for more details of the Negrello et al. (2007) model for strongly lensed DSFGs.
Both figures taken from Casey, Narayanan, and Cooray (2014), see that paper for further detail.

1.3.5 Cosmological properties of high-redshift DSFGs

1.3.5.1 Redshift Distribution

Despite the difficulties in pinpointing optical counterparts to SCUBA sources discussed in Section 1.3.4.1, several spectroscopic redshifts were obtained for early members of this population (e.g. Ivison et al. 1998; Barger et al. 1999; Lilly et al. 1999), indicating $1 \lesssim z \lesssim 3$, however these sources were necessarily bright at optical wavelengths, atypical for the population as a whole. Due to the FIRRC, over several years radio imaging of SCUBA sources was assembled, providing precise positions (Richards 2000; Ivison et al. 2002; Fomalont et al. 2006). Targetting these with the blue-sensitive Low Resolution Imaging Spectrograph (LRIS; Oke et al. 1995) on Keck I, Chapman et al. (2003, 2005) produced the first large sample of SMG redshifts, with a distribution indicating a median $z \sim 2.3$. The requirement of a radio detection however necessarily imposes a selection effect as described in Section 1.3.4.1: sources may be observed relatively consistently only up to $z \sim 3$, where detections become limited by the positive radio k-correction. Since these initial spectroscopic redshift, many more have been obtained through rest-frame UV and optical and CO emission lines, often utilising SED templates fitted to available photometry as priors.

Confirmation of a high-redshift origin has subsequently led to use of, and even construction of other M- and FIR facilities to examine DSFGs in ever-greater detail. Use of these has contributed to the breadth of deep multi-wavelength photometric data now available for many fields of the sky. While particularly accurate for "normal" galaxies observed from the UV out to the MIR (e.g.

Ilbert et al. 2009), photometric redshifts are also increasingly used for high-redshift DSFGs, and are substantially less observationally expensive to obtain than spectroscopic measurements. Such observations have allowed estimates of the redshift distribution of DSFGs selected by criteria other than that of SMGs. Due to this small range of temperatures dominating the Rayleigh-Jeans side of the dust peak, redshift produces a variation in FIR fluxes in FIR and mm bands, with *Herschel* preferentially selecting lower redshift DSFGs and SPT higher (although this telescope is insensitive to unlensed DSFGs which have a lower-redshift bias, see Chapter 2). The survey area, angular resolution and depth also affect source redshift distributions. Shallow, larger area surveys will preferentially select bright-end and closer galaxies, and higher resolution deeper observations further towards the faint end. A potential further contribution to the redshift distribution of FIR–mm sources is size evolution, with higher redshift galaxies possibly being smaller (e.g. Ikarashi et al. 2014).

Redshift distributions observed and theorised at *Herschel* SPIRE and SCUBA/APEX wavelengths are shown in Figure 1.17. Recent studies (Wardlow et al. 2011; Simpson et al. 2014) confirm the $z \sim 2.3$ median found by Chapman et al. (2005), well fit by a Gaussian with a peak at 11.1 Gyr and a width of 1.1 Gyr, however the population likely extends to higher redshifts than those found in those early surveys (e.g. Cox et al. 2011; Walter et al. 2012), with rare examples currently known as high as $z \sim 6$ (Riechers et al. 2013). The sub-population of high-redshift DSFGs which are strongly gravitationally lensed may exhibit a different redshift distribution as the lensing probability changes with redshift. This population is discussed in Chapter 2, along with facilities and bands particularly sensitive to detecting them, for example at 1.4 mm with the SPT, and the ability of wide-band correlators on interferometers operating in the mm to provide redshifts via CO lines.

1.3.5.2 Evolution

Indications exist for evolutionary links between DSFGs and AGN/QSOs, with a popular theory (Sanders et al. 1988) suggesting DSFGs are primarily mergers between gas-rich disc galaxies, which form stars rapidly, rising above the main sequence until the SMBHs combine and an AGN is triggered, which blows out the molecular gas, extinguishing star-formation, and the galaxy drops below the main sequence passing through an unobscured QSO stage and finally becomes a quiescent elliptical. While major mergers are the dominant mechanism initiating local ULIRGs, at $z > 1$ higher SFRs throughout the Universe may allow DSFGs to be simply a result of isolated evolution producing fragmenting gas-rich discs, and the truth is likely more "messy" than suggested by this simple picture with different studies indicating both a dominance of major-mergers (e.g. Engel et al. 2010) and secularly-evolving discs (e.g. Davé et al. 2010). A possible contaminant to high-redshift DSFG samples may be blends of unassociated lower $L_{\rm FIR}$ galaxies (Hayward et al. 2013), however most detailed studies of individual sources have revealed a single galaxy (or associated pair of merging components). High-redshift DSFGs likely do evolve into present-day ellipticals, and $z = 0$ elliptical galaxies have stellar ages consistent with such progenitors (Simpson et al. 2014), but the wide variety of physical properties of these

galaxies makes determining the exact nature of their direct and $z = 0$ descendants difficult, and it is not certain whether these eventually form the cores of the most massive ellipticals, or if most large galaxies experience a short starburst phase and become $L > L^*$ ellipticals today.

Determinations of the SFR and mass of the molecular gas reservoir (described in Section 1.3.4.3) can be used to estimate the duration of the starburst, assuming that the SFR remains at a similar value throughout the burst, that most of the gas is consumed, and that the burst duration is short enough to neglect significant gas inflow from the IGM. Estimates of the time spent as an SMG lie at of order 10 – 100 Myr (e.g. Greve, Ivison, and Papadopoulos 2003; Chapman et al. 2005; Tacconi et al. 2008), however this is model dependent and less well constrained than the contribution of such starbursts to the global SFRD. Such a duration gives a duty cycle of ~0.1 for starbursts within the $M \sim 10^{11}\,M_\odot$ population (Tacconi et al. 2008). Typical molecular gas masses are a few $\times\, 10^{10}\,M_\odot$, so assuming the conversion of a large fraction to stars will result in a contribution of ~10 – 30 % to the existing stellar mass. The starburst and decline after therefore provides movement in the SFR (y-axis) direction of the main sequence plot, but very little in the stellar mass (x-axis) direction. Many of these stars will also not survive until $z = 0$, with the exact mass being defined by the IMF.

The mechanics and result of a possible major merger-induced starburst origin of high-redshift DSFGs were discussed in Section 1.3.4.2. Not every member of this population exhibits indications of an ongoing merger, however should the system be viewed after coalescence, any remaining morphological disturbance may be difficult to observe in comparison to a powerful nuclear starburst. To determine whether such events may be the sole origin, the incidence rate and halo masses involved must be understood, most easily through comparison to cosmological simulations. Results from the Millennium simulation indicate that mergers alone are sufficient to reproduce the $z = 2$ DSFG population, but further evolution involving minor mergers and cold gas accretion is necessary to produce the $z = 0$ massive cluster elliptical galaxies. Narayanan et al. (2010) find that mergers can produce all SMGs, with the most luminous being formed by mergers of $\sim 10^{13}\,M_\odot$ haloes.

After the ~0.1 Gyr during which a galaxy may be classified as an SMG or similar, the SFR must decrease likely due to gas depletion through conversion to stars or AGN feedback. The likely scenario is a combination, although cold gas accretion from the IGM may reduce the effectiveness of the former mechanism. Alternatively the dust temperature could increase to a level such that the 850 µm flux density drops below the SMG limit, likely requiring strong AGN emission.

DSFGs and QSOs exhibit similar redshift distributions (Richards et al. 2006; Assef et al. 2011), and indeed similar comoving number densities (e.g. Hickox et al. 2012), however within individual high-redshift DSFGs the SMBH mass appears to be lower than expected for similarly massive local galaxies or high-redshift QSOs, indicating that SMBH growth occurs after a starburst (Alexander et al. 2008). DOGs have been suggested as a post-peak-starburst population of DSFGs, and indeed a larger fraction appear to be AGN dominated in the MIRs (Dey et al. 2008),

and tend to have larger stellar masses than those of traditional SMGs (Bussmann et al. 2012), however their exact connection to other high-redshift DSFG populations is not conclusively determined. Should a QSO result from a starburst phase, evidence suggests that only the most luminous QSO are typically triggered by a major merger, with moderate luminosity AGN (the number density of which peaks later) more likely activated by secular processes (Allevato et al. 2011).

Nuclear star formation, possibly resulting from a major merger is likely to produce a compact descendent assuming the gas fraction is high enough (Wuyts et al. 2010), and indeed a large fraction of passive galaxies at $z \sim 2$ (at $10^{-4}\,\mathrm{Mpc}^{-3}$) are known to be compact ($R_{\mathrm{eff}} \sim 1\,\mathrm{kpc}$; e.g. Trujillo et al. 2006; van Dokkum et al. 2008), yet such objects are rare locally (Bell et al. 2012). While some of this change may be the result of progenitor bias (the addition of larger passive galaxies to the population; van Dokkum and Franx 2001; Belli, Newman, and Ellis 2014), most of these galaxies may grow by dry minor mergers into the most massive ellipticals today (Naab, Johansson, and Ostriker 2009; van Dokkum et al. 2010). The ages of stellar populations in quiescent galaxies at $z = 2$ indicate formation $\sim 1-2\,\mathrm{Gyr}$ previously (Franx et al. 2003; Whitaker et al. 2013). The challenge of forming such objects may be resolved via two channels: a major merger at $z \gtrsim 3$ or little evolution since assemblage at even higher redshift (Wellons et al. 2015). The former of these methods appears to be supported by observations (Ikarashi et al. 2014; Toft et al. 2014), and may even indicate a dichotomy in high-redshift DSFG in which higher-redshift or more luminous starburst events result from mergers, while later or less intense star-formation occurs in isolated galaxies.

The spatial distribution of high-redshift DSFGs can provide not only an indication of their nature, but also of their evolution to which population of galaxies in the current and intermediate epochs, Should they evolve into the most massive elliptical galaxies today: those at the centre of clusters; strong clustering is expected to be seen, however evolution into "standard" $\sim \mathrm{L}^*$ galaxies (assuming very short starburst events could allow most galaxies of such a mass to experience a DSFG phase) would not show such high autocorrelation, see Figure 1.18.

Local $L > \mathrm{L}^*$ ellipticals are more strongly clustered ($r_0 = 7-12\,\mathrm{h}^{-1}\,\mathrm{Mpc}$; Willmer, da Costa, and Pellegrini 1998; Norberg et al. 2002) than spiral galaxies ($r_0 = 5.4\,\mathrm{h}^{-1}\,\mathrm{Mpc}$; Davis and Peebles 1983), however as expected from cosmological simulations and simple theory, the average comoving correlation length decreases with redshift (Carlberg et al. 2000; McCracken et al. 2001). A study of the spatial clustering of 870 µm the Large APEX BOlometer Camera (LABOCA; Siringo et al. 2009) sources supports the idea of evolution into local massive ellipticals. While the Extended Chandra Deep Field South (ECDFS) has a known deficit of massive SMGs, an autocorrelation length of $r_0 = 7.7^{+1.8}_{-2.3}\,\mathrm{h}^{-1}\,\mathrm{Mpc}$ was derived, similar to that of QSOs (Hickox et al. 2012). This is supported by other measurements (e.g. Viero et al. 2009), with the most luminous (Ivison et al. 2013) and even the highest redshift DSFGs (Capak et al. 2011; Walter et al. 2012) appearing to be strongly clustered within over-densities, often additionally hosting quasars. Much of the difference however results from the mass of the galaxy undergoing the burst: more massive galaxies are more likely to be found in the regions that have experienced

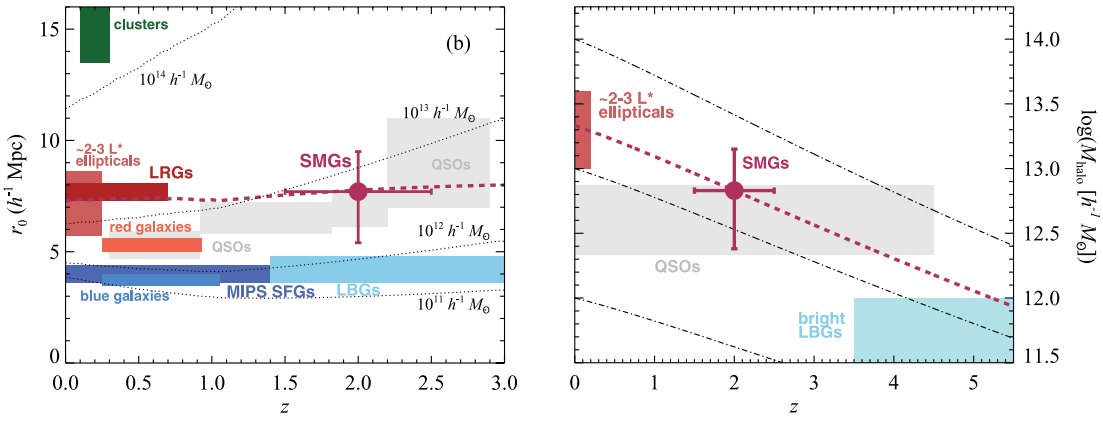

Figure 1.18. *Left:* The autocorrelation length of SMGs in relation to several other populations since $z = 3$. Thin black dotted lines show r_0 as a function of redshift for several masses of dark-matter halo. The dark red dotted line shows the expected evolution of the autocorrelation length given a realistic halo mass growth rate.
Right: The halo grown rate model used in the left hand figure, again comparing SMGs to several other galaxy populations. See also Figure 1.2.
Adapted from Hickox et al. (2012), see that work for details of the datasets used to produce these figures.

sustained high gas infall rates for longer — larger groups and clusters. The autocorrelation length of SMGs predicted by models varies with the assumptions used as to the nature of this population. Most current data suggest a short starburst (see Section 1.3.4.3) which indicates weaker clustering (Almeida, Baugh, and Lacey 2011) than longer duration events (Davé et al. 2010).

High-redshift DSFGs are a varied population spanning a wide range of redshifts and physical properties including stellar mass and the activity of their central SMBHs, united by a high SFR. The picture described above suggests an evolutionary path for these objects more complex than the original (Sanders et al. 1988) theory of local ULIRGs. The most luminous or high-redshift DSFGs are the result of major mergers and tend to transition through a luminous quasar phase into a compact elliptical at $z \gtrsim 2$, which continues to grow despite lying below the main sequence via dry minor mergers to form the core of the most massive cluster galaxies today. Some lower luminosity or redshift DSFG may also consist of mergers, but the fragmentation of unstable gas discs within isolated galaxies powers a significant fraction of this population, particularly the less optically obscured members, possibly becoming lower-luminosity quasars on their way to ~2 L^* elliptical galaxies in the present day.

Chapter 2

Lensed starburst galaxies

As described in Section 1.2.1, the primary PDR and H II region cooling lines are forbidden atomic and ionic transitions and are key diagnostics of the physical and chemical state of these phases of the ISM. In order to cool PDRs, these fine-structure lines have excitation temperatures of up to several hundred kelvin, and are therefore situated in the FIR regime of the spectrum. Above $z \sim 4$, ALMA and other (sub)mm ground-based facilities may be used to target these lines (e.g. Swinbank et al. 2012; Riechers et al. 2014b), however space-based observatories are required to avoid the low atmospheric transmission otherwise inevitable for lower redshift sources.

Herschel PACS spectra cover these lines in local galaxies, with observations of Mrk 231 (Fischer et al. 2010) and M 82 (Contursi et al. 2013) finding that some fraction of the [C II] emission traces outflowing neutral gas, albeit at a lower velocity than the ionised component traced by Hα. *Herschel* SPIRE spectra have also been presented of several local star-forming galaxies. The wavelengths observed by this instrument primarily cover high-J CO and several other molecular lines. Panuzzo et al. (2010) found turbulence to dominate the gas heating within M 82, the AGN in Mrk 231 was suggested to be responsible for the observed $J > 8$ CO lines in that system (van der Werf et al. 2010) and a low velocity molecular outflow was discovered in Arp 220 (Rangwala et al. 2011).

At higher redshifts, the primary ionic and atomic lines move into range of the SPIRE FTS, however *Herschel* is insufficiently sensitive to detect these lines from anything other than the most luminous galaxies. The magnification caused by strong gravitational lensing can however boost the flux densities of "normal" high-redshift DSFGs up to and above the values of these extreme systems, and high enough for FIR spectral lines to be detected by *Herschel*. This is exemplified by SMM J213511.6-010252, the Cosmic Eyelash (Swinbank et al. 2010b; described later), from which the [C II] 158 µm line was detected with the *Herschel* SPIRE FTS (Ivison et al. 2010c). Large-area FIR surveys performed by *Herschel* have overcome the scarcity of such systems and Valtchanov et al. (2011) obtained SPIRE FTS observations similar to that of Ivison et al. (2010c) of two of the first strongly lensed sources found by *H*-ATLAS, detecting [C II] and [O III] 88 µm.

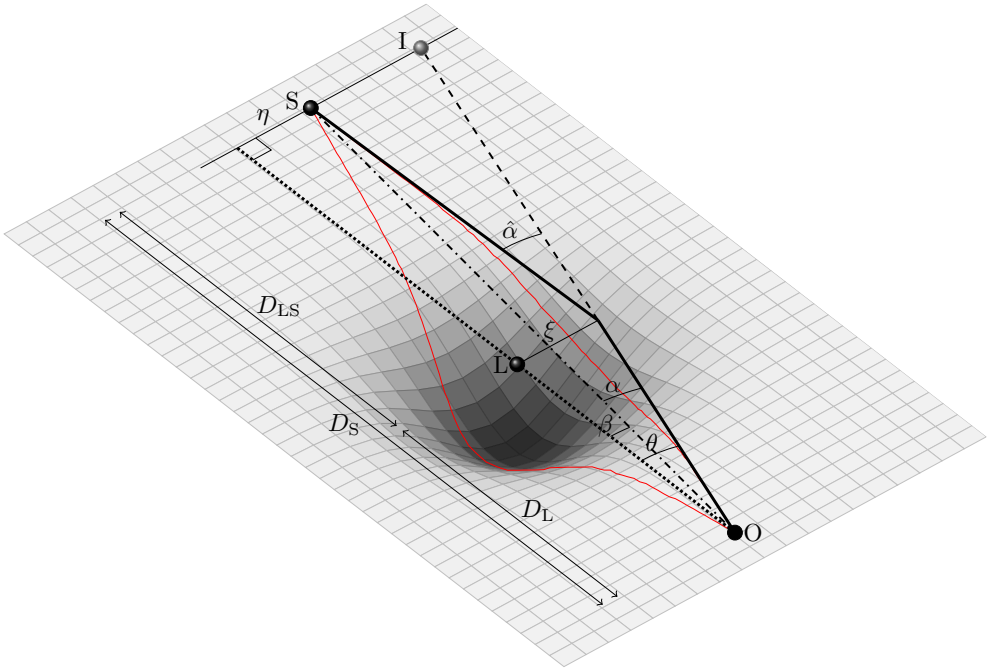

Figure 2.1. Geometry of gravitational lensing. Red lines indicate the shortest paths from the source S to the observer O: which light follows; the curvature of which causes the source to appear to lie at an image position I. Distances are angular distances (note that $D_{\rm L}$ is not a luminosity distance), such that $D_{\rm s} \neq D_{\rm L} + D_{\rm LS}$.

This chapter describes the assembly of a sample of 45 strongly lensed high-redshift DSFGs and a programme of SPIRE FTS observations to extend the Ivison et al. (2010c) and Valtchanov et al. (2011) results, along with the reduction techniques utilised on the observation data. The SPIRE FTS was uniquely able to perform these observations, and this dataset will fill in between the measurements of local ULIRGs and those of very high-redshift DSFGs from ALMA, covering the period of highest SFRD throughout the history of the Universe.

2.1 Strongly gravitationally lensed DSFGs

2.1.1 Gravitational lensing

Gravitational lensing is one of the predictions of general relativity: the distortion of spacetime by mass effectively *bending* the path of light, causing originally isotropic radiation to be deflected around a foreground mass, decreasing flux in certain directions and concentrating it along others. Light travels along geodesics and should there be intermediate matter, the path of these geodesics will differ from those in flat space. Multiple paths may exist for light from a background source to reach an observer, visible as multiple images usually on different sides of the lensing object.

Considering the point source geometry in Figure 2.1, the angle between the lensing object L and background source S is

$$\beta = \theta - \alpha = \theta - \frac{D_{\rm LS}}{D_{\rm S}}\hat{\alpha}. \tag{2.1}$$

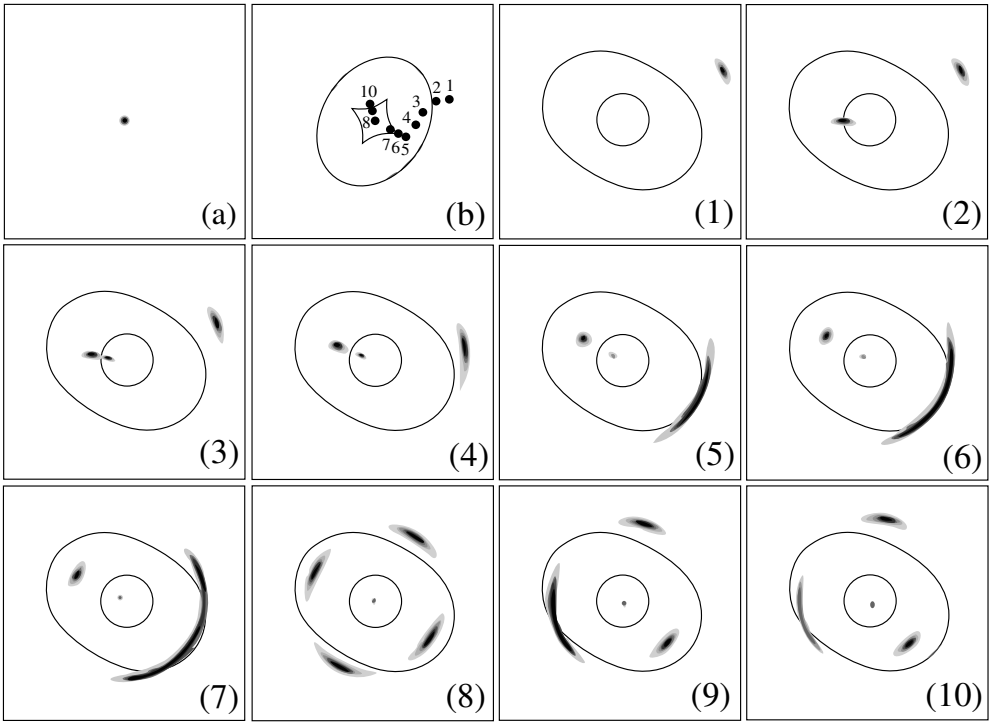

Figure 2.2. The lensed images resulting from different source positions behind an elliptical lensing potential.
Panel (a) shows the source plane morphology.
Panel (b) shows the source positions corresponding to panels (1) to (10) relative to the source plane caustics.
Panels (1) to (10) show the lensed images over the lens plane critical curves, with in particular panels (6) and (7) showing a cusp catastrophe, panel (8) showing an Einstein cross and Panel (9) showing a fold catastrophe.
Adapted from Kneib (1993).

Assuming L is a point source of mass M, general relativity predicts a deflection

$$\hat{\alpha} = \frac{4GM}{c^2 \xi}, \tag{2.2}$$

and after applying this and using $\theta = \xi / D_{\mathrm{L}}$, the true angle can be written as

$$\beta = \theta - \frac{D_{\mathrm{LS}}}{D_{\mathrm{L}} D_{\mathrm{S}}} \frac{4GM}{c^2 \theta}. \tag{2.3}$$

Should the source be perfectly positioned behind the lens, $\beta = 0$ and for any spherically symmetric lens mass distribution, for example the commonly used singular isothermal sphere (SIS), an *Einstein ring* will be seen at an angle

$$\theta_{\mathrm{E}} = \frac{D_{\mathrm{LS}}}{D_{\mathrm{S}}} \hat{\alpha} = \frac{D_{\mathrm{LS}}}{D_{\mathrm{S}}} \frac{4GM(< \xi)}{c^2 \xi} = \sqrt{\frac{D_{\mathrm{LS}}}{D_{\mathrm{L}} D_{\mathrm{S}}} \frac{4GM(< \theta_{\mathrm{E}})}{c^2}}. \tag{2.4}$$

A realistic matter distribution usually cannot be considered as a point or spherically symmetric mass, and so the deflection $\hat{\alpha}$ will become an integral over this distribution, for example a

singular isothermal ellipsoid (SIE). A background galaxy will also have some non-zero source-plane spatial extent and as surface brightness is conserved by gravitational lensing, the total magnification factor μ is equal to both the increase in surface area and the flux observed:

$$\mu = \det\left(\frac{\partial\beta}{\partial\theta}\right)^{-1} \tag{2.5}$$

$$= \frac{\theta}{\beta}\left(\frac{\mathrm{d}\beta}{\mathrm{d}\theta}\right)^{-1} \qquad \text{for a circularly symmetric lens.} \tag{2.6}$$

The magnification of each point in the lensed image depends on the distance of the corresponding source-plane point from a caustic, and as a source crosses a caustic, another image appears at a lens-plane critical curve and separates into two. Figure 2.2 shows how the source-lens alignment can produce large arcs and Einstein crosses and rings, magnifying the background source flux by tens or even higher, making such systems valuable targets to understand distant populations at flux densities and on spatial scales otherwise impossible.

2.1.2 Pre-*Herschel* strongly lensed high-redshift DSFGs

The intervening volume within which a lensing galaxy may be found increases with redshift of the background source, such that a higher redshift source is more likely to be strongly gravitationally lensed (Blain 1996; Weiß et al. 2013). Figure 2.3 displays this for a realistic population of dark-matter haloes, demonstrating this rise with redshift but a flattening above $z \sim 1$. With DSFGs also much more common at $z \gtrsim 1$, this suggests that a non-negligible proportion of the brightest FIR–mm sources will be strongly lensed. Several biases however exist for these selections of the brightest sources. While gravitational lensing is achromatic, spatial separation of emitting regions in the background galaxy will couple with the change in magnification with position relative to the caustics to create *differential magnification* (see Figure 2.3). Selections based on flux will therefore preferentially select objects where most luminosity arises from a compact region, for example a bright star-forming nucleus (Hezaveh, Marrone, and Holder 2012), and within any flux bin the less intrinsically luminous galaxies will generally be the more compact. This leads to complications in analysis of the intrinsic properties, with more extended components such as older stellar populations or cold CO $J = 1 \rightarrow 0$ emitting gas being less magnified than the hot core (Serjeant 2012).

Elliptical galaxies are typical lenses, as the lensing potential $\propto \sigma_{\mathrm{v}}^4$ (where σ_{v} is the velocity dispersion of a SIS), providing 5 – 10 times the lensing cross-section of spirals (Keeton and Kochanek 1998; Möller, Kitzbichler, and Natarajan 2007). Despite this knowledge, the rarity of galaxy-galaxy alignments of the necessary precision for strong lensing among this population, and the difficulty in finding lensing systems among the data of large optical–NIR surveys has greatly hampered searches for these useful events. In the FIR–mm regime however, as the number density of unlensed bright objects is low and foreground lensing galaxies typically do not emit strongly in these bands, strong lenses may be more easily identified (Blain 1996). To confirm the lensed status of candidates, redshifts from spectra of the foreground and background

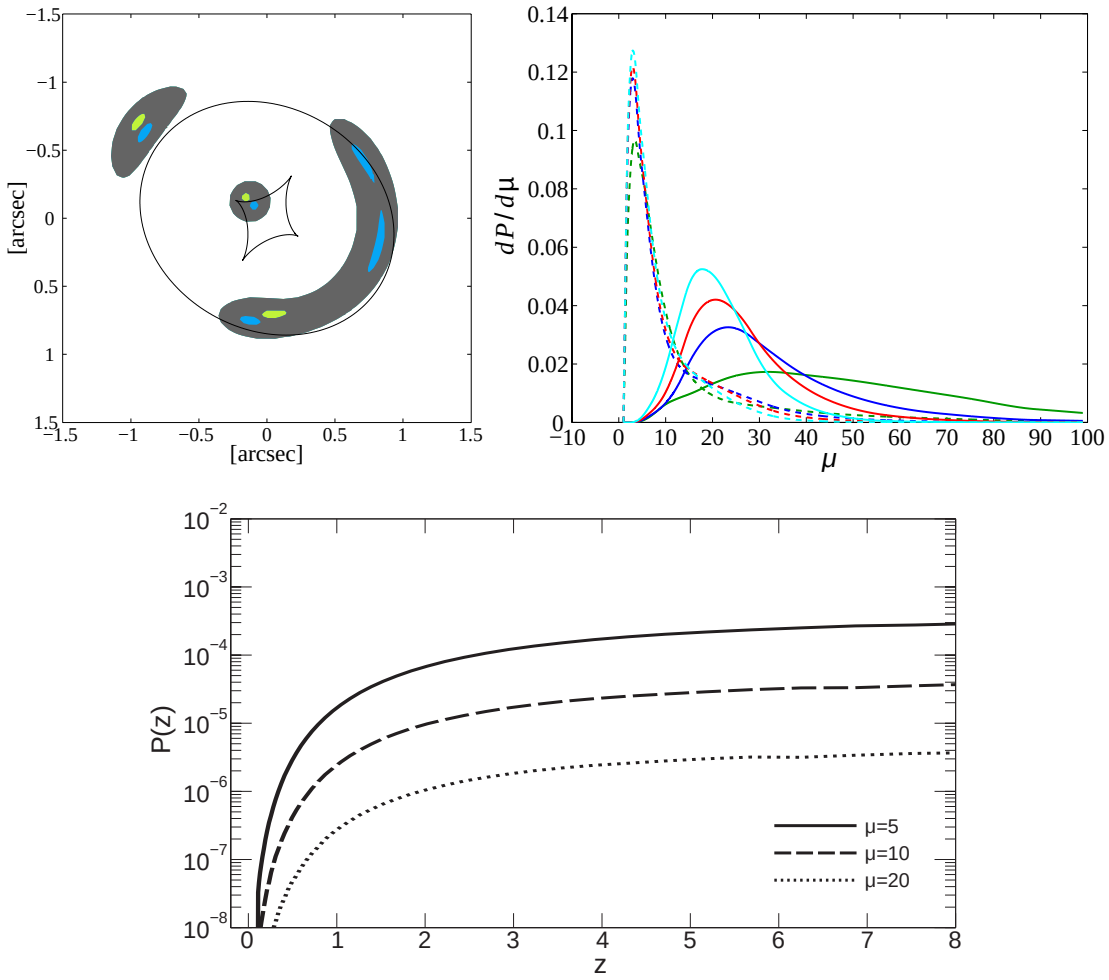

Figure 2.3. *Upper Left:* The effect of differential magnification, causing the green and blue components exhibit magnifications of 5.2 and 17.1 respectively. Taken from Hezaveh, Marrone, and Holder (2012).
Upper right: The effect of size on the magnification distribution of source counts: green curves represent point sources and blue, red and cyan represent source radii of 1, 3 and 8 kpc respectively. Solid curves correspond to $S_{1.4\,\mathrm{mm}} > 25$ mJy ($S_{500\,\mu\mathrm{m}} \gtrsim 350$ mJy), and dotted curves to $S_{1.4\,\mathrm{mm}} > 2.5$ mJy ($S_{500\,\mu\mathrm{m}} \gtrsim 35$ mJy). Taken from Hezaveh, Marrone, and Holder (2012).
Lower: The probability of a lensing event with redshift from models using a physically-motivated dark-matter halo population to reproduce observed DSFG lensing rates, indicating a strong drop-off in magnification-independent lensing probability at $z < 1$. No account is however made for size evolution. Taken from Weiß et al. (2013).

galaxies, or high angular resolution interferometric FIR–mm imaging is required.

MIPS J142824.0+352619 (hereafter HBoötes03) is a lensed DSFG with extensive detailed multi-wavelength observations, discovered before the most recent era of large-area FIR–mm surveys. Follow-up of a bright *Spitzer*/MIPS source with 350 μm CSO/SHARC-II imaging and NIR spectroscopy revealed a $z = 1.325$ DSFG lensed by an elliptical galaxy at $z = 1.034$ (Borys et al. 2006). The lack of spatial elongation in CO (Iono et al. 2006) or submm or radio continuum imaging (Borys et al. 2006) data suggests a low lensing amplification, with $\mu \sim 3$ estimated by Bussmann et al. (2013), however differential lensing (see later) may affect this source as the Hα emission appears to be extended (Swinbank et al. 2006). Lensing has enabled several FIR emission line detections: [C II] 158 μm (Hailey-Dunsheath et al. 2010), [O I] and [O III] (Sturm

et al. 2010), these are discussed further in Section 5.2.1.

Massive clusters can also strongly lens background sources (e.g. Gladders et al. 2003; Bayliss et al. 2011). The typical amplification is lower than produced by isolated galaxies, but the higher incidence rate of lensing per possible foreground object makes them useful targets around which to find mildly brighter examples of high-redshift galaxies, particularly at wavelengths where the cluster itself is faint. The above prompted the choice of massive clusters as the first SCUBA targets (Smail, Ivison, and Blain 1997; Chapman et al. 2002; Cowie, Barger, and Kneib 2002; Smail et al. 2002; Knudsen, van der Werf, and Jaffe 2003; Kneib et al. 2004). Even with most background sources experiencing modest 2 – 3 magnification factors, the few more strongly lensed objects were sufficient to push below the standard SCUBA ~2 mJy confusion limit (Blain, Ivison, and Smail 1998; Hughes et al. 1998) to determine number counts with intrinsic flux densities of 0.5 mJy (Blain et al. 1999). The faintest of these sources even passed below the ULIRG limit, allowing robust submm measurements of galaxies with SFRs of 80 $M_\odot yr^{-1}$ (Knudsen et al. 2009).

Another of the best studied pre-*Herschel* and -SPT examples is the Cosmic Eyelash, see Figure 2.4, serendipitously discovered in observations of the massive galaxy cluster MACS J2135-010217 (Swinbank et al. 2010b) and subsequently determined to be amplified by a net factor 37.5 ± 4.5 (Swinbank et al. 2011). NIR imaging revealed an ~4 arcsec-long source extended perpendicularly across the critical curve. Interferometric 870 µm observations and high spectral resolution CO line spectroscopy have resolved the $z = 2.32$ galaxy into several star-forming clumps of around 100 pc radius and 10^9 $M_\odot$ mass, mirrored about the critical curve. The flux and spatial resolution increase provided in this system by gravitational lensing has enabled detections of [C II] (Ivison et al. 2010c; which does not exhibit the deficit common in local ULIRGs), [C I], ^{13}CO and $C^{18}O$ among other species, indicating multiple kinematic components (Danielson et al. 2011) and strong cosmic ray heating of the molecular gas (Danielson et al. 2013). With a robust lens model, well-sampled SED and relatively modest dust mass and SFR in comparison to other similarly bright objects, the Cosmic Eyelash is routinely used for comparison with other high-redshift DSFGs. Chapter 4 describes our detection of a star-formation-powered molecular gas outflow in this galaxy, along with detections of several FIR fine-structure emission lines.

2.1.3 *Herschel* selection of strongly lensed high-redshift DSFGs

The extraordinary detail made available by the area and flux boost of strong lensing provides a compelling case for assembling a statistically significant sample, able to be used to probe evolution with redshift or luminosity of aspects of DSFGs unavailable with unlensed sources. The obvious difficulty (see Figure 2.3) lies in the low number density of strong lensing events, requiring large area surveys to cover such a sample. With SPIRE experiencing a confusion noise of 6 – 8 mJy in each of the three bands (Nguyen et al. 2010; Valiante et al. in prep.) in addition to instrument noise, 5σ point source limits of 33 – 45 mJy beam^{-1} are reached (Clements et al. 2010). To maximise the science output of this shallow imaging, large area surveys were therefore

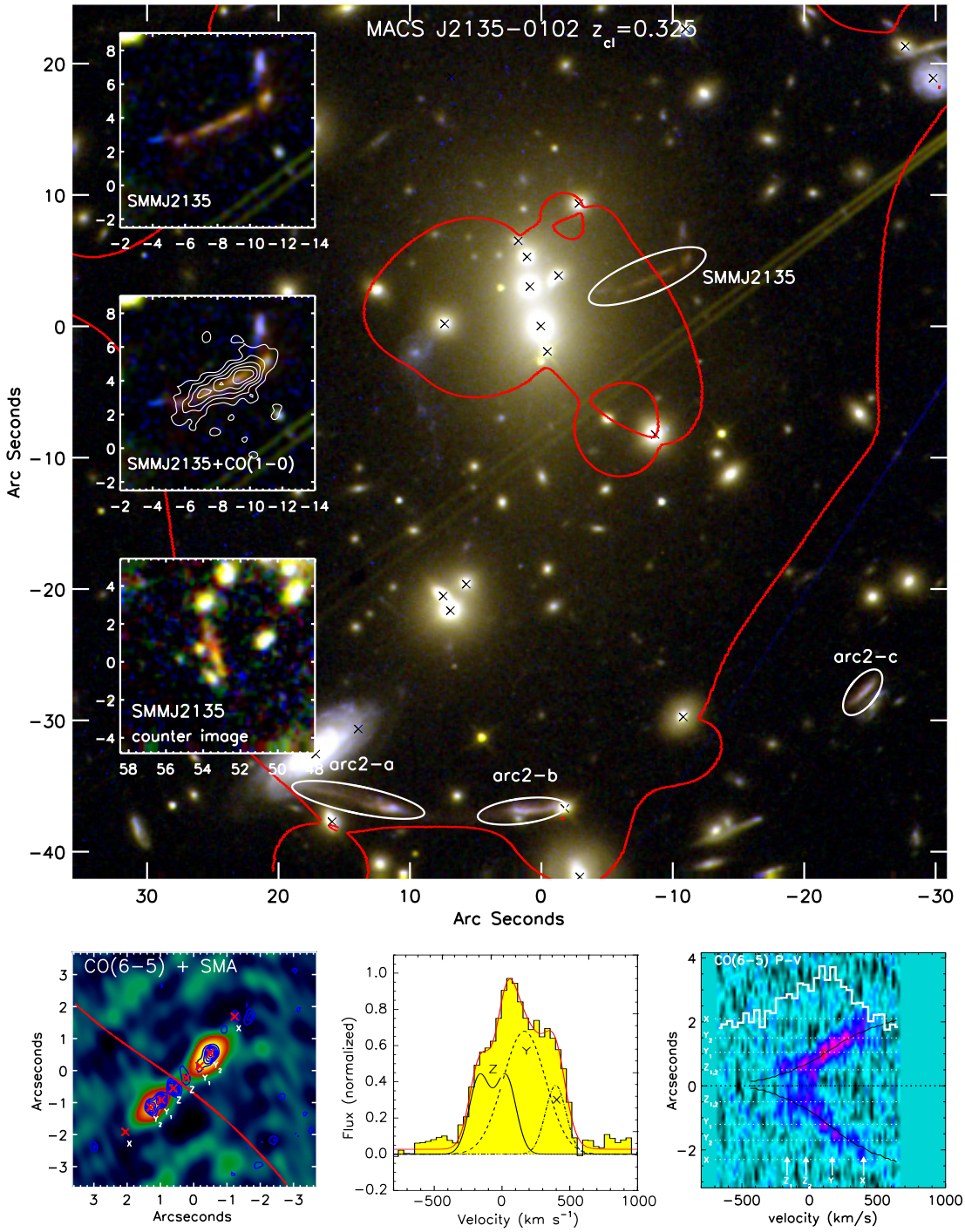

Figure 2.4. SMM J213511.6-010252, the Cosmic Eyelash, a $z = 2.3$ DSFG lensed by a factor 37.5 ± 4.5, with the wealth of data made accessible by the increased spatial resolution epitomising the power of strong gravitational lensing.
Upper: Hubble Space Telescope (*HST*) three colour image of the lensing cluster with the model critical curve shown in red. Insets show a zoomed image of SMM J2135-0102, the same with CO $J = 1 \rightarrow 0$ contours overlaid, and the counter image. Taken from Swinbank et al. (2011).
Lower left: CO $J = 6 \rightarrow 5$ overlaid with contours and labelled clumps from 880 µm the Submillimeter Array (SMA) data. The critical curve is again shown in red.
Lower middle: Composite CO spectrum, constructed from observations of most transitions up to $J = 8 \rightarrow 7$. The best-fitting multi-component model is overlaid. ^{12}CO composite spectrum Taken from Danielson et al. (2013).
Lower right: CO $J = 6 \rightarrow 5$ p-v plot along the major axis. Overlaid is the 1D CO spectrum (white histogram) and best-fitting model rotation curve (black). The spatial positions of the 880 µm emitting clumps are shown as white dashed lines, and the velocities of the Danielson et al. (2011) CO velocity components are shown with white arrows. Adapted from Swinbank et al. (2011).

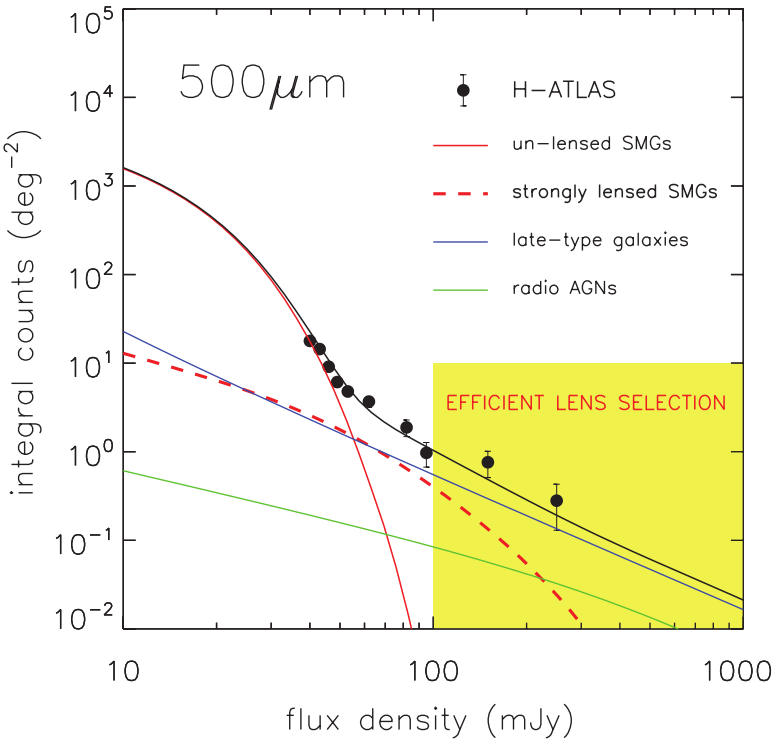

Figure 2.5. Theoretical number densities of the dominant populations contributing to the 500 μm EBL as a function of $S_{500\,\mu m}$. The region above 100 mJy is highlighted, showing flux densities where counts of unlensed DSFGs have dropped off, leaving only local spirals and blazars, both of which may be easily removed from source catalogues, and strongly lensed DSFGs, of which this method provides an efficient selection. Taken from Negrello et al. (2010).

undertaken: *H*-ATLAS and *Her*MES; perfectly suited for finding the rare bright end of the luminosity function, which includes strongly lensed galaxies.

Quantitative methods have been proposed to efficiently select samples directly from these large low resolution FIR–mm maps. Across the FIR–submm, few extragalactic populations contribute strongly to the (>1 mJy) source counts: low redshift late-type galaxies, blazars, and unlensed and lensed high-redshift DSFGs. At longer wavelengths, higher redshift DSFGs will tend to dominate source counts, however the increased distance necessarily reduces their measured flux densities and unlensed DSFGs become increasingly rare, reaching a few tens per deg^2 above 100 mJy at 250 μm, and are non-existent above 50 mJy by 850 μm. The increased probability of lensing with redshift (see Figure 2.3) mitigates this effect somewhat, so number counts of strongly lensed DSFGs decrease more slowly with wavelength. In addition the low bolometric luminosity of very low temperature grey-body functions strongly reduces the contribution of low-redshift star-forming galaxies to bright number counts at these longer wavelengths.

At 500 μm, flux density cuts of 80 or 100 mJy will select above the unlensed DSFG count drop-off, leaving lens candidates to provide a significant fraction of bright-end source counts: ∼0.4 deg^{-2} compared to ∼0.1 deg^{-2} for blazars, and ∼1 deg^{-2} for low-redshift spirals and starbursts (see Figure 2.5; Blain 1996; Perrotta et al. 2002, 2003; Negrello et al. 2007; Wardlow et al. 2013). Blazars and low-redshift spirals are identifiable via shallow radio and optical/NIR imaging

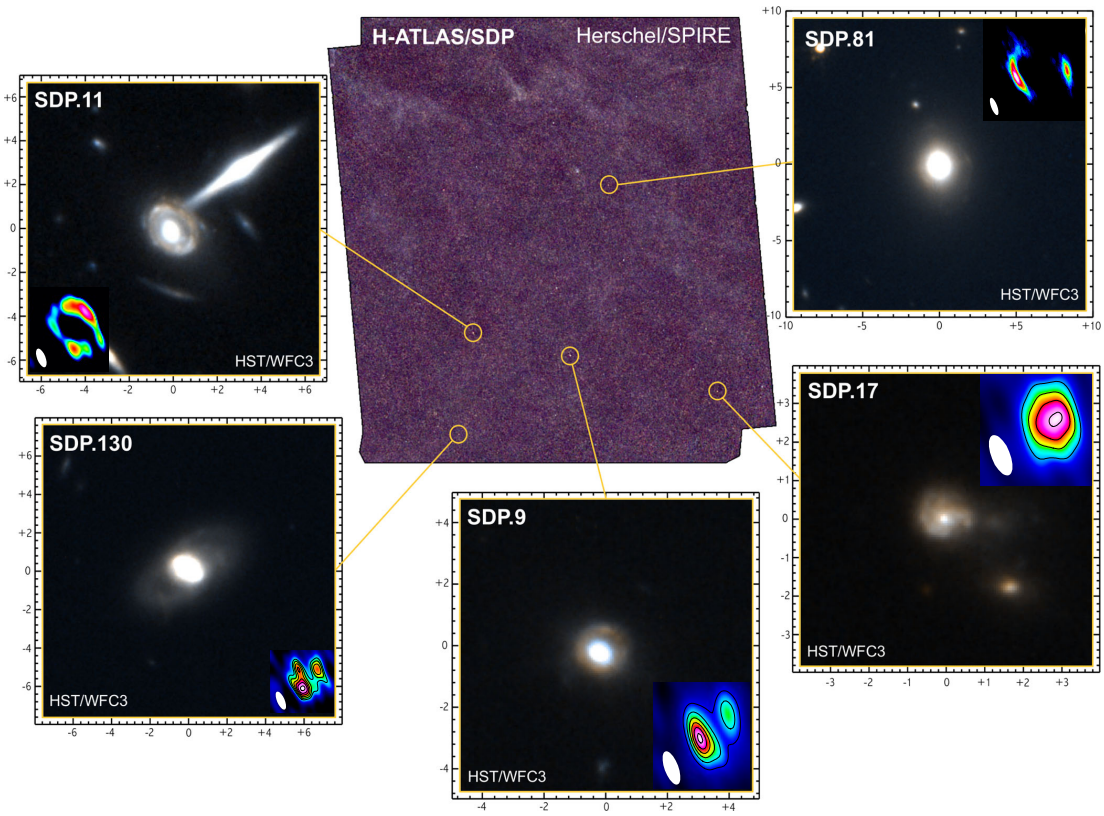

Figure 2.6. The Science Demonstration Phase (SDP) field of *H*-ATLAS, with *HST* imaging of each of the *Negrello 5*: the strongly lensed DSFGs found within. Overlaid on each *HST* image (and using the same angular scale) is an image from PdBI observations at the wavelength of a CO line in the background galaxy. Adapted from Negrello et al. (2014).

respectively, and may be removed to leave a sample of candidate strongly lensed high-redshift DSFGs.

This method was successfully demonstrated on the 14.4 deg^2 SDP of *H*-ATLAS, suggesting five strongly lensed candidate systems. Optical/NIR follow-up confirmed the presence of foreground lensing galaxies, and blind CO line redshifts and high angular resolution interferometric continuum observations the presence and morphology of the background DSFGs. Over the whole survey area of *H*-ATLAS, ~240 strongly lensed DSFGs are expected to be found, although not all may be identified as such (Negrello et al. 2007), providing a large sample of both high-flux DSFGs and an efficient method of locating strongly lensed systems.

In addition to *Herschel*, other facilities performing wide area surveys can detect strongly lensed DSFGs, notably SPT. At 1.4 mm, high-redshift dusty objects dominate the source counts between 4.4 – 15 mJy, with a tail extending to ~40 mJy (subdominant to synchrotron sources; Vieira et al. 2010). ALMA imaging of the brightest of these indicates at least the majority if not all are strongly lensed (Vieira et al. 2013).

2.2 Sample

Detailed multi-wavelength and spectral follow-up of individual sources can lead to great advances in our understanding of these objects, however still further and fainter detail may be found through stacking. Additionally, numbers of strongly lensed high-redshift DSFGs candidates from wide-area FIR and mm-wavelength surveys are now reaching levels permitting derivation of population statistics. Both of these arguments advise performing the desired SPIRE FTS observations on as large a sample of strongly lensed DSFGs as possible. The requirement of an FTS observation however necessitated high flux densities across 194 – 671 μm and coupled with the time expenditure (~4 h per source) limited the sample size.

The selection criteria used to select the sample, the list of galaxies chosen, and ongoing work into obtaining redshifts and deriving magnification factors are described below.

2.2.1 Selection of strongly lensed high-redshift DSFGs

The observations were split over two *Herschel* programmes. The sample of galaxies for the first was selected before the start of this thesis, I selected those for the second programme after completion of the *H*-ATLAS South Galactic Pole (SGP) observations.

Due to its previous multi-wavelength study, known high amplification and FIR flux densities, and detection of [C II] in a preliminary SPIRE FTS observation (Ivison et al. 2010c), the Cosmic Eyelash was chosen as the first member of the sample. Two other known lensed high-redshift DSFGs were also added: HBoötes03, described earlier and also with an existing [C II] detection, and AzTEC-ASTE-SXDF1101.001 (hereafter HXMM02; Ikarashi et al. 2011). These were observed with SPIRE photometry as part of *Her*MES.

The remainder of the sub-sample to be observed in the first programme was filled with lens candidates from *H*-ATLAS imaging. *H*-ATLAS mapped in the fast scan (60 arcsec s^{-1}) parallel mode (simultaneous 250, 350 and 500 μm SPIRE and 100 and 160 μm PACS imaging). Due to the low depth of the PACS maps (1σ ~30 and 40 mJy for the green and red bands respectively Ibar et al. 2010b), the selection of candidates from the *H*-ATLAS fields was based solely on the SPIRE flux densities. The first of these added to the sample were the five strongly lensed DSFGs discovered in the *H*-ATLAS SDP (part of the *H*-ATLAS galaxy and mass assembly (GAMA; Driver et al. 2009) 9 hr field; Figure 2.6), two of which were observed with the SPIRE FTS as a trial prior to the larger programme. Following the same method (removal of local spirals and blazars from $S_{500\,\mu\mathrm{m}} > 100$ mJy sources), a catalogue of lens candidates was produced for the remaining GAMA fields and the North Galactic Pole (NGP) field. This catalogue was then filtered by the criterion $S_{350\,\mu\mathrm{m}} \gtrsim 200$ mJy, and 16 were added to the sample.

Following a tentative detection of OH absorption in the spectrum of the Cosmic Eyelash obtained in the first programme, five repeat observations were added to the second programme in order to stack these data and confirm the detection. The primary sources of candidates included in the second programme was the *H*-ATLAS SGP field. Selections were made by a similar method as

used for the GAMA and NGP fields. The catalogues of sources in each band were matched and filtered by $S_{350\,\mu m} > 175$ mJy, $S_{350\,\mu m} > 0.7 S_{250\,\mu m}$ and $(S_{250\,\mu m} + S_{500\,\mu m}) > S_{350\,\mu m}$, ensuring consistently high flux densities across the three bands and that the most extremely blue and red (i.e. low and high-redshift) sources would be removed, as [C II] 158 µm, the brightest line, is only observable with SPIRE up to $z = 3.25$. Sources in this filtered list were checked with the NASA extragalactic database (NED), and any found to lie within 0.5 arcmin of a $z < 0.1$ galaxy or 0.15 arcmin of a QSO or H II region were removed. The NED results were finally hand checked for the remaining candidates to eliminate any other erroneous sources. This resulted in 12 targets, however being insufficient to fill the remaining programme slots, the two brightest from a list of candidates found in HeLMS were also added.

Seven other HeLMS candidates were added for observations only with the PACS photometer.

The final sample of 46 galaxies is shown in Table 2.1.

IAU Name	Short Name	R.A.	Dec	z	$S_{350\,\mu m}$ /mJy	Notes
HATLAS J090740.0−004200	SDP.9	136.9168	−0.7000	1.577[L]	328±24	
HATLAS J091043.0−000322	SDP.11	137.6795	−0.0562	1.784[L]	371±26	
HATLAS J090302.9−014127	SDP.17	135.7622	−1.6909	2.3050[L]	339±24	
HATLAS J090311.6+003906	SDP.81	135.7892	+0.6518	3.0425[F]	186±14	
HATLAS J091305.0−005343	SDP.130	138.2713	−0.8953	2.6256[F]	137±11	
HATLAS J085358.9+015537	G09-v1.40	133.4953	+1.9271	2.0894[Lp]	368±26	
HATLAS J083051.0+013224	G09-v1.97	127.7126	+1.5402	3.634[R]	305±22	
HATLAS J084933.4+021443	G09-v1.124	132.3892	+2.2453	2.4101[H]	249±18	HyLIRG, detailed study in Ivison et al. (2013)
HATLAS J091840.8+023047	G09-v1.326	139.6700	+2.5133	2.5811[H]	151±12	
HATLAS J114638.0−001132	G12-v2.30	176.6584	−0.1922	3.2588[H]	358±25	Detailed study in Fu et al. (2012)
HATLAS J113526.3−014606	G12-v2.43	173.8598	−1.7684	3.1275[H]	284±21	
HATLAS J115820.1−013753	G12-v2.257	179.5842	−1.6314	2.1909[H]	124±10	
HATLAS J142935.3−002836	G15-v2.19	217.3971	−0.4769	1.027[M]	438±31	Detailed study in Messias et al. (2014)
HATLAS J141351.9−000026	G15-v2.235	213.4666	−0.0075	2.4782[H]	217±16	
HATLAS J134429.4+303036	NA.v1.56	206.1230	+30.5095	2.3010[H]	466±33	

Continues

Table 2.1. The objects included in the final sample. 350 µm flux densities from SPIRE include a calibration uncertainty of 7 % (Swinyard et al. 2010; Bendo et al. 2013)
[B] Borys et al. (2006), [F] Frayer et al. (2011), [H] Harris et al. (2012), [K] Krips et al. (in prep), [L] Lupu et al. (2012), [Lp] Lupu et al. (in prep), [M] Messias et al. (2014), [R] Riechers et al. (in prep), [S] Swinbank et al. (2010b).

Table 2.1. Continued

IAU name	Short name	R.A.	Dec	z	$S_{350\,\mu m}$ /mJy	Notes
HATLAS J133649.9+291801	NA.v1.144	204.2078	+29.3002	2.2024[H]	286±21	
HATLAS J132859.3+292317	NA.v1.177	202.2470	+29.3909	2.778[K]	296±21	
HATLAS J132504.4+311537	NA.v1.186	201.2688	+31.2600	1.8358	227±17	New redshift, see Section 5.2.1 for further details
HATLAS J132427.0+284452	NB.v1.43	201.1134	+28.7471	1.676	371±27	See Chapter 3
HATLAS J133008.4+245900	NB.v1.78	202.5355	+24.9831	3.1112[R]	278±20	
HATLAS J125632.7+233625	NC.v1.143	194.1356	+23.6077	3.565[R]	289±21	
HATLAS J223829.0−304148	SA.v1.44	339.6212	−30.6969		207±15	
HATLAS J222536.3−295646	SA.v1.53	336.4016	−29.9462		200±17	
HATLAS J232531.4−302234	SB.v1.143	351.3811	−30.3763		227±17	
HATLAS J232623.0−342640	SB.v1.202	351.5961	−34.4447		178±13	
HATLAS J232419.8−323924	SC.v1.128	351.0825	−32.6568		244±18	
HATLAS J000912.6−300809	SD.v1.70	2.3028	−30.1360		273±20	
HATLAS J000722.3−352014	SD.v1.133	1.8429	−35.3374		193±15	
HATLAS J002625.1−341737	SD.v1.328	6.6048	−34.2937		186±14	
HATLAS J004736.0−272953	SE.v1.165	11.9003	−27.4983		197±15	
HATLAS J010250.7−311721	SF.v1.88	15.7116	−31.2892		253±19	
HATLAS J012407.3−281435	SF.v1.100	21.0307	−28.2433		271±20	
HATLAS J014834.7−303532	SG.v1.77	27.1446	−30.5924		220±17	
	HeLMS05	11.8089	+3.4154	1.195	246±18	No SPIRE spectrum
	HeLMS06	4.1086	+4.4368	2.5093	180±18	No SPIRE spectrum
	HeLMS09	12.9977	+6.3782	2.3920	202±15	No SPIRE spectrum
	HeLMS44	353.2311	−3.1930	2.6900	324±23	
	HeLMS45	351.1647	−4.6599	2.4730	227±17	
	HeLMS49	11.8473	+1.9641	1.441	293±21	No SPIRE spectrum
	HeLMS51	4.0661	+3.4102	2.7650	201±15	No SPIRE spectrum
	HeLMS61	353.2326	−5.5741	2.4024	186±14	No SPIRE spectrum
	HeLMS62	355.2147	−4.3280	3.503	197±15	No SPIRE spectrum
1HerMES S250 J142823.9+352619	HBoötes03	217.1003	+35.4387	1.325[B]	244±18	See Wardlow et al. (2013) for a summary of observations

Continues

Table 2.1. Continued

IAU name	Short name	R.A.	Dec	z	$S_{350\,\mu m}$ /mJy	Notes
1HerMES S250 J021830.5-053124	HXMM02	34.6278	−5.5254	3.39[R]	122±12	
MACS J2043.2-2144	MACS J2043	310.8092	−21.7442	2.04	300±21	No PACS observation
SMM J213511.6-010252	Eyelash	323.7985	−1.0475	2.32591[S]	429±64	See Chapter 4

2.2.2 Redshift search

While fitting an average SED to the available observed FIR–mm continuum flux densities can provide an estimate of the redshift, a grey-body spectrum is degenerate in redshift and dust temperature, therefore intrinsic properties of a high-redshift DSFG cannot be determined from photometry alone. Characterisation requires a redshift determination through subsequent spectral observations or an SED fit to much wider multi-wavelength counterparts flux densities including deep optical–NIR data.

Blind CO line searches using wide-band ground-based spectrometers have been the primary technique for redshift discovery for lensed high-redshift DSFGs over the past several years (e.g. Weiß et al. 2009a; Swinbank et al. 2010b; Harris et al. 2012; Lupu et al. 2012). Detection of two lines are required for a definite redshift determination, however using the available FIR–mm photometry as a prior, a single CO line observation can provide a strong likelihood of the redshift.

The relative power of this method in comparison to more traditional optical/NIR spectroscopy results from the much larger molecular gas reservoir in the background galaxy than within the lens or any other nearby unrelated galaxy, removing difficulties in cross-matching between wavebands, and also avoids the prerequisite precise position for optical spectroscopy (an even more difficult prospect for lensed starbursts due to the dominant optical flux density of the lens). This efficiency has even led to the production of dedicated instruments, such as Zpectrometer (Harris et al. 2007) on the Green Bank Telescope (GBT) and Z-Spec (Glenn et al. 2007) on APEX. Along with several FIR and millimetre wavelength interferometers, such as CARMA and PdBI, these facilities have provided redshifts for 32 of our galaxies at the time of writing.

In addition, our SPIRE spectra have provided two blind redshifts: 1.676 for NB.v1.43 and 1.8356 for NA.v1.186, both corrections to previously-determined erroneous values, and both confirmed via CARMA observations. Details of the first of these are presented in Chapter 3, along with further observational follow-up and characterisation of this galaxy. While the signal-to-noise of even [C II] in many of our spectra is insufficient to determine convincing redshift estimates, SPICA will likely be able to find the redshifts of even unlensed high-redshift DSFGs, see Chapter 3 for a discussion of this.

References for the known redshifts within our sample are given in Table 2.1.

2.2.3 Lens modelling

To fully understand the intrinsic properties of the background source, the lensing system must be modelled. As the deflection angle at each point consists of an integral over the lensing body, the mass distribution of the lens must be computed self-consistently with a source morphology for each pixel in the observed lensed image.

High resolution rest-frame UV and optical (e.g. Negrello et al. 2014) and FIR continuum (e.g. Bussmann et al. 2013; Hezaveh et al. 2013) and CO line (e.g. Gavazzi et al. 2011) imaging has been used to produce best-fitting models of several strongly lensed DSFGs. A variety of tools and methods have been used: LENSTOOL (Swinbank et al. 2011; Fu et al. 2012), SL_FIT (Wardlow et al. 2013), UV plane fitting (Bussmann et al. 2013; Hezaveh et al. 2013), and semilinear inversion techniques (Dye et al. 2014; Negrello et al. 2014) among others, ensuring no dependence upon a single methodology. Figure 2.7 displays several models produced of a single system, with velocity information from a CO observation providing evidence for two merging components.

Derived magnification factors are relatively widely distributed but usually $\lesssim 15$ (e.g. Bussmann et al. 2013; Wardlow et al. 2013), however SPT sources may have higher average magnification factors (Hezaveh et al. 2013). These values appear to indicate intrinsic FIR luminosities and dust masses higher than the population averages (e.g. Magnelli et al. 2012; Swinbank et al. 2014), however these objects are not population outliers and can still enable us to explore relatively "normal" high-redshift DSFGs in detail.

Non-coincidence or different spatial extents of the dominant regions emitting in different wavebands can lead to different determinations for the same source, and when coupled with differential magnification this effect can be exacerbated. For example, from SMA 880 µm and *HST*/WFC3 observations, Bussmann et al. (2013) and Negrello et al. (2014) find magnification factors of 10.9 ± 1.3 and $7.89^{+0.21}_{-0.25}$ respectively for *H*-ATLAS J091043.1-000321 (SDP.11), and 2.1 ± 0.3 and $3.09^{+0.19}_{-0.17}$ for *H*-ATLAS J091305.0-005343 (SDP.130).

To avoid the observational expense of high angular resolution NIR or (sub)mm interferometric imaging required to produce a full lensing model, an estimate of the magnification can be derived from the single-dish CO line measurements obtained as a matter of course to determine the source redshift (Harris et al. 2012). This method uses the observed intrinsic relationship between CO line luminosity and FWHM (see Figure 2.8), expected if the most gas-rich galaxies are to be found in the largest dark-matter haloes. These data reinforce the idea that the mass distribution of lensed DSFGs will be flatter than the underlying distribution, as less massive galaxies are more common, but require greater magnification to reach the same CO or FIR luminosity, and hence stronger (and rarer) lensing events.

A minority of these candidates have been found to benefit only slightly from gravitational lensing, instead representing an even more rare and luminous population with SFRs of several thousand $M_\odot yr^{-1}$ (e.g. Riechers et al. 2013), including such systems as DSFG-DSFG mergers (Ivison et al. 2013). These objects are the most intensely star-forming galaxies ever to exist, and the

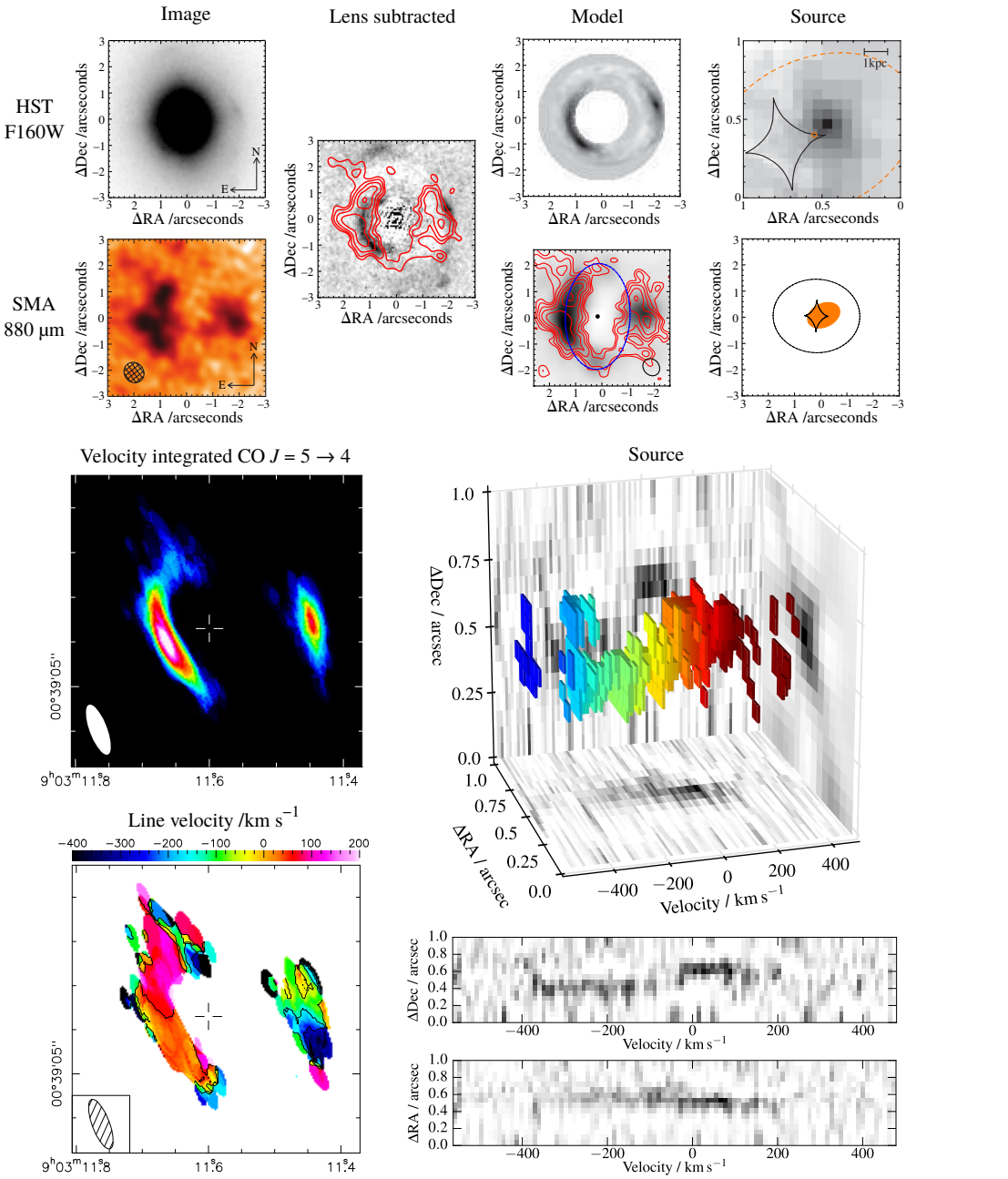

Figure 2.7. Gravitational lensing models of *H*-ATLAS J090311.6+003906 (SDP.81).
Upper half: Lens models from *HST*/WFC3 F160W and SMA 880 μm imaging of this system. The lensing galaxy was required to be subtracted from the F160W image before construction of a lens model via a semilinear inversion approach (Dye et al. 2014). The UV plane 880 μm data was used to construct the second model through the UVMCMCFIT tool. Both techniques produce a similar source position, however the half-light radius from the 880 μm data is larger. Adapted from Negrello et al. (2010, 2014), Bussmann et al. (2013), and Dye et al. (2014)
Lower half: An improvement to the above models using high angular resolution CO $J = 5 \rightarrow 4$ imaging from the PdBI. The velocity information available through observation of a spectral line (in comparison to the broad-band continuum data used above) allows additional reconstruction of the source kinematics and demonstrates that a major merger is likely responsible for the intense starburst ongoing within the background source. Slices through the model are displayed in the lower right hand plots and on the lower RA-velocity and rear Dec-velocity faces of the 3D diagram above. On the RA-Dec face of the 3D diagram is shown the velocity-integrated source, similar in appearance to that derived from the F160W imaging.

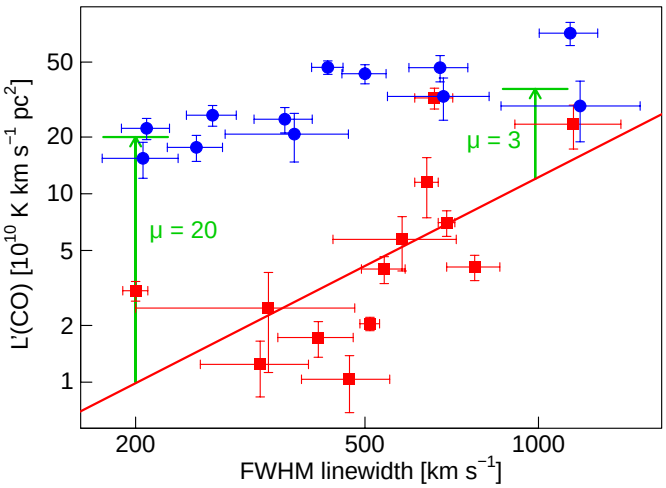

Figure 2.8. Magnification estimate from the observed $L'_{\mathrm{CO}\,1\to0}$ vs line FWHM. Literature observations of unlensed sources are shown in red, with a power-law fit. Observed values for a lensed sample are displayed in blue, with estimate magnification factors shown in green. These estimates are used for three of our sources which are included in the sample displayed, but do not have more robust magnification determinations from full lens modelling. Taken from Harris et al. (2012), see that work for details of the sources plotted.

most likely progenitors of the most massive BCGs.

2.3 Observations

The primary dataset consists of 45 *Herschel* SPIRE FTS spectra. 42 of these were obtained in the *Herschel* observation programmes OT1_RIVISON_1 (hereafter OT1) and OT2_RIVISON_2 (hereafter OT2). In addition, the two spectra of SDP.81 and SDP.130 obtained in the programme GT1_IVALTCHA_1 and presented in Valtchanov et al. (2011) were also included in the final observation set, as was a repeat observation of MACS J2043 obtained in the programme OT2_MREX_2 .

With only shallow PACS imaging included in *H*-ATLAS, insufficiently deep to detect several sources, and none available for many others, we also obtained additional PACS 100 and 160 µm photometry to complement the longer-wavelength SPIRE photometric data, providing wider coverage of the dust peak emission throughout our sample. These observations were included in the same OT1 and OT2 programmes as the spectra, such that most sources were targetted with one FTS and two PACS observations at different spacecraft orientations and to be combined into a single mini scan map during reduction. As with the spectra, the PACS imaging of Valtchanov et al. (2011) was included in the final dataset. Due to repetitions of FTS observations of the Cosmic Eyelash and the resulting free PACS slots, PACS mini scan maps but not SPIRE spectra were obtained of seven additional lens candidates from HeLMS.

Table 2.2 lists each observation performed.

2.3.1 FIR spectroscopic observations with the SPIRE FTS

The Spectral and Photometric Imaging REceiver (SPIRE; Griffin et al. 2010) FTS operates in a Mach-Zehnder configuration (Zehnder 1891; Mach 1892), utilising two beam splitters, one before and one after the Spectrometer MEChanism (SMEC). The instrument layout is displayed in Figure 2.9. The first beam splitter is illuminated by the observed light from the primary mirror, and by an internal reference source (see later), while the second beam splitter feeds to the two detector arrays. The instrument enclosure typically remains at ~4.7 K during observations of

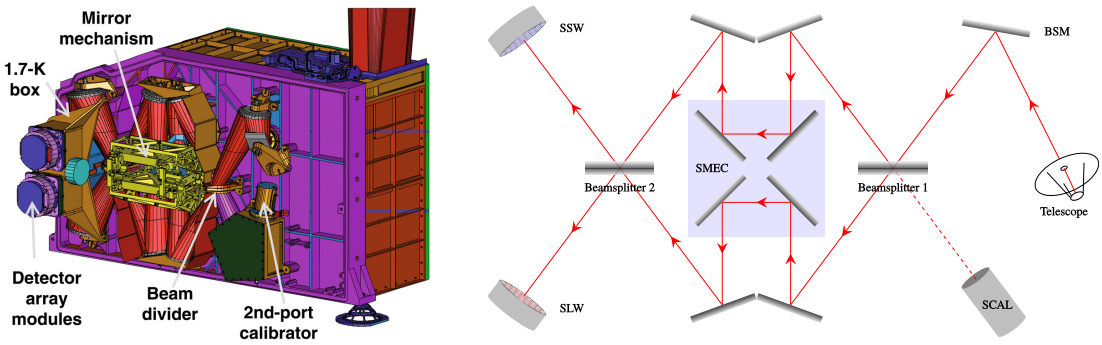

Figure 2.9. The Spectral and Photometric Imaging REceiver (SPIRE; Griffin et al. 2010) Fourier transform spectrometer (FTS)
Left: The FTS side layout. Taken from Griffin et al. (2010).
Right: Schematic diagram of the light path inside the FTS.

faint sources or dark areas of sky, but the variations of tens of mK experienced can produce a measurable effect on the observed spectrum for our very faint sources.

The SMEC is the heart of the FTS, containing one double-sided scanning mirror, the displacement of which creates the light optical path difference (OPD) and hence the phase difference necessary for interference. For high resolution observations, such as those producing our dataset, each scan of the mirror takes 66.6 s, producing a maximum OPD of 12.56 cm, which results in a spectral resolution of 0.0398 cm^{-1} = ~1.184 GHz.

The internal spectrometer calibration source (SCAL; Hargrave et al. 2006) was designed to provide a reference SED, however the thermal emission from the lamp produces an additional contribution to the observed flux, complicating measurements of faint sources. Even unused, with the lamp switched off, as during our observations, the SCAL remains at (and emits at) instrument temperature, producing a small flux contribution, but one that must still be removed in processing.

The SLW array contains 19 bolometric detectors covering 303 – 671 µm, closely packed into a hexagonal arrangement and operated at 0.3 K. Each beam has a FWHM on sky of ~35 arcsec (frequency dependent), and beams are separated by 51 arcsec. The SSW array contains 37 detectors (two of which are non-operational) covering 194 – 313 µm, and even at the low-wavelength end the FTS beam is ~17 arcsec (Swinyard et al. 2010), much larger than the maximum 2 arcsec pointing error of *Herschel* (Pilbratt et al. 2010). As displayed in Figure 2.10, the beams of several of these detectors overlap. Our sources are for the most part unresolved or have angular extents smaller than the ~19 arcsec beam size of the central detector of each array (e.g. G09.v1.124 consists of multiple galaxies, the brightest of which, W and T, are separated by 10.5 arcsec; Ivison et al. 2013), so SLWC3 and SSWD4 should contain all flux from the source.

Due to the success of Valtchanov et al. (2011) in using an equal length dark sky observation to estimate the background in SPIRE spectra of SDP.81 and SDP.130, the *Herschel* science operations team scheduled similar dark sky measurements on the same day as each of our observations, with at least as many mirror scan repetitions as the longest science spectral observation of the day (usually ours).

Each observation consisted of 100 repetitions (100 forward and 100 reverse scans of the SMEC mirror), totalling 13 320 s integration time on source. This was performed during a single pointing, with the source in the centre of the field of view (FOV) (covered by SLWC3 and SSWD4), and with little overhead due to the spacecraft being static throughout, resulting in a total time of 13 932 s per observation including overheads.

2.3.2 FIR continuum observations with the PACS photometer

Following Valtchanov et al. (2011), as part of the OT1 and OT2 programmes, we obtained two cross-linked mini-scans of each source, (oriented at the recommended 70° and 110°). However, because of the non-detection at 70 µm in that paper, and similarly to *H*-ATLAS, we opted for

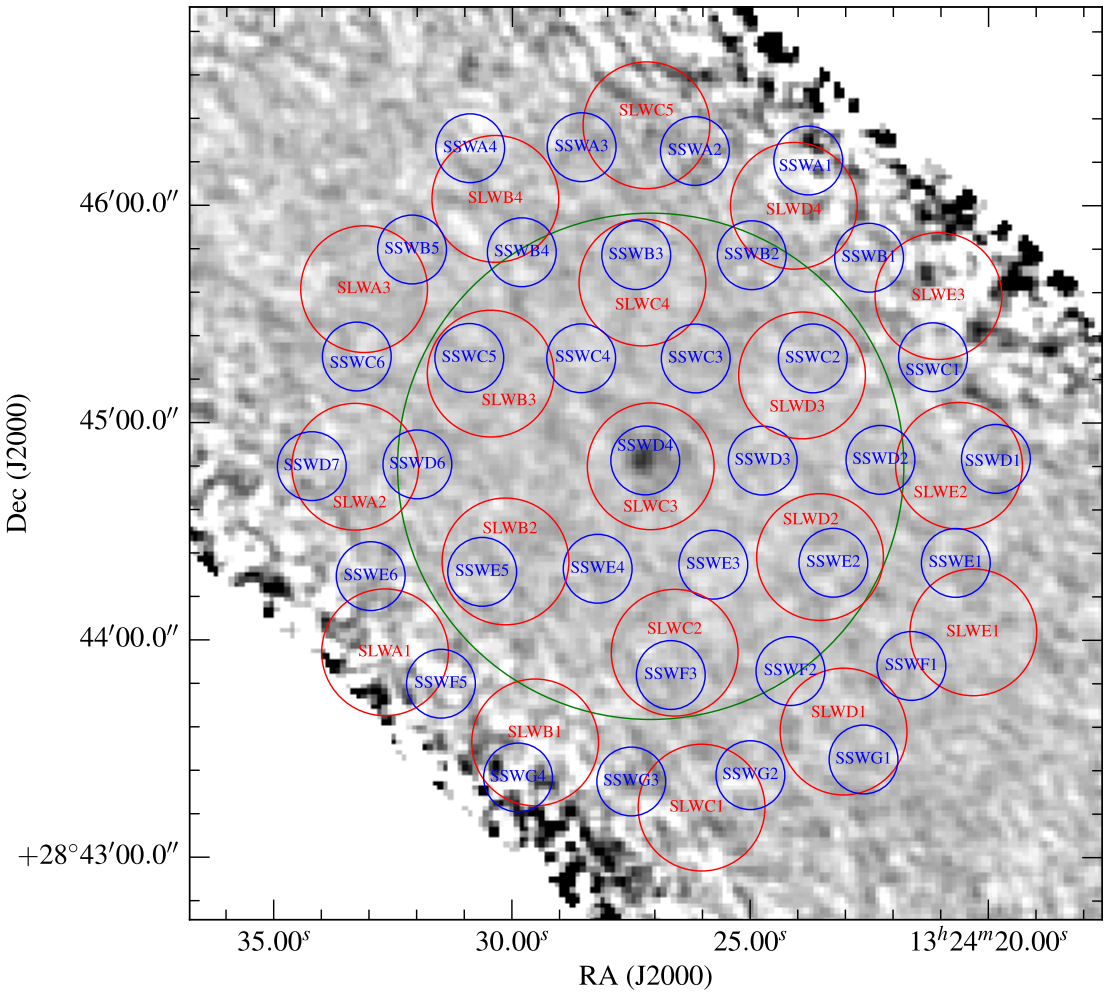

Figure 2.10. Sky positions of FTS bolometer array beams overlaid on the 100 µm PACS mini scan map of NB.v1.43 (see Chapter 3). Beams from the SLW array (303 – 671 µm) are shown with 35 arcsec diameter red circles, and SSW (194 – 313 µm) beams are shown with 19 arcsec diameter blue circles. The nominal field of view free of distortion caused by the instrument is shown as a green circle of ~2 arcmin diameter. The six overlapping pairs of beams surrounding the central pair, which include SLWC4 and SSWB3 are used for background estimation and referred in the text as *off axis detectors*.

the green and red (100 and 160 µm) bands. Noise levels should be similar in the blue and green bands, however these galaxies should be brighter at 100 µm than at 70 µm.

Each orientation consisted of 10 × 3 arcmin scan leg lengths, which at a medium scan speed of 20 arcsecs^{-1} resulted in a 90 s integration for a total of 3 min on source. Combined with 2 × 186 s of observation overhead, 59 s of calibration and 180 s for slewing and other overheads, the total observation time was 791 s.

2.3.3 List of observations

Source	Instrument	Integration time /s	Date	Programme	Notes
SDP.9	SPIRE	13320	2011-11-07	OT1	
	PACS	90	2011-12-02	OT1	
	PACS	90	2011-12-02	OT1	
SDP.11	SPIRE	13320	2012-11-18	OT1	
	PACS	90	2011-10-18	OT1	
	PACS	90	2011-10-18	OT1	
SDP.17	SPIRE	13320	2012-11-18	OT2	
	PACS	90	2011-12-02	OT1	
	PACS	90	2011-12-02	OT1	
SDP.81	SPIRE	13320	2010-06-01	GT1	Presented in Valtchanov et al. (2011) and Chapter 3
	PACS	90	2010-06-03	GT1	70 and 160 µm maps
	PACS	90	2010-06-03	GT1	70 and 160 µm maps
SDP.130	SPIRE	13320	2010-06-01	GT1	Presented in Valtchanov et al. (2011)
	PACS	90	2010-06-03	GT1	70 and 160 µm maps
	PACS	90	2010-06-03	GT1	70 and 160 µm maps
G09-v1.40	SPIRE	13320	2011-11-06	OT1	
	PACS	90	2012-04-24	OT1	
	PACS	90	2012-04-24	OT1	
G09-v1.97	SPIRE	13320	2011-11-08	OT1	
	PACS	90	2011-11-10	OT1	
	PACS	90	2011-11-10	OT1	
G09-v1.124	SPIRE	13320	2012-11-18	OT2	
	PACS	90	2012-04-13	OT1	
	PACS	90	2012-04-13	OT1	
G09-v1.326	SPIRE	13320	2011-11-07	OT1	
	PACS	90	2011-11-28	OT1	

Continues

Table 2.2. *Herschel* observations of the sample of strongly lensed high-redshift DSFGs. SPIRE spectrometer observations consist of 100 forward and 100 reverse scans of the SMEC mirror. The two PACS photometer observations of each source consist of 10×3 arcmin scan legs oriented at 70° and 110° respectively, and combined during processing into a single mini scan map.

Table 2.2. Continued

Source	Instrument	Integration time /s	Date	Programme	Notes
	PACS	90	2011-11-28	OT1	
G12-v2.30	SPIRE	13320	2012-07-07	OT1	
	PACS	90	2011-11-27	OT1	
	PACS	90	2011-11-27	OT1	
G12-v2.43	SPIRE	13320	2012-07-07	OT1	
	PACS	90	2011-07-14	OT1	
	PACS	90	2011-07-14	OT1	
G12-v2.257	SPIRE	13320	2012-07-07	OT1	
	PACS	90	2011-07-14	OT1	
	PACS	90	2011-07-14	OT1	
G15-v2.19	SPIRE	13320	2012-02-04	OT1	
	PACS	90	2011-07-09	OT1	
	PACS	90	2011-07-09	OT1	
G15-v2.235	SPIRE	13320	2012-02-04	OT1	
	PACS	90	2012-01-12	OT1	
	PACS	90	2012-01-12	OT1	
NA.v1.56	SPIRE	13320	2012-07-22	OT1	
	PACS	90	2011-11-27	OT1	
	PACS	90	2011-11-27	OT1	
NA.v1.144	SPIRE	13320	2012-08-03	OT1	
	PACS	90	2011-12-03	OT1	
	PACS	90	2011-12-03	OT1	
NA.v1.177	SPIRE	13320	2012-08-03	OT1	
	PACS	90	2011-11-27	OT1	
	PACS	90	2011-11-27	OT1	
NA.v1.186	SPIRE	13320	2012-06-18	OT1	
	PACS	90	2011-07-11	OT1	
	PACS	90	2011-07-11	OT1	
NB.v1.43	SPIRE	13320	2012-08-02	OT1	Presented in George et al. (2013) and Chapter 4
	PACS	90	2011-11-27	OT1	
	PACS	90	2011-11-27	OT1	

Continues

Table 2.2. Continued

Source	Instrument	Integration time /s	Date	Programme	Notes
NB.v1.78	SPIRE	13320	2012-08-02	OT1	
	PACS	90	2011-12-03	OT1	
	PACS	90	2011-12-03	OT1	
NC.v1.143	SPIRE	13320	2012-07-21	OT1	
	PACS	90	2011-07-11	OT1	
	PACS	90	2011-07-11	OT1	
SA.v1.44	SPIRE	13320	2012-12-03	OT2	
	PACS	90	2012-11-27	OT2	
	PACS	90	2012-11-27	OT2	
SA.v1.53	SPIRE	13320	2012-12-02	OT2	
	PACS	90	2012-11-27	OT2	
	PACS	90	2011-11-27	OT2	
SB.v1.143	SPIRE	13320	2012-12-29	OT2	
	PACS	90	2012-12-12	OT2	
	PACS	90	2012-12-12	OT2	
SB.v1.202	SPIRE	13320	2012-12-03	OT2	
	PACS	90	2012-12-12	OT2	
	PACS	90	2012-12-12	OT2	
SC.v1.128	SPIRE	13320	2012-12-03	OT2	
	PACS	90	2012-12-12	OT2	
	PACS	90	2012-12-12	OT2	
SD.v1.70	SPIRE	13320	2012-12-28	OT2	
	PACS	90	2012-12-25	OT2	
	PACS	90	2012-12-25	OT2	
SD.v1.133	SPIRE	13320	2012-12-28	OT2	
	PACS	90	2012-12-11	OT2	
	PACS	90	2012-12-11	OT2	
SD.v1.328	SPIRE	13320	2012-12-29	OT2	
	PACS	90	2012-12-11	OT2	
	PACS	90	2012-12-11	OT2	
SE.v1.165	SPIRE	13320	2012-12-29	OT2	
	PACS	90	2012-12-25	OT2	

Continues

Table 2.2. Continued

Source	Instrument	Integration time /s	Date	Programme	Notes
	PACS	90	2012-12-25	OT2	
SF.v1.88	SPIRE	13320	2012-07-08	OT2	
	PACS	90	2012-07-15	OT2	
	PACS	90	2012-07-15	OT2	
SF.v1.100	SPIRE	13320	2012-07-08	OT2	
	PACS	90	2012-07-15	OT2	
	PACS	90	2012-07-15	OT2	
SG.v1.77	SPIRE	13320	2012-07-17	OT2	
	PACS	90	2012-06-25	OT2	
	PACS	90	2012-06-25	OT2	
HeLMS05	PACS	90	2013-01-06	OT2	
	PACS	90	2013-01-06	OT2	
HeLMS06	PACS	90	2013-01-06	OT2	
	PACS	90	2013-01-06	OT2	
HeLMS09	PACS	90	2013-01-11	OT2	
	PACS	90	2013-01-11	OT2	
HeLMS44	SPIRE	13320	2013-01-08	OT2	
	PACS	90	2013-01-01	OT2	
	PACS	90	2013-01-01	OT2	
HeLMS45	SPIRE	13320	2012-12-29	OT2	
	PACS	90	2013-01-01	OT2	
	PACS	90	2013-01-01	OT2	
HeLMS49	PACS	90	2013-01-06	OT2	
	PACS	90	2013-01-06	OT2	
HeLMS51	PACS	90	2013-01-06	OT2	
	PACS	90	2013-01-06	OT2	
HeLMS61	PACS	90	2013-01-01	OT2	
	PACS	90	2013-01-01	OT2	
HeLMS62	PACS	90	2012-12-26	OT2	
	PACS	90	2012-12-26	OT2	
HBoötes03	SPIRE	13320	2012-02-05	OT1	
	PACS	90	2011-11-27	OT1	

Continues

Table 2.2. Continued

Source	Instrument	Integration time /s	Date	Programme	Notes
	PACS	90	2011-11-27	OT1	
HXMM02	SPIRE	13320	2012-02-05	OT1	
	PACS	90	2012-02-14	OT1	
	PACS	90	2012-02-14	OT1	
MACS J2043	SPIRE	13320	2012-10-28	OT2	
	SPIRE	18248	2013-04-15	OT2_MREX_2	137 repetitions
Eyelash	SPIRE	13320	2011-04-24	OT1	Presented in George et al. (2014)
	SPIRE	13320	2012-11-17	OT2	as above
	SPIRE	13320	2012-11-24	OT2	as above
	SPIRE	13320	2012-11-24	OT2	as above
	SPIRE	13320	2012-12-01	OT2	as above
	SPIRE	13320	2012-12-02	OT2	as above
	PACS	90	2011-11-17	OT1	
	PACS	90	2011-11-17	OT1	

2.4 Reduction of these *Herschel* data

All *Herschel* data are processed by standard pipelines at the Herschel Science Centre (HSC) and made available through the Herschel Science Archive (HSA). These data may also be reprocessed, using user-input parameters, by copies of these pipelines (each a jython script) included within the Herschel Interactive Processing Environment (HIPE; Ott 2010), a software environment available for download that may be used to view and manage *Herschel* data. HIPE is regularly updated with new tools, calibration values, and slight updates to these pipelines. *Herschel* data is managed as a set of *products*. Through the data processing pipelines, several of these products are exported under the name of *levels*, starting from the raw data: Level 0, and finishing with Level 2 or Level 2.5, the format of which varies depending on the observation type, but for our observations consists of point source calibrated spectra or mosaiced PACS maps.

The stages of the pipelines used are described below, with the operations performed, differences to the standard scripts, and the data products exported at each stage.

2.4.1 SPIRE FTS

The reprocessing pipeline is first described, followed by a description of additional background subtraction and line fitting steps.

2.4.1.1 FTS reduction pipeline

The raw data obtained by the spectrometer are processed into a spectrum of unit Jy with dispersion in GHz. A graphical representation of the standard pipeline (Fulton et al. 2010) is shown in Figure 2.11, and a brief description is now given.

Level 0 – Level 0.5

The operations here are identical for the photometer and spectrometer: performing the engineering conversion from the raw readouts of the bolometers, SMEC, temperature sensors and other telescope and instrument sensors to timelines with meaningful units. This step is not repeated for typical reprocessing, and the Level 0.5 data products are simply read in as the starting point.

Level 0.5 – Level 1

This stage is the heart of the pipeline, combining the Level 0.5 data products to create an interferogram of the observations recorded for each scan with each detector, and then performing a Fourier transform to create a frequency domain spectrum.

Timeline modification

The Level 0.5 Spectrometer Detector Timeline Product (SDT) consists of r.m.s. voltage timelines, such that each measured time has an associated positive voltage. These timelines are first modified by several steps, detailed below:

First level deglitching

This step removes glitches due to instantaneous-like events such as cosmic ray hits, by assuming a delta function glitch signature, and replacing them via polynomial interpolation.

Non-linearity correction

The bolometer responses change over the wide dynamic range, so a non-linearity correction is required, particularly for bright fluxes. Calibration tables based on data from models and determined over the life of the telescope are used.

Bath temperature correction

The instrument temperature drifts during observations, with fluctuations on a timescale much quicker than a single scan. This affects all detectors in an array, producing correlated noise. A correction voltage timeline is produced from the thermistor and dark channels and subtracted from the input detector timelines.

Clipping correction

Clipped voltages must be corrected to avoid problems when converting to interferograms, and are replaced by a polynomial interpolated to the five points before and after.

Time domain phase correction

The detector timelines must finally be corrected for delays due to the thermal response of the detectors, and the readout electronics.

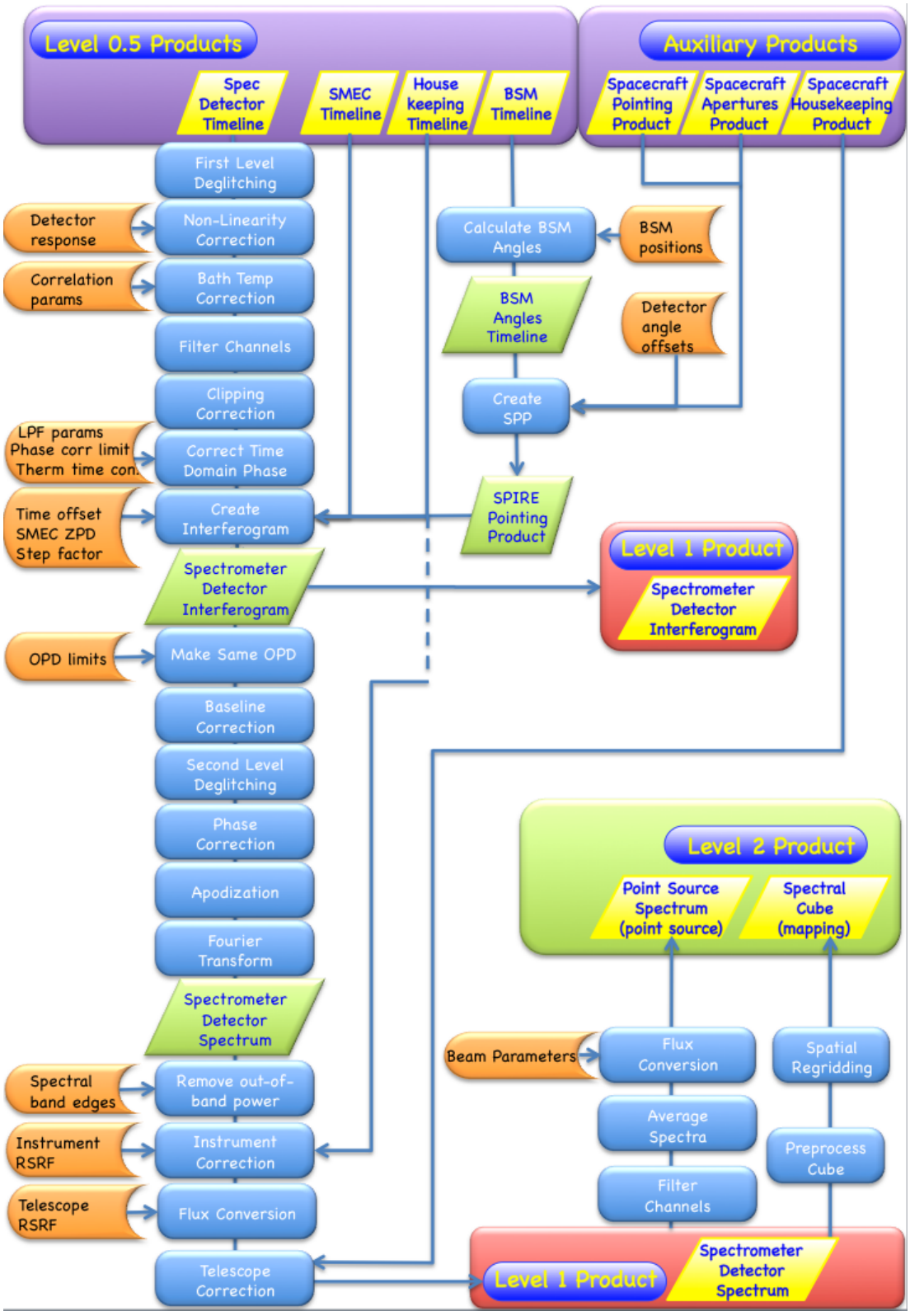

Figure 2.11. Stages of the FTS standard pipeline. Taken from the SPIRE Pipeline Specification Manual, a copy of which may be found at http://herschel.esac.esa.int/hcss-doc-13.0/print/spire_psm/spire_psm.pdf.

Interferogram creation

Before Fourier transformation to wavenumber/frequency domain, interferograms must be created, mapping detector samples to SMEC positions. The first step is to interpolate the SMEC position timeline to be regularly spaced in OPD. Each detector has a unique scaling factor and position of zero OPD, so this is performed on an individual basis. The voltage timeline of each detector is then mapped onto the time positions of the modified SMEC timeline. These raw interferograms are then exported.

Interferogram modification

Further corrections must be applied to the data, best performed while still a function of OPD.

Baseline correction

The baseline portion of the intensity incident on the detectors is removed via modelling it as the low frequency Fourier components.

Second level deglitching

Glitches in the interferograms need to be removed before transforming. At each OPD, the 200 scans are compared and any value above a certain deviation level is replaced with the average of the other scans.

Phase correction

Interferograms may not be symmetric about the point of zero OPD. The non-linear component of this phase is removed for each scan for each detector, leaving only a random component due to noise.

Apodisation

An FTS produces a sinc function instrumental line shape. To reduce the secondary maxima, an apodisation function may optionally be applied, the default being Norton-Beer 1.5. As the spectral resolution is reduced with apodisation, this step was skipped.

Fourier transform

The interferograms are then Fourier transformed, giving a set of spectra with dispersion in wavenumber.

Modify spectra

These spectra contain not only signal from the observed source, but also (much larger) contributions from thermal emission from the telescope and instrument. Improving models of this emission has been a significant area of continuing work throughout the life of the telescope and since EOL.

Instrument correction

The instrument emission is modelled as the instrument relative spectral response function (RSRF) multiplied by a black body function at the mean temperature

during the scan. The instrument RSRF is applied for each scan direction independently.

Extended source flux conversion

At this stage of the pipeline, the angular size of the source relative to that of the detector beam is unknown, and so an extended source is assumed for the conversion of the spectra from units of V/GHz to flux density per sold angle with units of W m^{-2} Hz^{-1} sr^{-1}. The RSRF for each particular detector is used, derived from calibration observations of the telescope and thermal model of the primary and secondary mirrors.

Telescope correction

The contribution from the telescope is now removed, modelled based upon the temperatures recorded from 12 thermometers during the observation.

These extended-source calibrated spectra are also now exported as the final constituents of the Level 1 products.

Level 1 – Level 2

This stage performs the point source calibration (using Uranus as the primary calibrator), a suitable approximation due to the small angular extent of our sources in comparison to the beam size, transforming the spectrum value unit to Jy. The pipeline additionally provides optional steps to average the 200 individual scans into a total spectrum from each bolometer and select which of these to output for further processing.

As of HIPE v12, the pipeline interpolates spectra back to LSR, so each spectrum is on the same wavelength scale, this occurs at the output step of both Level 2 and Level 1. Previous to this the correction for telescope radial velocity toward the source had to be performed later by the user.

2.4.2 Background subtraction

I reprocessed the data from each observation using the pipeline described above within HIPE. Continual updates to HIPE mean the data presented in later chapters uses different version of the program, the specific version used is described in each chapter.

The ~0.2 Jy galaxies of the sample are much fainter than the expected targets of the FTS. This is somewhat offset by the sensitivity being found to surpass pre-launch predictions, and continual improvements to the calibration data, in particular the mean telescope RSRF (Hopwood et al. 2015), derived from all daily dark-sky spectra. Additional processing beyond the standard pipeline is still required however due to the low flux densities involved.

With no canonical method used to estimate the contribution of thermal emission from the telescope and instrument components to fine structure and noise in these spectra, several methods were trialled to determine the best background subtraction technique.

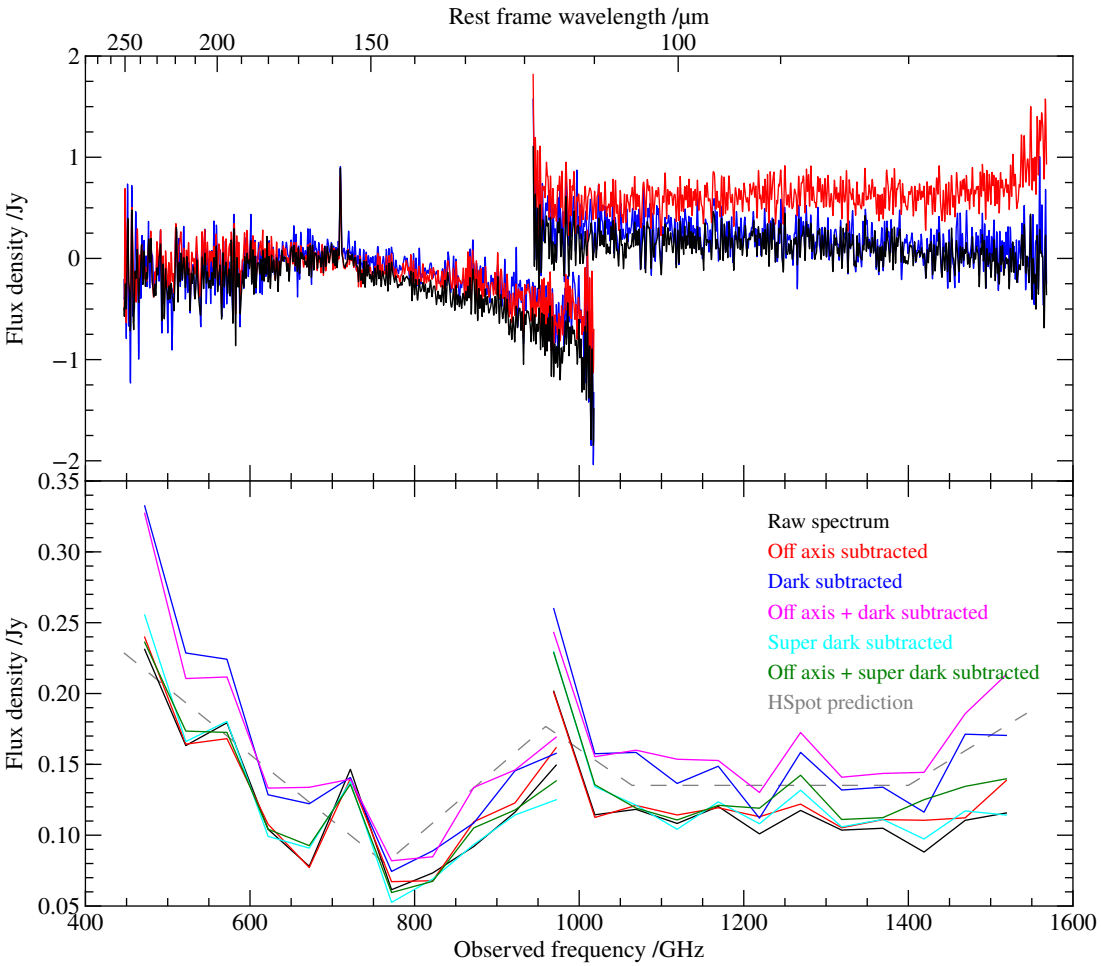

Figure 2.12. *Upper:* Central detector (SSWD4 on the left and SLWC3 on the right) spectra of NB.v1.43 (see Chapter 3). The raw spectra output by the HIPE pipeline are displayed in black, and the resulting spectra after subtraction of the daily dark spectrum and average off axis spectrum are displayed in blue and red respectively. Discontinuities between the SSW and SLW spectra are common in this dataset, resulting from slight temperature differences between the two bolometer arrays.
Lower: Standard deviation of the central detector spectra before and after application of a variety of background subtraction techniques. The empirical noise prediction from the *Herschel* observation planning tool HSpot is displayed as a dashed grey line.

Dark subtraction

Ivison et al. (2010c) and Valtchanov et al. (2011) used the central pixel dark sky spectrum taken on the same day as an estimate of the background.

Off axis subtraction

The six detectors in each band arranged around the central detector and viewing overlapping areas of sky (SSWB3, SSWC2, SSWC5, SSWE2, SSWE5 and SSWF3 for the SSW array, and SLWB2, SLWB3, SLWC2, SLWC4, SLWD2 and SLWD3 for the SLW array; see Figure 2.10), hereafter referred to as the *off axis* detectors can also be used. The mean spectrum of those is taken with the same bolometer array and instrument temperature as the central pixel science observation.

Off axis + dark subtraction

Subtracting the average off axis spectrum from the dark After performing off axis subtraction on the target spectrum, a further extension is to perform off axis subtraction on the dark observation and subtract that from the target spectrum.

Super dark subtraction

As no strong spectral lines appear in most spectra, and the galaxies lie at different redshifts, other on-source spectra taken on the same day can be used as a background estimate. A *super dark* can be constructed by averaging the dark spectrum and those of all others taken on the same day.

Off axis + super dark subtraction

This combines the previous two methods, performing off axis subtraction on all observations taken on the same day, then averaging the dark and other spectra into a super dark and subtracting from the target spectrum.

For consistency and as a result of its typically low noise (see Figure 2.12), off axis subtraction was used for all sources.

The continuum level of the spectra is strongly affected by even slight variations in the temperature of the mirror and instrument components, making the FTS unsuitable for SED measurements of faint targets, and requiring a fit to available photometry, in particular the three SPIRE flux density values.

An FTS determines the flux density of an observed source by splitting the input light, causing a difference in length between the two optical paths, and measuring the result of interference of these beams.

For a monochromatic source of wavelength λ and an OPD δ, the phase difference between these paths is $2\pi\frac{\delta}{\lambda} = 2\pi\bar{\nu}\delta$, where $\bar{\nu}$ is the wavenumber. For a polychromatic source, the interferogram can therefore be expressed as

$$I_\delta = \int_{-\infty}^{\infty} S_{\bar{\nu}}[1 + \exp(i2\pi\bar{\nu}\delta)]\,\mathrm{d}\bar{\nu}. \tag{2.7}$$

Neglecting the constant term as customary, the source spectrum can be recovered by an inverse Fourier transform

$$S_{\bar{\nu}} = \int_{-\infty}^{\infty} I_\delta \exp(-i2\pi\bar{\nu}\delta)\,\mathrm{d}\delta. \tag{2.8}$$

The OPD for any physical instrument cannot be taken out to infinity however, and so for symmetrical maximum OPD limits $\pm\Delta$, $I(|\delta| > \Delta) = 0$, equivalent to multiplication by a boxcar function. After the Fourier transform, the corresponding effect of this multiplication on the spectrum is a convolution by the Fourier transform of a boxcar function

$$S'_{\bar{\nu}} = S_{\bar{\nu}} * \int_{-\Delta}^{+\Delta} \exp(i2\pi\bar{\nu}\delta)\,\mathrm{d}\delta \tag{2.9}$$

$$= S_{\bar{\nu}} * \frac{2\Delta\sin(2\pi\bar{\nu}\Delta)}{2\pi\bar{\nu}\Delta} \tag{2.10}$$

$$= S_{\bar{\nu}} * 2\Delta\mathrm{sinc}(2\pi\bar{\nu}\Delta). \tag{2.11}$$

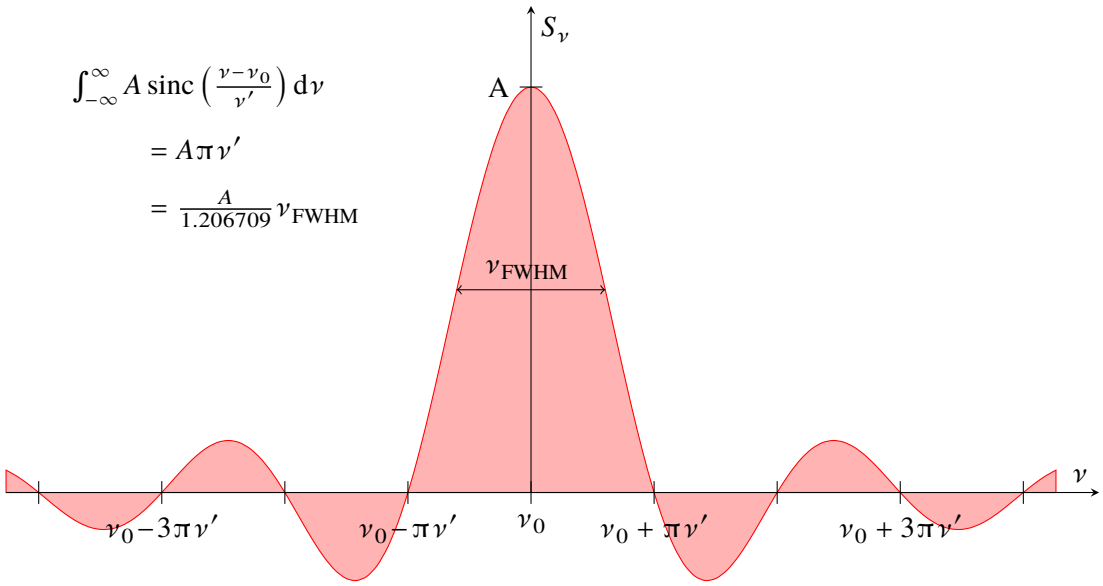

Figure 2.13. The sinc function: the function by which the source spectrum is convolved to produce the spectrum measured by the SPIRE FTS.

Lines in the FTS spectra must therefore be fit with a sinc function, shown in Figure 2.13.

The SPIRE FTS has a maximum OPD of $\Delta \sim 0.14\,\mathrm{m}$, however limitations in the instrument reduce the effective value to 0.125 m such that the spectral resolution $\frac{c_0}{2\Delta} = \pi\nu'$ is 1.2 GHz. The FWHM is therefore

$$\nu_{\mathrm{FWHM}} = 3.79099\nu' = 1.2067 \times 1.2\,\mathrm{GHz} \sim 1.44\,\mathrm{GHz} = 280-970\,\mathrm{km\,s^{-1}}. \tag{2.12}$$

The integral of a sinc function and hence the line flux is

$$F_{\mathrm{line}} = \int_{-\infty}^{\infty} A\frac{\sin\left(\frac{\nu-\nu_0}{\nu'}\right)}{\left(\frac{\nu-\nu_0}{\nu'}\right)}\mathrm{d}\nu \tag{2.13}$$

$$= A\pi\nu' = A\,1.2\,\mathrm{JyGHz} = 1.2 \times 10^{-17}\,A\,\mathrm{Wm^{-2}} \tag{2.14}$$

$$= 0.380A\pi(1+z)\lambda_{\mathrm{rf;\mu m}}\,\mathrm{Jy\,km\,s^{-1}}. \tag{2.15}$$

As the output spectrum of an FTS contains correlated noise, uncertainty margins of line fit parameters (ν_0 and A) are not straightforward to determine. Likely the optimal method to calculate these uncertainties is to add fake signal to the raw Level 0 bolometer readouts and process this through the pipeline, allowing a comparison of the input and measured parameters. The processing time requirements and difficulty in applying this to stacked observations however force the use of alternative techniques. Several different methods were used through this thesis as no method is obviously superior, these are explained below.

The first method is bootstrap uncertainties. The best-fitting velocity and amplitude are first determined from the spectrum. Next, 10 000 sets of 200 random scans are chosen from the 200 individual scans of each observation. The scans in each set are averaged to produce a spectrum

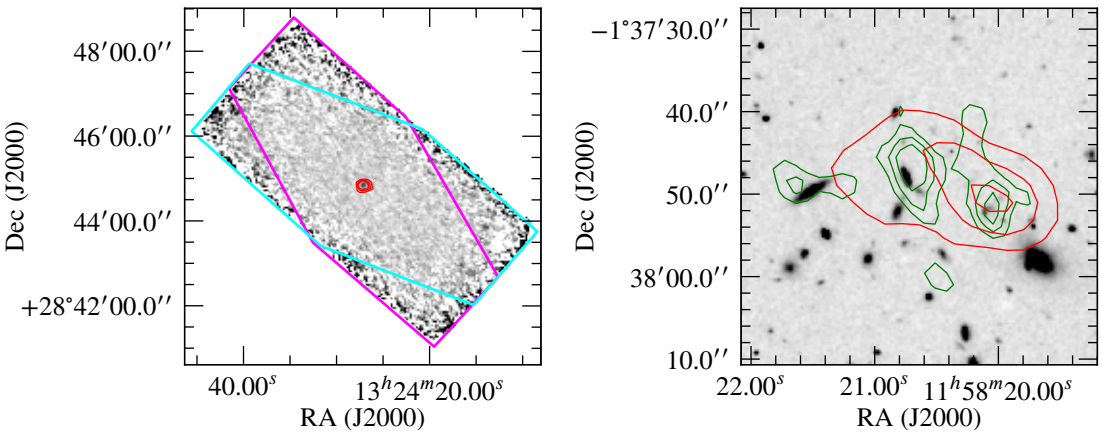

Figure 2.14. *Left:* A typical 100 µm PACS mini scan map (in this case targetting NB.v1.43 — see Chapter 3). Overlaid in red are the unresolved 160 µm contours. Magenta and cyan lines show the approximate outlines of the regions covered by the individual observations at 70° and 110° PA orientations. *Right:* Zoom in on a more complex PACS source emission profile, with background greyscale *HST* F110W imaging. Two low-redshift spiral galaxies provide significant 100 µm flux (green contours), but emit less strongly at 160 um (red contours) and will contribute negligibly at the SPIRE wavelengths.

to which a sinc profile can be fitted, using the the best-fitting velocity and amplitude as initial guesses. The standard deviation of the resulting 10 000 velocity and amplitude measurements is then taken as the line fit uncertainty. True line features can be distinguished from noise by splitting full set of scans in half and averaging, the feature should persist at the same position in both new spectra. This process can be repeated, with the feature expected to be visible in most of the four resultant spectra.

The second method is to generate 20 jackknife subsets of the 200 scans of each observation, each time omitting the next 10 consecutive scans. The variances of line fit parameters are again then determined by fitting the spectral lines in the mean of each subset.

The third method involves cutting a region of the spectrum around a line, subtracting the best-fitting line profile (with parameters x) and calculating the variance (s^2) of the remaining noise, and an estimate of the uncertainty in this variance $\sigma(s^2) = \sqrt{\frac{2s^4}{n-1}}$. The best-fitting line parameters are then found x' that leave the noise variance equal to $s^2 + \sigma(s^2)$, such that the line profile parameter uncertainties can be estimated as $x - x'$.

The second and third methods are used in Chapter 3 and Chapter 4, however the first method is used in Chapter 5 and will be used in any future work as it does not require an arbitrary choice of 10 scans as in the second method, and is a more common and possibly more statistically robust technique than the third method.

2.4.3 PACS

As with the SPIRE FTS data, I used a modified version of the standard pipeline, followed by further measurements outside HIPE. This pipeline is first described, and then the additional processing and measurement steps, with example final maps shown in Figure 2.14.

2.4.3.1 PACS photometer pipeline

As with the SPIRE FTS, the raw measurements need to be converted into usable science data, this is performed by a pipeline (Wieprecht et al. 2009), a quick description of which is given below.

Level 0 – Level 0.5

This stage is similar to that performed in the SPIRE FTS pipeline, converting detector readouts to physical units, additionally masking crosstalk between certain pixels and calculating angles on sky.

Level 0.5 – Level 1

This stage applies the flat-field correction to convert units from Volts into Jy/pixel. Additionally the median pixel values are subtracted to correct for pixel-to-pixel signal level variations, and a flux non-linearity correction is applied, although this has no effect at the low flux densities of our sources.

Level 1 – Level 2

This stage produces a map for each orientation of the telescope.

High-pass filtering and masking

$1/f$ noise (with a power spectrum of the form $S_\nu = \nu^{-\alpha}$) is encountered in many situations within nature. It is additionally found within electronic devices, including the PACS detectors, and is indeed the main source of noise in PACS photometer data, where it has an index $\alpha \sim 0.5$: between that of white noise ($\alpha = 0$), and pink noise ($\alpha = 1$).

A positive value of α results in highest power at low frequencies, and as a result a high-pass filter can be used to reduce the effect of this noise. For extended sources an alternative method MadMap (Cantalupo et al. 2010) is therefore recommended, but point sources are cleaned well and this technique is used within PEP, HLS, *H*-ATLAS and other *Herschel* surveys. The pipeline subtracts the result of a moving-median boxcar filter from the timeline data, removing power in Fourier components of lower frequency than the user-adjustable filter width. A width (in readouts) larger than the masking radius, of around 20 and 30 arcsec (corresponding to 40 and 60 arcsec on sky) in the green and red bands respectively, is recommended. The source must be masked before application of the high-pass filter (HPF), with suggested masking methods being a circular patch over the apparent/expected source location, or a flux 3σ cut. If a source is not sufficiently masked, the median values can contain source flux (which is then removed), resulting in visible 'troughs' on the produced map and lower measured flux densities. Larger masking and HPF radii are thus recommended for brighter sources.

A circular patch mask was found in all cases to produce better noise filtering than a flux sigma cut, which also allowed some low significance source flux to be removed,

and so after an initial reduction with no masking (to ensure the location of the source within the map was known), a circular mask was set.

Bad data removal

While some data were removed during Level 0 processing, further are removed at this stage: those collected at non-uniform scan speeds (i.e. during the turnarounds between scan legs), and outlying data by a second deglitching routine.

Projection

The projection process uses an implementation of the DRIZZLE algorithm (Fruchter and Hook 2002). For our observations, the pixel sizes of the final maps were set to 1.4 and 2.1 arcsec in the green and red bands respectively, and due to the high redundancy of mini scan map data, a drop fraction/pixfrac of 0.1 was able to be used, helping to reduce losses in image quality due to convolution with the large camera pixel footprint.

Level 2 – Level 2.5

This stage combines the two maps (one for each telescope orientation) into a final image, see Figure 2.14.

After processing through the pipeline, the 100 and 160 µm maps for each source were ready for flux measurements to be performed.

2.4.3.2 Flux measurement

Source fluxes were estimated from these maps through aperture photometry. Several corrections must be applied to a value obtained by simply summing the flux within a circular region around the source however, which are described below.

The background flux and variance were estimated by a generalisation of random aperture photometry: bootstrapping identical numbers of pixels to those within an aperture placed over the source from a large area of the map free of of other visible sources.

After subtraction of the background flux estimated to lie within the aperture, the remaining source flux will underestimate the true value due to the PSF which spreads some fraction of the flux out to radii larger than encircled by the aperture. Encircled energy fraction (EEF) functions are provided for the three PACS bands, and displayed in Figure 2.15.

After correction for the EEF, a further correction is required due to flux losses caused by application of the HPF. The loss becomes larger with smaller mask radii, smaller HPF width, larger apertures, and longer wavelength (see Figure 2.15). Mask radii of 20 arcsec and greater are sufficient to cover the majority of the HPF lobes and recover almost all of the input flux.

To determine the source flux uncertainty, the background flux variance was combined with an estimate of the contribution from the choice of source mask radius, high-pass filter radius and aperture radius (with encircled energy fraction correction), found by varying each of these parameters and determining the standard deviation of the measured flux.

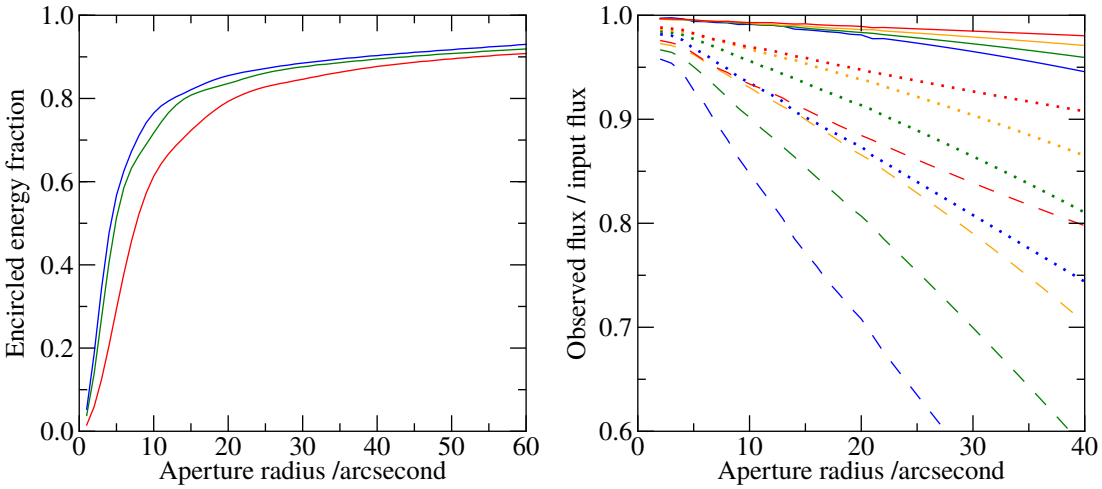

Figure 2.15. *Left:* Encircled energy fraction (EEF) of a point source, as a function of radius, for the different PACS bands, with 70, 100 and 160 µm shown in blue, green and red respectively.
Right: The flux reduction observed due to application of a HPF. Red, orange, green and blue lines denote HPF widths of 40, 30, 20 and 10 readouts respectively, and solid, dotted and dashed lines represent 20, 12 and 4 arcsec source masking radii. Data interpolated from Fig. 19 of Popesso et al. (2012)

Measured fluxes for the sample are presented in Chapter 5.

Chapter 3

FIR spectroscopy of a lensed starburst: a blind redshift from *Herschel*

This chapter primarily describes work published in George et al. (2013):
FIR spectroscopy of a lensed starburst: a blind redshift from *Herschel*

3.1 Introduction

High-resolution studies of individual DSFGs typically rely upon interferometric CO-line observations, necessitating precise knowledge of their redshifts. These remain notoriously difficult to obtain, due to the difficulty in pinpointing their positions, and their faintness in the optical. However, the lensed DSFG population assembled from large-area FIR–mm surveys: members of which would often otherwise be below the detection limit of such surveys; has proved to be within reach of a range of new ground-based, broadband spectroscopic instrumentation (e.g. Harris et al. 2012). Very recently, Weiß et al. (2013) have also demonstrated the power of ALMA, particularly at $z > 4$ where the 3 mm atmospheric window always contains a line.

This chapter presents the first blind determination of a redshift using FIR spectroscopic observations from space – a key step towards demonstrating the feasibility of integral-field FIR spectroscopy as planned for the joint Japan Aerospace Exploration Agency (JAXA)-ESA mission, SPICA (e.g. Swinyard et al. 2009). Throughout the chapter we use *WMAP*7 cosmology (Komatsu et al. 2011) with $H_0 = 70.4\,\mathrm{km\,s^{-1}\,Mpc^{-1}}$, $\Omega_\mathrm{m} = 0.272$ and $\Omega_\Lambda = 0.728$.

3.2 Discovery observations

The NGP is one of a number of fields observed as part of the *Herschel* Astrophysical Terahertz Large Area Survey, (*H*-ATLAS; Eales et al. 2010) with the *Herschel Space Observatory* (Pilbratt et al. 2010). The acquisition and reduction of parallel-mode data from SPIRE (Griffin et al. 2010) and PACS (Poglitsch et al. 2010) are described in detail by Ibar et al. (2010b), Pascale et al. (2011) and Rigby et al. (2011). See Chapter 1 for further details.

The SPIRE imaging led quickly to the selection of HATLAS J132427.0+284452 (hereafter NB.v1.43) as a bright $\left(S_{350\,\mu\mathrm{m}} \gtrsim 200\,\mathrm{mJy};\ \text{all bands} \geqslant 30\,\sigma\right)$, potentially distant $\left(\left\{S_{250\,\mu\mathrm{m}}, S_{500\,\mu\mathrm{m}}\right\} < S_{350\,\mu\mathrm{m}}\right)$, lensed starburst. This source is included in a number of follow-up campaigns, where we have been studying the brightest of these objects (e.g. Negrello et al. 2010; Fu et al. 2012; Omont et al. 2013).

The surface density of $S_{350\,\mu\mathrm{m}} \gtrsim 300\,\mathrm{mJy}$ lens candidates is likely around $1/40\,\mathrm{deg}^{-2}$ (M. Negrello, priv. comm.), plausibly placing this source among the most strongly lensed known DSFGs.

3.3 Detailed follow-up observations

Much deeper PACS data were subsequently obtained from the OT1 programme, OT1_RIVISON_1 , recording data simultaneously at 100 and 160 µm for a total of 3 min, and reaching $\sigma \approx$ 10 and 12 mJy respectively.

Approximately 30 min of high-resolution 7 GHz continuum data were acquired using the National Radio Astronomical Observatory's (NRAO's) Very Large Array (VLA) during 2011 June. The observation was performed in A configuration, with 64 × 2 MHz channels in each of two intermediate frequencies (IFs), each IF with dual polarisation, recording data every 1 s. 3C 286 was observed every few minutes to determine accurate complex gain solutions and bandpass corrections, and to set the absolute flux density scale. Using natural weighting, the resulting map has a circular 0.3 arcsec synthesised beam FWHM and an r.m.s. noise level of 10 µJy beam^{-1}.

870 µm imaging data were obtained using the SMA as part of programme 2011B-S044, with 9.7 hr of total integration time in the compact, extended, and very extended array configurations, with baselines covering 20 – 400 m, and the receivers tuned such that the upper sideband was centred on 870 µm. The blazar, 1924−292, was used as the bandpass calibrator and Titan was used for absolute flux calibration. The nearby quasar, 1310+323, was used to track the complex gains.

Following a tentative line detection using Zpectrometer (Harris et al. 2007) on NRAO's GBT, plausibly CO $J = 1 \rightarrow 0$ at $z = 2.3078$ (Harris et al. 2012), we obtained 4.4 hr on-source using all six of the 15 m antennas of IRAM's PdBI. These data were taken during 2011 January, in A configuration, with the 2 mm receivers tuned to 139.380 GHz, corresponding to the rest-frame frequency of CO $J = 4 \rightarrow 3$ at that redshift. No CO line emission was visible within limits compatible with the $J = 1 \rightarrow 0$ flux and further follow-up of NB.v1.43 was put on hold, pending a more robust redshift determination. We use these data here because they provide a usefully deep $\left(0.1\,\mathrm{mJy\,beam}^{-1}\right)$, high-resolution (0.68 arcsec × 0.45 arcsec, position angle (PA) 55°) 2 mm continuum image.

Via our interferometric imaging (2 mm contours overlaid in Figure 3.1) it is immediately obvious that the FIR source is coincident with the ∼10 arcsec giant arc reported by Gladders et al. (2003), strongly lensed by the rich foreground cluster RCS J132427+2845.2, at $z = 0.997 \pm 0.017$

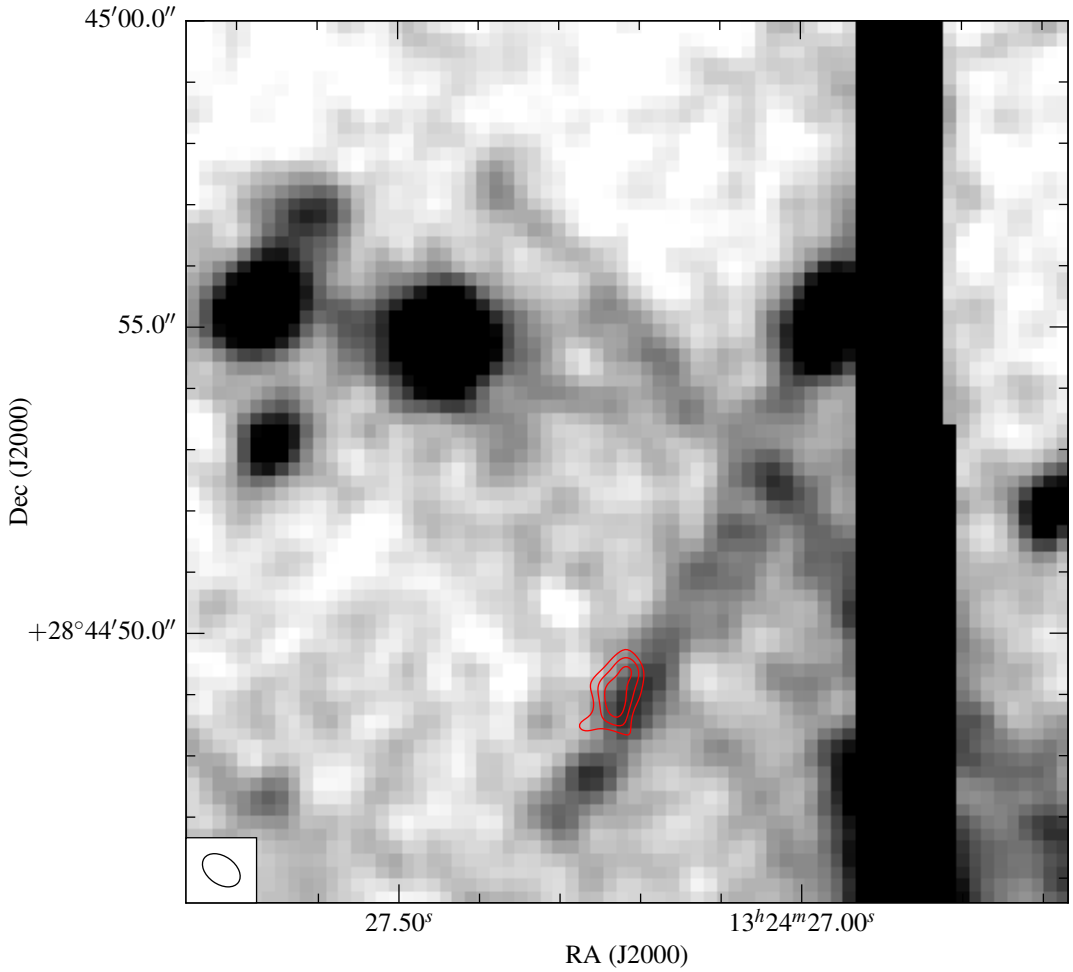

Figure 3.1. Continuum emission at 2 mm, as observed by PdBI PdBI with a 0.68 arcsec × 0.45 arcsec (PA 55°) synthesised beam, overlaid as contours on *r*-band imaging from the Canada-France-Hawaii Telescope (CFHT) (Gladders et al. 2003). The lensed arc is oriented NW–SE. The other elongated features are diffraction spikes caused by two bright, nearby stars. Both the brightest cluster galaxy and cluster centre are over 20 arcsec from the arc (Gladders and Yee 2005).

(Gladders and Yee 2005).

3.4 Far-IR and CO spectroscopy

3.4.1 A blind redshift from the SPIRE FTS

During 2012 August 02, NB.v1.43 was observed with a single pointing of the SPIRE FTS for 3.7 hr, the spectrum covering $\lambda_{\rm obs}$ = 194 – 671 µm The data were processed using the *Herschel* data processing pipeline (Fulton et al. 2010) within HIPE v10. The calibration data used include the telescope RSRF which is derived from all dark-sky spectra observed over the lifetime of the telescope. Since publication of this chapter, the calibration data have been updated and so slight differences will exist between the spectrum presented in this chapter and in Chapter 5. Spectra from detectors arranged around the central 'on-source' detector were averaged to produce a local

Table 3.1. Continuum flux densities.

Wavelength		S_ν		Notes
100	μm	41 ± 4[a]	mJy	*Herschel* PACS
160	μm	180 ± 14[a]	mJy	*Herschel* PACS
250	μm	347 ± 25[b]	mJy	*Herschel* SPIRE
350	μm	378 ± 28[b]	mJy	*Herschel* SPIRE
500	μm	268 ± 21[b]	mJy	*Herschel* SPIRE
870	μm	30.2 ± 5.2	mJy	SMA
2	mm	1.2 ± 0.1	mJy	IRAM PdBI
3.5	mm	200 ± 170	μJy	CARMA
4.3	cm	350 ± 30	μJy	VLA
21	cm	1.95 ± 0.24	mJy	VLA (FIRST)

[a] Errors include 3 and 5 % calibration uncertainties at 100 and 160 μm, respectively.

[b] Errors include the contribution due to confusion and a 7 % calibration uncertainty has been added in quadrature (Valiante et al., in preparation).

background measurement, and subtracted from the source spectrum.

The $^2P_{3/2} \rightarrow {}^2P_{1/2}$ [C II] transition at rest-frame 157.74 μm is one of the brightest lines seen in the FIR waveband, providing up to 1 % of $L_{\rm IR}$ (measured across rest-frame 8 – 1000 μm) in star-forming galaxies (Stacey et al. 1991). Within the spectral range covered by the SPIRE FTS in our observations of lensed starburst galaxies, this line is likely to be the most significant; indeed, it is often the only transition detected (e.g. Ivison et al. 2010c).

The SPIRE FTS spectrum of NB.v1.43, shown in Figure 3.2, displays a 7.5 σ marginally resolved (1.2 GHz spectral resolution) emission line at (709.9 ± 0.4) GHz. Attributing this to [C II] indicates a redshift, $z = 1.677 \pm 0.001$. No other lines were detected, with $3\sigma <$ 200, 230, 150 and 600 Jy km s^{-1} for [O III] 88 μm, [N II] 122 μm, [O I] 146 μm and [N II] 205 μm respectively, meaning that this redshift remained likely yet unconfirmed at this point.

3.4.2 Redshift confirmation via CO

To verify the SPIRE FTS redshift determination, we used CARMA to search for the CO $J = 2 \rightarrow 1$ line ($\nu_{\rm rest} = 230.538$ GHz), which should be redshifted to approximately $\nu_{\rm obs} = 86.0$ GHz for $z = 1.68$. Observations were carried out using the 3 mm receivers during 2012 November 23 in D configuration (11 – 146 m baselines), with 2.3 hr spent on source. The blazars 1310+323 and 0927+390, were used for complex gain calibration and to derive the bandpass shape. Absolute flux densities should be accurate to within ~15 %. We obtained an 8 σ detection of line emission, close

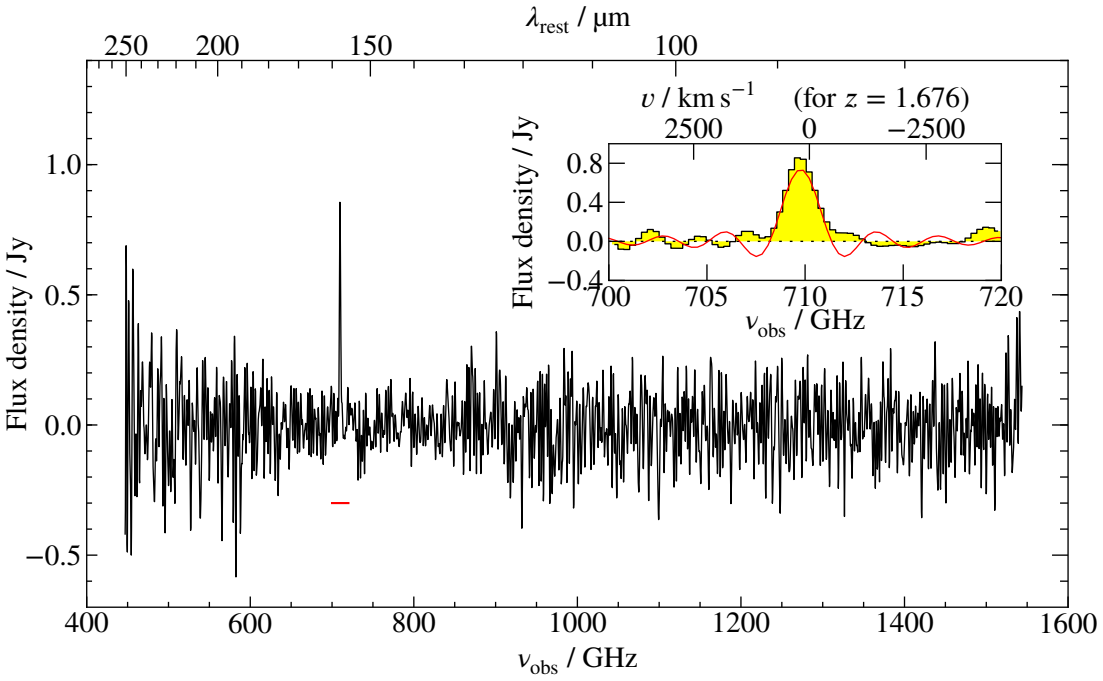

Figure 3.2. The continuum-subtracted *Herschel* SPIRE FTS spectrum. No other features correspond to expected transition lines.
Inset: Zoomed in on the region indicated by the red line in the parent plot. Velocity scale corresponds to [C II] at $z = 1.676$. The best-fitting sinc profile is overlaid in red.

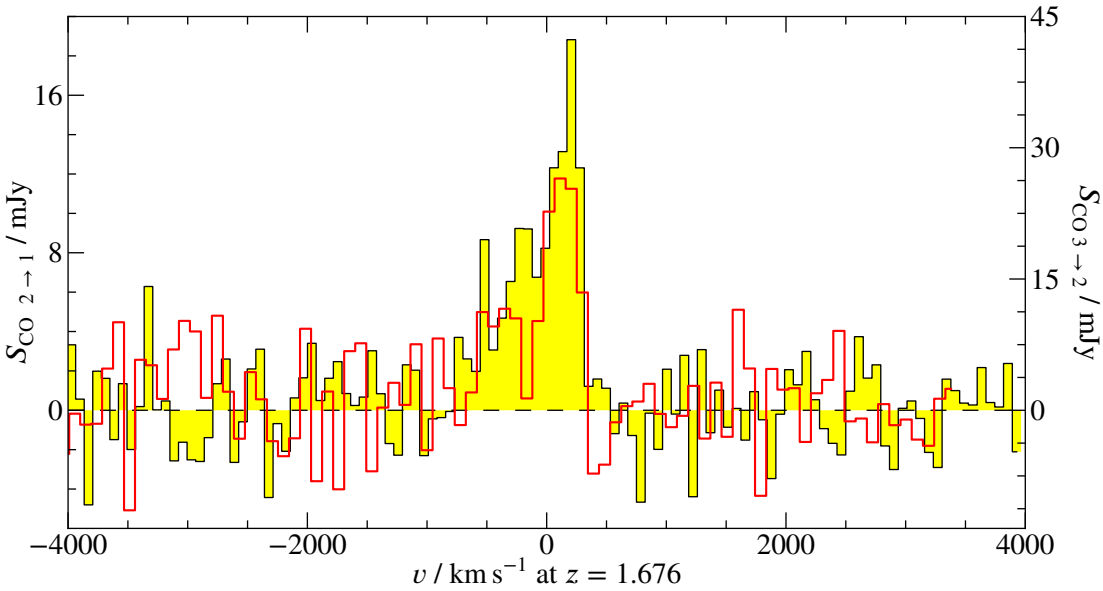

Figure 3.3. CO $J = 2 \rightarrow 1$ spectrum from CARMA, binned to 20.8 MHz, with the CO $J = 3 \rightarrow 2$ IRAM PdBI spectrum shown in red, binned to 40 MHz and put on the same brightness temperature ($T_{\rm b}$) scale.

to the expected frequency – see Figure 3.3 – thus confirming the redshift, with $z = 1.676 \pm 0.001$. The 34.8 GHz GBT line is therefore presumably spurious.

We also imaged the source in CO $J = 3 \rightarrow 2$ with the IRAM PdBI, also during 2012 November. We obtained 1.1 h of integration time, using all six of the 15 m antennas, this time in D configuration – the most compact. The observing frequency was set to 129.028 GHz,

corresponding to the redshifted frequency of CO $J = 3 \rightarrow 2$ ($\nu_{\mathrm{rest}} = 345.796\,\mathrm{GHz}$) for $z = 1.68$. Again, we found a bright $3\,\sigma$ emission line at the expected frequency, (Figure 3.3).

The two line profiles are consistent with one another; neither can be described well with a single Gaussian, suggesting that their shape is due to either a merger or a rotating, gas-rich disk (e.g. Engel et al. 2010; Ivison et al. 2013). The line width (deduced from fits using a single Gaussian), $(500 \pm 140)\,\mathrm{km\,s^{-1}}$ FWHM, is typical of those seen for DSFGs (Greve et al. 2005).

3.5 Discussion

Characterisation of the dust emission of NB.v1.43 was performed by fitting the power-law dust temperature model of Kovács et al. (2010) to the continuum flux densities detailed in Table 3.1. The fit is shown in Figure 3.4 and a description of this model is now given, see the above article for more details.

The luminosity density of a grey body can be expressed as

$$L_\nu = 4\pi\, A\, \epsilon_\nu\, B_\nu(T), \tag{3.1}$$

where A is the projected area and other denotations are as in Equation 1.4. Generalising this for a distribution of dust masses and temperatures,

$$L_\nu = 4\pi A \epsilon_\nu \int B_\nu(T) \frac{M_\mathrm{d}(T)}{M_\mathrm{d;tot}}\,\mathrm{d}T. \tag{3.2}$$

Using a power-law dust temperature model

$$\frac{\mathrm{d}M_\mathrm{d}(T)}{\mathrm{d}T} = M_0\, T^{-\gamma}, \tag{3.3}$$

the mass of dust $M_\mathrm{d}(T)$ at each temperature T can be determined by integrating to find the total dust mass $M_\mathrm{d;tot} = M_0 \int_{T_\mathrm{c}}^{\infty} T^{-\gamma}\,\mathrm{d}T$, so

$$\frac{\mathrm{d}M_\mathrm{d}(T)}{\mathrm{d}T} = M_\mathrm{d;tot}\,(\gamma - 1)\,T_\mathrm{c}^{\gamma-1}\,T^{-\gamma}. \tag{3.4}$$

The dust mass temperature index γ is taken to be 7.2, an appropriate value for both local and high-redshift starbursts (e.g. Magnelli et al. 2012), and the cutoff temperature T_c is typically 20 – 40 K.

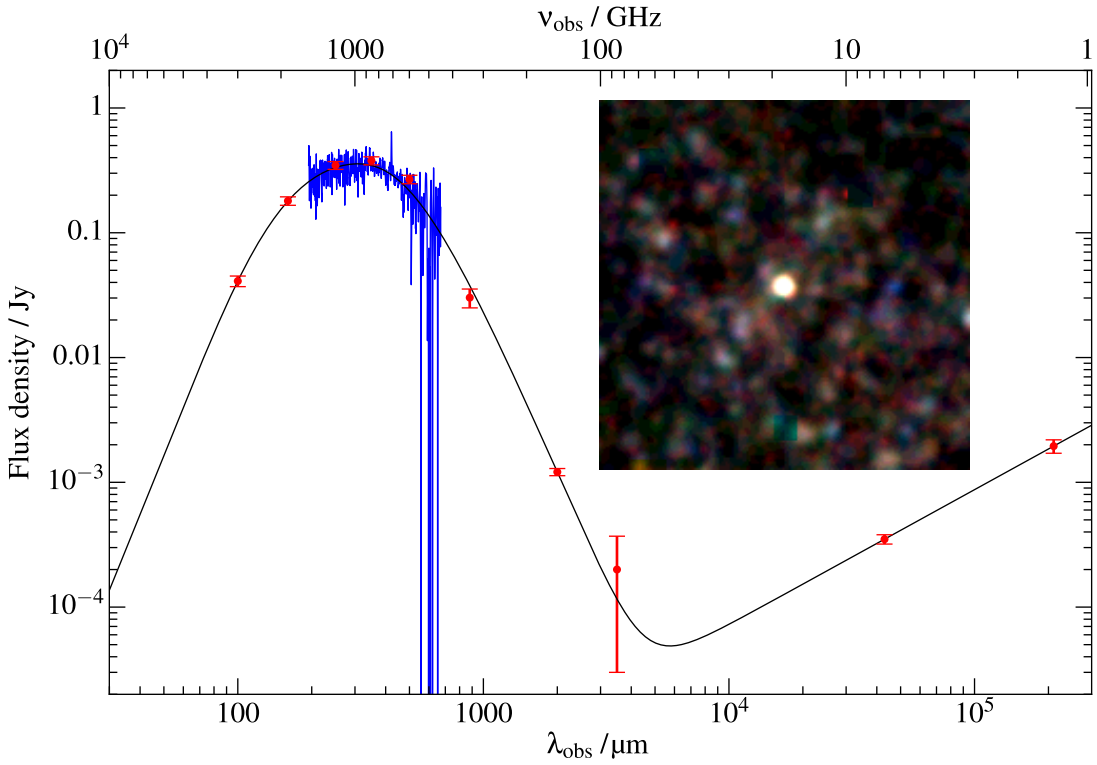

Figure 3.4. FIR-through-radio SED of NB.v1.43 with the best-fitting synchrotron and power-law temperature distribution dust model shown in black. The FTS spectrum is shown in blue.
Inset: 15-arcmin × 15-arcmin false-colour image of NB.v1.43 in the three *Herschel* SPIRE filters.

Applying this to Equation 3.2, the luminosity density becomes

$$L_\nu = \frac{8\pi h}{{c_0}^2} A\,(\gamma-1)\,T_c^{\gamma-1}\,\nu^3\,\epsilon_\nu \int_{T_c}^{\infty} \frac{T^{-\gamma}}{\exp\left(\frac{h\nu}{k_B T}\right)-1}\,\mathrm{d}T \tag{3.5}$$

$$= \frac{8\pi h}{{c_0}^2}\left(\frac{k_B}{h\nu}\right)^{\gamma-1} A\,(\gamma-1)\,T_c^{\gamma-1}\,\nu^3\,\epsilon_\nu \int_0^{\frac{h\nu}{k_B T_c}} \frac{x^{\gamma-2}}{e^x-1}\,\mathrm{d}x \quad \text{using } x=\frac{h\nu}{k_B T} \tag{3.6}$$

$$= \frac{8\pi h}{{c_0}^2} A \left(\frac{k_B}{h}\right)^{\gamma-1} (\gamma-1)\,T_c^{\gamma-1}\,\nu^{4-\gamma}\,\epsilon_\nu\,\zeta_{\frac{h\nu}{k_B T_c}}(\gamma-1)\,\Gamma(\gamma-1) \tag{3.7}$$

where $\zeta_b(a)$ is the incomplete Riemann zeta function, and $\Gamma(a)$ is the gamma function.

Using the optical depth-based formulation of emissivity described in Section 1.2.2, $\varepsilon_\nu = (1 - e^{-\tau_\nu})$, and the formulation of optical depth from Kovács et al. (2010)

$$\tau_\nu = \kappa_0 \left(\frac{\nu}{\nu_0}\right)^\beta \frac{M_d}{A}, \tag{3.8}$$

the observed flux density from a source emitting in this nature at a redshift z therefore is

$$S_{\nu_{\rm obs}} = \frac{(1+z)\,\mu}{4\pi D_{\rm L}^2} L_{(1+z)\,\nu_{\rm obs}} \tag{3.9}$$

$$\begin{aligned} &= \mu \frac{2h}{{c_0}^2} \frac{A}{D_{\rm L}^2} (\gamma - 1)\,\Gamma(\gamma - 1) \left(\frac{k_{\rm B} T_{\rm c}}{h}\right)^{\gamma-1} (1+z)^{5-\gamma}\, \nu_{\rm obs}^{4-\gamma} \\ &\qquad \zeta_{\frac{h(1+z)\nu_{\rm obs}}{k_{\rm B}T_{\rm c}}} (\gamma - 1) \left(1 - \exp\left[-\kappa_0 \left\{\frac{(1+z)\,\nu_{\rm obs}}{\nu_0}\right\}^{\beta} \frac{M_{\rm d;tot}}{A}\right]\right) \\ &\qquad + C\left[(1+z)\,\nu_{\rm obs}\right]^{\alpha}, \end{aligned} \tag{3.10}$$

where a synchrotron component has also been added. These flux densities can then be fit to measured values. Free parameters are μ, A, C, α β, γ, $M_{\rm d;tot}$ and $T_{\rm c}$, however for this source β and γ were set to 1.5 and 7.2 respectively, and a range of constant values were trialled for A, such that five free parameters were fit for each A value. The total infrared luminosity and dust temperature are fairly well constrained, however the dust emission area and dust mass are correlated with each other and inversely with the amplification. As the fitted μA was fairly constant, the amplification did not converge to the same value for each emission area input. It is difficult therefore to determine constraints on the amplification, however the projected area equates to a 2.6 kpc radius area, consistent with values measured from interferometric imaging (see Section 1.3.4.3), suggesting the amplification may be low. Derived quantities from the fit for NB.v1.43 are detailed in Table 3.2.

Of the (350 ± 30) μJy integrated flux density at 7 GHz, (270 ± 25) μJy (77 ± 10 per cent) is in a compact component at RA = 13:24:27.225, Dec. = +28:44:49.01 (±0.02, J2000), with a best-fit deconvolved size of (0.45 ± 0.05) arcsec × (0.09 ± 0.05) arcsec, PA (152 ± 4)°. Comparing this with the 2 mm emission (RA = 13:24:27.229 ± 0.004, Dec. = +28:44:49.07 ± 0.06, J2000, (1.0 ± 0.2) arcsec × <0.3 arcsec, PA 152° ± 9°) suggests that the radio emission is significantly more compact than the dusty star-forming material, suggestive of a non-starburst origin. The radio spectral index, α (where $S_\nu \propto \nu^\alpha$) is steeper than the typical $\alpha = -0.8$, adding credibility to the idea that an AGN dominates the radio emission (e.g. Ibar et al. 2010a).

The widely-used Helou, Soifer, and Rowan-Robinson (1985) parametrisation of the FIRRC,

$$q_{\rm IR} = \log_{10}\left(\frac{\frac{F_{\rm FIR}/{\rm W\,m^{-2}}}{3.75\times10^{12}}}{S_{1.4\,{\rm GHz}}/{\rm W\,m^{-2}\,Hz^{-1}}}\right), \tag{3.11}$$

where the FIR flux was originally estimated from the *IRAS* bands as

$$F_{\rm FIR} = \int_{42.5\,\mu{\rm m}}^{122.5\,\mu{\rm m}} S_\lambda \,{\rm d}\lambda = 1.26\times10^{-14}\left(2.58 S_{60\,\mu{\rm m}} + S_{100\,\mu{\rm m}}\right), \tag{3.12}$$

produces a typical value $q_{\rm IR} \sim 2.4$ (e.g. Yun, Reddy, and Condon 2001; Ivison et al. 2010d), consistent with the local value (Bell 2003), and appearing to show little redshift evolution (Sargent et al. 2010b; Barger et al. 2012), although see (Ivison et al. 2010a; Magnelli et al.

Property	Value
Dust temperature (T_d) /K	33.1 ± 3.2
M_d /10^9 $\mu^{-1}M_\odot$	1.07 ± 0.15
$A_{projected}$[a] /kpc^2	21.4 ± 5.7
L_{IR} /10^{13} $\mu^{-1}L_\odot$	2.91 ± 0.12
Synchrotron spectral index α	-1.08 ± 0.09
q_{IR}	1.85 ± 0.09
SFR[b] /μ^{-1} $M_\odot$ yr^{-1}	4,300
[C II] $I_{[C\,II]}$ /Jy km s^{-1}	486 ± 52
[C II] FWHM /km s^{-1}	800 ± 64
[C II] $L_{[C\,II]}$ /10^{10} μ^{-1} $L_\odot$	5.80 ± 0.62
CO $J = 2 \rightarrow 1$ I_{CO} /Jy km s^{-1}	11.3 ± 1.4
CO $J = 2 \rightarrow 1$ FWHM /km s^{-1}	640 ± 270
CO $J = 2 \rightarrow 1$ L_{CO} /10^8 μ^{-1} $L_\odot$	1.64 ± 0.20
CO $J = 3 \rightarrow 2$ I_{CO} /Jy km s^{-1}	11.5 ± 3.5
CO $J = 3 \rightarrow 2$ FWHM[c] /km s^{-1}	450 ± 170
CO $J = 3 \rightarrow 2$ L_{CO} /10^8 μ^{-1} $L_\odot$	2.50 ± 0.76
$r_{3\rightarrow2/2\rightarrow1}$	0.45 ± 0.15
M_{gas}[d] /10^{11} μ^{-1} $M_\odot$	3.6 ± 0.6
SFE[d] /$L_\odot$ $M_\odot^{-1}$	83

[a] From fitting an SED to the dust emission.

[b] Following Murphy et al. (2011b).

[c] From fitting a Gaussian with its mean constrained to that of the $J = 2 \rightarrow 1$ fit.

[d] Average determined via CO $J = 2 \rightarrow 1$ and $J = 3 \rightarrow 2$.

Table 3.2. Dust and spectral line properties of NB.v1.43.

2015) for evidence of a tentative decline with increasing redshift. Alternative definitions of q_{IR} are presented in Ivison et al. (2010a) and Kovács et al. (2010), replacing F_{FIR} with F_{IR} to take advantage of the longer-wavelength coverage commonly available in the present day. These works choose different normalisation constants, the former using the same as that in Helou, Soifer, and Rowan-Robinson (1985), and the latter opting for 9×10^{14} Hz for a better comparison with the Helou, Soifer, and Rowan-Robinson (1985) definition. Adopting as in these works a F_{IR} (measured across rest-frame 8 – 1000 µm) based definition, we find a value $q_{IR} = 1.85 \pm 0.09$, rather lower than that usually seen and again consistent with an AGN-related contribution to the radio luminosity (e.g. Donley et al. 2005).

The [O III] 88 µm line was not detected. An [O III] line of similar s/n to [C II] was observable from SDP.81 (which also has $q_{IR} \sim 1.8 \pm 0.1$ – Valtchanov et al. 2011), this time suggesting that

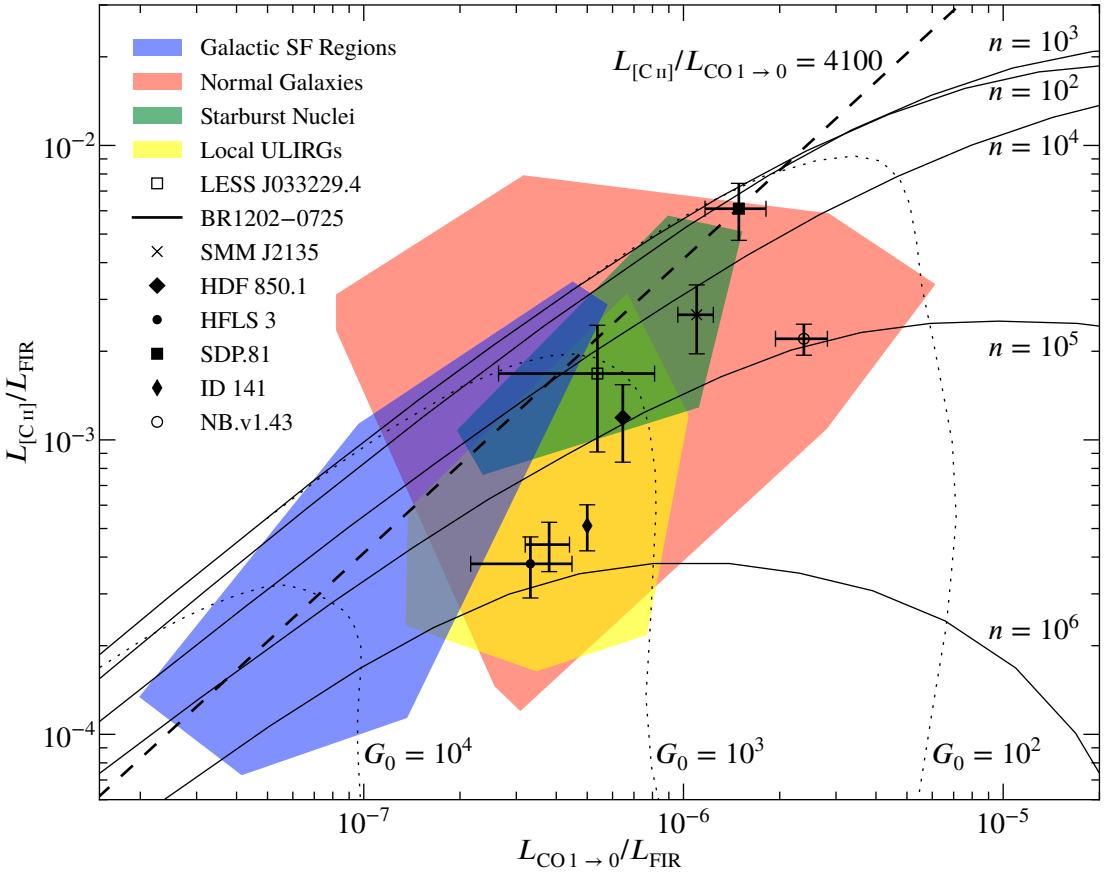

Figure 3.5. Diagnostic plot, adapted from Hailey-Dunsheath et al. (2010), based on the model of a slab illuminated from both sides, with identical corrections applied to $L_{[C\,II]}$ (×0.7 – non-PDR emission) and $L_{CO\,1\text{–}0}$ (×2.0 – assuming optically thick emission is only received from the front face of the slab). Shaded regions are approximate coverage of local objects. Neglecting differential lensing magnification, n and G_0 estimates are magnification-independent. Also shown are other high-redshift starbursts: LESS J033229.4−275619 (De Breuck et al. 2011), BR1202−0725 (Wagg et al. 2012), SMM J2135-0102 (Ivison et al. 2010c), HDF 850.1 (Walter et al. 2012), HFLS 3 (Riechers et al. 2013), *H*-ATLAS SDP.81 (Valtchanov et al. 2011), and HATLAS ID 141 (Cox et al. 2011). Where necessary, literature values have been converted using $r_{2\to1/1\to0} \sim 0.84 \pm 0.13$, and the ratios obtained by integrating under the NB.v1.43 SED: $L_{FIR(42.5-122.5\,\mu m)} = 0.69 \times L_{(40-500\,\mu m)} = 0.63 \times L_{IR(8-1000\,\mu m)}$.

the AGN has a greater influence in SDP.81 than in NB.v1.43 (Abel et al. 2009).

CO is commonly used to trace molecular gas reservoirs. Estimates of the $J = 1 \to 0$ line flux can be derived from the higher-J line fluxes assuming Rayleigh-Jeans brightness temperature (T_b) ratios, e.g. $r_{2\to1/1\to0} \sim 0.84 \pm 0.13$ and $r_{3\to2/1\to0} \sim 0.52 \pm 0.09$ (Ivison et al. 2011; Bothwell et al. 2013): consistent with the T_b ratio measured here for $r_{3\to2/2\to1}$, 0.45 ± 0.15. Adopting $\alpha_{CO} = 0.8\,M_\odot(K\ km\ s^{-1}\ pc^2)^{-1}$, as is usual for starburst galaxies (e.g. Bolatto, Wolfire, and Leroy 2013), we derive a H_2 + He mass, $M_{gas} = (3.6 \pm 0.6) \times 10^{11}\,\mu^{-1} M_\odot$, having averaged the $J = 2 \to 1$ and $3 \to 2$ measurements. Following Harris et al. (2012) and Bothwell et al. (2013), a rough magnification estimate can be derived from the $J = 1 \to 0$ luminosity and linewidth, yielding $\mu \approx 11$.

An independent estimate of the gas mass can be derived via the gas-to-dust mass ratio, M_{gas}/M_d. For 1/3 solar metallicity, this is 220^{+180}_{-90} (Sandstrom et al. 2013), suggesting $M_{gas} = 2.4^{+2.0}_{-1.0} \times$

$10^{11}\,\mu^{-1}\mathrm{M}_\odot$, consistent with our CO-based estimate, albeit with a large uncertainty. These estimates of the gas mass correspond to a star-formation efficiency $60 \lesssim L_{\mathrm{IR}}/M_{\mathrm{gas}} \lesssim 220\,\mathrm{L}_\odot\,\mathrm{M}_\odot^{-1}$, and a gas-consumption timescale $M_{\mathrm{gas}}/\mathrm{SFR} \sim 30-100\,\mathrm{Myr}$, consistent with those typically measured for DSFGs (e.g. Greve et al. 2005).

Using the PDR model displayed in Figure 3.5, representing the FUV illuminated surface of an interstellar cloud, we estimate $n \sim 10^{4.8}\,\mathrm{cm}^{-3}$ and $G_0 \sim 10^{2.3}$, a number density and FUV radiation field strength comparable with other high-redshift starbursts. These models assume all CO emission is produced in PDRs, neglecting any contribution from quiescent gas or turbulent heating which provide plausible explanations for the comparatively large $L_{\mathrm{CO1\to0}}/L_{\mathrm{FIR}}$ in this object, as may increased metallicity. Differential magnification might also affect these derived properties, if the CO and FIR emission are not co-spatial (e.g. Fu et al. 2012).

Without a detailed mass model of the cluster lens, it is not possible to investigate the extent of differential magnification of the DSFG, but we can nonetheless attempt a plausibility test of the statistical likelihood. Following Serjeant (2012), we modelled a SIE with a 20 arcsecond critical radius and ellipticity of 0.2, with the same submillimetre galaxy model used in that paper. As with the galaxy-scale lenses in Serjeant (2012), we found Figure 3.5 to be largely unaffected by differential magnification, even for $\mu > 10$. However, the aspect ratio of the observed-frame optical emission suggests a high magnification and large angular extent, implying long-baseline interferometric measurements may resolve out some of the emission, as discussed in Section 3.4.2.

3.6 Implications for far-IR integral-field spectroscopy

The Space Infrared telescope for Cosmology and Astrophysics (SPICA; Swinyard et al. 2009) is a planned successor to *Herschel*. Thermal emission from the 80 K primary telescope of *Herschel* is six orders of magnitude brighter than the FIR background; with a dish temperature of 6 K, SPICA should be two orders of magnitude more sensitive than any previous FIR facility.

The SpicA FAR-infrared Instrument (SAFARI) is an imaging FTS proposed for SPICA, covering $34-210\,\mu\mathrm{m}$ $\left([\mathrm{O\,I}]\,63\,\mu\mathrm{m}\text{ to }z=2.3\right)$ over a 2 arcmin × 2 arcmin field of view with an intended spectral resolution R ∼ 2000 and sensitivity < few × $10^{-19}\,\mathrm{Wm}^{-2}$ (5σ : 1 hr; Swinyard et al. 2009).

Our observation of [C II] from NB.v1.43 provides $I_{[\mathrm{C\,II}]} = (1.15 \pm 0.12) \times 10^{-17}\,\mathrm{Wm}^{-2}$ An [O I] line of this flux will likely be observable to several σ within two seconds of integration with SPICA. While such sources will likely be known before a SPICA pointing, the ability of *Herschel* to obtain a blind redshift provides confidence that with observations of order 1 hr, the much more sensitive SPICA will pinpoint redshifts of multiple unlensed few-mJy CIB sources (potentially several from each spectrum – Clements et al. 2007; Raymond et al. 2010), reducing the need for the blind CO line searches typically required today. With such integration times, blind fine-structure line detections are feasible and a gateway to detailed imaging/dynamical studies with ALMA.

3.7 Conclusions

We present the first blind redshift to have been obtained via *Herschel* spectroscopy. The galaxy, at $z = 1.676$, is lensed by a rich galaxy cluster at $z = 1.0$ into an arc of length ~10 arcsec. A lensing model will be presented in Fu et al. (in preparation).

This source appears to be a merger or disk-like system, with a best-fit $L_{\rm IR}$ of $2.91 \times 10^{13}\ \mu^{-1}\ {\rm L}_{\odot}$, dust temperature of $T_{\rm d} = 33$ K, and SFR of $4300\ \mu^{-1}\ {\rm M}_{\odot}{\rm yr}^{-1}$, and a compact AGN-related contribution to the radio flux density.

The observed [C II] flux is $(1.15 \pm 0.12) \times 10^{-17}$ W m^{-2}, suggesting an [O I] line of similar flux could be detected by SPICA to 5σ with an integration time of order 3 s. Even many unlensed DSFGs may require no more than ≈1 h of integration. The feasibility of blind line detections will not only directly advance our knowledge of high-redshift systems and their interstellar media, but act as a gateway to detailed imaging and spectral studies with (sub)mm interferometers such as ALMA.

3.8 Subsequent work

Since publication of this work, a lens model has been presented in Bussmann et al. (2013). This model uses only two nearby galaxies visible in new Keck-II/NIRC2 imaging to reproduce the SMA data, suggesting a magnification factor $\mu = 2.8 \pm 0.4$, however with only a single image, lens parameters are not strongly constrained. Assuming this magnification factor and corresponding demagnified half-light radius of (3.44 ± 0.44) kpc are correct, the intrinsic infrared luminosity, SFR, dust mass and molecular gas mass are $(1.04 \pm 0.15) \times 10^{13}\ {\rm L}_{\odot}$, $1500\ {\rm M}_{\odot}{\rm yr}^{-1}$, $(1.7 \pm 0.5) \times 10^{9}\ {\rm M}_{\odot}$ and $(1.3 \pm 0.3) \times 10^{11}\ {\rm M}_{\odot}$ respectively, placing this source on the HyLIRG limit.

This model however does not attempt to reproduce the much more extended optical emission, as does another modelling effort using *HST* and Keck imaging, due to the poor configuration constraints (Calanog et al. 2014). Future X-ray imaging may help, providing additional data on the matter distribution of the nearby clusters, however despite the interest of this system with visible very extended stellar emission and a compact star-forming core, a satisfactory and complete understanding of this source may not be found in the near future.

Chapter 4

Herschel reveals a molecular outflow in a $z = 2.3$ ULIRG

This chapter primarily describes work published in George et al. (2014):
Herschel reveals a molecular outflow in a z = 2.3 ULIRG.

4.1 Introduction

The combined radiation and mechanical energy output of massive stars and AGN is capable of driving massive outflows of interstellar gas, see Section 1.2.4.2 for further details. The increased global SFR at high-redshift suggests that outflows should be more common and powerful than in the local Universe, and evidence from blueshifted absorption lines of Mg II and other species indicates that this is likely the case (e.g. Weiner et al. 2009; Banerji et al. 2011). The majority of outflowing gas appears to arise from strongly star-forming, high-mass galaxies with outflow strength increasing with SFR surface density $\Sigma_{\rm SFR}$ (Newman et al. 2012).

Previous studies of high-redshift outflows have generally utilised UV lines (e.g. Steidel et al. 2010; Martin et al. 2012), which are generated within ionised material and thus insensitive to any molecular phase, critical to determination of whether superwinds or *in situ* star-formation dominates the reduction in interstellar molecular gas and SFR density at early epochs. As discussed in Section 1.2.4.2, detection of blueshifted OH absorption is strong evidence for a molecular phase within these outflows. Despite the likely higher prevalence of superwinds at high-redshift, and the potential advantages of observing OH, the FIR rest-frame wavelengths of these transitions necessitate the use of space-based facilities. The consequential small apertures have meant OH observations have been restricted to local galaxies (see Section 1.2.4.2).

Gravitational lensing provides a means to circumvent these limitations. The galaxy, SMM J2135-0102, hereafter the Cosmic Eyelash, was identified in the field of a massive, lensing cluster via ground-based 870 µm imaging (Swinbank et al. 2010b). Subsequent imaging with high spatial resolution constrained the lensing model, showing that the Cosmic Eyelash is resolved into an ~5 arcsec long arc, mirrored about the critical curve, with a total magnification $\mu = 37.5 \pm 4.5$

(Swinbank et al. 2011). CO measurements of its velocity field reveal a disc with rotation speed 320 km s^{-1}, dominated by several star-forming clumps, each of radius 100 – 200 pc, distributed across a radius of ~2 kpc.

This chapter describes the discovery of a molecular outflow from the Cosmic Eyelash at $z = 2.326$, as betrayed by the detection of the 119 µm OH transition in absorption during a number of long integrations with the *Herschel Space Observatory* (Pilbratt et al. 2010). Throughout, we use *Planck* 2013 cosmology (Planck Collaboration et al. 2014b) with $H_0 = 67.8\,\mathrm{km/sMpc^{-1}}$, $\Omega_\mathrm{m} = 0.307$ and $\Omega_\Lambda = 0.693$.

4.2 Observations

Due to its high magnification, correspondingly high FIR flux densities and previous in-depth studies (e.g. Ivison et al. 2010c; Danielson et al. 2011, 2013), the Cosmic Eyelash was included in our programme of deep *Herschel* (Pilbratt et al. 2010) SPIRE FTS (Griffin et al. 2010) observations (e.g. Valtchanov et al. 2011; George et al. 2013, George et. al. in preparation).

We initially observed the Cosmic Eyelash as part of OT1_RIVISON_1 : a 3.7 h integration using the central detectors of the SPIRE arrays, comprising 200 scans with the FTS mirror. The data were processed using the *Herschel* data processing pipeline (Fulton et al. 2010) within HIPE v11. The local background was estimated as the mean spectrum observed by the rings of detectors surrounding the central detector.

The resulting spectrum covering $\lambda_\mathrm{obs} = 194 – 671$ µm provided strong detections of several fine-structure lines, along with a tentative indication of OH absorption. We then obtained five additional 3.7 h integrations as part of OT2_RIVISON_2 , processing these using the same method as the first observation, in order that the spectra may be co-added. We rejected one of these, due to inconsistencies across several wavelength ranges likely caused by poor background estimation as a result of one of the surrounding detectors producing corrupt data. The combined integration time of the useful data is therefore 19 h.

4.3 Results and discussion

The continuum-subtracted rest-frame stack of our observations provides a significant detection of [C II] 158 µm, as previously identified by Ivison et al. (2010c), alongside new detections of [N II] 122 µm [O III] 88 µm and [O I] 63 µm. The previous, tentative indication of OH absorption is confirmed.

The low angular resolution of the SPIRE FTS is unable to spatially resolve individual kinematic components within the Cosmic Eyelash, instead producing a galaxy-integrated spectrum. The velocity separation of the clumps partially alleviates this complication however, allowing a comparison of the detected lines with the previous CO measurements. The stack at 119.233 µm is displayed in Figure 4.1, along with a comparison of the OH absorption with the rest-frame

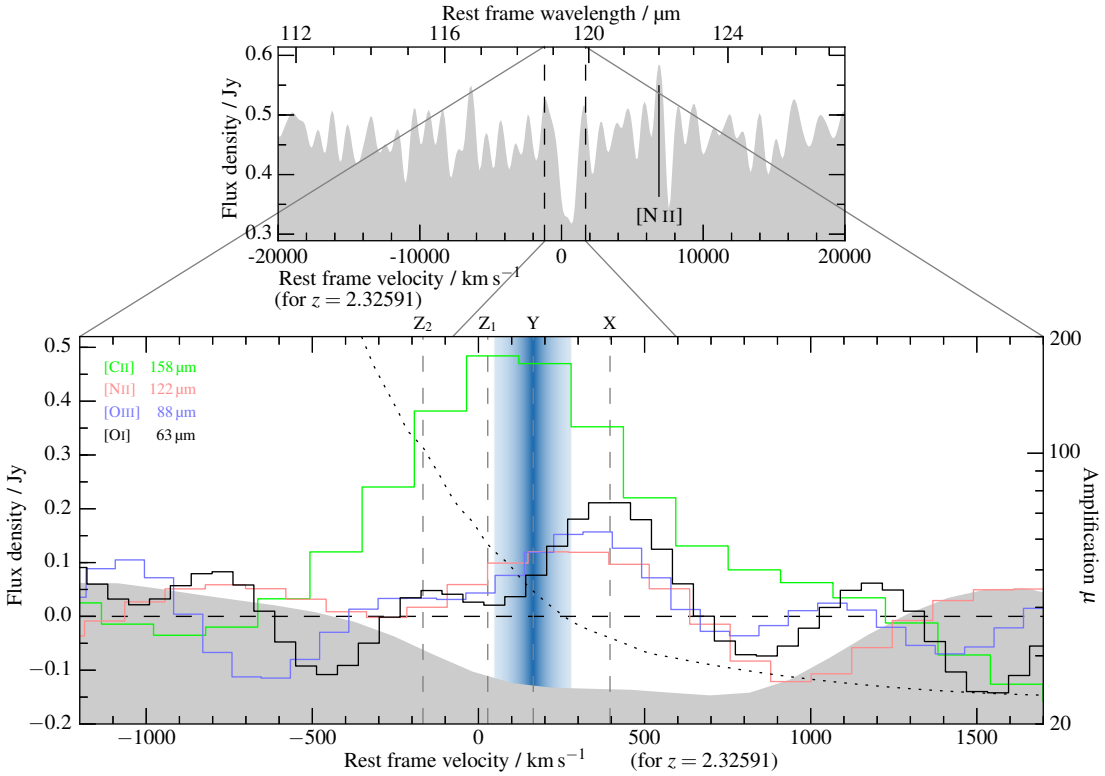

Figure 4.1. *Upper*: Rest-frame stack centred on the OH 119.233 μm line at $z = 2.32591$, the low-J luminosity-weighted redshift derived in Swinbank et al. (2011). The continuum flux level is normalised to that from the SED (Ivison et al. 2010c). The vertical black dashed lines demarcate the region displayed in the right-hand plot.
Lower: Zoom-in on the OH absorption line with the rest-frame primary atomic and ionic fine-structure emission lines in the SPIRE FTS spectral range overplotted. The lensing amplification as a function of velocity is shown as a dotted black line, suggesting a higher amplification for [C II] relative to the other emission lines. Note that the SPIRE FTS produces a sinc line profile, with a width constant in frequency, and that all of the atomic and ionic lines are spectrally unresolved. Vertical dashed lines are displayed at the velocities of the CO-bright clumps identified in Danielson et al. (2013). The vertical shaded region corresponds to the derived median and 1σ velocity of the OH feature assuming two identical components and corresponds to a shift of $(-240 \pm 110)\,\mathrm{km\,s^{-1}}$ relative to the CO clump 'X', which contains the densest molecular gas, and which we associate with the primary source of the [N II], [O III] and [O I] emission (see Section 4.3.1).

fine-structure emission lines.

4.3.1 Atomic and ionic fine-structure lines

To determine the properties of the observed FIR lines, we fitted each with a sinc profile, as appropriate for an FTS spectrum (Swinyard et al. 2014). The resulting line measurements are detailed in Table 4.1, with errors conservatively estimated as the maximum obtained via the use of two methods.

The first method involves applying the jackknife technique to the individual FTS scans (200 for each observation). We generate 20 subsets of 190 scans, neglecting 10 consecutive scans at a time, fit a sinc profile to each line and determine the variance of the fit parameters from the 20 subsets. The second method requires cutting a region around each spectral line, estimating the

Transition (μm)	Velocity ($km\,s^{-1}$)	Flux ($Jy\,km\,s^{-1}$)	Amplification	Luminosity ($10^9\,L_\odot$)
Low-*J* CO	0		37.5 ± 4.5	
[C II] 158	100 ± 140	280 ± 80	50 ± 20	1.2 ± 0.6
[N II] 122	290 ± 100	60 ± 30	36 ± 12	0.5 ± 0.3
[O III] 88	330 ± 130	50 ± 40	35 ± 17	0.6 ± 0.5
[O I] 63	400 ± 90	50 ± 30	33 ± 12	0.8 ± 0.6
OH 119	160 ± 110	-180 ± 60	33 ± 5	-1.6 ± 0.6

Table 4.1. FIR line properties from fitting sinc profiles (as appropriate for an FTS), with errors determined via jackknife data sets. Velocities are relative to the low-*J* CO luminosity-weighted redshift of $z = 2.32591$ (Swinbank et al. 2011). All fine-structure lines are unresolved (1.44 GHz FWHM), with luminosities calculated using the lensing amplification factors derived for their observed velocities (Swinbank et al. 2011). The OH properties were derived by integrating over all flux less than the continuum level and assuming two identical components, and assume an amplification corresponding to a source velocity of $(400 \pm 50)\,km\,s^{-1}$.

variance and standard deviation of the variance of that region. Best-fitting and 1σ line parameters are then calculated such that subtracting a sinc profile with those values returns residuals with the estimated and 1σ variances.

Intriguingly, several of the fine-structure line velocities appear to be offset from the literature redshift, derived from intensity-weighted low-*J* CO emission, used to define the zero velocity in Figure 4.1 and Table 4.1, with the H II region lines at higher velocities than [C II], a PDR line. We observe the peak [O I] emission at $(400 \pm 90)\,km\,s^{-1}$, an unexpected value given the status of this transition as a primary coolant of dense PDRs, and hence typically colocated with [C II]. The CO component, 'X', was identified in Danielson et al. (2011, 2013) to be the most active site of massive star-formation in the Cosmic Eyelash, with a velocity of $\sim 400\,km\,s^{-1}$. The [N II] and [O III] transitions require the presence of an ionising source, and considering the large uncertainties on the velocity offsets, we associate these lines with this CO component, acknowledging that the molecular and ionised gas may not be completely cospatial. The material traced by these lines appears to be very different from that observed in CO and with the SMA, with individual line profiles displaying no structure, although the spectral resolution of the FTS may smear out finer details. A simultaneous fit to the four fine-structure lines yields a mean velocity $v_{\rm fs} = (220 \pm 120)\,km\,s^{-1}$ relative to the low-*J* CO luminosity-weighted redshift of $z = 2.32591$.

In contrast to several other high-redshift starbursts (e.g. Ferkinhoff et al. 2011; Valtchanov et al. 2011), we observe a line-to-continuum flux deficit similar to that seen in local ULIRGs (Luhman et al. 2003). Most of the FIR lines have luminosity-to-$L_{\rm FIR}$ ratios slightly below the mean of those of the local Brauher, Dale, and Helou (2008) sample (Figure 4.2), consisting of low-redshift normal star-forming galaxies, starbursts and AGN, compared to which the Cosmic Eyelash possesses an order-of-magnitude higher FIR luminosity. A comparison (Figure 4.2) to the $z \sim 0.1$ ULIRG sample of Farrah et al. (2013) reveals comparable line luminosities and

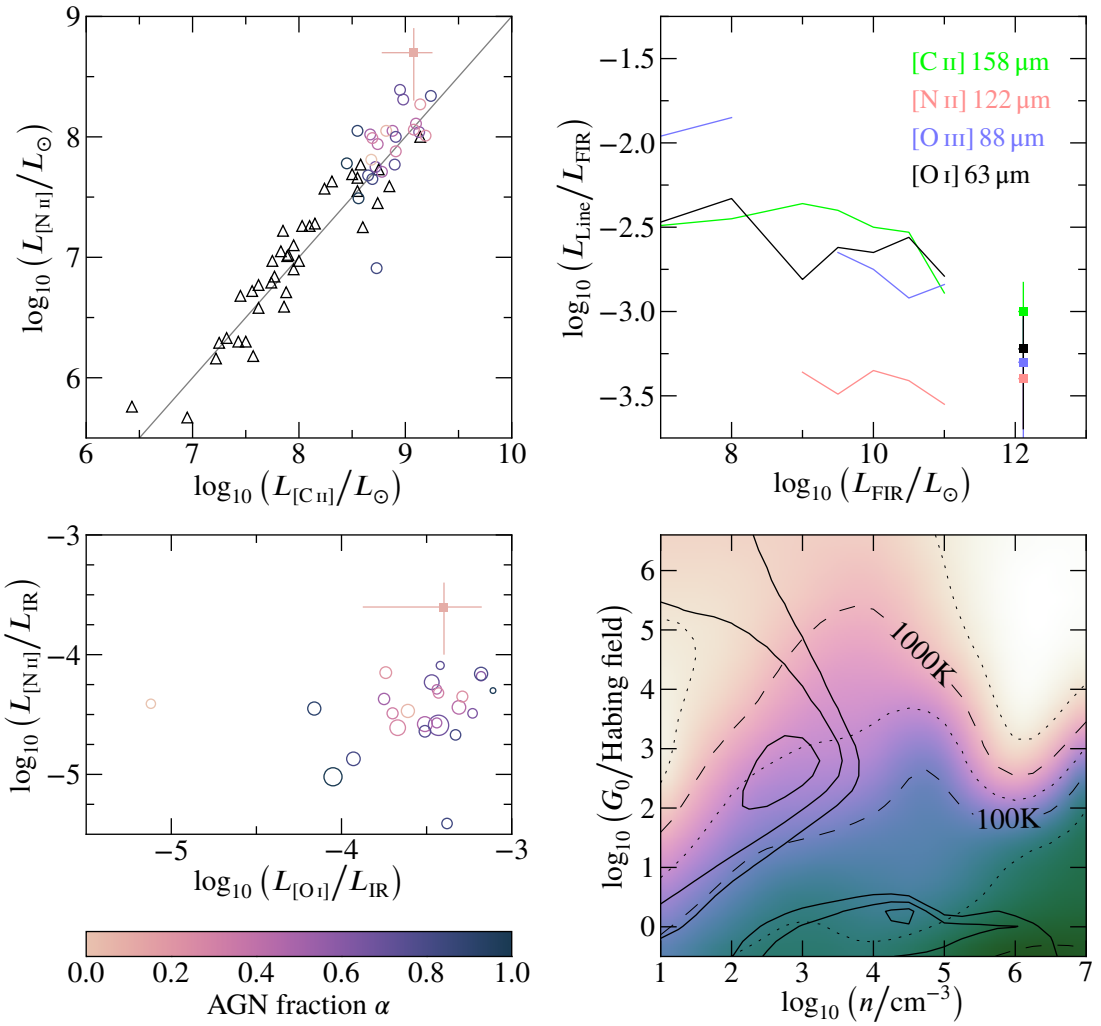

Figure 4.2. Properties of the atomic and ionic fine-structure lines.
Upper left: Comparison of line luminosities in the Cosmic Eyelash (filled square) with local ULIRGs (coloured open circles, colour map as in lower left plot; Farrah et al. 2013) and local galaxies of various types (black open triangles; Brauher, Dale, and Helou 2008). The line $L_{[\mathrm{N\,II}]} = 0.1\,\mathrm{L}_{[\mathrm{C\,II}]}$ is shown in grey.
Upper right: Mean line-to-FIR luminosity ratios for several lines in the Brauher, Dale, and Helou (2008) sample. the Cosmic Eyelash values are denoted by squares.
Lower left: Line-to-IR luminosity ratios in Farrah et al. (2013) and the Cosmic Eyelash (square). Colour map displays the fractional contribution of AGN to L_{bol}, with marker area proportional to L_{bol}.
Lower right: Estimated χ^2 contours for CO clump, 'X' (Danielson et al. 2011), of the Cosmic Eyelash (red) overlaid on the PDR surface temperature model from Kaufman, Wolfire, and Hollenbach (2006), suggesting n and G_0 values of 10^{2-3} (see text for caveats).

L_{line}-to-L_{IR} ratios in the Cosmic Eyelash, with the exception of [N II] which is stronger in the Cosmic Eyelash than for any galaxy in that study.

The [C II] results in particular are interesting, with the derived luminosity a factor of 4 lower than estimated in Ivison et al. (2010c). The earlier value was derived assuming a smaller lensing amplification (32.5) and using a Gaussian rather than a sinc fit, from a much shallower spectrum calibrated with the asteroid Vesta (Uranus is now used). Our estimate gives a line luminosity-to-L_{IR} ratio of 0.06 %. With a [C II]/[N II] ratio of 2.5, similar to that tentatively observed in LAE-2

by Decarli et al. (2014, and much lower than its companion SMG in that paper), H II regions may make a major contribution to the [C II] luminosity. An intriguing, if perhaps unlikely scenario is a strong contribution to the [C II] emission from the outflow itself, which would suggest a lower amplification (due to increased source velocity) and hence higher luminosity.

With the [O I] emission appearing to arise from within CO clump, 'X', we fit several observed parameters for this clump to the PDR models presented in Kaufman, Wolfire, and Hollenbach (2006). We assume an FIR luminosity for this clump, $L_{\rm FIR}^{\rm X} = L_{\rm FIR}^{\rm tot} \times {\rm SFR}^{\rm X}/{\rm SFR}^{\rm tot}$, and that 50 % of [C II] emission arises from the [O I]-producing PDRs within this clump (a value likely overestimated should the observed [C II]–[O I] velocity offset prove genuine and H II regions contribute strongly to the [C II] luminosity).

The [C I] 370 µm/[C I] 609 µm ratio from Danielson et al. (2011) should additionally probe the deeper regions ($A_{\rm V} \sim 2-4$; Kaufman, Wolfire, and Hollenbach 2006). As indicated in the lower-right panel of Figure 4.2, these parameters indicate a gas density $n \sim 10^2 - 10^3$ cm^{-3} and incident FUV flux $G_0 \sim 10^2 - 10^3$ Habingfields (Figure 4.2) within CO clump 'X', consistent with Danielson et al. (2013). The above values both increase as the [C II]/[O I] ratio drops, with Danielson et al. (2013) estimating $n \sim 10^3$ cm^{-3} for the molecular gas within clump 'X'.

With dissimilar photon energies required for production of the species involved, but comparable critical densities, the relative luminosity $L_{\rm [O\,III]}/L_{\rm [N\,II]}$ is a sensitive diagnostic of the interstellar radiation field hardness, little affected by gas density. We observe $L_{\rm [O\,III]}/L_{\rm [N\,II]} = 1.2 \pm 1.2$ in the Cosmic Eyelash, with the models presented in Ferkinhoff et al. (2011) thus indicating production within an H II region surrounding a starburst with an effective temperature of 35 000 K or within a narrow-line region with ionisation parameter ~ -3.5 (both models assume solar). To investigate the likelihood of an AGN-associated narrow-line region, we estimate the maximum possible AGN luminosity from the SED. We use the IR SED fitting method introduced in Mullaney et al. (2011), and extended in Del Moro et al. (2013) to fit to the available photometry from MIR to submm wavelengths. This SED fitting method allows the decomposition of the AGN and host contribution to the galaxy's IR emission. The best-fitting result requires no AGN contribution, attributing the whole of the IR emission to the host galaxy. To place a constraint on the AGN IR emission, we assume an upper limit that corresponds to 10 % of the resulting total emission from the best fit. This, along with the higher total $L_{\rm [N\,II]}$ and $L_{\rm [C\,II]}$ and low G_0 inferred above, is consistent with a situation in which SMGs possess more extended star-formation than local ULIRGs, generated by large, low-ionisation H II regions (e.g. Biggs and Ivison 2008; Hainline et al. 2009; Menéndez-Delmestre et al. 2009; Ivison et al. 2011; Swinbank et al. 2011).

4.3.2 OH absorption

Due to the relatively poor spectral resolution of the SPIRE FTS, we do not see a readily-identifiable P-Cygni profile in the 119 µm OH feature and as such we fitted it with two identical components constrained to have the rest-frame frequency separation of the line doublet, suggesting a velocity offset of (160 ± 110) km s^{-1} (see Figure 4.1 and Table 4.1) with respect to

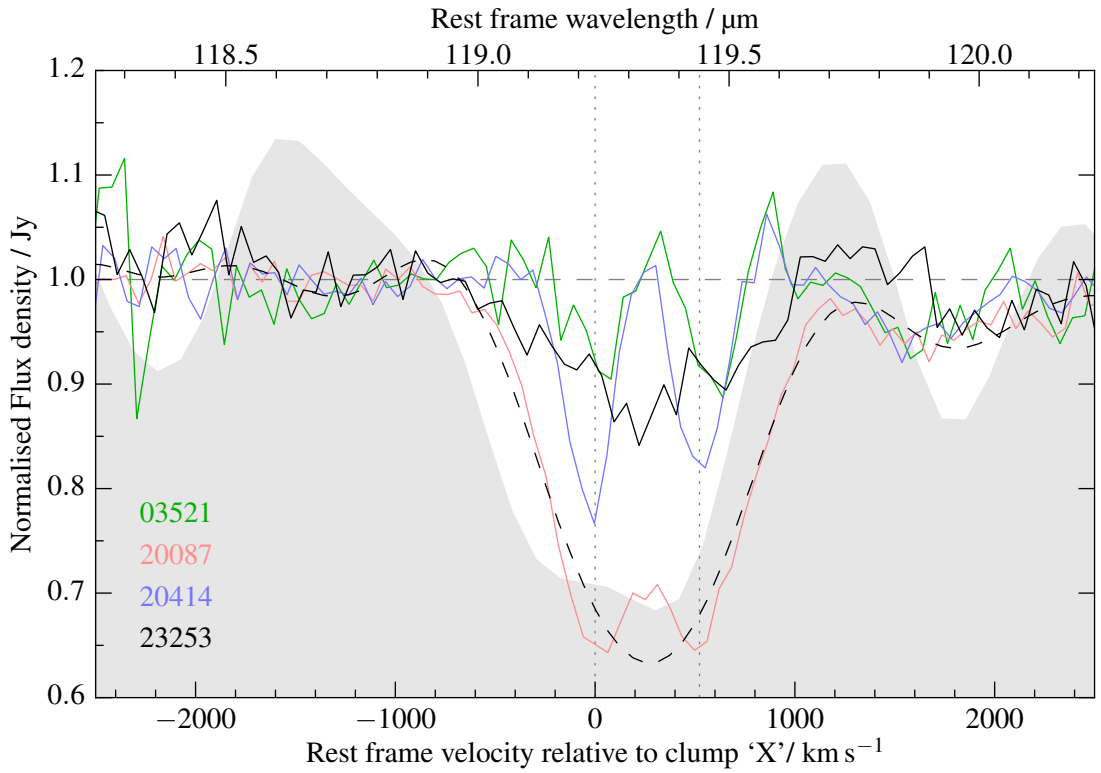

Figure 4.3. Normalised OH profile of the Cosmic Eyelash compared to those of the four starburst-dominated (AGN contribution <25 % of L_{IR}) sources in the local sample of Spoon et al. (2013), observed with *Herschel*/PACS (Poglitsch et al. 2010). The low maximum and median blueshift velocities of these (including the Cosmic Eyelash) are typical of systems with low AGN contributions (see Figure 4.4). Vertical dotted lines denote the rest-frame velocities of the OH doublet. The velocity scale in this figure is set relative to that of the assumed driving source (such that the luminosity-weighted low-*J* CO redshift for the system as a whole corresponds to −400 km s^{-1}). Note that the SPIRE FTS produces an FWHM of ~570 km s^{-1} at this observed frequency, with the PACS spectrometer producing an FWHM of <290 km s^{-1} for the displayed observations. Shown as a black dashed line is the 20087 spectrum deconvolved with the PACS spectral profile and then convolved with the SPIRE spectral profile, producing a very similar profile to that observed in the Cosmic Eyelash.

the low-*J* CO luminosity-weighted redshift of $z = 2.32591$ (Swinbank et al. 2011). Requiring strong active star-formation from dense material as the primary driver, as with the [N II], [O III] and [O I] lines, we associate the OH source with CO clump, 'X' (Danielson et al. 2013), at $v \sim 400\,\mathrm{km\,s^{-1}}$ corresponding to a mean velocity of the OH of $(-240 \pm 110)\,\mathrm{km\,s^{-1}}$. Rupke, Veilleux, and Sanders (2005) require $v < -50\,\mathrm{km\,s^{-1}}$ for classification as an outflowing wind. As such, this (−180 ± 40) Jy km/s feature represents the highest redshift observation of outflowing molecular gas. Plausibly, even higher velocity gas may be found closer to the driving source, at optical depths too great to be observed by the FTS, however the more extended visible outflow will provide the main effect on the galaxy and ISM as a whole.

No other OH transitions are observed, consistent with the faint 79 μm cross-ladder transition observations in Spoon et al. (2013). Multiple transitions have been detected in the nearby quasar, Mrk 231 (González-Alfonso et al. 2014), with several showing absorption fluxes comparable to that of the 119 μm doublet, suggesting that the 119 μm lines are optically thick in that system, or that the radiatively excited upper levels are more highly populated. The large FWHM of the

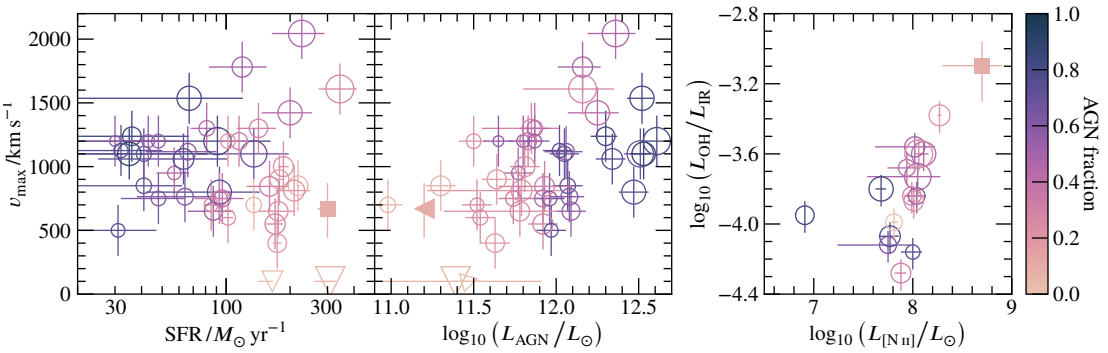

Figure 4.4. *Left*: Comparison of the Cosmic Eyelash to local ULIRGs from Spoon et al. (2013) and Veilleux et al. (2013). Marker colour denotes the fractional AGN contribution to $L_{\rm bol}$ (see left-hand colour bar), with enclosed marker area proportional to $L_{\rm bol}$. the Cosmic Eyelash is displayed with a filled marker, and appears typical of sources with little AGN contribution within that sample, with $L_{\rm AGN}$ the primary determinant of $v_{\rm max}$. The AGN luminosity indicated for the Cosmic Eyelash is derived from the estimated maximum 10 % contribution to $L_{\rm IR}$ (see Section 4.3.1).
Right: Comparison with the Spoon et al. (2013) and Farrah et al. (2013) samples. The much lower OH-to-IR luminosity ratios of the ULIRGs of that sample likely indicates higher OH optical thickness or larger OH covering fractions.

FTS spectral profile makes it difficult to determine the underlying line structure; however, a comparison to the velocities of the four clumps indicates that it is likely that the outflow does not have a covering factor of unity.

In Figure 4.3, we compare the 119 µm OH absorption feature of our stacked spectra, to that of starburst-dominated sources from the Spoon et al. (2013) sample. The normalised, integrated, absorbed flux, −380 Jy km/s, is at the high end of those in that sample, including both starburst- and AGN-dominated sources.

Following Spoon et al. (2013), we define $v_{\rm max}^{\rm obs}$ as the velocity at which a B-spline fitted to the blue absorption wing crosses the continuum flux density. Correcting for turbulence (100 km s^{-1}; as used in Spoon et al. 2013), and instrumental spectral resolution (1.2 GHz) in quadrature, we obtain an estimate for the maximum velocity of outflowing molecular gas: $v_{\rm max}^{\rm mol} = -670$ km s^{-1} for $v_{\rm source} = 400$ km s^{-1}, with Spoon et al. (2013) estimating the uncertainty on $v_{\rm max}^{\rm mol}$ obtained in this method as ± 200 km s^{-1}. This similarity to the maximum predicted for starburst-driven outflows (~700 km s^{-1}; Martin 2005) suggests highly efficient momentum transfer within the Cosmic Eyelash.

It is additionally instructive to compare this result with outflows from high-redshift galaxies determined from UV absorption lines. Winds from SMGs should likely possess qualities of both these, and of outflows from local ULIRGs. Figure 4.4 shows our detection in relation to those presented in Spoon et al. (2013) and Veilleux et al. (2013), with the Cosmic Eyelash occupying the lower-right corner of the $v_{\rm max}^{\rm mol}$–SFR plot, typical of the sources with low fractional AGN contributions to $L_{\rm bol}$. A correlation of $v_{\rm max}^{\rm UV}$ with SFR surface density $\Sigma_{\rm SFR}$ in such high-redshift galaxies has been identified (Chen et al. 2010; Kornei et al. 2012; Newman et al. 2012). $\Sigma_{\rm SFR}$ is typically found in high-redshift SMGs to be between that in low-redshift ULIRGs and high-redshift 'normal' galaxies, suggesting comparatively high expected $v_{\rm max}^{\rm UV}$

within the Cosmic Eyelash and other SMGs; however, the observed ionised components may have velocities systematically different from that of the molecular phases, with Banerji et al. (2011), Kornei et al. (2012) and Martin et al. (2012) finding $v_{\rm max}^{\rm UV}$ similar to $v_{\rm max}^{\rm mol}$ for the Cosmic Eyelash within galaxies of substantially lower $\Sigma_{\rm SFR}$.

With an inclination 60° ± 8°, determined by Swinbank et al. (2011) for the Cosmic Eyelash, we now consider the solid angle into which molecular gas may be ejected. An angle of 140° perpendicular to the disc is suggested by the ULIRG samples of Rupke, Veilleux, and Sanders (2005), Spoon et al. (2013) and Veilleux et al. (2013) in which 2/3 of the OH detections show outflows, consistent with the OH detection in the Cosmic Eyelash. More collimated winds are however advocated by the lower detection rates of blueshifted optical or UV absorption-line features in sources of lower SFR at both low (Rupke, Veilleux, and Sanders 2005) and high-redshift (Kornei et al. 2012; Martin et al. 2012). Such a disparity could exist, should there be a difference in wind structure between those driven by AGN and starbursts, or those generated in the disturbed morphologies of late-stage mergers. Our measurements for the Cosmic Eyelash are consistent with the above literature, suggesting that in starburst-dominated sources it is likely that the SFR or $\Sigma_{\rm SFR}$ are primary determinants of the opening angle, with AGN contributing particularly to $v_{\rm max}$ (Figure 4.4). A systematic difference in opening angle may however be difficult to disentangle from both the wind velocity and occurrence rate as a function of various host galaxy properties, in particular $\Sigma_{\rm SFR}$, particularly if observational constraints restrict classification to those of the highest absorbed flux or $v_{\rm max}$.

Recent simulations have shown starburst-powered outflow rates of up to 1000 $\rm M_\odot\ yr^{-1}$ (Hopkins et al. 2013b), consistent with mass-loading factors, $\eta = \dot{M}_{\rm outflow}/{\rm SFR}$, which locally are of the order of a few and – as with $v_{\rm max}$ – exhibit a positive correlation with AGN luminosity (Feruglio et al. 2010; Cicone et al. 2014; González-Alfonso et al. 2014). At higher redshift, high-mass starbursting galaxies (of which SMGs are an important sub-population) may dominate the global gas mass returned to the IGM (Newman et al. 2012).

An estimate of the mass-outflow rate from the Cosmic Eyelash can be determined from the column density of ground-state OH molecules via a physical model, such as that presented in González-Alfonso et al. (2014), a modified version of which is now detailed.

Radially outflowing material occurs within a region surrounding a driving source at a radius $r > r' > R$, such that the OH column density $N_{\rm OH}(\Omega) = \int_r^R n_{\rm OH}(r', \Omega)\ {\rm d}r'$. Mass conservation then requires that $n_{\rm OH}(r', \Omega)\ r'^2\ v(r', \Omega)$ (where $v(r')$ is the OH velocity at radius r') is constant across r' at any Ω, leading to the mass outflow rate

$$\dot{M} = m_{\rm H_2}\, X_{\rm OH}^{-1}\, n_{\rm OH}(r)\, r^2\, v(r) \int w(\Omega)\ {\rm d}\Omega, \tag{4.1}$$

where $m_{\rm H_2}$ is the mass of a hydrogen molecule, $X_{\rm OH} = n_{\rm OH}/n_{\rm H_2}$ and the angular dependence has been moved to a factor $w(\Omega)$. To find a functional form for this equation, the mass conservation at r can be expressed as a function of the column density $N_{\rm OH}$ via the use of a simple linear

velocity model $v(r') = v + \frac{V-v}{R-r}(r' - r)$, where $v = v(r)$ and $V = v(R)$, resulting in

$$n_{\mathrm{OH}} r^2 v = N_{\mathrm{OH}} \frac{Rv - rV}{R - r} \left[\frac{1}{r} - \frac{1}{R} + \frac{V - v}{Rv - rV} \ln\left(\frac{Vr}{vR}\right) \right]^{-1}. \tag{4.2}$$

To complete this model we derive an estimate of the column density from the observed absorption, based on the derivation presented at
https://safe.nrao.edu/wiki/pub/Main/MolInfo/ColumnDensityCalculation-MangumShirley.pdf.

Starting from the definition of optical depth $\mathrm{d}\tau_\nu = \kappa_\nu \, \mathrm{d}s$, and expanding the absorption coefficient κ in terms of the population densities n_1 and n_2 in levels 1 and 2 respectively, the stimulated radiation coefficients B_{12} and B_{21}, and the line profile function ϕ_ν, we obtain

$$\tau_\nu = \phi_\nu \frac{h\nu}{4\pi} \int (n_1 B_{12} - n_2 B_{21}) \, \mathrm{d}s. \tag{4.3}$$

Using the relationship between the Einstein rate coefficients and the level degeneracies $g_1 B_{12} = g_2 B_{21}$, B_{21} and n_2 can be factored out

$$\tau_\nu = \phi_\nu \frac{h\nu}{4\pi} B_{21} \int n_2 \left(\frac{g_2}{g_1} \frac{n_1}{n_2} - 1 \right) \mathrm{d}s, \tag{4.4}$$

and assuming a constant temperature and level densities consistent with thermal equilibrium $\frac{n_2}{n_1} = \frac{g_2}{g_1} \exp\left(-\frac{h\nu}{k_{\mathrm{B}} T}\right)$

$$\tau_\nu = \phi_\nu \frac{h\nu}{4\pi} B_{21} \left[\exp\left(\frac{h\nu}{k_{\mathrm{B}} T}\right) - 1 \right] \int n_2 \, \mathrm{d}s. \tag{4.5}$$

Integrating over the line profile $\int \phi_\nu \, \mathrm{d}\nu = 1$, and rearranging to calculate the column density $N_2 = \int n_2 \, \mathrm{d}s$,

$$N_2 = \frac{4\pi}{h\nu} \frac{1}{B_{21}} \left[\exp\left(\frac{h\nu}{k_{\mathrm{B}} T}\right) - 1 \right]^{-1} \int \tau_\nu \, \mathrm{d}\nu. \tag{4.6}$$

As the system is in thermal equilibrium, N_2 is related to the total OH column density by $\frac{N_{\mathrm{total}}}{N_2} = \frac{Q}{g_2} \exp\left(\frac{E_2}{k_{\mathrm{B}} T}\right)$ where Q is the *partition function*: the sum of the probabilities of a system being in each possible state, giving

$$N_{\mathrm{total}} = \frac{4\pi}{h\nu} Q \frac{1}{B_{21}} \frac{1}{g_2} \frac{\exp\left(\frac{E_2}{k_{\mathrm{B}} T}\right)}{\exp\left(\frac{h\nu}{k_{\mathrm{B}} T}\right) - 1} \int \tau_\nu \, \mathrm{d}\nu. \tag{4.7}$$

Several parametrisations can now be introduced to reformulate this expression into a function of T and ν. The stimulated emission coefficient B_{21} can be more fundamentally represented in terms of the dipole matrix element μ_{12}, via its relationship to the spontaneous emission coefficient $A_{21} = \frac{64\pi^4 \nu^3}{3h{c_0}^3} |\mu_{12}|^2$ and the definition $A_{21} = \frac{2h\nu^3}{{c_0}^2} B_{21}$.

Assuming no interactions between possible excitation state types, the total energy is the sum of the energy possessed in each of these types, and hence the partition function is a product of the

partition function for each state type, which for molecules is

$$Q = \sum_i g_i \exp\left(-\frac{E_i}{k_\mathrm{B}T}\right) = Q_\mathrm{electronic}\, Q_\mathrm{vibrational}\, Q_\mathrm{rotational}\, Q_\mathrm{nuclear}. \tag{4.8}$$

The $^2\Pi_{3/2}$ $J = \frac{3}{2} \rightarrow \frac{5}{2}$ transition is low-energy and rotational, so OH is in the ground electronic ($Q_\mathrm{electronic} = 1$) and vibrational ($Q_\mathrm{vibrational} = 1$) states,

$$Q = Q_\mathrm{rotational}\, Q_\mathrm{nuclear} = \sum_{J,K,I} g_J\, g_K\, g_I \exp\left(-\frac{E_{JK}}{k_\mathrm{B}T}\right), \tag{4.9}$$

where the total energy level degeneracy level has been expanded as a product of the rotational (g_J and g_K) and spin (g_I) degeneracies. For all molecules $g_J = 2J + 1$, for linear molecules $g_K = 1$, and for non-identical nuclei $g_I = 1$, so

$$Q = \sum_{J=0}^{\infty} (2J+1) \exp\left(-\frac{E_{JK}}{k_\mathrm{B}T}\right) \simeq \frac{k_\mathrm{B}T}{hB_0} \exp\left(\frac{hB_0}{3k_\mathrm{B}T}\right) \tag{4.10}$$

where the latter expression is an approximation derived by McDowell (1988).

As we are considering outflowing gas, a change to integration of optical depth over velocity via $\frac{\mathrm{d}\nu}{\nu} = \frac{\mathrm{d}v}{c_0}$ is also useful.

Applying these three parametrisations gives

$$N_\mathrm{total} = \frac{3h}{8\pi^3 S\mu^2} \frac{1}{g_2} \frac{k_\mathrm{B}}{hB_0} T \frac{\exp\left[\frac{1}{T}\left(\frac{E_2}{k_\mathrm{B}} + \frac{hB_0}{3k_\mathrm{B}}\right)\right]}{\exp\left(\frac{h\nu}{k_\mathrm{B}T}\right) - 1} \int \tau_\nu \,\mathrm{d}v, \tag{4.11}$$

and finally applying specific numerical values for OH,

$$\frac{N_\mathrm{OH}}{\mathrm{cm}^{-2}} = 6.7 \times 10^{10} \left(\frac{T_\mathrm{ex}}{\mathrm{K}}\right) \frac{\exp\left(\frac{130\,\mathrm{K}}{T_\mathrm{ex}}\right)}{\exp\left(\frac{121\,\mathrm{K}}{T_\mathrm{ex}}\right) - 1} \left(\frac{\int \tau(v)\,\mathrm{d}v}{\mathrm{km\,s^{-1}}}\right). \tag{4.12}$$

This is plotted in Figure 4.5.

Physically motivated model parameter values are: $X_\mathrm{OH} = 5 \times 10^{-6}$ (Goicoechea and Cernicharo 2002), $\int w(\Omega)\,\mathrm{d}\Omega = \frac{2}{3} \times 4\pi$, $r = 100\,\mathrm{pc}$ (motivated by the size of components 'X' and 'Y'; Swinbank et al. 2011), $R = 200\,\mathrm{pc}$, $v(r) = v = 670\,\mathrm{km\,s^{-1}}$, $v(R) = V = 100\,\mathrm{km\,s^{-1}}$ and $\int_{-670}^{-100} \tau(v)\,\mathrm{d}v = 2000\,\mathrm{km\,s^{-1}}$. Danielson et al. (2013) determine a kinetic temperature $T_\mathrm{K} = 200\,\mathrm{K}$ within component 'X', however as described in Section 1.2.1.2, the OH radical will be subthermally excited to a much lower temperature. The incident 119 µm radiation field may even dominate, providing 121 K as an upper limit to the excitation temperature. The observed 119 µm absorption therefore suggests a maximum mass-outflow rate of $55\,\mathrm{M_\odot\,yr^{-1}}$, and hence a mass loading $\lesssim$0.8 for the $70\,\mathrm{M_\odot\,yr^{-1}}$ SFR of CO clump 'X' (Swinbank et al. 2011). We note that the above parameters are determined only poorly and mass-outflow rates estimated from this single transition are likely to be extremely uncertain. Particularly insecure are the estimates

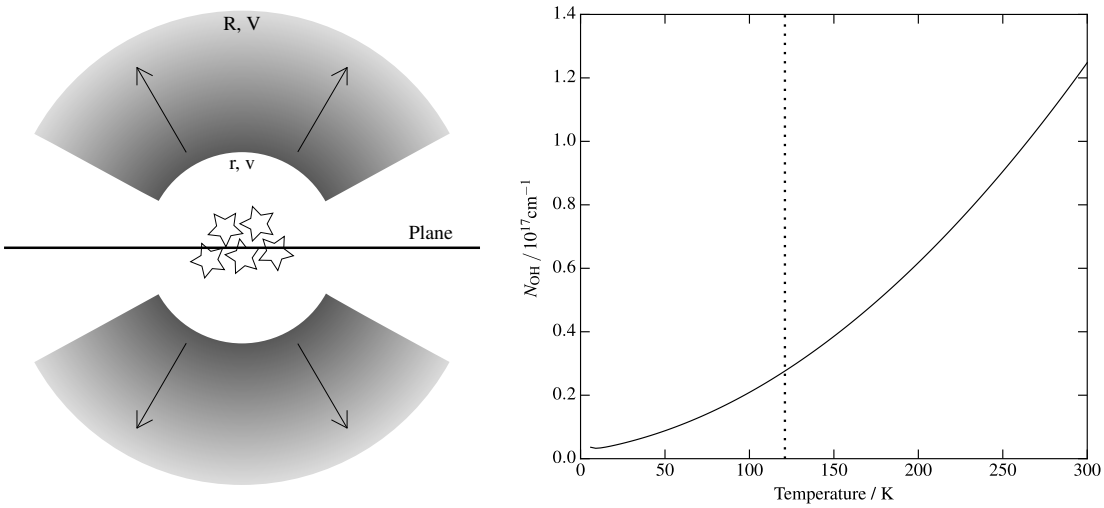

Figure 4.5. *Left:* Geometry of the model used, with the opening angle being approximated as $\int w(\Omega)\,\mathrm{d}\Omega = \frac{2}{3}\times 4\pi$. *Right* Temperature dependence of the OH column density calculated from an integrated optical depth. As the temperature increases, the populations of upper levels become subsequently larger at the expense of that of the ground state $^2\Pi_{3/2}\ J = \frac{3}{2}\ \rightarrow$, reducing the column density. A dotted line is shown at 121 K, the temperature assumed for the outflow in the mass calculation.

of temperature, integrated optical depth and X_{OH}: a lower excitation temperature increases the fraction of OH in the ground state and hence available to absorb incident photons (Figure 4.5), and the OH abundance was determined from local GMCs, whereas this outflow may be launched from a region dominated by atomic gas, and the outflow likely contains multiple phases regardless.

The estimated mass-outflow rate contributes sub-dominantly to the total gas-reduction rate, which is primarily by star-formation (300 $\mathrm{M}_\odot$/yr, estimated from the rest-frame 8 – 1000 µm luminosity of Ivison et al. 2010c, corrected for the more recent lensing amplification Swinbank et al. 2011 and using the relation of Murphy et al. 2011b). This suggests that the $2.5\times10^{10}\,\mathrm{M}_\odot$ of molecular gas within the Cosmic Eyelash (Danielson et al. 2013), will be exhausted on a time-scale of ≈60 Myr, primarily through star-formation, but as we note above, the calculated mass-outflow rate is extremely uncertain. high-redshift SMGs are conjectured to have duty cycles of ≈100 Myr (e.g. Hickox et al. 2012; Bothwell et al. 2013), comparable to that estimated here for molecular gas removal, suggesting little conversion of atomic to molecular gas, or gas input from the IGM.

The velocity required for outflowing gas to become unbound or to join the hot intracluster medium cannot be determined reliably without knowledge of the dark-matter halo mass and the location of the Cosmic Eyelash within that halo. However, utilising the estimated stellar mass, $M_\star = 3\times10^{10}\,\mathrm{M}_\odot$ (Swinbank et al. 2010b), alongside table 7 from Moster et al. (2010), suggests $M_{\mathrm{DM}}(r_{\mathrm{vir}}) = 2\times10^{12}\,\mathrm{M}_\odot$. This value neglects potential SMG clustering (e.g. Hickox et al. 2012) so may underestimate the true halo mass. The escape velocity from a dark-matter halo with a Navarro–Frenk–White profile (Navarro, Frenk, and White 1997) with this virial mass, a virial radius of 100 kpc and a concentration parameter $c = 10$, is ∼1000 km s^{-1}, somewhat higher than the v_{max} calculated above for the Cosmic Eyelash, supporting the suggestion that AGN are required for full expulsion of interstellar material from massive galaxies. star-formation-

powered outflows such as the one we have found in the Cosmic Eyelash are likely unable to escape the dark-matter halo and may merely serve to maintain the elevated SFR of SMGs though a fountain mechanism.

4.4 Conclusions

We present the first detection of OH absorption in a high-redshift galaxy, exploiting the SPIRE FTS aboard *Herschel*, and interpret this as a starburst-driven molecular outflow.

We additionally detect emission lines of [C II], [N II], [O III] and [O I], finding line luminosities similar to local ULIRGs and indicative of a significant contribution to the [C II] luminosity from H II regions. PDR models indicate n and G_0 values of $10^{2–3}$ cm^{-3} and $10^{2–3}$ Habing fields, respectively.

The 119 µm OH absorption is blueshifted by $(240 \pm 110)\,\mathrm{km\,s^{-1}}$ relative to the star-forming clump, 'X', pinpointed previously by low-J CO observations, and which we associate with the observed [N II] [O III] emission. This molecular component to a starburst-driven wind, possesses a maximum velocity of $(700 \pm 200)\,\mathrm{km\,s^{-1}}$, smaller than the escape velocity expected for the dark-matter halo. A large fraction of the available molecular gas could thus be converted into stars via a burst protracted by the resulting gas fountain, until an AGN-driven outflow can eject the remaining gas.

4.5 Subsequent work

Since publication of this work, another observation of star-formation-driven outflowing molecular gas in a $z > 0$ galaxy has been presented in Geach et al. (2014). While the redshift is lower at $z = 0.7$, the mass outflow rate is similar at $(80 \pm 25)\,\mathrm{M_\odot yr^{-1}}$ and also arises from a compact region of high star-formation surface density.

Chapter 5

Measurement and stacking of the full dataset

This chapter presents the full set of 45 SPIRE spectra described in Chapter 2, along with the corresponding PACS mini scan maps. Through analysis of the dataset as a whole, constraints may be placed on the strengths of faint spectral lines, and through stacks of the spectra, gas properties can be derived as a function of redshift, infrared luminosity and dust temperature.

5.1 Spectral energy distributions and dust emission

The comparative ease with which broad-band continuum imaging of a galaxy may be obtained, and the limited detail revealed from SED fitting to the few data points used for selection makes multi-wavelength follow-up of a source a critical first step toward a more thorough understanding.

As described in Chapter 2, the sample of galaxies used in this thesis was selected from their *Herschel* SPIRE 250, 350 and 500 µm flux densities. The SPIRE colours and redshifts are displayed in Figure 5.1, appearing relatively similar to the Cosmic Eyelash at their respective redshift although typically with greater $S_{250\,\mu\mathrm{m}}/S_{350\,\mu\mathrm{m}}$ and $S_{350\,\mu\mathrm{m}}/S_{500\,\mu\mathrm{m}}$ ratios than that system. This is expected due to the very high magnification factor experienced by the the Cosmic Eyelash, which allows a less-extreme galaxy with a lower SFR and therefore likely lower dust temperature to reach flux densities comparable to the others within this sample.

The redshift distribution of strongly-lensed DSFGs predicted by Negrello et al. (2007) has a higher mean value than observed in our sample (see inset of Figure 5.1). This is likely due to the different flux density cuts used, with our $S_{350\,\mu\mathrm{m}} > 200$ mJy subsample of the lens candidates preferentially selecting lower redshift objects than the $S_{500\,\mu\mathrm{m}} > 100$ mJy used in that work.

5.1.1 100 and 160 µm flux density measurements

To complement the SPIRE measurements across the flux density peak and provide stronger constraints of the rest-frame MIR, which is a good AGN diagnostic, 100 and 160 µm PACS mini

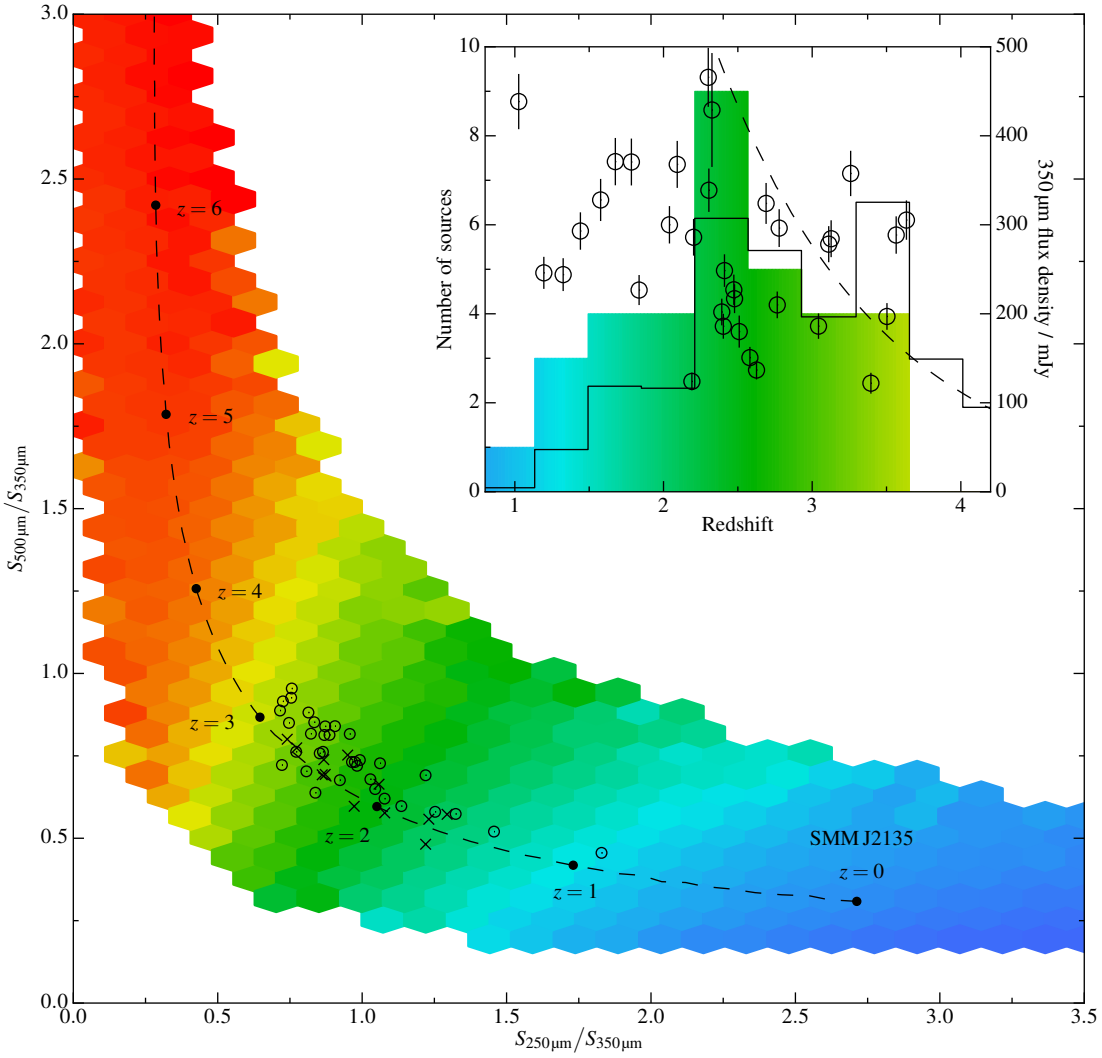

Figure 5.1. *Herschel* SPIRE flux density ratios of the sample. Sources with known redshifts are displayed as empty circles, those without as crosses. Underlaid are a dashed line displaying the expected flux density ratios of the Cosmic Eyelash with changing redshift determined from the SED presented in Ivison et al. (2010c), and shading displaying the observed colours of 1e8 grey-body-emitting sources with a range of redshifts, dust temperatures, dust masses, dust spectral emissivity indices and a flux density measurement uncertainty of 10 %, based on Figure 1 of Amblard et al. (2010).
Inset: Redshift distribution of sources in the sample. The shaded histogram displays the number of sources within our sample in redshift bins of $\Delta z = 0.36$, and the area under the solid line displays the predicted redshift distribution of strongly lensed DSFGs with $\{S_{250\,\mu m}, S_{350\,\mu m}, S_{500\,\mu m}\} > 100$ mJy from Negrello et al. (2007) scaled to the same number of sources. Overplotted circles show the 350 μm flux densities of those sources included in the redshift distribution, with vertical lines showing uncertainties. The dashed line represents the 350 μm flux density expected to be observed from an Eyelash-like galaxy at different redshifts, indicating that the $z > 3$ galaxies in our sample are on average not only brighter after lensing but much more intrinsically luminous than that object, as the lensing amplifications experienced will likely not be higher than the value of 37.5 ± 4.5 in that system.

scan maps of each source were obtained and processed as described in Chapter 2. Archival PACS mini scan imaging of the Cosmic Eye covered the Cosmic Eyelash, and so were additionally processed and then combined with our two scans to produce a deeper image, particularly useful as this field has the largest number of sources visible in the region around the target galaxy.

Measured flux densities are shown in Table 5.1 along with their SPIRE 250, 350 and 500 µm and SMA 880 µm measurements, these latter primarily from Bussmann et al. (2013).

Source	z	Amplification	$S_{100\,\mu m}$ / mJy	$S_{160\,\mu m}$ / mJy	$S_{250\,\mu m}$ / mJy	$S_{350\,\mu m}$ / mJy	$S_{500\,\mu m}$ / mJy	$S_{880\,\mu m}$ / mJy
SDP.9	1.577	8.8 ± 2.2	300 ± 15	515 ± 23	478 ± 34	328 ± 24	171 ± 14	24.8 ± 3.3
SDP.11	1.784	10.9 ± 1.3	134 ± 10	335 ± 24	421 ± 30	371 ± 26	221 ± 17	30.6 ± 2.4
SDP.17	2.3050	4.9 ± 0.7	66 ± 7	215 ± 19	354 ± 25	339 ± 24	220 ± 17	54.7 ± 3.1
SDP.81	3.0425	15.9 ± 0.7^{D}	–	51 ± 5	133 ± 11	186 ± 14	165 ± 14	78.4 ± 8.2
SDP.130	2.6256	2.1 ± 0.3	–	45 ± 8	118 ± 9	137 ± 11	104 ± 9	36.7 ± 3.9
G09-v1.40	2.0923	15.3 ± 3.5	65 ± 4	245 ± 13	396 ± 28	368 ± 26	228 ± 17	61.4 ± 2.9
G09-v1.97	3.634	6.9 ± 0.6	16 ± 3	125 ± 15	249 ± 18	305 ± 22	269 ± 20	85.5 ± 4.0
G09-v1.124	2.4101	1.1 ± 0.1	34 ± 7	140 ± 24	217 ± 16	249 ± 18	209 ± 16	50.0 ± 3.5
G09-v1.326	2.5812	5.0 ± 1.0^{H}	23 ± 3	80 ± 15	126 ± 10	151 ± 12	128 ± 11	18.8 ± 1.6
G12-v2.30	3.2588	9.5 ± 0.6	47 ± 11	180 ± 30	317 ± 23	358 ± 25	291 ± 21	86.0 ± 4.9
G12-v2.43	3.1275	17.0 ± 11.0^{H}	58 ± 3	171 ± 11	279 ± 20	284 ± 21	205 ± 16	48.6 ± 2.3
G12-v2.257	2.1909	13.0 ± 7.0^{H}	22 ± 6	87 ± 18	119 ± 9	124 ± 10	101 ± 9	–
G15-v2.19	1.026	9.7 ± 0.7^{M}	820 ± 24	1140 ± 53	802 ± 56	438 ± 31	200 ± 15	–
G15-v2.235	2.4778	1.8 ± 0.3	31 ± 5	87 ± 6	189 ± 14	217 ± 16	176 ± 14	33.3 ± 2.6
NA.v1.56	2.3010	11.7 ± 0.9	74 ± 4	265 ± 19	462 ± 33	466 ± 33	343 ± 25	73.1 ± 2.4
NA.v1.144	2.2024	4.4 ± 0.8	57 ± 6	185 ± 10	294 ± 21	286 ± 21	194 ± 15	36.8 ± 2.9
NA.v1.177	2.778	–	40 ± 3	158 ± 14	268 ± 19	296 ± 21	249 ± 18	50.1 ± 2.1
NA.v1.186	1.8358	–	55 ± 6	142 ± 9	241 ± 18	227 ± 17	165 ± 13	–
NB.v1.43	1.676	2.8 ± 0.4	40 ± 4	175 ± 24	342 ± 25	371 ± 27	251 ± 19	30.2 ± 2.2
NB.v1.78	3.1112	13.0 ± 1.5	82 ± 4	210 ± 16	271 ± 20	278 ± 20	203 ± 16	59.2 ± 4.3
NC.v1.143	3.565	11.3 ± 1.7	22 ± 3	94 ± 8	209 ± 16	289 ± 21	264 ± 20	97.2 ± 6.5
SA.v1.44	1.5^{p}	–	82 ± 6	200 ± 14	252 ± 18	207 ± 15	100 ± 9	–
SA.v1.53	1.654^{f}	–	57 ± 3	170 ± 23	194 ± 16	200 ± 17	119 ± 14	–

Continues

Table 5.1. FIR continuum flux densities of the sample. 250, 350 and 500 µm data from *H*-ATLAS and *Her*MES, uncertainties include a 7 % calibration uncertainty (Swinyard et al. 2010; Bendo et al. 2013). 100 and 160 µm uncertainties include 2.75 % and 4.25 % calibration uncertainties respectively (PACS Photometer - Point-Source Flux Calibration document 2011, a copy of which may be found at http://herschel.esac.esa.int/twiki/pub/Public/PacsCalibrationWeb/pacs_bolo_fluxcal_report_v1.pdf). 880 µm data from Bussmann et al. (2013) and Swinbank et al. (2010b). Where not otherwise noted, amplification values are taken from (Bussmann et al. 2013).
[p] guess from photometric data alone.
[f] guess from a possible (low significance) spectral feature and photometric data.
[D] ALMA Partnership et al. (2015)
[H] Estimate from CO line luminosity and FWHM from Harris et al. (2012)
[M] Messias et al. (2014)
[S] Swinbank et al. (2011)

Table 5.1. Continued

Source	z	Amplification	$S_{100\,\mu m}$ / mJy	$S_{160\,\mu m}$ / mJy	$S_{250\,\mu m}$ / mJy	$S_{350\,\mu m}$ / mJy	$S_{500\,\mu m}$ / mJy	$S_{880\,\mu m}$ / mJy
SB.v1.143	2.7[p]	–	17 ± 5	90 ± 15	176 ± 13	227 ± 17	176 ± 14	–
SB.v1.202	2.318[f]	–	30 ± 10	78 ± 17	154 ± 12	178 ± 13	123 ± 11	–
SC.v1.128	2.4[p]	–	25 ± 5	115 ± 13	213 ± 16	244 ± 18	169 ± 13	–
SD.v1.70	1.854[f]	–	133 ± 11	335 ± 23	353 ± 25	273 ± 20	156 ± 13	–
SD.v1.133	1.600[f]	–	125 ± 15	223 ± 22	237 ± 17	193 ± 15	108 ± 10	–
SD.v1.328	2.7[p]	–	8 ± 4	70 ± 9	138 ± 11	186 ± 14	149 ± 12	–
SE.v1.165	3.2[p]	–	31 ± 3	112 ± 9	171 ± 13	197 ± 15	146 ± 12	–
SF.v1.88	1.929[f]	–	60 ± 5	160 ± 9	268 ± 19	253 ± 19	168 ± 14	–
SF.v1.100	2.8[p]	–	46 ± 3	131 ± 9	258 ± 19	271 ± 20	204 ± 16	–
SG.v1.77	2.2[p]	–	51 ± 3	150 ± 14	238 ± 18	220 ± 17	127 ± 13	–
HeLMS05	1.195	–	80 ± 8	216 ± 15	300 ± 22	246 ± 18	170 ± 15	–
HeLMS06	2.5093	–	11 ± 3	70 ± 10	130 ± 15	180 ± 18	130 ± 15	–
HeLMS09	2.3920	–	25 ± 3	83 ± 15	163 ± 13	202 ± 15	142 ± 12	–
HeLMS44	2.6900	–	16 ± 6	140 ± 14	250 ± 18	324 ± 23	247 ± 19	–
HeLMS45	2.4730	–	32 ± 3	125 ± 7	219 ± 16	227 ± 17	166 ± 13	–
HeLMS49	1.441	–	125 ± 6	320 ± 20	367 ± 25	293 ± 21	170 ± 14	–
HeLMS51	2.7650	–	26 ± 3	120 ± 12	176 ± 13	210 ± 15	134 ± 11	–
HeLMS61	2.4024	–	16 ± 3	55 ± 8	153 ± 12	186 ± 14	152 ± 13	–
HeLMS62	3.503	–	3 ± 3	66 ± 7	149 ± 12	197 ± 15	188 ± 15	–
HBoötes03	1.325	3.0 ± 1.5	108 ± 5	275 ± 16	323 ± 23	244 ± 18	140 ± 34	18.4 ± 2.5
HXMM02	3.39	4.4 ± 1.0	14 ± 3	56 ± 11	92 ± 10	122 ± 12	113 ± 11	66.0 ± 5.4
MACSJ2043	2.04	–	–	–	224 ± 17	300 ± 21	255 ± 19	–
Eyelash	2.32591	37.5 ± 4.5[S]	25 ± 3	131 ± 7	366 ± 55	429 ± 64	325 ± 49	106.0 ± 12.0

5.1.2 SED fits

To estimate stellar and dust properties of the sources, we modelled the spectral energy distribution of their infrared emission. As in Chapter 3 we use the method presented in Kovács et al. (2010), a detailed description of which is given in Section 3.5, which models the mass of dust M_d emitting at a temperature T by a thermally-motivated power law, $\frac{d\,M_d}{dT} \propto T^{-\gamma}$. For consistency, all sources are modelled using with this method, regardless of previous independent determinations of their SED.

Following the results of a study of unlensed high-redshift DSFGs fit using this model (Magnelli et al. 2012) the dust mass power law index γ is fixed as 7.2 ± 0.3: the value best fitting local starbursts (see Kovács et al. 2010); the dust spectral emissivity index β is fixed as 2.0 ± 0.2: the true value however likely varies inversely with temperature (see Section 1.2.2); and the synchrotron spectral index is fixed as -0.75 ± 0.20 for objects with fewer than two photometric measurements at $\lambda_{rf} > 4$ mm. Gravitational amplification values are primarily taken from (Bussmann et al. 2013) which are derived from SMA data and used in preference to values

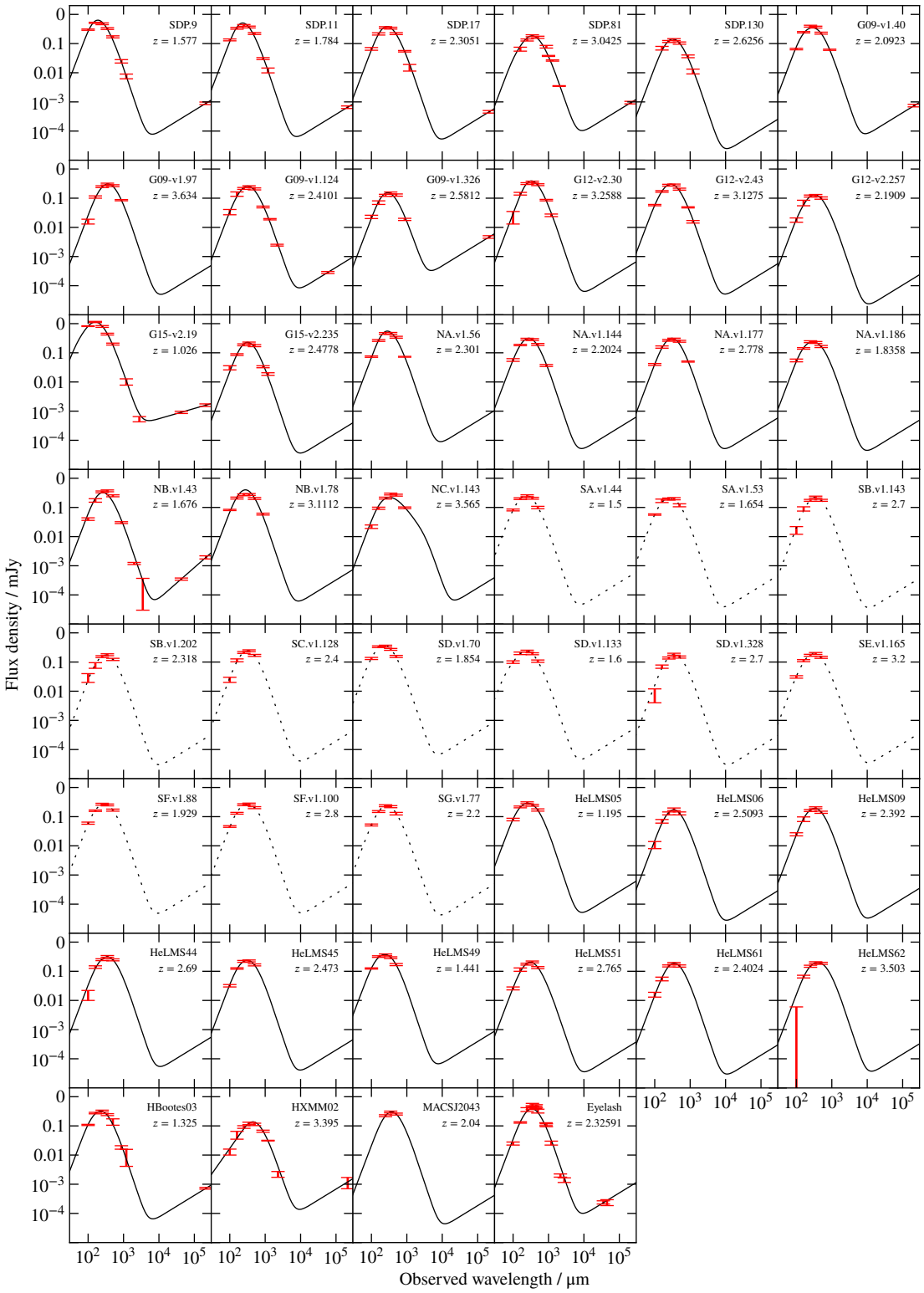

Figure 5.2. SED fits to available FIR–radio photometry for objects in the sample, using the power-law dust temperature distribution model of Kovács et al. (2010). Sources selected from the *H*-ATLAS SGP field do not have secure redshifts and fits for these objects are performed assuming a best-guess redshift and are shown as a dotted line.

derived from NIR imaging (e.g. Calanog et al. 2014; Dye et al. 2014), due to the likelihood of a physical separation (and hence amplification difference) of the starburst and existing stellar population (Fu et al. 2012; Dye et al. 2015). Source-plane physical extents are also taken where possible from Bussmann et al. (2013), and otherwise assumed to have a diameter of 3 ± 2 kpc for all objects except the known HyLIRG G09-v1.124 which is modelled with a diameter 22 ± 3 kpc (Ivison et al. 2013). The available photometry measurements and our fits are shown in Figure 5.2.

Source	Amplification	μM_{H_2}	μL_{IR}	L_{IR}	SFR	M_d	$T_{d;cutoff}$	q_{IR}
		/ 10^{11} $M_\odot$	/ 10^{12} $L_\odot$	/ 10^{12} $L_\odot$	/ $M_\odot$ yr^{-1}	/ 10^8 $M_\odot$	/ K	
SDP.9	8.8 ± 2.2	1.9	65.5 ± 2.4	7.4 ± 1.9	1100 ± 300	2.5 ± 1.0	35.1 ± 3.4	2.54 ± 0.10
SDP.11	10.9 ± 1.3	2.4	57.7 ± 2.3	5.3 ± 0.7	800 ± 100	3.1 ± 0.9	34.0 ± 1.6	2.52 ± 0.10
SDP.17	4.9 ± 0.7	4.3	73.4 ± 3.1	15.0 ± 2.2	2200 ± 300	13.9 ± 4.2	27.5 ± 1.7	2.51 ± 0.12
SDP.81	15.9 ± 0.7	3.8	57.1 ± 4.0	3.6 ± 0.3	500 ± 50	2.6 ± 0.5	38.8 ± 3.8	1.81 ± 0.13
SDP.130	2.1 ± 0.3	1.7	32.9 ± 2.8	15.7 ± 2.5	2300 ± 400	23.6 ± 6.6	24.8 ± 1.4	–
G09-v1.40	15.3 ± 3.5	3.3	61.0 ± 2.1	4.0 ± 0.9	600 ± 130	3.2 ± 1.0	43.2 ± 2.9	2.28 ± 0.11
G09-v1.97	6.9 ± 0.6	5.0	142.2 ± 6.0	20.6 ± 2.0	3100 ± 300	5.8 ± 1.9	46.0 ± 1.6	–
G09-v1.124	1.1 ± 0.1	2.2	51.8 ± 4.9	47.1 ± 5.9	7000 ± 900	97.2 ± 12.6	23.0 ± 1.6	2.09 ± 0.22
G09-v1.326	5.0 ± 1.0^{H}	2.7	36.4 ± 1.9	7.3 ± 1.5	1100 ± 200	5.3 ± 1.7	28.8 ± 4.4	1.08 ± 0.12
G12-v2.30	9.5 ± 0.6	7.1	134.8 ± 7.0	14.2 ± 1.2	2100 ± 170	6.3 ± 1.8	33.9 ± 1.2	–
G12-v2.43	17.0 ± 11.0^{H}	1.3	127.6 ± 3.8	7.5 ± 4.8	1100 ± 700	2.4 ± 1.6	31.3 ± 3.0	–
G12-v2.257	13.0 ± 7.0^{H}	1.4	21.4 ± 1.2	1.6 ± 0.9	250 ± 130	5.7 ± 3.7	20.7 ± 2.3	–
G15-v2.19	9.0 ± 1.0	2.9	54.8 ± 2.0	5.7 ± 0.5	800 ± 100	2.5 ± 0.8	34.7 ± 1.9	2.78 ± 0.07
G15-v2.235	1.8 ± 0.3	3.5	44.1 ± 1.8	24.5 ± 4.2	3700 ± 600	20.5 ± 6.0	34.6 ± 1.8	–
NA.v1.56	11.7 ± 0.9	5.8	96.8 ± 4.4	8.3 ± 0.8	1200 ± 110	6.7 ± 1.8	30.6 ± 1.7	–
NA.v1.144	4.4 ± 0.8	1.8	56.1 ± 2.1	12.7 ± 2.4	1900 ± 400	6.7 ± 2.2	40.4 ± 3.7	–
NA.v1.177	[a]	4.2	87.5 ± 3.0	31.2 ± 23.8	4700 ± 3600	11.1 ± 8.4	42.4 ± 3.2	–
NA.v1.186	[a]	3.6	30.0 ± 1.3	25.0 ± 18.4	3700 ± 2700	44.7 ± 42.5	39.0 ± 2.2	–
NB.v1.43	2.8 ± 0.4	3.6	29.9 ± 1.3	10.7 ± 1.6	1600 ± 200	24.4 ± 4.9	23.7 ± 1.2	1.67 ± 0.09
NB.v1.78	13.0 ± 1.5	4.6	159.8 ± 7.2	12.3 ± 1.4	1800 ± 200	1.5 ± 0.5	50.8 ± 4.4	–
NC.v1.143	11.3 ± 1.7	6.2	129.0 ± 6.1	11.4 ± 1.9	1700 ± 300	59.3 ± 64.1	56.4 ± 3.7	–
SA.v1.44	[p]	–	22.3 ± 0.9	0.8 ± 0.8	120 ± 130	1.7 ± 1.7	22.9 ± 2.1	–
SA.v1.53	[f]	–	22.2 ± 0.8	27.4 ± 19.8	4100 ± 3000	38.8 ± 33.2	39.9 ± 1.9	–

Continues

Table 5.2. Properties from the SED fits described in Section 5.1.2. In addition, H_2 masses from CO measurements are shown, taken from Iono et al. (2006, 2012), Frayer et al. (2011), Fu et al. (2012), Harris et al. (2012), Lupu et al. (2012), Danielson et al. (2013), Ivison et al. (2013), and Messias et al. (2014) and several unpublished measurements primarily from CARMA and PdBI. These were converted to $L_{CO\,J=1\rightarrow0}$ where necessary by the brightness temperature ratios given in Bothwell et al. (2013), and then to a molecular gas mass via a conversion factor of $0.8\,M_\odot(\mathrm{K\ km\ s^{-1}\ pc^2})^{-1}$. Note that the SED fits utilise other available flux density measurements in addition to those displayed in Table 5.1. SFR calculations follow Murphy et al. (2011b).
[H] amplification estimate from CO line luminosity and FWHM from Harris et al. (2012).
[a] amplification fit a dust emission radius of (1.5 ± 1.0) kpc.
[p] redshift guess from photometric data alone, in addition to the assumed area of [a].
[f] redshift guess from a possible (low significance) spectral feature and photometric data, in addition to the assumed area of [a].

Table 5.2. Continued

Source	Amplification	μM_{H_2} / 10^{11} $M_\odot$	μL_{IR} / 10^{12} $L_\odot$	L_{IR} / 10^{12} $L_\odot$	SFR / $M_\odot$ yr^{-1}	M_d / 10^8 $M_\odot$	$T_{d;cutoff}$ / K	q_{IR}
SB.v1.143	p	–	51.9 ± 3.2	20.1 ± 16.5	3000 ± 2500	17.9 ± 16.3	37.7 ± 3.7	–
SB.v1.202	f	–	32.5 ± 3.1	23.8 ± 20.5	3600 ± 3100	22.9 ± 21.1	39.0 ± 4.5	–
SC.v1.128	p	–	46.5 ± 2.4	19.2 ± 15.3	2900 ± 2300	16.6 ± 14.3	37.3 ± 3.2	–
SD.v1.70	f	–	58.9 ± 2.8	1.4 ± 1.5	200 ± 200	1.1 ± 1.1	26.7 ± 2.6	–
SD.v1.133	f	–	30.3 ± 3.9	0.3 ± 0.4	40 ± 60	0.5 ± 0.7	21.9 ± 2.0	–
SD.v1.328	p	–	42.1 ± 2.7	20.2 ± 16.3	3000 ± 2400	20.9 ± 19.5	37.6 ± 3.4	–
SE.v1.165	p	–	85.2 ± 3.3	1.7 ± 1.7	250 ± 300	0.9 ± 0.9	28.5 ± 2.9	–
SF.v1.88	f	–	37.3 ± 1.4	27.6 ± 20.3	4100 ± 3000	30.7 ± 26.3	40.1 ± 2.3	–
SF.v1.100	p	–	85.4 ± 2.8	53.7 ± 39.4	8000 ± 5900	25.6 ± 24.6	47.4 ± 2.8	–
SG.v1.77	p	–	45.7 ± 1.7	1.3 ± 1.3	190 ± 200	1.4 ± 1.4	25.6 ± 2.4	–
HeLMS05	a	–	14.1 ± 0.6	13.8 ± 10.2	2100 ± 1500	56.5 ± 50.4	33.5 ± 1.9	–
HeLMS06	a	–	33.1 ± 2.2	14.1 ± 12.1	2100 ± 1800	16.1 ± 15.0	34.8 ± 3.8	–
HeLMS09	a	–	37.6 ± 1.8	22.6 ± 17.2	3400 ± 2600	22.7 ± 19.8	38.5 ± 3.0	–
HeLMS44	a	–	76.9 ± 4.4	25.9 ± 20.0	3900 ± 3000	21.1 ± 18.9	39.9 ± 3.0	–
HeLMS45	a	–	52.9 ± 1.9	29.9 ± 22.5	4500 ± 3400	18.6 ± 16.3	41.3 ± 2.8	–
HeLMS49	a	–	30.5 ± 1.0	26.2 ± 19.1	3900 ± 2900	28.6 ± 23.1	39.6 ± 2.0	–
HeLMS51	a	–	57.3 ± 2.6	2.0 ± 2.1	290 ± 300	1.7 ± 1.7	27.2 ± 2.9	–
HeLMS61	a	–	31.6 ± 1.6	10.5 ± 9.6	1600 ± 1400	17.3 ± 16.9	32.3 ± 4.1	–
HeLMS62	a	–	86.7 ± 7.5	42.5 ± 33.3	6300 ± 5000	29.5 ± 57.2	44.7 ± 3.3	–
HBoötes03	3.0 ± 1.5	1.0	21.0 ± 0.9	7.0 ± 3.4	1000 ± 500	6.9 ± 3.8	38.0 ± 6.2	2.30 ± 0.09
HXMM02	4.4 ± 1.0	3.4	58.4 ± 6.5	13.3 ± 3.3	2000 ± 500	26.2 ± 7.7	23.0 ± 2.3	1.51 ± 0.22
MACSJ2043	a	–	32.7 ± 4.2	6.1 ± 7.9	900 ± 1200	25.5 ± 30.7	28.1 ± 6.3	–
Eyelash	37.5 ± 4.5	5.6	62.3 ± 2.9	1.7 ± 0.2	250 ± 30	2.4 ± 0.6	33.3 ± 3.4	2.15 ± 0.26

Determined total infrared luminosities and dust masses are comparable to those obtained for these galaxies through other methods, such as via MAGPHYS (Negrello et al. 2014), or a single grey-body component (Bussmann et al. 2013). SFRs are however higher than those suggested by MAGPHYS due to the different calibrations used.

The lensed status of this sample however complicates the modelling of their SEDs, and in many cases differential amplification effects must be taken into account should optical–NIR flux density measurements be included (e.g. Negrello et al. 2014; Ma et al. 2015) as the starburst may not be cospatial with existing stellar populations (e.g. Fu et al. 2012; Dye et al. 2015).

These derived properties among others are detailed in Table 5.2.

Correlations and distributions of the fitted parameters are shown in Figure 5.3. Unsurprisingly, amplification factors tend to increase with redshift and decrease with increasing dust mass and L_{IR}, caused by the underlying luminosity and amplification probability distributions. The Cosmic Eyelash is an outlier here with its very high amplification factor. Without 850 µm or similar flux densities to constrain the Rayleigh-Jeans side of the dust peak, the uncertainty on cutoff dust temperatures is of order a few kelvin. The temperatures have a weak positive trend with

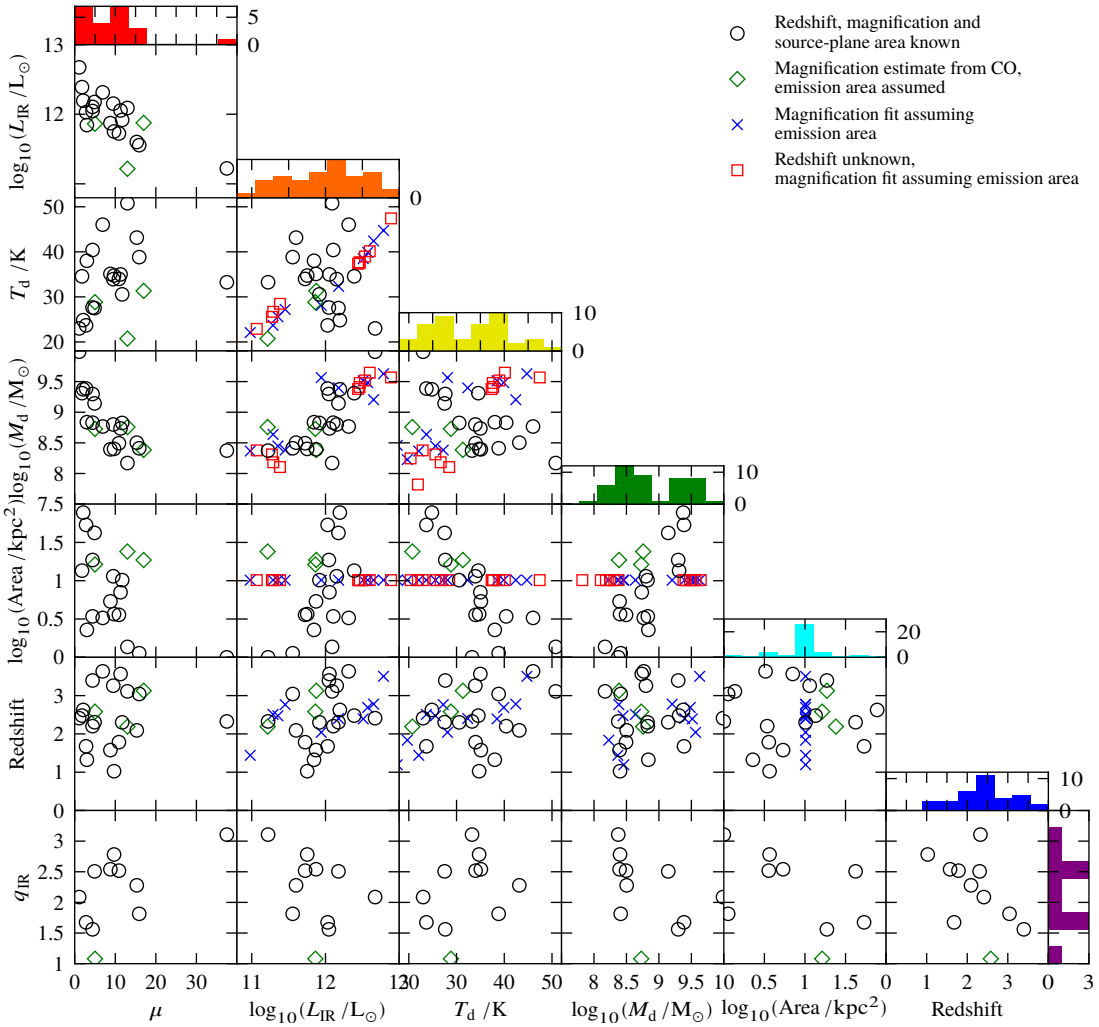

Figure 5.3. Distributions and correlations of SED fit parameters.
Black circles represent systems with known redshifts and lens models, primarily from Bussmann et al. (2013).
Green diamonds represent three systems with known redshifts, but amplification factor estimates only from their CO line characteristics (Harris et al. 2012).
Blue crosses represent sources with known redshifts, but no existing lens model. An emission diameter of 3 ± 2 kpc is assumed and used to fit the magnification.
Red squares represent similar sources, but additionally without a definite redshift: the fit is therefore performed assuming the redshifts given in Table 5.1.

redshift, but stronger negative correlations with area and dust mass. These latter correlations are primarily a side effect of the model used, and fitted masses should be viewed in knowledge of this dependence upon the input emission area and temperature, and as such gas masses derived from these dust masses will be inferior to those from CO observations. An insufficient number of the sample have published radio measurements to derive any meaningful conclusions from the q_{IR} estimates. Differential lensing preferentially selects compact star-forming regions, but as the luminosity of an optically thick body scales with area and typically $\tau_{100\,\mu m;rf} \sim 1$, there is a complex relationship between the luminosity distributions of lensed and unlensed populations. Further details of specific galaxies are given in Section 5.2.1.

Source	$F_{[\mathrm{O\,I}]\,63\,\mu\mathrm{m}}$ / 10^{-18} W m^{-2}	$F_{[\mathrm{O\,III}]\,88\,\mu\mathrm{m}}$ / 10^{-18} W m^{-2}	$F_{[\mathrm{N\,II}]\,122\,\mu\mathrm{m}}$ / 10^{-18} W m^{-2}	$F_{[\mathrm{C\,II}]\,158\,\mu\mathrm{m}}$ / 10^{-18} W m^{-2}	$\mu L_{[\mathrm{C\,II}]\,158\,\mu\mathrm{m}}$ / 10^{9} L$_{\odot}$	$L_{[\mathrm{C\,II}]}/L_{\mathrm{FIR}}$ / 10^{-4}
SDP.9	–	3.2 ± 1.4	$3\sigma < 0.6$	2.3 ± 0.8	10 ± 4	2.5 ± 0.9
SDP.11	–	4.8 ± 1.4	$3\sigma < 1.5$	9.7 ± 0.9	58 ± 5	15.3 ± 1.6
SDP.17	$3\sigma < 3.4$	$3\sigma < 3.6$	$3\sigma < 1.3$	$3\sigma < 2.1$	$3\sigma < 24$	$3\sigma < 5.2$
SDP.81	$3\sigma < 3.5$	3.3 ± 0.8	2.9 ± 1.3	5.3 ± 2.1	116 ± 46	32.7 ± 13.1
SDP.130	$3\sigma < 2.7$	2.2 ± 1.0	1.7 ± 0.9	$3\sigma < 4.9$	$3\sigma < 76$	$3\sigma < 36.8$
G09-v1.40	$3\sigma < 6.0$	$3\sigma < 3.3$	1.7 ± 0.7	4.1 ± 1.3	36 ± 11	10.2 ± 3.3
G09-v1.97	$3\sigma < 4.0$	$3\sigma < 2.0$	$3\sigma < 1.0$	–	–	–
G09-v1.124	$3\sigma < 3.0$	$3\sigma < 2.3$	$3\sigma < 2.0$	3.5 ± 1.6	44 ± 20	14.0 ± 6.4
G09-v1.326	$3\sigma < 2.8$	$3\sigma < 1.9$	$3\sigma < 1.2$	$3\sigma < 4.5$	$3\sigma < 66$	$3\sigma < 29.2$
G12-v2.30	$3\sigma < 3.2$	$3\sigma < 1.0$	$3\sigma < 1.6$	$3\sigma < 10.8$	$3\sigma < 278$	$3\sigma < 32.3$
G12-v2.43	$3\sigma < 0.5$	$3\sigma < 1.4$	$3\sigma < 3.5$	$3\sigma < 5.0$	$3\sigma < 117$	$3\sigma < 17.2$
G12-v2.257	$3\sigma < 3.8$	$3\sigma < 2.5$	$3\sigma < 1.5$	$3\sigma < 3.1$	$3\sigma < 30$	$3\sigma < 23.6$
G15-v2.19	–	–	$3\sigma < 3.3$	8.3 ± 1.3	13 ± 2	3.8 ± 0.6
G15-v2.235	$3\sigma < 3.8$	$3\sigma < 2.0$	$3\sigma < 1.3$	5.6 ± 1.7	74 ± 23	26.2 ± 8.1
NA.v1.56	$3\sigma < 3.7$	$3\sigma < 2.5$	$3\sigma < 1.5$	5.0 ± 1.5	55 ± 17	8.8 ± 2.8
NA.v1.144	$3\sigma < 3.1$	$3\sigma < 3.0$	$3\sigma < 1.8$	$3\sigma < 5.0$	$3\sigma < 50$	$3\sigma < 14.6$
NA.v1.177	$3\sigma < 4.1$	$3\sigma < 2.7$	$3\sigma < 2.3$	$3\sigma < 1.8$	$3\sigma < 32$	$3\sigma < 5.9$
NA.v1.186	–	$3\sigma < 2.6$	$3\sigma < 2.8$	4.3 ± 1.0	28 ± 7	15.5 ± 3.7
NB.v1.43	–	$3\sigma < 1.2$	$3\sigma < 0.5$	8.7 ± 0.8	45 ± 4	23.5 ± 2.4
NB.v1.78	$3\sigma < 3.1$	1.4 ± 0.7	$3\sigma < 1.4$	$3\sigma < 2.6$	$3\sigma < 59$	$3\sigma < 6.8$
NC.v1.143	$3\sigma < 2.8$	$3\sigma < 1.4$	$3\sigma < 2.8$	–	–	–
HeLMS-44	$3\sigma < 0.8$	$3\sigma < 3.7$	$3\sigma < 0.3$	4.5 ± 1.6	73 ± 26	15.4 ± 5.6
HeLMS-45	$3\sigma < 3.0$	$3\sigma < 2.8$	$3\sigma < 0.8$	$3\sigma < 4.6$	$3\sigma < 62$	$3\sigma < 19.3$
HBoötes03	–	$3\sigma < 3.2$	$3\sigma < 3.7$	3.9 ± 0.8	11 ± 2	8.7 ± 1.9
HXMM02	$3\sigma < 2.0$	$3\sigma < 1.8$	$3\sigma < 4.0$	–	–	–
MACSJ2043	$3\sigma < 4.5$	$3\sigma < 2.1$	1.3 ± 0.5	3.8 ± 0.8	32 ± 7	16.5 ± 3.9
Eyelash	2.0 ± 0.5	1.2 ± 0.6	1.5 ± 0.3	5.4 ± 0.8	62 ± 9	15.6 ± 2.5

Table 5.3. Far-IR line properties from fitting sinc profiles with uncertainties derived by bootstrapping the individual scans (200 per observation) at the velocities suggested by fitting the standard scan-averaged spectra.

5.2 SPIRE FTS observations

Several FTS spectra from this dataset have been published previously. Here we include re-reductions of those data along with the new spectra. The data pipeline and background subtraction process is described in Chapter 2, and the resulting spectra are shown in Figure 5.4 along with a cut-out spectral region around the [C II] 158 µm line.

Measurements of spectral line fluxes are performed by fitting a sinc function to spectra constructed from bootstrapped samples of the individual scans as described in Section 2.4.2. The fluxes are shown in Table 5.3.

5.2.1 Comments on individual objects

SDP.9 (*J090740.0-004200*): This is the lowest redshift and brightest of the original five strongly lensed DSFGs found in *H*-ATLAS (Negrello et al. 2010). NIR imaging suggests a nearly-complete Einstein ring, (Negrello et al. 2014), however dust emission is dominated by the SE region (Bussmann et al. 2013). Despite calculating almost identical dust emission luminosities,

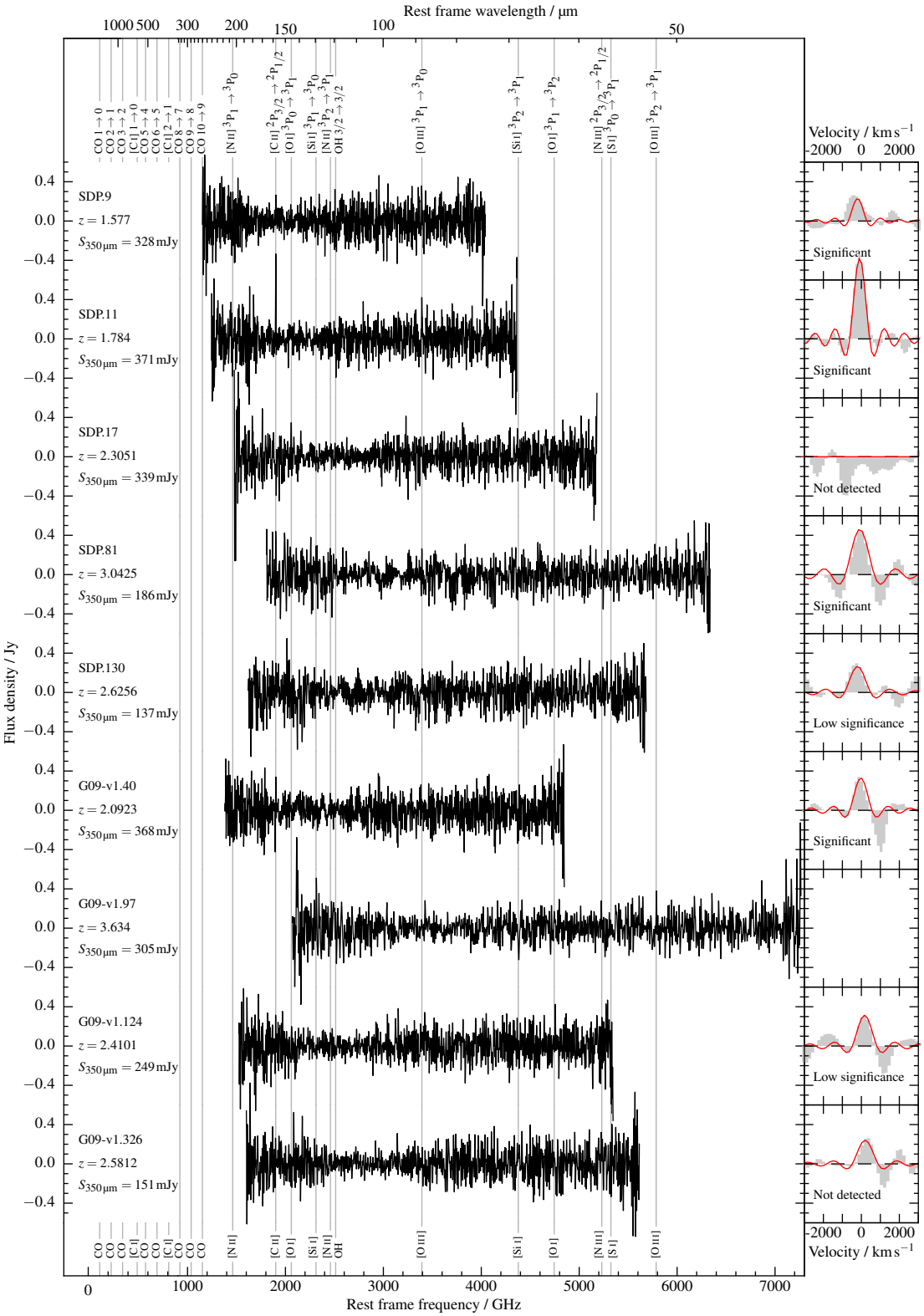

Figure 5.4. *Left:* The rest-frame *Herschel* SPIRE FTS spectra. Underlaid are markers of the positions of the primary spectral lines. Where redshifts are unknown, the spectra are displayed with an approximate photometric redshift, in some cases fitted to the position of a spectral feature potentially corresponding to the [C II] line (see right hand panels).
Right: $\pm 3000\,\mathrm{km\,s^{-1}}$ cuts around the position of the [C II] 158 μm line, with best-fitting sinc profile shown in red. Fit centres are allowed to move by $\pm 200\,\mathrm{km\,s^{-1}}$ to reflect redshift uncertainties.

Figure 5.4. Continued

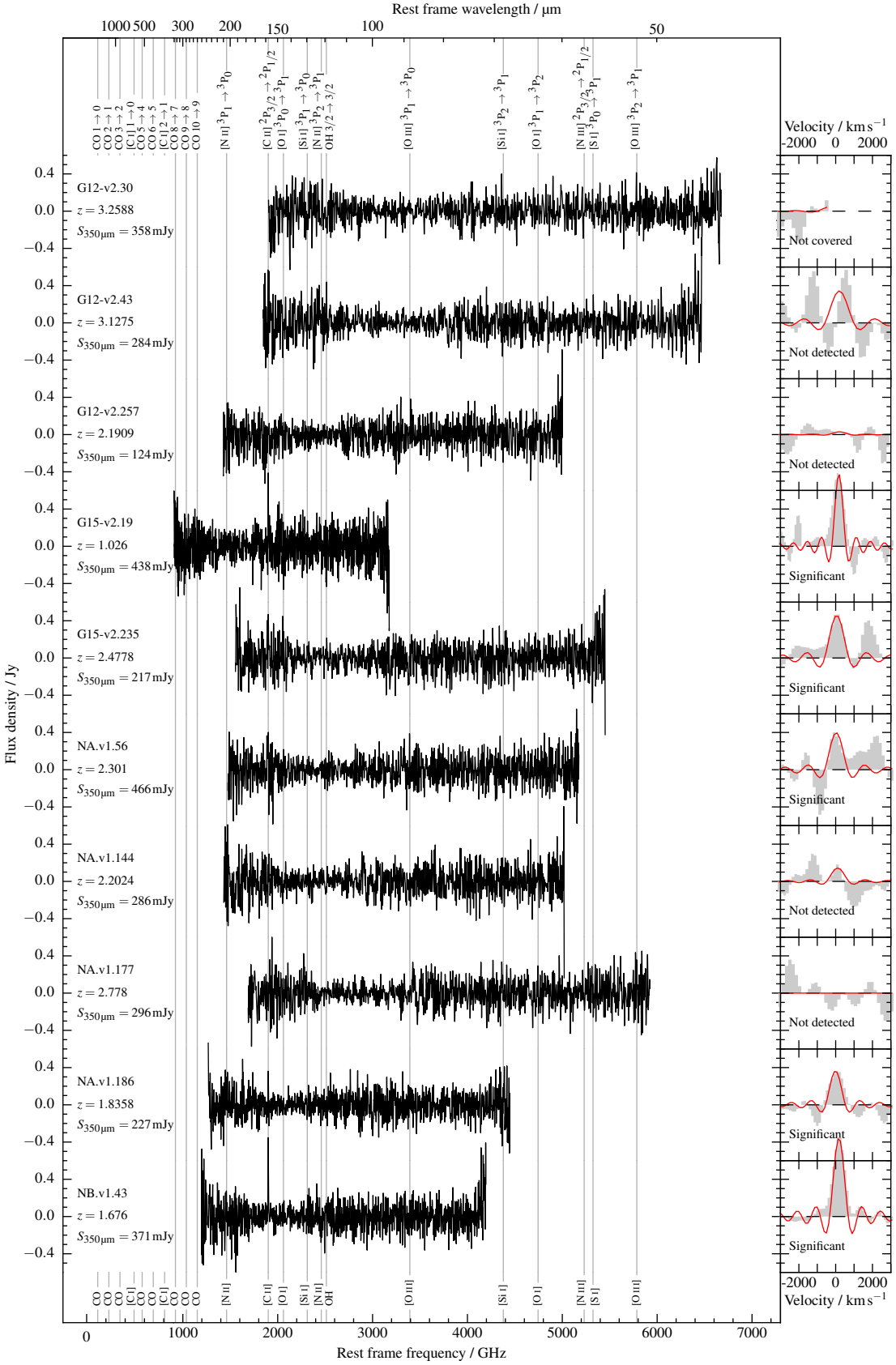

Figure 5.4. Continued

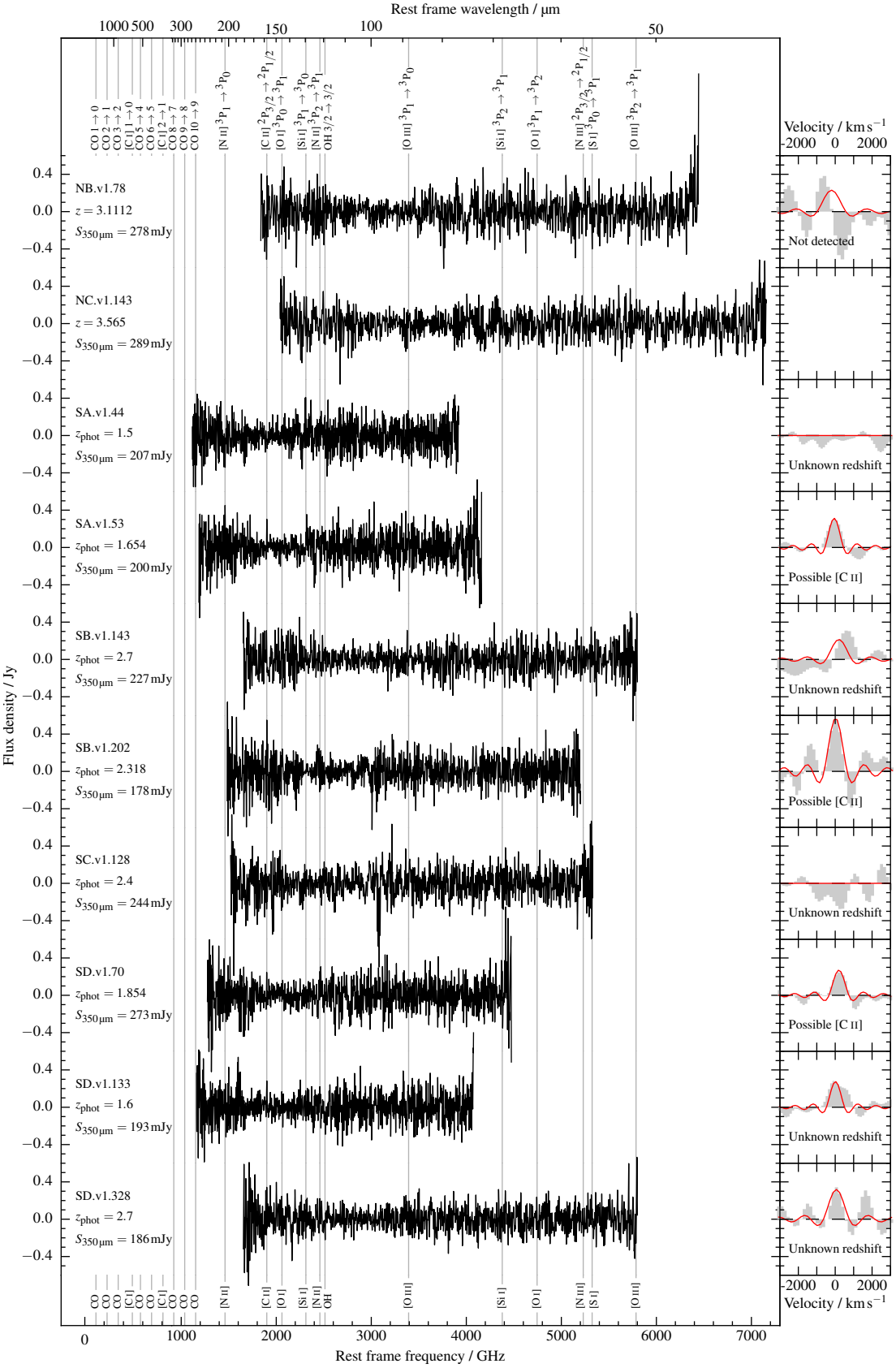

Figure 5.4. Continued

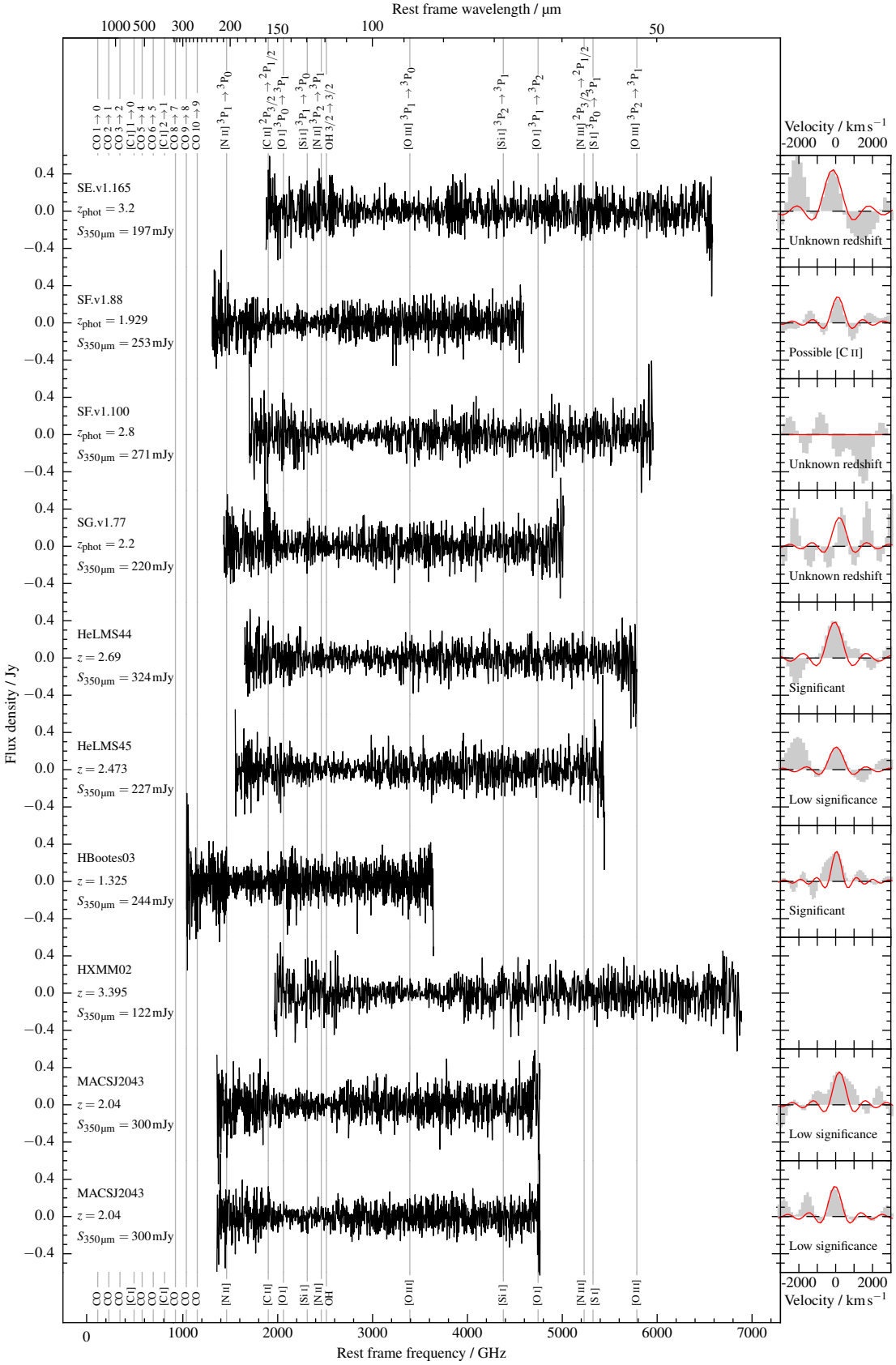

Figure 5.4. Continued

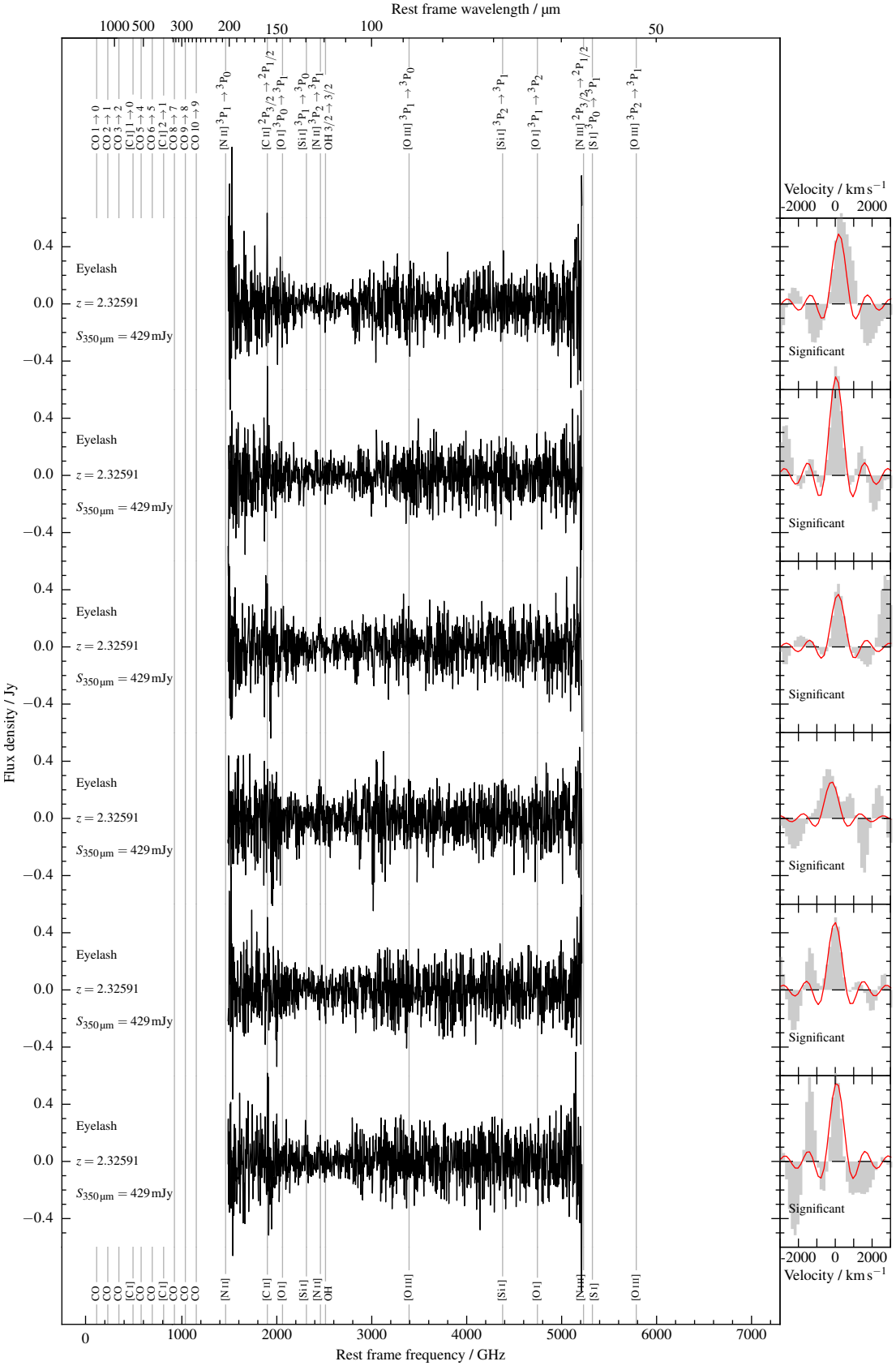

the SFR we derive using our chosen calibration: that presented in Murphy et al. (2011a) and recommended by the review of Kennicutt and Evans (2012); is a factor of 3 higher than value reported by Negrello et al. (2014). We find a relatively low $L_{[\mathrm{C\,II}]\,158\,\mu\mathrm{m}}$-to-$L_{\mathrm{FIR}}$ ratio of $(2.5 \pm 0.9) \times 10^{-4}$.

SDP.11 (*J091043.0-000322*): NIR imaging shows this object as a full yet elongated Einstein ring, with substructure that may result from source plane clumps. Dust emission does not exhibit the same brightness distribution, with the northern and southern regions dominant. A $(7.5 \pm 2.3) \times 10^{-18}$ W m^{-2} [O I] 63 µm line has been observed with PACS (Verma et al. in prep.). We find the [C II] line to have a flux $(9.7 \pm 0.9) \times 10^{-18}$ W m^{-2}, 50 % higher than a recent measurement from z(Redshift) and Early Universe Spectrometer-2 (ZEUS-2; Ferkinhoff et al. 2014) on APEX (Ferkinhoff et al. 2014).

SDP.17 (*J090302.9-014127*): With a complex NIR light profile, this system is difficult to separate into clear foreground and background components. The lensed image is not resolved into multiple components by the SMA in even the most extended configuration, suggesting a relatively low amplification factor and hence high intrinsic luminosity. Despite this, the large emission area suggested by Bussmann et al. (2013) would indicate a comparatively modest star formation rate surface density, making our [C II] non-detection interesting should that parameter be a key driver of the line-to-FIR continuum deficit.

SDP.81 (*J090311.6+003906*): This galaxy is lensed into two arcs, exquisitely revealed by recent long-baseline ALMA imaging (ALMA Partnership et al. 2015). These data have been used to produce a detailed reconstruction of the source-plane emission (Dye et al. 2015), which exhibits 200 pc-scale clumps. We use the amplification derived for the dust emission from this modelling effort: 15.9 ± 0.7: which is higher than an estimate from lower resolution SMA data (11.1 ± 1.1; Bussmann et al. 2013), and also higher than the amplification estimated for the optical emission: 10.2 ± 0.5; which appears not to be co-spatial with the rest-frame FIR emission (Dye et al. 2015), as is common for starbursts (e.g. the Antennae Galaxies). An estimate of the source-plane emission radius from those data: (0.5 ± 0.2) kpc; is also used in our SED fitting. The SPIRE FTS spectrum is presented in Valtchanov et al. (2011) (programme GT1_IVALTCHA_1), but for consistency we reprocess the data here. Due to the different method of background subtraction (off-axis vs. dark sky) we find a substantially lower [C II] flux. However, as the off-axis method produced reduced noise over the dataset as a whole, and is used in the reduction of SPIRE spectra of other similarly faint targets (e.g. Magdis et al. 2014; Gullberg et al. 2015), we use our measurement throughout this chapter. Despite the lower line flux, this object still appears to possess the highest $\mu L_{[\mathrm{C\,II}]}$ and $L_{[\mathrm{C\,II}]}/L_{\mathrm{FIR}}$ values of our sample.

SDP.130 (*J091305.0-005343*): With a modest ~ 2× amplification this galaxy has significantly lower flux densities than the target threshold, and Valtchanov et al. (2011) found no lines in the FTS spectrum. Using newer calibration data, we find possible H II region emission, however the non-detection of [C II] 158 µm indicates these are likely noise.

G09-v1.40 (*J085358.9+015537*): This galaxy is visible in K_{s} band imaging as an almost-

complete Einstein ring, consequently experiencing a high magnification factor of ~15. The source-plane object may be highly elongated (Calanog et al. 2014). We detect [C II].

G09-v1.97 (*J083051.0+013224*): This source is lensed by two foreground galaxies at different redshifts. While it possesses one of the largest $\mu L_{\rm IR}$ values of the sample, the high redshift means [C II] is not covered by the FTS.

G09-v1.124 (*J084933.4+021443*): Uniquely within our sample this object is known to be essentially unlensed, its broad CO lines suggesting a very high intrinsic luminosity, confirmed by a range of follow-up observations which showed a system of four separate DSFGs, two of which are individually over the HyLIRG limit (Ivison et al. 2013). These two brightest are resolved in our PACS imaging, but together only provide a low significance [C II] feature. Recent NIR spectroscopy has revealed a broad-line AGN in this system (Oteo et al. in prep.), which will be responsible for some fraction of its FIR flux.

G09-v1.326 (*J091840.8+023047*): Available SMA imaging is consistent with a point source and no counterpart is found in *HST* or Keck imaging. Should this be an unlensed DSFG it would possess a SFR of ~5000 $\rm M_{\odot} yr^{-1}$, higher than any component of the known HyLIRG G09-v1.124, so we instead assume the amplification estimate of 5 ± 1 from Harris et al. (2012) derived from its CO luminosity and FWHM. No FIR cooling lines are observed in the FTS spectrum, however the flux densities lie below the target threshold.

G12-v2.30 (*J114638.0-001132*): A detailed study of this galaxy is presented in Fu et al. (2012), indicating a complex system in which the existing stellar population is quadruply-lensed by a net factor of over 2× that of the offset starburst, which provides some of this highest 500 and 880 µm flux densities in our sample. This redshift represents the limit of the FTS coverage of the [C II] line, which therefore lies in the noisiest region of the spectrum and is not detected.

G12-v2.43 (*J113526.3-014606*): Multiple lensed images are not resolved in the 880 µm SMA data, however a faint source visible in *HST* F110W and Keck/NIRC2 $K_{\rm s}$ imaging is likely a foreground lensing galaxy. With an apparent $\mu L_{\rm IR} > 10^{14.1}\,\rm L_{\odot}$, among the highest of our sources, we assume the large amplification estimate of Harris et al. (2012): 17 ± 11. As with G12-v2.30, the [C II] line lies within the high-noise end region of the spectrum, and no FIR lines are observed.

G12-v2.257 (*J115820.1-013753*): An image displaying the PACS contours overlaying *HST* F110W imaging is shown in Figure 2.14. The two spirals visible at 100 µm will be unresolved within the SPIRE beam but likely contribute very little to the measured flux densities at the longer wavelengths. No lensing model is available, though this object has one of the lowest 350 µm flux densities within our sample indicating a low $\mu L_{\rm IR}$ and likely $\mu \lesssim 5$. We however take the published amplification estimate of 13 ± 7 from Harris et al. (2012). As with the other low flux density sources, we do not find any emission line features.

G15-v2.19 (*J142935.3-002836*): This object is the brightest (and lowest redshift) within our sample. A detailed study is presented in Messias et al. (2014) indicating a gas-rich (25% of baryonic mass) merger of two source-plane components lensed into an almost complete Einstein

ring. The redshift is too low for the spectrum to cover [O I] and [O III], but a strong [C II] feature is found. Additionally, we detect 119 µm OH $^2\Pi_{3/2}$ $J = \frac{3}{2} \rightarrow \frac{5}{2}$ absorption. With no strong evidence of an AGN (Messias et al. 2014) we, as with a similar detection within the Cosmic Eyelash (see Chapter 4), attribute this to a SNe-driven outflow of molecular gas.

G15-v2.235 (*J141351.9-000026*): This galaxy is weakly lensed by a cluster with only a single elongated image visible, suggesting a high intrinsic luminosity. We find [C II] and the second-highest $L_{[\mathrm{C\,II}]}/L_{\mathrm{FIR}}$ ratio of the sample.

NA.v1.56 (*J134429.4+303036*): This source has the highest 350 and 500 µm flux densities in our sample, visible as two well-defined arcs in SMA imaging. We detect [C II] emission.

NA.v1.144 (*J133649.9+291801*): Available optical–NIR imaging is insufficiently deep to detect a lensing galaxy, however the 880 µm morphology indicates that this object is likely lensed with a small Einstein radius. A second tentative source at $z = 2.3078$ was suggested by a blind CO line search (Harris et al. 2012). We do not detect any spectral lines.

NA.v1.177 (*J132859.3+292317*): This source is resolved into a single elongated image in SMA data, and likely also responsible for a faint arc in Keck NIRC2 Ks imaging. No lens models has been produced so far, and we do not detect any lines.

NA.v1.186 (*J132504.4+311537*): A feature suggestive of [C II] at $z = 1.836$ found in our FTS spectrum was followed up with CARMA, extending the 3 mm spectrum below the nominal 85 GHz tuning range. to detect CO $J = 2 \rightarrow 1$. A redshift of 1.8358 was confirmed, negating the previous estimate of $z = 2.635$. With no published deep NIR or interferometric FIR–mm imaging, a lens model has not been produced.

NB.v1.43 (*J132427.0+284452*): NIR images of this galaxy display an $\approx 10''$ long arc with little curvature: much more spatially extended than is visible in submm data which arises from a small area toward the centre. Our FTS spectrum along with its detection of strong [C II] emission was presented in Chapter 3, however since publication of those data, a lensing model has been published. Lensing bodies are likely either two galaxies or a nearby cluster (see Bussmann et al. 2013, for a discussion), with a (relatively uncertain) lensing amplification factor of 2.8 ± 0.4 derived for the dust emission. Calculations in this chapter utilise that value.

NB.v1.78 (*J133008.4+245900*): With > 200 mJy flux densities in all SPIRE bands and at 160 µm, despite a redshift above 3, this galaxy has the highest μL_{IR} of the sample and a warm dust temperature caused by its small radius and hence high SFR surface density. Coupled with the position of the [C II] line within the spectrum, our non-detection of that transition is therefore perhaps unsurprising.

NC.v1.143 (*J125632.7+233625*): The lens has a redshift low enough for it to be visible in SDSS imaging and similarly to NB.v1.78, the background galaxy has a high μL_{IR} and an even higher dust temperature and SFR surface density, however the high redshift of this source means that [C II] 158 µm is not covered by the FTS spectrum.

H-ATLAS SGP sources: Without definite redshifts, it is difficult to glean much from these

sources. Several have low significance SPIRE spectral features potentially corresponding to [C II], with the corresponding redshifts listed in Table 5.1.

HeLMS sources: Only two of these galaxies were observed with the FTS, HeLMS-44 exhibiting [C II] emission. Further multiwavelength follow-up of these objects has not yet been published, rendering any conclusive determinations of their properties or lensing amplification difficult.

HBoötes03 (*J142824.0+352619*): This is a well-studied high-redshift DSFGs (also known as MIPS J142824.0+352619) discovered before the wide area *Herschel* and SPT surveys (Borys et al. 2006; Swinbank et al. 2006). *Herschel* PACS detections of [O III] ($(3.7 \pm 0.8) \times 10^{-18}$ W m^{-2}) and [O I] ($(7.8 \pm 1.9) \times 10^{-18}$ W m^{-2}) are presented in Sturm et al. (2010), and a $(19.8 \pm 3.0) \times 10^{-18}$ W m^{-2} [C II] detection with CSO/z(Redshift) and Early Universe Spectrometer (ZEUS; Stacey et al. 2007) in Hailey-Dunsheath et al. (2010). This latter value is particularly significant, being a factor of 5 higher than our measurement (fit shown in Figure 5.4). We are unsure as to the reason for the magnitude of this discrepancy.

HXMM02 (*J021830.5−053124*): This object (also known as Orochi or SXDF1100.001) was included due to its previous in-depth study (Ikarashi et al. 2011; Iono et al. 2012). The small lens Einstein radius and amplification however give it the lowest 250 and 350 µm flux densities in our sample, which when coupled with its high redshift (such that the FTS spectrum does not cover [C II]), mean no FIR lines are found. The dust mass temperature index of 7.2, used to fit all other galaxies is insufficient to account for the high PACS flux densities, with the best-fitting value being 5.7. This suggested additional mass of hot dust, coupled with the low $q_{\rm IR}$ value (assuming a synchrotron spectral index of -0.75) indicates the presence of an AGN.

MACS J2043 (*J204314.2−214439*): In addition to our FTS spectrum, we include an additional 133 repetition observation of MACS J2043 as part of programme OT1_MREX_1 , finding [C II]. Further details of this object will be presented by Rex et al. (in prep.).

Cosmic Eyelash (*J213511.6−010252*): SMM J2135-0102 is one of the most well-studied high-redshift DSFGs, its 37.5 ± 4.5 amplification factor enabling the spatial and spectral resolution of 3–4 massive star-forming clumps (e.g. Swinbank et al. 2010b, 2011; Ivison et al. 2010c; Danielson et al. 2013). After a tentative detection of OH 119 µm absorption in the OT1 observation of this source, we included 5 repeat observations of that object in OT2. A detailed examination of that data is presented in Chapter 4, however for consistency we reprocess that data again here. [C II] appears at a higher velocity in the original spectrum than the repeats, however while individual spectra may exhibit slight noise-related velocity differences, the fit to the combined spectrum of all Eyelash observations (as in that chapter) should be relatively robust.

5.3 Analysis

5.3.1 [C II] 158 µm as a diagnostic

The [C II] $^2P_{3/2} \rightarrow ^2 P_{1/2}$ 158 µm transition is often the brightest FIR emission line and in particular with ALMA now operational, interest in the interpretation of [C II] observations has increased over recent years. Its formation in both H II regions and PDRs, and apparent relative decrease in efficiency with increasing SFR however mean much is still to be understood in regards to its potential use as a gas diagnostic.

The strength of FIR cooling lines increases with input FUV luminosity and hence $L_{\rm FIR}$. The fraction of energy transmitted via these lines is not constant however, with a decrease in the $L_{\rm line}/L_{\rm FIR}$ ratio with increasing $L_{\rm FIR}$ well known in the local Universe (Luhman et al. 2003), such that the brightest ULIRGs exhibit the highest deficits. The relationship also holds in spatially resolved measurements (Díaz-Santos et al. 2014), with lower values found in the nucleus of LIRGs than the extended body of the disc.

Several theories have been proposed to explain the deficit. The ionisation parameter U and hence dust temperature and SFR surface density appears to be strongly correlated with the line-to-continuum ratio (Díaz-Santos et al. 2013), with the most extreme values of all three found in the dense merging nuclei of low-redshift ULIRGs, see Figure 5.11 for the effect of Ionisation parameter $U = \frac{\phi_{\rm H}}{n_{\rm face}c}$ on [C II]. Dust grain charging in higher radiation fields, leading to a lower photoelectric gas heating efficiency may also play an effect (Malhotra et al. 1997). Column density will also have an effect as [C II] is primarily produced in PDRs, with a small H II region contribution (e.g. Abel 2006), and the column density at which the C^+/C/CO transition occurs is governed by the ionisation parameter and dust extinction. FIR continuum radiation however can also be produced by non-PDR sources. Lines of sight through high optical depth molecular material to a PDR and starburst inside will observe a substantial continuum contribution from this molecular region, and indeed the H II region close to the ionising source (see Figure 5.11). This both increases the FIR emission, and as shown in the figure, at very high column densities the optical depth to the lines may become large enough to actually reduce the observed flux.

At high redshift this effect appears to continue, albeit potentially to a lower extent (e.g. Stacey et al. 2010). While SFRs can often equal or exceed those found in local ULIRGs, significant differences exist in the distribution of gas and star-formation within these two populations. As gas masses are often high enough to form several starbursting clumps throughout the disc, rather than concentrating star formation within a single central region (e.g. Swinbank et al. 2010b), a larger volume of gas may be illuminated with a lower flux of ionising photons, producing both a smaller U value and optical depth.

Díaz-Santos et al. (2013) and Gullberg et al. (2015) discuss the deficit and correlations with other parameters, in particular emission area and molecular gas mass, in further detail at low

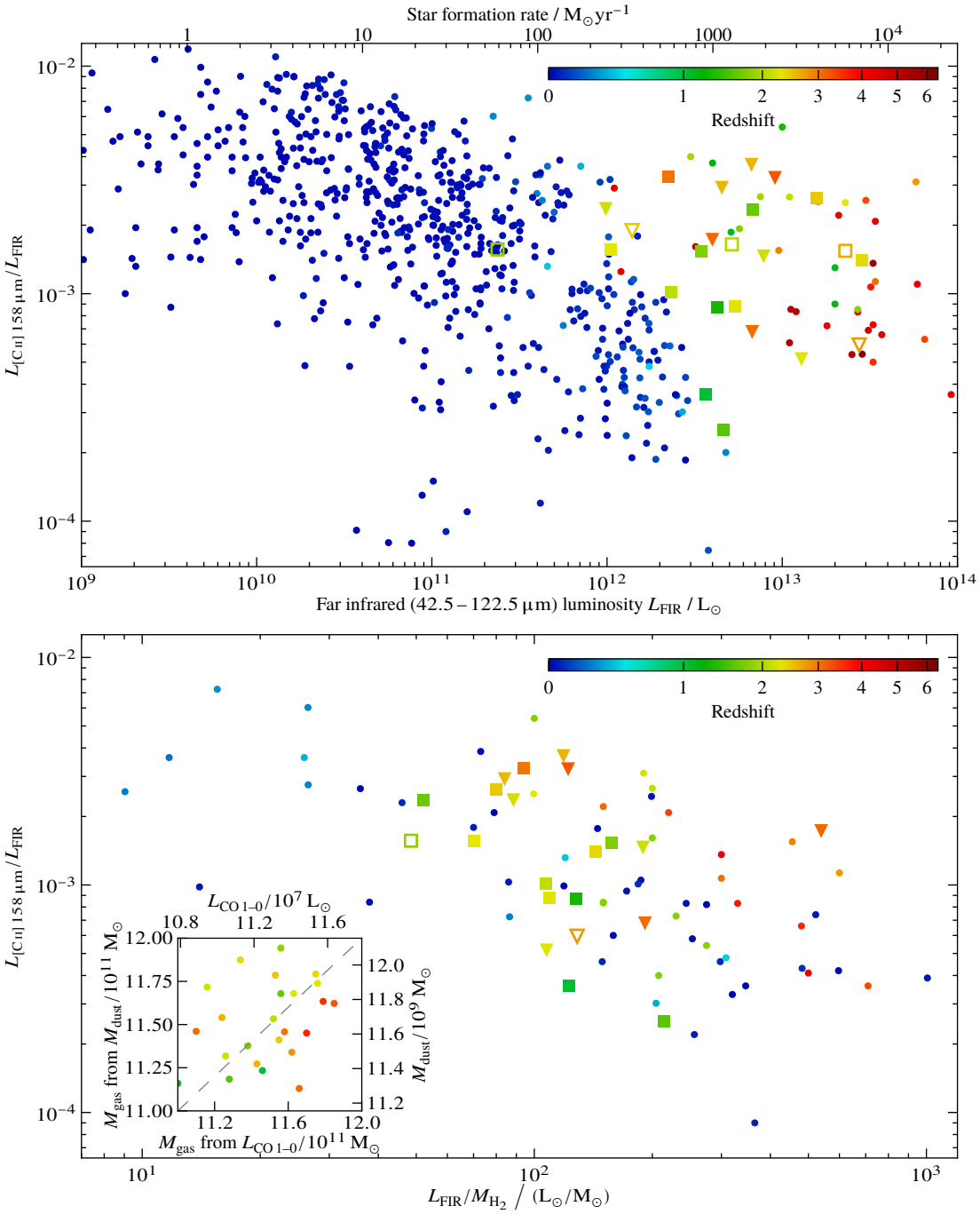

Figure 5.5. *Upper*: The $L_{[C\,II]}/L_{FIR}$ deficit locally and at high-redshift in starburst-dominated galaxies. Point from this work are shown as squares or downward arrows indicating 3σ upper limits. Filled points have FIR luminosities corrected for magnification, non-filled points use magnification estimates from SED fitting. Low-redshift points taken from Brauher, Dale, and Helou (2008), Díaz-Santos et al. (2013), Sargsyan et al. (2014), González-Alfonso et al. (2015), Ibar et al. (2015), and Rosenberg et al. (2015). $z \sim 1$ points from Stacey et al. (2010), Farrah et al. (2013), and Magdis et al. (2014). Higher redshift points taken from Cox et al. (2011), Swinbank et al. (2012), Wagg et al. (2012), Riechers et al. (2013), De Breuck et al. (2014), Riechers et al. (2014b), Rawle et al. (2014), and Gullberg et al. (2015) Where necessary, luminosities have been scaled from literature measurements by the mean of the values from our SED fits $L_{FIR}(42.5-122.5\,\mu m) = 0.60\,L_{IR}(8-1000\,\mu m)$.
Lower: The [C II] to continuum ratio as a function of L_{FIR}/M_{H_2}, which should correlate more strongly than the continuum luminosity alone (e.g. Graciá-Carpio et al. 2011). Gas masses are determined from integrated-galaxy CO observations, converted to $J = 1 \rightarrow 0$ luminosities where necessary by the ratios presented in Bothwell et al. (2013).

and high redshift respectively.

Our $L_{[\mathrm{C\,II}]\,158\,\mu\mathrm{m}}/L_{\mathrm{FIR}}$ measurements are plotted in Figure 5.5 along with values from local and high-redshift starburst-dominated galaxies. Gravitational lensing has allowed us to push intrinsic luminosities towards or even below those of many local ULIRGs, and these sources occupy much of the space between the highest redshift ALMA detections (primarily with $L_{\mathrm{FIR}} > 10^{13}\,\mathrm{L}_{\odot}$ and low-redshift points (with $L_{\mathrm{FIR}} < 3 \times 10^{12}\,\mathrm{L}_{\odot}$). A spread in $L_{[\mathrm{C\,II}]\,158\,\mu\mathrm{m}}/L_{\mathrm{FIR}}$ is observed, from $\sim 3 \times 10^{-3} - 3 \times 10^{-4}$, suggesting the local relation does not hold to these redshifts, however the non-detections may have lower ratios. These values appear to confirm other observations indicating that (for starburst-dominated systems at least) the deficit is lower within high-redshift ULIRGs than their low-redshift counterparts, likely resulting from a lower intensity of ionising radiation due to their similar total star formation occurring over a larger volume.

We see only a weak trend of decreasing line-to-continuum ratio with increasing dust temperature (Figure 5.9), however our dust temperatures are both not necessarily comparable to those derived with a single grey-body component and are dependent upon the assumed dust emission area. These derived areas are fairly uncertain, with variation in the net amplification value found for the same system in different studies (e.g. Bussmann et al. 2013; Negrello et al. 2014; Dye et al. 2015), and with most reconstructions relying on rest-frame optical or cool dust emission, both of which likely exhibit different spatial extents to that of the [C II] emission.

The line-to-continuum ratio is however expected to correlate more strongly with $L_{\mathrm{FIR}}/M_{\mathrm{H_2}}$ (e.g. Graciá-Carpio et al. 2011), and our measurements plotted in Figure 5.5 (using gas masses derived from CO luminosities) agree with this theory. Dust mass does not appear to be a good proxy for gas mass in this sample of galaxies, as displayed in Figure 5.5, however as explained above these dust masses depend upon the assumed emission area.

In addition to the total IR luminosity, the FIR lines, as coolants of star-formation-heated gas, may be used to trace the instantaneous SFR. As often the brightest, the [C II] line is of primary interest. The conversion is however non-linear due to the changing efficiency of these lines with increasing SFR. Sargsyan et al. (2014) and Herrera-Camus et al. (2015) provide discussions of the effectiveness of [C II] as a SFR tracer in the local Universe, noting that [C II] can provide measurements consistent with other star-formation tracers such as PAH emission and MIR emission lines, however any calibration may require additional corrections to be applicable to more strongly star-forming sources, in which cases SFRs derived from continuum measurements may be superior. Literature calibrations from these local samples are presented in the form $\frac{\mathrm{SFR}}{\mathrm{M_{\odot}yr^{-1}}} = A\left(\frac{L_{[\mathrm{C\,II}]}}{\mathrm{L_{\odot}}}\right)^{B}$, where $A = 1.22 \times 10^{-8}$, $(1.0 \pm 0.2) \times 10^{-7}$ and 1.00×10^{-7} and $B = 1.034$, 1 and 0.983 from De Looze et al. (2011), Sargsyan et al. (2014) and Herrera-Camus et al. (2015) respectively. For our lowest-uncertainty [C II] flux, that of the Cosmic Eyelash, these suggest SFRs of 40, 165 and $120\,\mathrm{M_{\odot}yr^{-1}}$, the range reflecting the inherent dispersion in $L_{[\mathrm{C\,II}]}$/SFR ratios observed. An equivalent calibration derived from high-redshift points is $\frac{\mathrm{SFR}}{\mathrm{M_{\odot}yr^{-1}}} = 3.02 \times 10^{-9}\left(\frac{L_{[\mathrm{C\,II}]}}{\mathrm{L_{\odot}}}\right)^{1.18}$ (De Looze et al. 2014), with the higher exponent value accounting for the decreasing line-to-continuum ratio in galaxies with the high infrared

Stack	$L_{[\mathrm{O\,I}]\,63\,\mu\mathrm{m}}$ / $10^8\,\mathrm{L}_\odot$	$L_{[\mathrm{O\,III}]\,88\,\mu\mathrm{m}}$ / $10^8\,\mathrm{L}_\odot$	$L_{[\mathrm{N\,II}]\,122\,\mu\mathrm{m}}$ / $10^8\,\mathrm{L}_\odot$	$L_{[\mathrm{O\,I}]\,146\,\mu\mathrm{m}}$ / $10^8\,\mathrm{L}_\odot$	$L_{[\mathrm{C\,II}]\,158\,\mu\mathrm{m}}$ / $10^8\,\mathrm{L}_\odot$
Mean L_{line}	2.8 ± 2.0	4.2 ± 2.5	3.9 ± 2.0	0.8 ± 1.0	20.4 ± 9.4
Stack	$\mu L_{[\mathrm{O\,I}]\,63\,\mu\mathrm{m}}$ / $10^9\,\mathrm{L}_\odot$	$\mu L_{[\mathrm{O\,III}]\,88\,\mu\mathrm{m}}$ / $10^9\,\mathrm{L}_\odot$	$\mu L_{[\mathrm{N\,II}]\,122\,\mu\mathrm{m}}$ / $10^9\,\mathrm{L}_\odot$	$\mu L_{[\mathrm{O\,I}]\,146\,\mu\mathrm{m}}$ / $10^9\,\mathrm{L}_\odot$	$\mu L_{[\mathrm{C\,II}]\,158\,\mu\mathrm{m}}$ / $10^9\,\mathrm{L}_\odot$
Mean μL_{line}	10 ± 11	13 ± 8	7 ± 5	3 ± 5	39 ± 8
$z < 2.2$	–	$3\sigma < 70$	$3\sigma < 35$	$3\sigma < 11$	34 ± 12
$2.2 < z < 2.7$	$3\sigma < 50$	$3\sigma < 50$	$3\sigma < 35$	$3\sigma < 40$	42 ± 23
$2.7 < z$	$3\sigma < 120$	$3\sigma < 100$	$3\sigma < 130$	–	–
$L_{\mathrm{IR}} < 12.9$	$3\sigma < 70$	$3\sigma < 50$	$3\sigma < 29$	$3\sigma < 25$	41 ± 11
$12.9 < L_{\mathrm{IR}} < 13.2$	$3\sigma < 100$	$3\sigma < 70$	$3\sigma < 50$	$3\sigma < 50$	36 ± 27
$13.2 < L_{\mathrm{IR}}$	$3\sigma < 150$	$3\sigma < 150$	< 130	–	–
$T_{\mathrm{d}} < 30$	$3\sigma < 40$	$3\sigma < 36$	$3\sigma < 22$	$3\sigma < 21$	41 ± 10
$30 < T_{\mathrm{d}} < 39$	–	$3\sigma < 90$	$3\sigma < 70$	–	33 ± 31
$39 < T_{\mathrm{d}}$	–	–	–	–	–

Table 5.4. Line flux measurements from stacked spectra.

luminosity visible at such distances. For the Cosmic Eyelash, this calibration suggests a SFR of $230\,\mathrm{M}_\odot\mathrm{yr}^{-1}$, remarkably consistent with the $250\,\mathrm{M}_\odot\mathrm{yr}^{-1}$ we estimate from the photometric infrared luminosity fit.

An extension to these $L_{[\mathrm{C\,II}]}$–SFR relationships is to use local resolved galaxies to consider surface densities. Díaz-Santos et al. (2013) derive a relationship for the nuclei of a large sample of LIRGs which appears to hold for high-redshift objects (Díaz-Santos et al. 2014), and which rearranged is:

$$\log_{10}\left(\frac{\mathrm{area}}{\mathrm{kpc}^2}\right) = \log_{10}\left(\frac{L_{\mathrm{IR}}}{\mathrm{L}_\odot}\right) + \frac{\log_{10}\left(\frac{L_{[\mathrm{C\,II}]}}{L_{\mathrm{FIR}}}\right) - 1.21 \pm 0.24}{0.35 \pm 0.03}. \tag{5.1}$$

The suggested emission surface areas of our sample are typically within a factor of a few of the demagnified areas we have used (primarily from the lens modelling of Bussmann et al. 2013), compatible with the low-redshift scatter. Only in some systems with [C II] non-detections (e.g. SDP.17) or very high $L_{[\mathrm{C\,II}]}/L_{\mathrm{FIR}}$ ratios are these areas substantially different to our assumed source plane extents. It should be noted however that as described earlier, the demagnified areas we use are fairly uncertain.

5.3.2 Stacking

Only the brightest FIR cooling lines are seen in the individual spectra, so to search for faint transitions, and determine the evolution of properties of the population as a whole, we stacked sets of spectra in the rest frame, as the noise should reduce as $\sqrt{n}$. Two stacking procedure variants are used.

The first uses only spectra of sources with known amplification factors. Each spectrum is baseline-subtracted by fitting a B-spline, then converted from observed-frame flux densities to

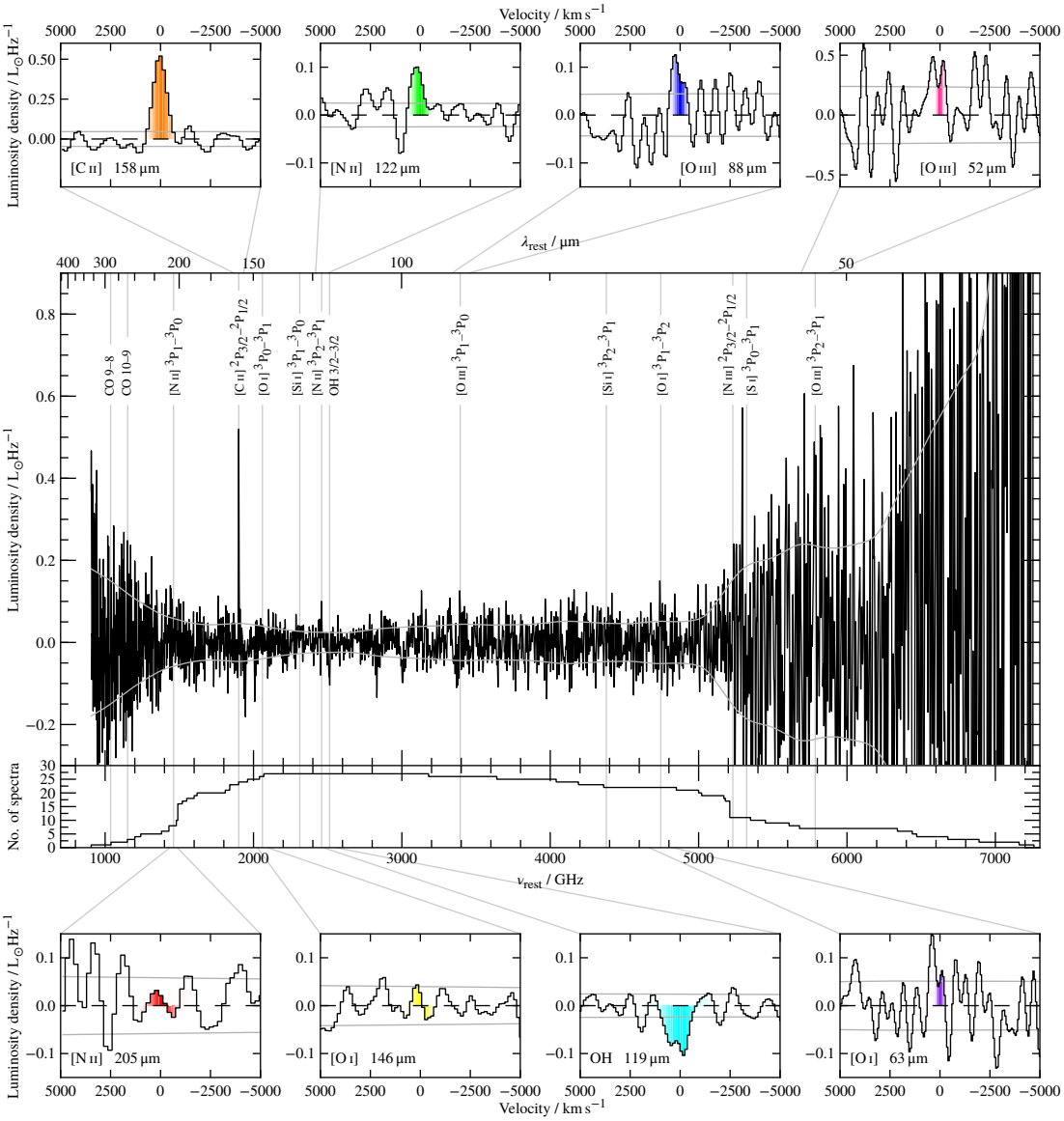

Figure 5.6. *Centre upper*: Rest frame stack of all spectra, with markers denoting the positions of the primary spectral features expected.
Centre lower: The number of spectra contributing to this stacked spectrum.
Upper and lower: $\pm 5000\,\mathrm{km\,s^{-1}}$ cuts around the positions of the primary atomic and ionic spectral lines analysed elsewhere in this chapter, plus the OH 119 µm doublet.

rest-frame luminosity densities using the known amplification and redshift. An empty output spectrum covering the total range is created, with a resolution equivalent to the maximum of the individual spectra (altered by the blueshifting step above). Each rest frame spectra is interpolated to find the luminosity density at the value of each output spectrum dispersion element, and these luminosity densities are then averaged using $1/\sigma^2$ weighting. This enables the demagnified mean line luminosities to be calculated.

The second involves blueshifting all SEDs to the rest-frame and estimating their relative observed FIR fluxes. One galaxy is selected as a ‘master’, and all measured spectra are scaled by the necessary factor to make their SED fluxes equal to that of the ‘master’. The spectra are then

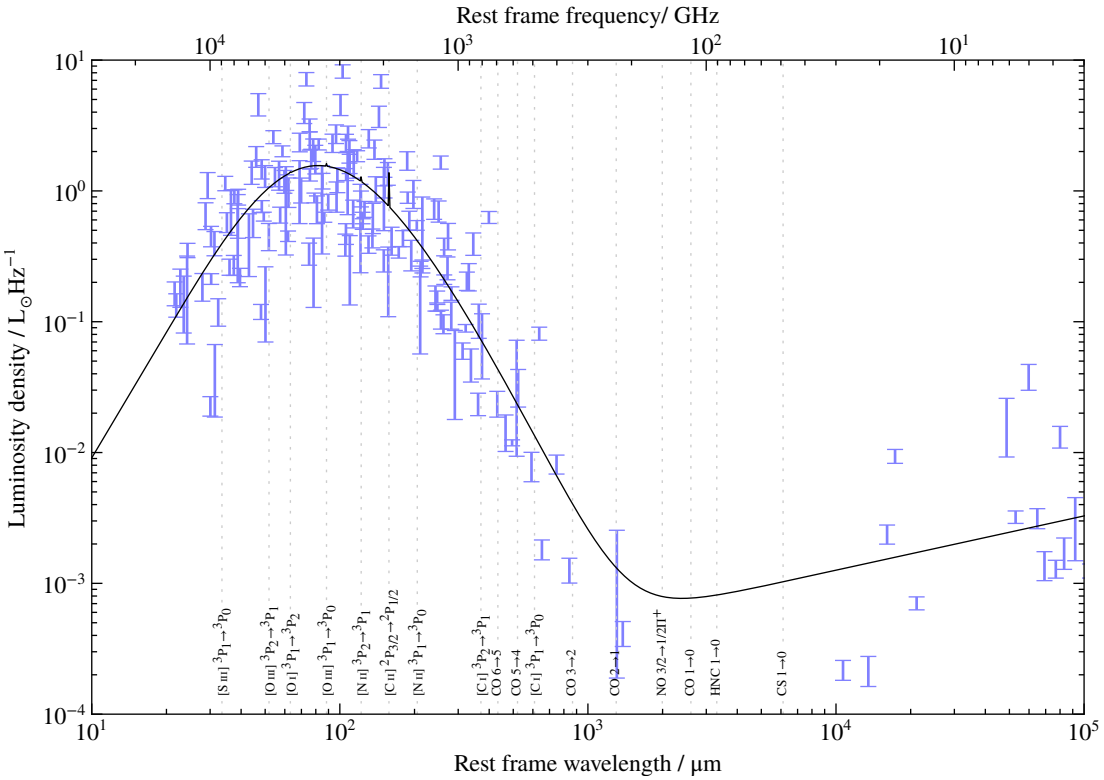

Figure 5.7. The mean SED (black) derived from fitting the power-law dust temperature distribution model used elsewhere to all demagnified photometry points (blue) of the members of the sample for which a lensing model is available. Spectral lines have been added assuming the luminosities tabulated in Table 5.4 and a FWHM of 500 km s^{-1}.

combined as above, and as amplification factors (with their associated uncertainties) are not required, the line measurement uncertainties are reduced and all spectra with known redshifts can be used, regardless of whether a lens model exists. This allows an estimate of the mean $\mu L_{\rm line}$ to be calculated.

The spectrum resulting from the first method is displayed in Figure 5.6, and these lines have been added to the mean rest-frame demagnified FIR–radio SED shown in Figure 5.7. Particularly interesting is the 119 μm OH feature, of which robust detections are only seen in the G09-v2.19 and the Cosmic Eyelash individual spectra, the latter being presented in Chapter 4. Blueshifted OH has also been observed at high redshift in emission (Riechers et al. 2014b). This feature provides further evidence that outflowing molecular gas may be common within the high-redshift DSFG population, if difficult to observe. However, further analysis of this detection is beyond the scope of this chapter.

To determine average properties as a function of luminosity, redshift and dust temperature, we further stacked several subsets of our spectra. For each of these parameters, we binned our sources into three roughly equal-size groups. For each spectral line of interest, the sources within each bin were further separated into those with a detection of that line, and those without. We performed a rest-frame stack of the spectra of the three subsets of objects within each bin: ‘all’, ‘detected’ and ‘undetected’. Spectral line fluxes of these stacked spectra were then determined

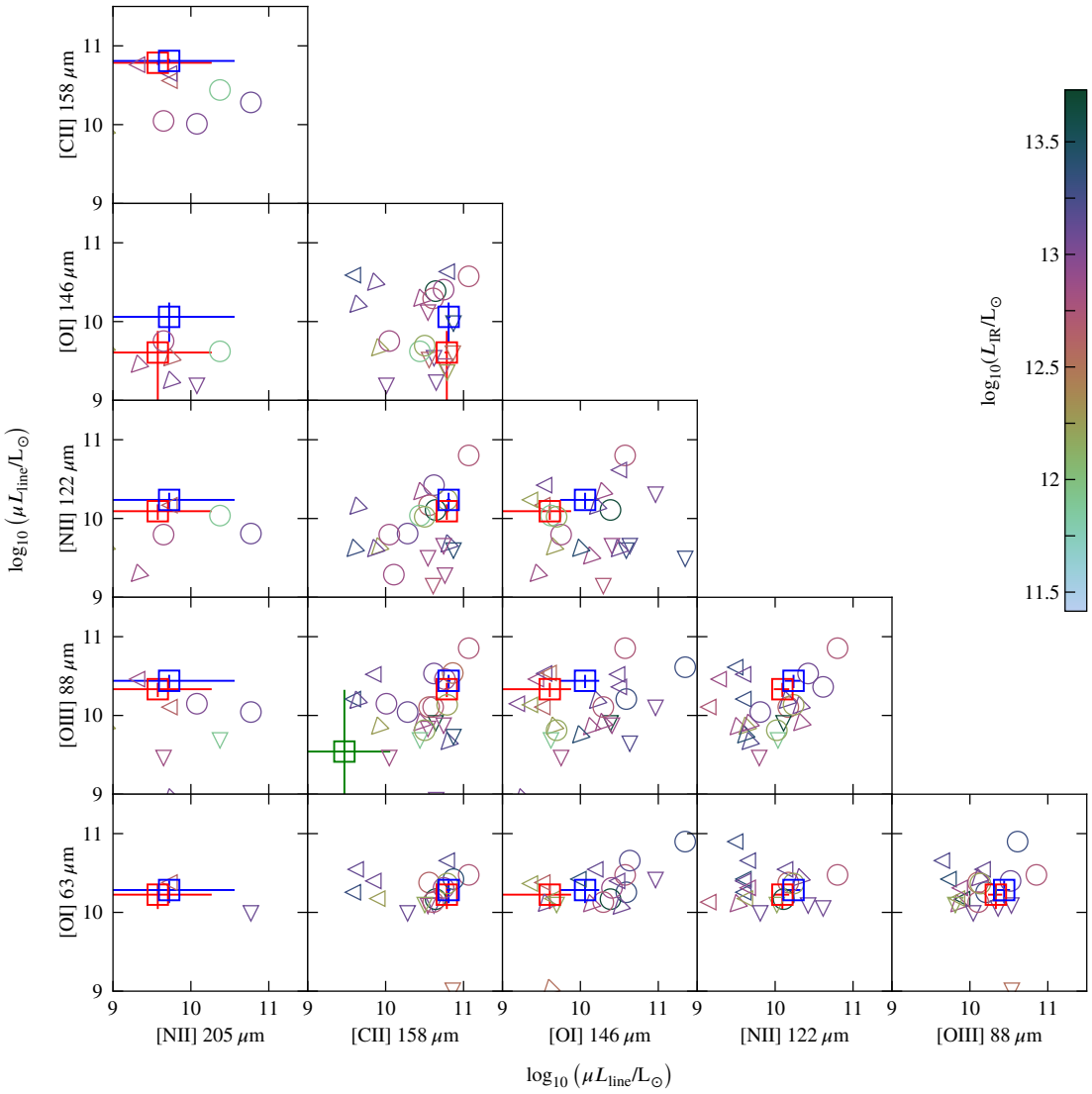

Figure 5.8. Relative strengths of the primary fine-structure emission lines covered by the spectra. Circles and arrows show values for individual sources, with colour denoting $\mu L_{\rm IR}$ as shown by the right hand scale bar. Red squares show measured values from the stack of all spectra, blue squares from the stack of all spectra with individual $L > 3\sigma$ detections of the relevant lines and green squares the stack of all spectra without individual line detections.

with the same method as for the individual spectra. The measured values are tabulated in Table 5.4 and shown in Figure 5.9. Unfortunately only [C II] has a high enough s/n to determine any trends from the binned stacks. Line ratios from the full stack are displayed in Figure 5.8, along with those from the individual spectra.

5.3.3 Modelling

To gain further insight into the physical conditions within and relative emission from H II regions and PDRs we carried out model calculations using version 13.03 of the spectral synthesis code Cloudy, last described in Ferland et al. (2013). These calculations were based upon those of Abel et al. (2005), self-consistently modelling the transition from a H II region through a PDR

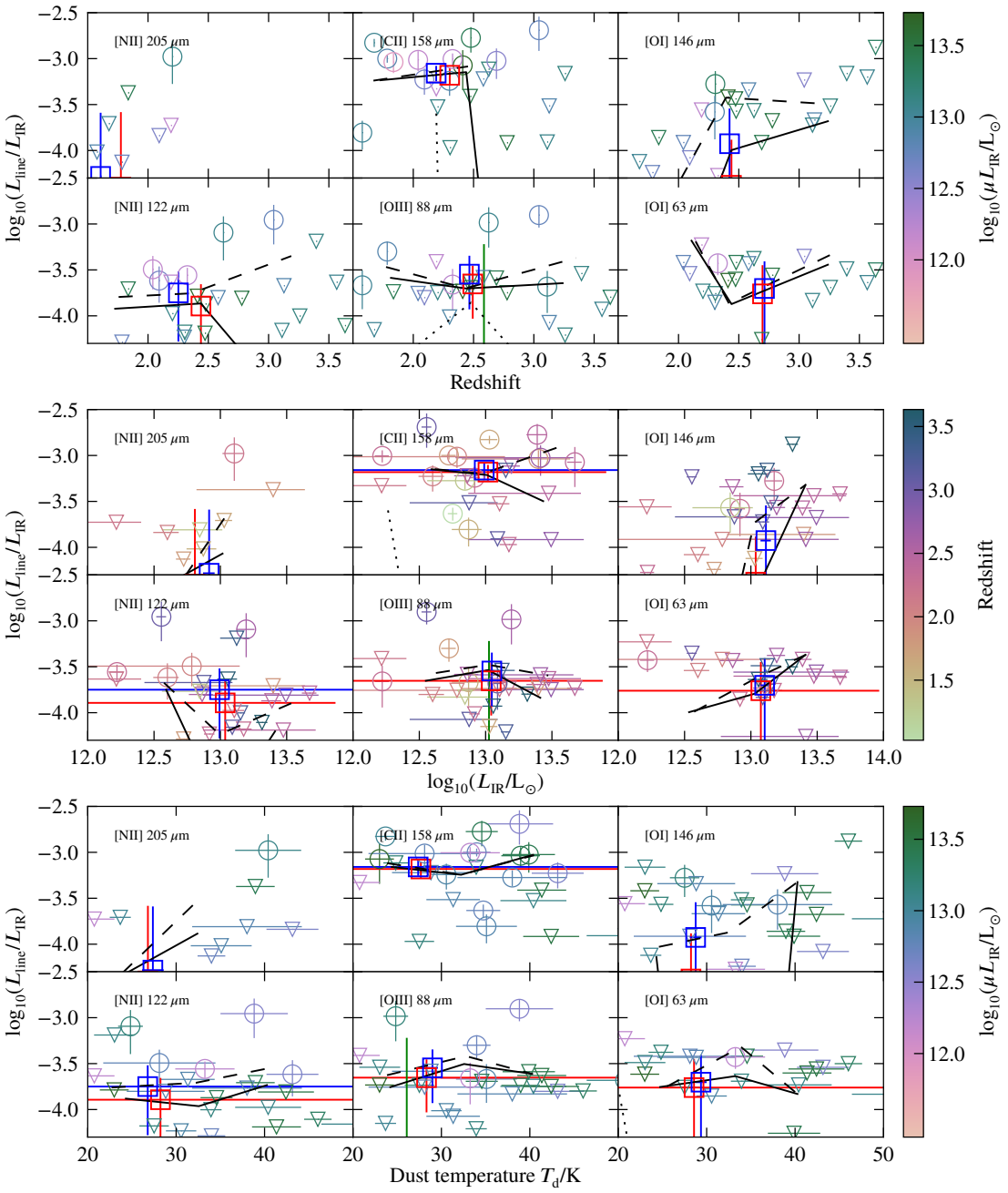

Figure 5.9. Relative line strength of the strongest fine-structure lines covered by a reasonable number of spectra as a function of z, $L_{\rm IR}$ and $T_{\rm d}$.
In each panel circles and arrows display individual sources, with colour denoted by the right hand scale. Red squares show measured values from the stack of all spectra, blue squares from the stack of all spectra with individual $L > 3\sigma$ detections and green squares the stack of all spectra without individual detections. Black lines show line strengths measured from spectra binned into three groups based upon their source properties. Within each bin, measurements from the stack of all spectra, only those with individual detections, and those without individual detections are shown as solid, dashed and dotted lines respectively.
Upper: Relative line strength as a function of redshift.
Middle: Relative line strength as a function of $L_{\rm IR}$, similar to that shown in Figure 5.5.
lower: Relative line strength as a function of $T_{\rm d}$, which will be related to SFR surface density such that a decrease in the line to continuum ratio with increasing $T_{\rm d}$ may be expected.

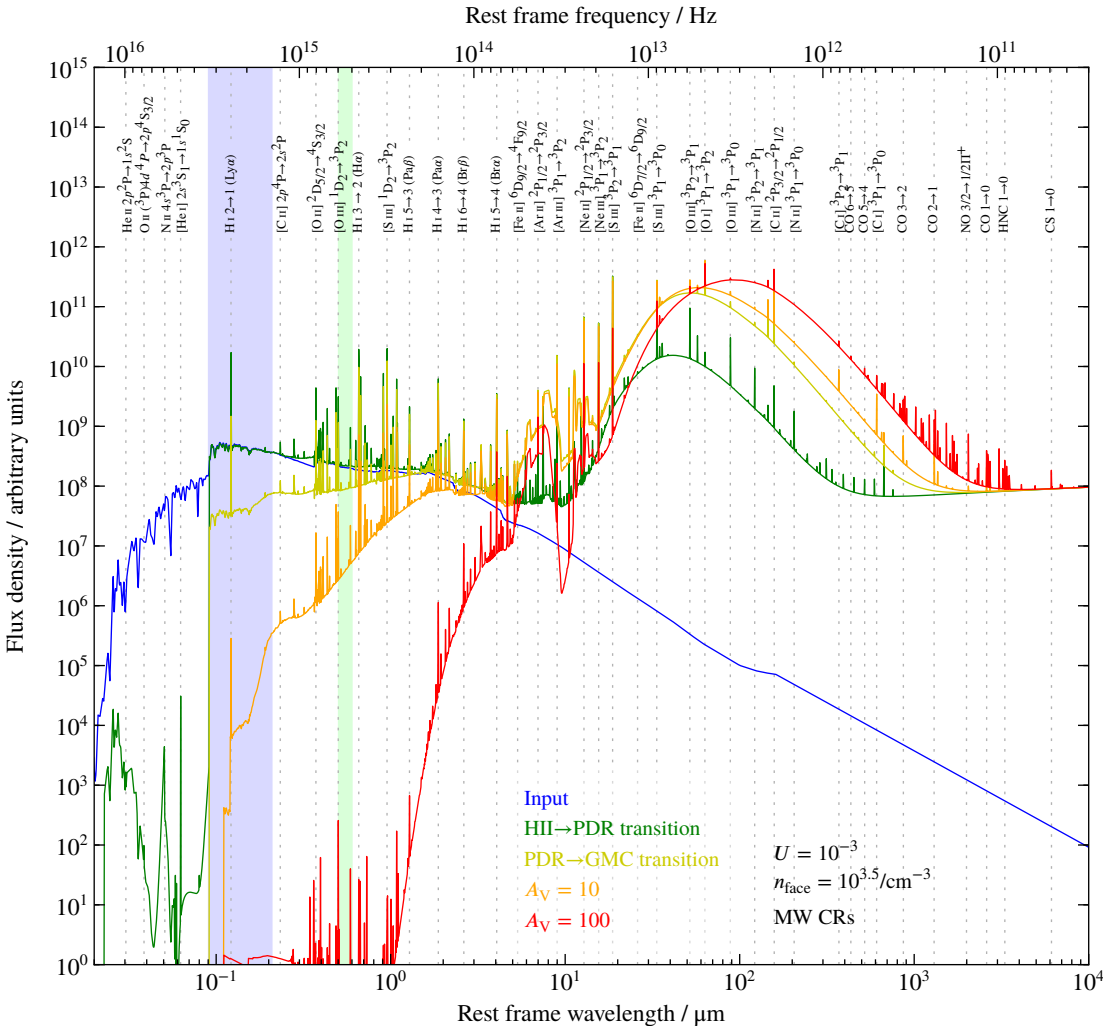

Figure 5.10. FUV–radio continuum at several depths through a molecular cloud from a Cloudy simulation. The spectral regime contributing to G_0: the non-ionising FUV radiation field; is indicated by a blue band, and the regime within the FWHM of the V band (and hence measured by A_V) is indicated by a green band. Spectral lines are shown with a FWHM of 500 km s^{-1}.

to a molecular cloud through assumption of constant pressure. For comparison with this and subsequent works (e.g. Abel et al. 2009; Fischer et al. 2014), many of the same parameter values are used, others described below are however changed to be more applicable to high-redshift star-forming galaxies.

The input stellar continuum was obtained from Starburst 99 (Leitherer et al. 1999), using the latest Geneva evolutionary tracks (with zero rotation Ekström et al. 2012), and the default stellar atmosphere models (Lejeune, Cuisinier, and Buser 1997; Hillier and Miller 1998; Pauldrach, Hoffmann, and Lennon 2001), with a Kroupa (2001) IMF and an assumption of constant star formation for 10^7 years before the observation time.

The Cloudy simulations assume a spherical cloud around the ionising source, with a covering factor of unity and run to a column density of $10^{17} - 10^{24.5}$ cm^{-2}, in steps of $10^{0.5}$ cm^{-2}. The hydrogen number density at the inner face of the model $n_{\mathrm{H;face}} \sim n_{\mathrm{H\,II}}$, and the U: the ratio of

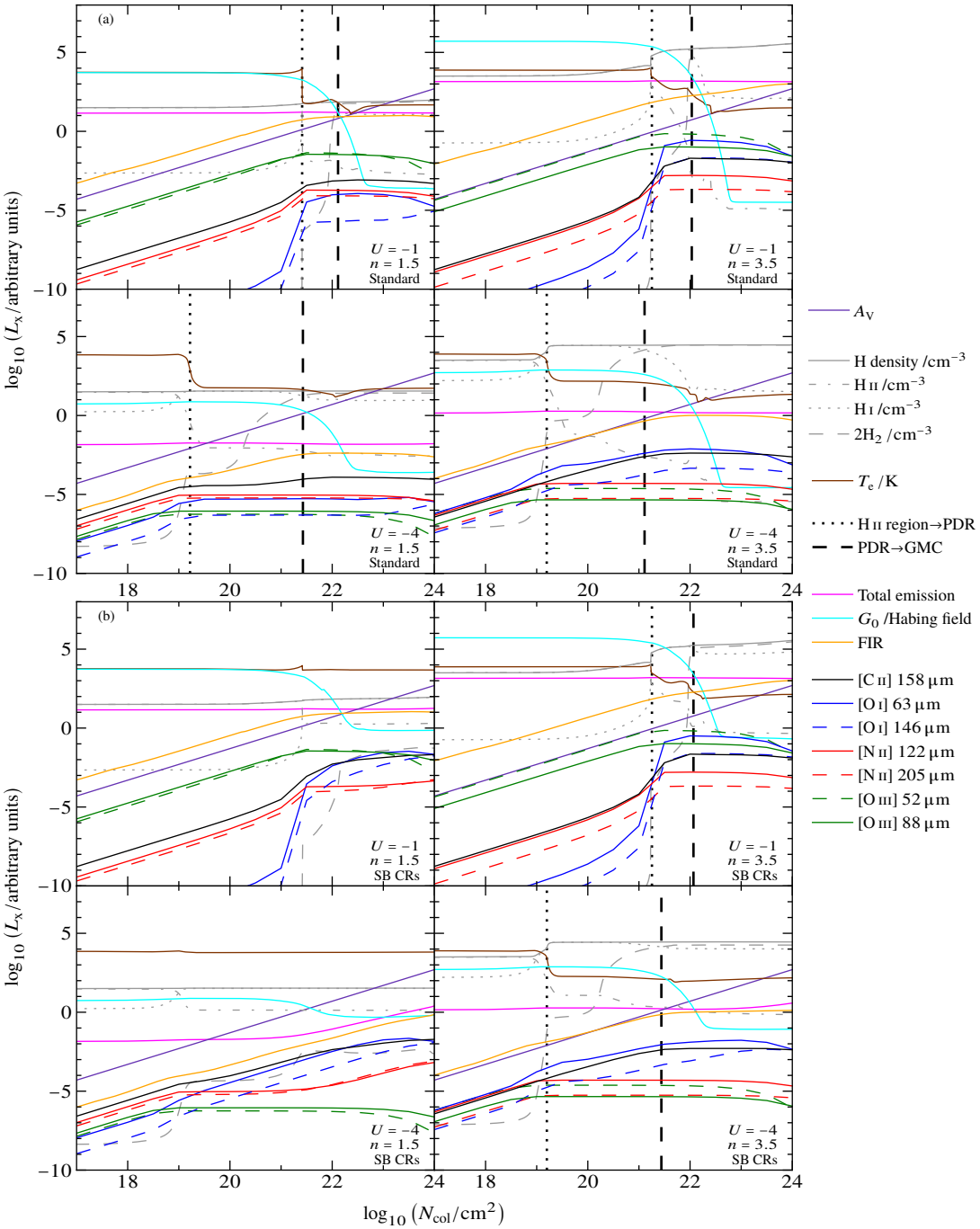

Figure 5.11. Gas properties and observed line and continuum intensities as a function of cloud column density.
Upper four panels (a): Two U and n_{face} values with all "standard" parameters, including a Milky Way-like cosmic ray ionisation rate and magnetic field of initial value 100 µG.
(b): The same but with a cosmic ray ionisation rate 10^3 times larger, as expected within a starburst galaxy.
Vertical lines denote the chosen H II region-to-PDR transition ($n_{H^+}/n_{H;tot} = 0.01$), and the PDR-to-molecular cloud transition ($2n_{H_2}/n_{H;tot} = 0.5$). In the left hand starburst-cosmic ray panels, these criteria are not reached.

Figure 5.11. Continued
(c): Magnetic pressure 10× lower than in the standard model. *(d)*: No magnetic pressure.

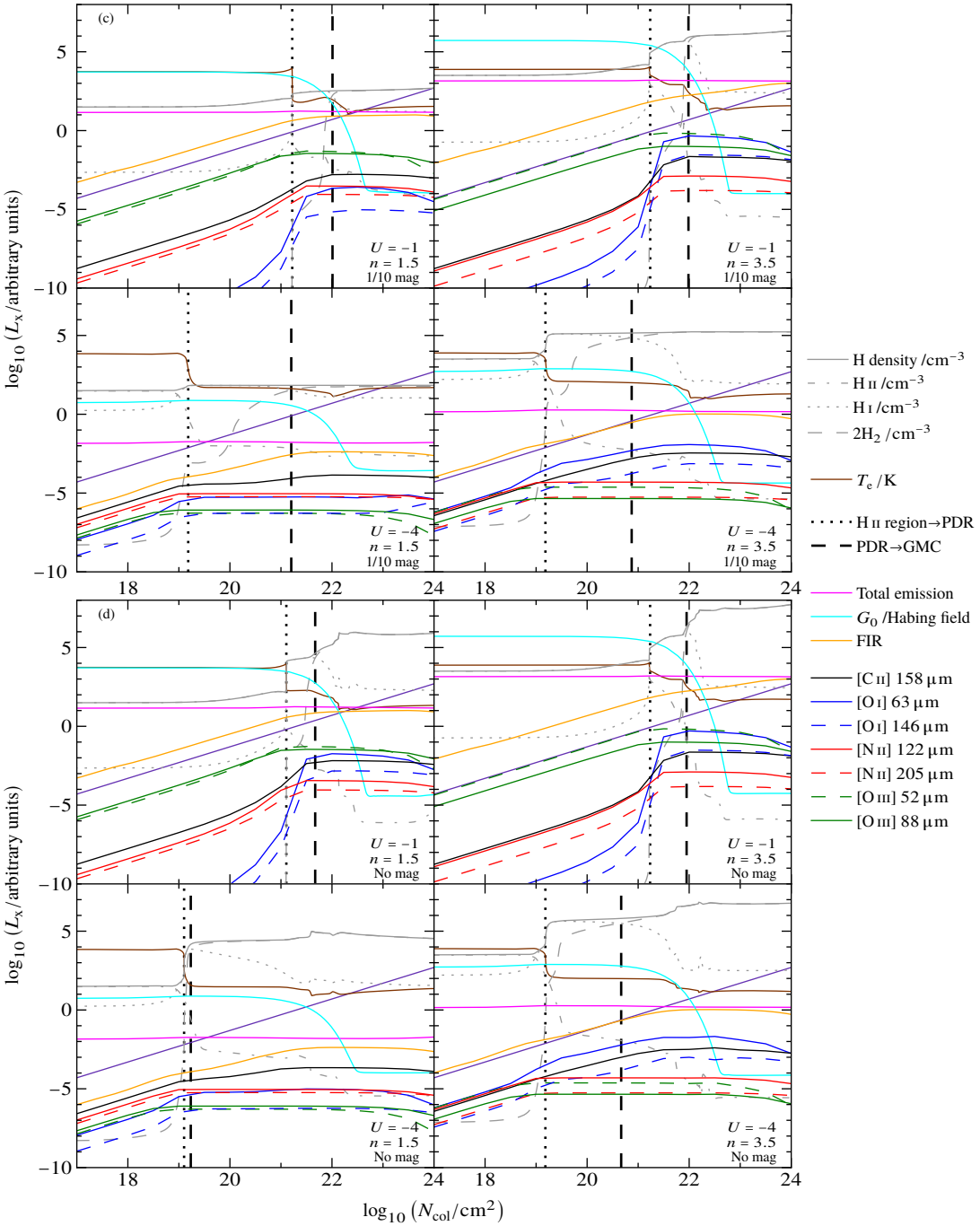

the ionising photon flux ϕ_H to n_{face}, were both varied to produce a grid of models for each column density endpoint.

Despite the high redshifts at which our sources lie, chemical evolution is thought to progress quickly within massive galaxies and high-redshift DSFGs (e.g. Nagao et al. 2012), so solar metallicity is assumed in both this input spectrum and the Cloudy gas. The relative Cloudy chemical species abundances are set to the "ISM" setting, with the "Orion" grain-size distribution

used: which is deficient in small grains in comparison to the Milky Way ISM as a whole; to reflect the likely destruction of some fraction of small grains by sputtering and SNe shocks in star-forming environments in high-redshift DSFGs. The standard model assumes a Milky Way-like cosmic ray ionisation rate of 5×10^{-17} s^{-1}, and a magnetic field with the form $B_{\mathrm{depth}} = 100\,\mu\mathrm{G}\left(\frac{n_{\mathrm{H;depth}}}{n_{\mathrm{H;face}}}\right)^{2/3}$ that dominates the pressure at high column density.

Figure 5.10 shows the evolution of the output SED with increasing column density towards the energy input source.

Three modifications to this model were also trialled to explore the effects of variation of some of these parameter value choices on the resultant continuum and line fluxes. The first utilised a starburst-appropriate cosmic ray ionisation rate of 5×10^{-14} s^{-1} (Acero et al. 2009; Papadopoulos 2010). The second utilised a magnetic pressure 10× lower than in the standard model, and the third removed magnetic pressure entirely, such that only radiation pressure and thermal gas pressure contribute.

Shown in Figure 5.11 are continuum and line intensities as a function of depth through the cloud at four different combinations of U and n_{face}. As in Abel et al. (2005), the H II region to PDR transition is taken as the point at which $n_{\mathrm{H^+}}/n_{\mathrm{H;tot}} = 0.01$, and the PDR to molecular cloud transition at $2n_{\mathrm{H_2}}/n_{\mathrm{H;tot}} = 0.5$. As the constant pressure nature of this model causes the gas density to vary with temperature and hence depth through the cloud (see Figure 5.11), the mean gas density within the PDR limits n_{PDR} is calculated for comparison to other PDR models which assume a single gas density (e.g. Kaufman et al. 1999; Meijerink, Spaans, and Israel 2007). The non-ionising FUV continuum measure G_0 is also calculated at the inner edge of the PDR for comparison to these models. The values of these parameters as a function of U and n_{face} for the standard model is shown in Figure 5.12.

As the ionisation parameter increases, the H II region extends to higher column densities and the H II region lines become stronger, in particular the [O III] lines. The non-ionising FUV continuum decreases with column density (assuming a constant dust-to-gas ratio), however as the PDR begins at higher column density, the continuum drop-off therefore begins towards the outer edge of the H II region in high-U environments, and so is relatively (but not absolutely) weaker than in lower flux regions.

At higher gas number densities, the gas density increases rapidly at the PDR boundary, reflecting the traditional "illuminated surface of a cloud" view of these environments. At low-n_{face}, the density remains fairly constant throughout, more smoothly transitioning between phases, however the gas temperature still drops rapidly upon entering the PDR.

With a "starburst" cosmic ray ionisation rate, several changes are observed, particularly at low gas density and ionisation flux. At higher column densities, cosmic rays can become the dominant energy source and increase the total radiated output, particularly at $\lambda > 100\,\mu$m. As the cosmic ray ray rate we use is a constant, whereas at constant U the input stellar flux increases with n_{face}, the cosmic rays have a lower effect at high n_{face}. Despite this, the high column density gas temperature remains a factor of a few higher than in the Milky Way cosmic ray model.

At lower $n_{\rm face}$, the temperature can remain almost constant throughout, and the H II region–PDR–molecular cloud boundary criteria imposed above are not met anywhere. Our Cloudy model suggests several differences to the findings of Meijerink et al. (2011) in this regime, with the PDR lines, in particular [O I] 63 μm, being several orders of magnitude brighter than in the Milky Way cosmic ray model, and most lines continuing to increase in output luminosity with column density as the number density of ionised species remains non-negligible.

The "standard" model utilises a relatively strong magnetic field that dominates the pressure at higher column densities, such that the product of the gas density and temperature is not constant, as would be expected with thermal pressure alone. Magnetic field variations will therefore primarily affect molecular, and to a lesser extent atomic, lines. A 10× lower magnetic pressure shifts the column densities at which the phase boundaries occur to lower $N_{\rm col}$, particularly the PDR–GMC transition at low U. As expected the H II region lines and [C II] are not strongly affected, but [O I] increases in strength. Complete removal of the magnetic field causes a large change in gas densities as the product of temperature and density now must be constant. Additionally, the PDR–GMC transition at low U and low $n_{\rm face}$ now occurs at a column density two orders of magnitude lower than in the standard model.

The [O I] line flux is more strongly dependent than [C II] on both cosmic rays and magnetic fields, resulting in line ratio variations, The model used for further analysis must therefore reconcile with our low measured [O I]/[C II] value. As the [O I] line flux remains similar to, or greater than, the [C II] flux across the parameter space with both starburst cosmic rays and no magnetic field, these models cannot be reconciled with observations and are discounted. The model with 1/10 of the standard magnetic pressure produces slightly higher line ratio values than the standard model. The standard model is therefore used for the remainder of this chapter, with the caveat that the magnetic field and cosmic ray ionisation rate are likely incorrect, and further work is required to ameliorate the discrepancy between the observations and predicted starburst properties.

Figure 5.12 displays the application of the model to our observed values, with further description of each panel given below.

The [C II] 158 μm and [O I] 63 μm lines often dominate the gas cooling from a PDR typical of a starburst galaxy, the [O I]/[C II] ratio increasing with both gas density and temperature (at these conditions primarily a function of G_0, via dust grain photoelectric heating). The dust grains themselves re-emit most of the incident FUV radiation in the FIR, and as a result the luminosity ratio ([O I] + [C II])/FIR, typically ~0.1 % in high-redshift DSFGs (see Figure 5.5), provides an estimate of the efficiency of gas heating. This value is however affected by the non-negligible fraction of [C II] produced in H II regions, the strong dependence of the carbon ionisation front upon metallicity via dust, and the optical thicknesses of the lines, in particular $\tau_{\rm [O\,I]\ 63\ \mu m} \sim 1-3$. As neither line is excited strongly within molecular regions, the ratio remains relatively constant with increasing column density. We observe a relatively high [C II]/[O I] value of ~7, and hence a likely $n_{\rm face}$ of $10^{2.5}-10^{3}$ cm^{-3}. This is not the case for all individual galaxies within the sample, with at least the Cosmic Eyelash (Chapter 4) and SDP.11 (Ferkinhoff

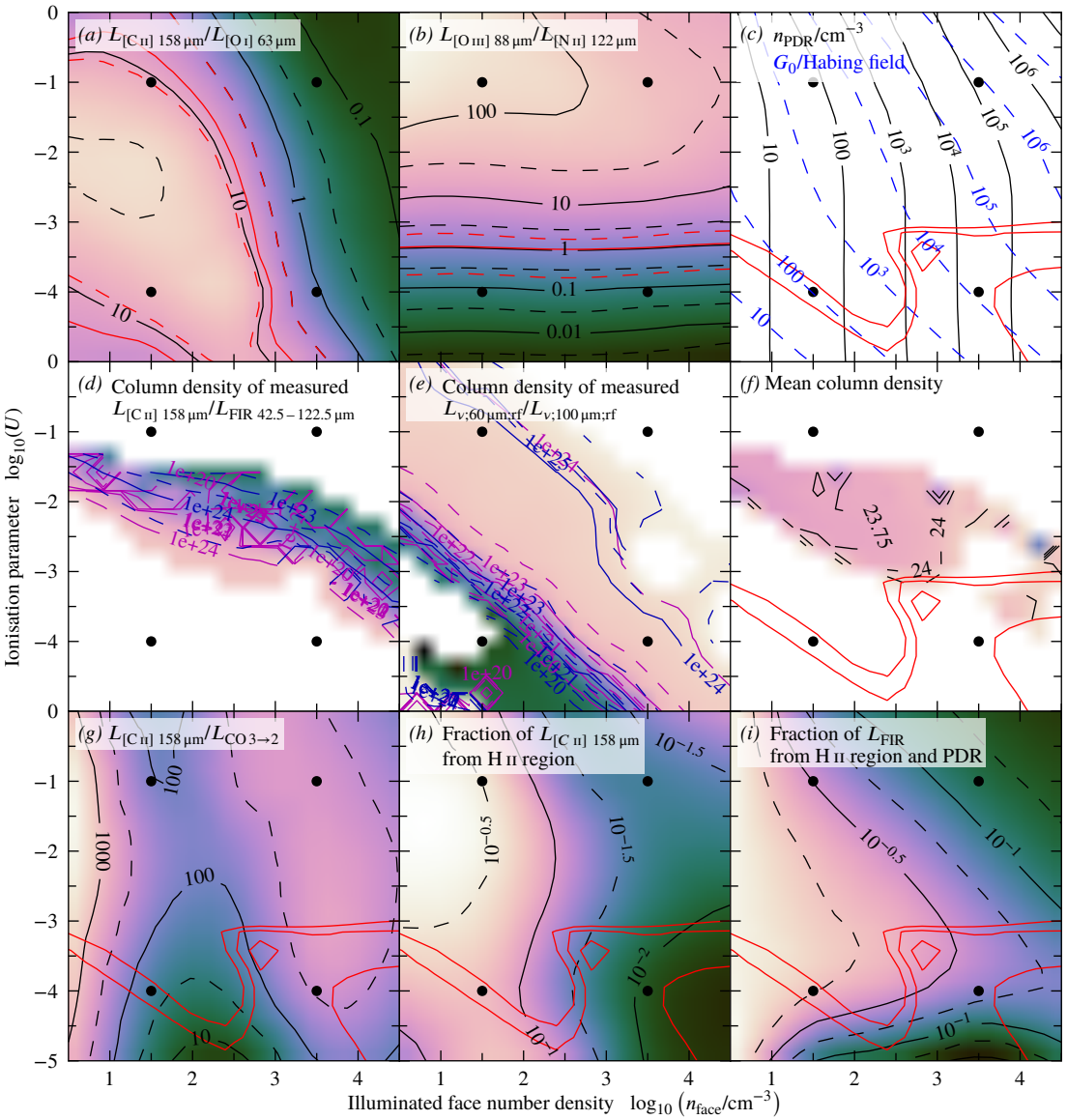

Figure 5.12. Average ISM properties of the total stack as a function U and $n_{H;face}$ determined from our Cloudy models. Black dots indicate the values of U and n_{face} shown in Figure 5.11.
(a): [C II] 158 µm/[O I] 63 µm, this value varies little with U and n_{face} after the GMC transition is reached, with [C II] dominating at low densities and photon fluxes. Red contours display our observed value.
(b): [O III] 88 µm/[N II] 122 µm, with similar critical densities but different ionisation energies, this value is primarily a function of U across most of the parameter space. Red contours display our observed value.
(c): Parameters describing PDR conditions as used in Kaufman et al. (1999). Black contours show the mean hydrogen number density within the PDR. Dashed blue contours show the incident FUV radiation field (6 – 13.6 eV) in units of the local value, the Habing field. Red contours display the best fit constructed from *(a)* and *(b)*.
(d): The column density range within which $1\,\sigma$ of the observed value of $L_{[C\,II]}/L_{FIR}$ is reached. Purple and blue contours show the minimum and maximum of the column density range respectively.
(e): The column density range within which $1\,\sigma$ of the observed value of $L_{\nu;100\,\mu m(rf)}/L_{\nu;60\,\mu m(rf)}$ is reached.
(f): Mean of the ranges in *(d)* and *(e)*. The U and n_{face} ranges suggested here do not overlap those from panel *(c)*, so we assume a column density of 23.5 for panels *(g)* – *(i)*.
(g): Expected [C II] 158 µm/CO $J = 3 \to 2$ ratio. This CO transition is expected to trace the warmer dense molecular clouds in which star-formation occurs better than more easily excited lower-J transitions.
(h): The fraction of the observed [C II] flux produced within the H II region.
(i): The fraction of the observed FIR flux produced at column densities lower than the PDR →molecular region boundary.

et al. 2014) exhibiting more similar line fluxes.

With similar critical densities but different ionisation potentials, the ratio [O III] 88 µm / [N II] 122 µm provides a good tracer of the effective temperature of the ionising source. Both lines increase in intensity as the H II region becomes larger with higher input FUV flux, however the [O III] line increases much more rapidly. We measure similar line fluxes, indicating that the ionisation parameter is relatively low, $\sim 10^{-3.3}$.

Plotted in Figure 5.12 panel *(c)* are G_0 and $n_{\rm PDR}$ contours across the U, $n_{\rm face}$ parameter space. The mean PDR density $n_{\rm PDR}$ is essentially U independent at low incident radiation fluxes, increasing at a slightly higher rate than $n_{\rm face}$, however at high incident fluxes the pressures of all phases are much greater and the density must increase even more rapidly upon entering the PDR to compensate. $U \times n_{\rm face}$ is proportional to the input flux, and G_0 reflects this fairly well across the whole parameter space. Our observations suggest $U \sim 10^{-3.5}$ and $G_0 \sim 10^3 - 10^4$ Habing fields.

The relative FIR line strengths depend upon gas temperature, density and ionisation structure. The FIR continuum strength however also changes with these parameters, in particular as U increases dust absorbs a larger fraction of photons so a lower cooling fraction occurs via line emission. In addition, the continuum strength will increase with column density as FIR lines become optically thick and many of the strongest only emit in PDRs and H II regions, unlike dust which can continue to emit from within molecular material (see Figure 5.11). The [C II]/FIR ratio therefore provides a volume in U–$n_{\rm face}$–$N_{\rm col}$ space, plotted in panel *(d)* of Figure 5.12. The similarly column density dependent ratio $S_{100\,\mu{\rm m;rf}}/S_{60\,\mu{\rm m;rf}}$ is plotted in panel *(e)*. These colours should be fairly reliable as the quantum grain heating option (described in Guhathakurta and Draine 1989) was enabled in order to more accurately model the dust emission SED, particularly from small grains. Only the total $L_{\rm dust}$ is reliable without this option. Together these can suggest best-fitting values for all three components of the parameter space. The U and $n_{\rm face}$ ranges suggested by these two measures does not overlap strongly with the values suggested by the line ratios alone, however the continuum is likely to be more affected by emission from non-star-forming environments than the spectral lines. We therefore assume the stronger emission-line constraints along with an estimated column density of $10^{23.5}\,{\rm cm}^{-2}$, and using these several predictions can be made.

The CO rotational lines are important tracers of molecular gas, with material emitting the mid-J lines such as $J = 3 \rightarrow 2$ expected to be more strongly correlated with FIR cooling lines such as [C II] 158 µm than more easily excited lower-J transitions. Our best-fitting model suggests a mean CO $J = 4 \rightarrow 3$ luminosity 100 – 300 times lower than that of [C II], at around several $\times 10^7\,{\rm L}_\odot$, a similar ratio to that presented in Chapter 3, and a little higher than in local ULIRGs (e.g. Papadopoulos, Isaak, and van der Werf 2007).

Predictions can also be made of the contribution from different phases to the observed line and continuum luminosities. In the most extreme cases the H II region contribution to the observed [C II] 158 µm flux may reach 60 % (Abel 2006), however we estimate only a few percent of the value we observe arises from these environments. The origin of the FIR flux appears to be

primarily the molecular region outside the PDR, an important fact to consider when comparing against other models that treat only PDRs (e.g. Kaufman et al. 1999).

5.4 Conclusions

A large set of SPIRE FTS observations of high-redshift DSFGs contribute significantly to the number of FIR fine-structure emission line detections from this population. The brightest lines from individual galaxies indicate a $L_{[\mathrm{C\,II}]\,158\,\mu\mathrm{m}}$-to-$L_{\mathrm{FIR}}$ ratio of $\sim 10^{-3}$, however when stacking all spectra, including those from galaxies where the [C II] line is too faint to be seen, a mean luminosity of $2 \times 10^9\,\mathrm{L}_\odot$ is found, indicating a lower $L_{[\mathrm{C\,II}]\,158\,\mu\mathrm{m}}/L_{\mathrm{FIR}}$ value of 3×10^{-4}, more consistent with local ULIRGs. Using a grid of Cloudy models to determine properties of the mean ISM properties, we estimate an ionisation parameter value $U = 10^{-3.3}$ and a PDR density of $n_{\mathrm{PDR}} \sim 10^3\,\mathrm{cm}^{-3}$. The mean observed [O I] 63 µm luminosity cannot be explained by a cosmic ray rate predicted to exist in this population, and magnetic field variations will also affect line ratios, therefore further, more sensitive observations will be required to constrain theories and model predictions of high-redshift DSFGs.

Chapter 6

Conclusion

The peak SFRD of the universe occurred at $z \sim 2-3$. Much of this star-formation occurred in small, isolated galaxies fuelled by infalling cold IGM material funnelled along dark-matter filaments, however the most intensely star-forming events involved the mergers of two massive gas-rich galaxies. These are theorised to form the cores of massive ellipticals today, potentially via a quasar stage, and are therefore of keen interest to our understanding of galaxy evolution. Stars are formed from the ISM, and in turn their emission causes dramatic effects within this gas, therefore the knowledge of physical properties and conditions within the ISM is key to understanding the internal processes of galaxies, particularly at this critical evolutionary stage. H II regions, and dense PDRs and molecular gas trace star-formation, however high dust masses eliminate most emission at wavelengths shorter than the MIR. The primary observable H II region and PDR cooling lines therefore lie in the FIR, in particular [C II] 158 μm, commonly the brightest IR line. The redshift of this population places these lines in the regime covered by the *Herschel* SPIRE FTS, however the high redshifts also lower the flux density of such galaxies below the sensitivity of that instrument. Gravitational lensing can boost the apparent area and brightness of galaxies, and strongly lensed high-redshift DSFGs are relatively easily selected from wide area FIR surveys. This thesis has presented *Herschel* SPIRE FTS spectra of a sample of strongly lensed high-redshift DSFGs, which allow us to characterise physical properties of this population otherwise inaccessible with contemporary astronomical science facilities.

Chapter 3 describes the detection of the [C II] 158 μm line in the SPIRE spectrum of one of our sample of strongly lensed DSFGs, providing the first "blind" redshift determination using *Herschel*. H II region lines appear comparatively weak in this galaxy however. The asymmetric double-peaked nature of low-J CO lines obtained through follow-up observations indicates a merger origin of the starburst powering the FIR emission, and an estimate of the mass of molecular gas within the system consistent with that found assuming a dust-to-gas mass ratio. Comparing the estimated flux of the $J = 1 \rightarrow 0$ line to that of [C II] 158 μm and the FIR continuum suggests a larger reservoir of molecular gas than observed among other strongly lensed high-redshift DSFGs, however its ISM otherwise appears typical of this population. The compactness of radio continuum emission coupled with the radio spectral slope and FIRRC measure suggests AGN emission contributes strongly to the radio output of the galaxy.

The determination of a "blind" redshift using *Herschel* provides hope that the much more sensitive SPICA, through the 6000 pixels of SAFARI, will be able to find redshifts of multiple unlensed high-redshift DSFGs in a single few-hour pointing.

Chapter 4 describes measurements from several repeat observations of the Cosmic Eyelash, a galaxy previously studied in detail due to its very high amplification factor. We detect several FIR transitions including the H II region lines [O III] 88 µm and [N II] 122 µm, which appear to be dominated by the most strongly star-forming of the massive clumps previously found in velocity-resolved CO observations. Additionally, we present the first detection of a massive molecular outflow at high-redshift, similar to those exhibited in nearby ULIRGs. We attribute the origin of this outflow to the same star-forming clump as the H II region lines, suggesting a maximum velocity of 700 km s^{-1}. This outflow appears to be driven by the combined feedback of star-formation rather than an AGN.

Our detections of OH 119 µm absorption in two of the brightest galaxies of the sample the Cosmic Eyelash and G15.v2.19, and in the rest-frame stack of demagnified spectra indicates that molecular outflows are likely common within this population, and further observations with ALMA or SPICA will confirm whether star-formation alone is the usual driver, whether star-formation is capable of causing the outflowing gas to become unbound, and if so what fraction of molecular and total gas mass is lost through this process in comparison to conversion to stars.

Chapter 5 shows results from our full sample of spectra, including measurements of spectral lines from sub stacks at different redshifts, luminosities and dust temperatures. We find that while individually-detected [C II] lines indicate $L_{[\mathrm{C\,II}]}/L_{\mathrm{FIR}} \sim 3 \times 10^{-3}$, the stack of all spectra including those in which [C II] is not bright enough to be detected suggests a value 3.6×10^{-4}. While this may be lower than expected, the selection criteria preferentially satisfy compact galaxies that may be more similar to local ULIRGs than the unlensed population as a whole. No strong trends of variation of this ratio with redshift or L_{IR} are found, however the number of sources within each bin is too low to draw any conclusions. A weak decrease with increasing dust temperature is observed. The [O I] line particularly appears to be weaker in our mean stack than found in several individual galaxies, indicating that the mean PDR has a relatively low density. The lack of known redshifts and robust lens models hampers efforts to measure weak lines somewhat, so as future observations and models are performed, these stacks could be reproduced to investigate if further conclusions could be drawn. Using a set of ISM models, we estimate H II region and PDR gas densities of $\sim 10^3$ and $10^{3.5}$ cm^{-3}, an ionisation parameter of $10^{-3.3}$, and a column density of $10^{23.5} - 10^{24}$ cm^2. These values are fairly typical of those expected within this population, however the large contribution to the FIR flux from molecular regions suggests simpler PDR-only simulations may be insufficient to model the ISM within such galaxies.

In summary, the spectra and analysis presented here contributes to our knowledge of strongly star-forming galaxies at the epoch of peak star-formation, both individually and as a whole population. The population appears varied, with values of $L_{[\mathrm{C\,II}]}/L_{\mathrm{FIR}}$ reaching from that observed in local

spirals to dense ULIRGs, however weak mean [O I] emission suggests lower gas densities than are observed in local ULIRGs. Molecular outflows may well be common among these galaxies, but further observations will be required to confirm this and the evolutionary effect they have.

Strongly lensed galaxies, either these selected from *Herschel* data or similar selections from SPT will remain critical to our understanding of the inner processes of high-redshift galaxies for years to come as they represent the best opportunity to investigate individual galaxies in detail. Long-baseline ALMA imaging will allow resolution down to few-hundred-parsec scales in dust, CO and [C II] emission, with the spectral lines adding important dynamical information. Using these data, lens models will improve and could be retroactively applied to the observations presented in this thesis, along with new observations from APEX/ZEUS-2, APEX/FLASH and ALMA and future facilities such as SPICA and SKA. SPICA in particular, observing a range of lines including [O I] 63 μm, [O III] 52 μm, [S III] 33 μm and others, should dramatically improve on the results obtained in this thesis. Improvements in PDR models are also required, to investigate the effect of cosmic rays, turbulence and magnetic fields on observed lines, and these will conclusively reveal the processes at work within the ISM. Optical/NIR imaging with JWST and E-ELT of the existing stellar population will be important to examine observed offsets between this and the starburst components, and determine the source-plane morphologies. Together these improvements over the next 10 – 20 years will bring a major leap in our understanding of galaxy evolution.

Glossary

6df 6dF Galaxy Survey (Jones et al. 2004): aimed to measure redshifts and peculiar velocities of 150 000 galaxies out to $z \sim 0.15$ 1

ACT Atacama Cosmology Telescope (Swetz et al. 2011): a 6 m microwave telescope designed to measure CMB anisotropies, located on Cerro Toco 1, 4, 32

AGB Asymptotic giant branch star, inside which hydrogen and helium are fused in shells around the core 13, 22

AGN Active galactic nucleus, an actively-accreting (and emitting) SMBH . . . . . v, 6, 8, 13, 23, 26–28, 30, 34, 36, 39, 45, 46, 48–50, 53, 96–98, 100, 101, 104–109, 112, 113, 115, 130–132, 149, 150, 161

ALMA Atacama Large Millimeter/Submillimeter Array: 50×12 m antennas covering ~0.3 – 3 mm, plus a smaller compact array, located at the Llano de Chajnantor Observatory 7, 10, 30, 35, 39, 43, 45, 46, 53, 54, 61, 89, 99, 100, 129, 133, 135, 150, 151, 153

α_{CO} Conversion factor from CO $J = 1 \rightarrow 0$ luminosity to molecular gas mass 41, 42

APEX Atacama Pathfinder EXperiment (Güsten et al. 2006), a single prototype 12 m ALMA dish at the Llano de Chajnantor Observatory 34, 48, 65, 129, 151, 156, 158, 164

Arp 220 The archetypal and nearest ULIRG, aka IC 1127 . . . . . 24, 26, 35, 53

A_V Total extinction in the V band (~551 nm) measured in magnitudes 16, 20, 34

AzTEC The AzTEC 144 element bolometer array camera (Wilson et al. 2008), primarily images at ~1.1 mm, now located on the LMT 30, 32

BAO Baryon acoustic oscillation 1, 4

BCG Brightest cluster galaxy, typically the most massive and central galaxy of a cluster . . . 6, 68

β Spectral index of the change in UV luminosity density of a young SSP with increasing wavelength, typically ~−2 13

Big Bang Theorised infinite density origin of the Universe 13.8×10^9 yr before present . . . 1, 3

black hole A space-time singularity, surrounded by an event horizon at the Schwarzschild radius 44, 45

BLAST Balloon-bourne Large Aperture Submillimeter Telescope (Pascale et al. 2008), flew 4 flights from 2003 to 2010 . . . . . 33, 47

BOSS Baryon Oscillation Spectroscopic Survey (Dawson et al. 2013), part of SDSS-III . . . 1

BPT Baldwin-Phillips-Terlevich (Baldwin, Phillips, and Terlevich 1981) diagram [N II]/Hα vs [O III]/Hβ 17

BzK A galaxy selected by its photometry in the B, z and K bands, often a high-redshift star-forming galaxy 39

CARMA Combined Array for Research in Millimeter-wave Astronomy, 23 antennas, Inyo Mountains . . . . . v, 65, 92, 93, 120, 131

CDFS Chandra Deep Field South, located at 03:32:28 -27:48:30 and includes the Hubble Ultra-Deep Field (HUDF) 155

CDM Cold dark-matter, $v_{dark-matter} \ll c$ 6

CFHT Canada-France-Hawaii Telescope, 3.6 m, optical/NIR telescope on Mauna Kea . . . 91

CGM Circumgalactic medium 4

CIB Cosmic infrared background, the combined emission of galaxies over all redshifts that is observed in the infrared 27, 28, 99

[C II] 158 µm $^2P_{3/2} \rightarrow ^2 P_{1/2}$, the primary FIR fine-structure emission line of C II with an excitation temperature of 92 K, see Section 1.2.1.1 . . . v, ix, xii, 9–11, 15, 17, 18, 42, 53, 57, 58, 62, 63, 65, 92, 93, 97–100, 102–106, 113, 123, 124, 129–136, 139, 145–151, 160

Cloudy Spectral synthesis code performing photoionisation model calculations, last described in Ferland et al. (2013) 139, 141, 143, 145, 146, 148

CMB Cosmic microwave background, emission from the surface of last scattering, now an approximately ~2.7 K black-body 1–4, 27, 36, 153, 154, 158, 161, 163

CMF Core mass function, the distribution of masses of pre-stellar cores 20, 21

CO Carbon monoxide, the most common molecule in the ISM after hydrogen and a useful tracer of molecular gas . . . v, xii, 9–12, 17, 19, 20, 23, 26, 40–44, 47, 48, 53, 56–59, 61, 65–67, 89, 90, 92–94, 97–99, 102–107, 111, 113, 117, 120, 122, 130, 131, 133–135, 146, 147, 149–151

^{12}CO The most common chemical variant of CO, containing the isotopes ^{12}C and ^{16}O . . . 10, 20, 59

^{13}CO CO containing the rarer isotope ^{13}C, the slight emission frequency change means its lines are usually optically thin 10, 58

C^{18}O CO containing the rarer isotope ^{18}O, the slight emission frequency change means its lines are usually optically thin 58

COBE *COsmic Background Explorer*, a satellite launched in 1989 to measure the CMB . . . 27,

***H*-ATLAS** *Herschel* Astrophysical Terahertz Large Area Survey (Eales et al. 2010), 550 deg^2, simultaneously imaging in 5 bands across 100 – 500 μm . . . 33, 34, 47, 53, 60–62, 66, 67, 69, 70, 85, 89, 117, 119, 123, 131, 160, 162

Hβ Hydrogen 4–2 transition, aka Balmer-beta 486.1 nm 17, 45, 154

HCN The molecule HCN, primarily emits from the densest regions within GMCs 19, 20, 157

He Helium, the second most abundant element 3, 13, 21, 41, 98

HeLMS *Her*MES Large Mode Survey, a 270 deg^2 SPIRE-only extension to *Her*MES 34, 63, 69, 132

***Her*MES** *Herschel* Multi-tiered Extragalactic Survey (Oliver et al. 2012), programme with *Herschel* observing many fields with different depths 34, 36, 60, 62, 117, 157

Herschel *Herschel Space Observatory* (Pilbratt et al. 2010), a FIR telescope with a 3.5 m primary mirror, containing the instruments HIFI, PACS and SPIRE . . . iii, v, 28, 33–36, 38, 47, 48, 53, 56, 58, 61, 62, 69, 70, 72, 76, 81, 85, 89, 91–93, 95, 99–102, 107, 113, 115, 116, 124, 132, 149–151, 156, 157, 160–162

H I Neutral hydrogen 18, 42

[H I] 21 cm 21 cm ground-state spin-flip emission line of hydrogen 42

HIFI Heterodyne Instrument for the Far Infrared, aboard *Herschel*, a high resolution spectrometer 157

high-redshift There is no accepted definition, but commonly $z \gtrsim 1$ . . . . . v, 1, 4, 8–10, 13, 17, 18, 24, 27, 29–32, 34–51, 53, 54, 56, 58, 60–63, 65, 66, 72, 94, 98–101, 104, 108, 109, 112, 113, 118, 132–136, 138, 141, 143–145, 148–151, 154, 155, 162

H II Ionised hydrogen . . . vii, 9, 11, 12, 15–18, 22, 39, 42, 53, 63, 104, 106, 113, 129, 133, 139, 141, 142, 144–147, 149, 150, 160

HIM Hot intercloud medium 15

HIPE *Herschel* Interactive Processing Environment (Ott 2010) 76, 80, 81, 84, 91, 102

HMXB High mass X-ray binary, a binary star system in which a compact remnant captures stellar wind ejecta from its massive companion 46

HNC HNC, similar in characteristics to HCN 20

HPF High-pass filter, a filter removing power at low frequencies 85–87

HSA *Herschel* Science Archive 76

HST *Hubble Space Telescope* 59, 61, 66, 67, 84, 100, 130

HyLIRG Hyper-luminous infrared galaxy, defined by possessing $L_{\rm IR} > 10^{13} {\rm L}_{\odot}$ 40, 63, 100, 120, 130

ICM Intracluster medium 4

IF Intermediate frequency 90

IGM Intergalactic medium, the dominant repository of baryons in the Universe 4, 29, 49, 109, 112, 149, 163

IMF Initial mass function, the distribution of masses found within a newly-formed SSP 20–22, 39, 40, 49, 141, 163

IR Infrared, the spectral regime from 700 nm to ~1 mm . . . v, 11, 14, 17, 20, 21, 24, 26–28, 30, 36, 38, 39, 44, 97, 105, 106, 108, 135, 149, 154

IRAC Infrared Array Camera, an instrument on board *Spitzer* imaging at 3.6 – 8 μm . . . 36, 163

IRAM Institut de Radioastronomie Millimétrique 32, 90, 92, 93, 156, 159

IRAS The *InfraRed Astronomy Satellite* (Neugebauer et al. 1984), 57 cm diameter, performed full-sky mapping at 12, 25, 60 and 100 μm 24, 26, 29, 38, 96, 161

IRS Infrared Spectrograph on board *Spitzer* 26, 163

ISM Interstellar medium, the gas and dust between stars within a galaxy . . . . . v, 6, 8–11, 13, 15–20, 22, 23, 39, 40, 42, 53, 101, 107, 143, 144, 146, 148–151, 154, 159, 161

J Total angular momentum . . . xii, 10, 19, 23, 26, 41–43, 53, 56, 59, 67, 90, 92–94, 97, 98, 111, 112, 120, 131, 134, 146, 147, 149, 153

JAXA Japan Aerospace Exploration Agency 89

JCMT James Clerk Maxwell Telescope; located on Mauna Kea, host to SCUBA . . . 30, 34, 36, 161

JWST James Webb Space Telescope 7, 151

k-correction k-correction 31, 36, 37, 47

Keck The W. M. Keck Observatory consists of two 10 m optical/NIR telescopes on Mauna Kea 47, 100, 130, 131

l CMB angular frequency 1

LABOCA Large APEX bolometer camera (Siringo et al. 2009): a 870 μm camera with a 11 arcsec FOV 50, 158

$L_{\mathbf{bol}}$ Bolometric luminosity 21, 105, 108

LESS LABOCA ECDFS Submillimeter Survey (Weiß et al. 2009b): APEX/LABOCA 870 μm coverage of the ECDFS field 35, 44, 47

$L_{\mathbf{FIR}}$ Far-infrared luminosity: commonly measured across 42.5 – 122.5 μm . . . 48, 66, 99, 104, 123, 129, 131, 133–136, 146, 148, 150

SCUBA-2 Submillimetre Common-User Bolometer Array 2 (Holland et al. 2013): upgrade of SCUBA 30, 33, 35

SDP Science Demonstration Phase of *H*-ATLAS: a 14.4 deg^2 region in the GAMA-9 hr field 61, 62

SDSS Sloan Digital Sky Survey 1, 34, 131, 154

SED Spectral energy distribution . . . v, xi, xii, 21, 22, 26, 27, 30, 34–37, 39, 46, 47, 58, 65, 70, 82, 95, 97, 98, 103, 106, 115, 116, 118–122, 129, 134, 137, 138, 144, 147

SFE Star formation efficiency: there are various definitions, usually SFR or $L_{\rm IR}$ per unit gas mass 97

SFH Star formation history 40

SFR Star formation rate: usually an average over a whole galaxy, in $\mathrm{M_\odot yr^{-1}}$ . . . 13, 24–29, 31, 34, 36, 39, 44–46, 48, 49, 51, 58, 66, 97, 99–101, 106, 108, 109, 111, 113, 115, 120, 121, 129–131, 133, 135, 136, 140, 155, 156, 159, 162, 163

SFRD Star formation rate density: an average measure of the SFR of the Universe, in $\mathrm{M_\odot yr^{-1} Mpc^{-3}}$ 25, 28, 29, 49, 54, 149, 163

SGP South Galactic Pole: a field covered by *H*-ATLAS 62, 119, 131

SHARC-II 350 and 450 μm camera located on CSO (Dowell et al. 2003) 33, 57

SIE Singular isothermal ellipsoid: an ellipsoid variant of a SIS 56, 99

sinc $\sin(x)/x$ 93, 103–105

SIS Singular isothermal sphere: a simple dark-matter halo mass profile $\rho(r) = \sigma^2/(2\pi G r^2)$ 55, 56, 162

SKA Square Kilometre Array: when completed will cover 0.05 – 30 GHz with a total aperture area of ~1 km^2, located in South Africa and Australia 7, 42, 151

SLED Spectral line energy distribution 10, 41

SMA Submillimeter Array: 8 × 6 m antennas, located on Mauna Kea . . . 45, 59, 66, 67, 90, 92, 100, 104, 117, 118, 129–131

SMBH Supermassive black hole: a black hole at the centre of a galaxy with $M > \sim 10^5\,\mathrm{M_\odot}$ 27, 40, 45, 46, 48, 49, 51, 153

SMEC Spectrometer mechanism: the mirror-moving mechanism at the heart of the SPIRE FTS 69, 70, 72, 77, 79

SMG Submillimetre galaxy: traditionally refers to a high-redshift galaxy exhibiting $S_{850\,\mu\mathrm{m}} > 5$ mJy 21, 29, 31, 32, 34, 35, 39, 40, 42–45, 47–51, 106, 108, 109, 112, 113

SN Supernova: the explosion marking the death of a massive star, typically releasing ~10^{44} J of kinetic energy . . . . . iii, 7, 8, 13, 15, 20–23, 36, 131, 144, 156

SPICA The Space Infrared telescope for Cosmology and Astrophysics, a planned 3.5 m

WMAP *Wilkinson Microwave Anisotropy Probe*: a spacecraft measuring CMB anisotropies 1, 4, 89, 161

X-ray A photon with a wavelength approximately $0.01 - 10\,\mathrm{nm} \sim 0.1 - 100\,\mathrm{keV}$ 4, 10, 23, 29, 45, 46, 100, 157

Z Metallicity: a measure of the abundance of elements other than hydrogen and helium 8, 13, 20, 21, 41, 42, 98, 99, 106, 143, 145

z Redshift: a measure of recession velocity $z = (\lambda_{\mathrm{obs}} - \lambda_{\mathrm{emit}})/\lambda_{\mathrm{emit}}$ . . . v, xi, xii, 2–10, 13, 19, 25–32, 34–40, 42, 43, 46–51, 53, 56–66, 82, 83, 89, 90, 92–94, 96, 97, 99–104, 107, 109, 113, 115, 116, 119–124, 129–132, 134–138, 140, 143, 149, 150, 153, 164, 180

ZEUS z(Redshift) and Early Universe Spectrometer (Stacey et al. 2007): spectrometer operating in the 350 and 450 µm windows 132

ZEUS-2 z(Redshift) and Early Universe Spectrometer-2 (Ferkinhoff et al. 2014): $200 - 850$ µm spectrometer located on APEX 129, 151

Zpectrometer An ultra-wideband 26.5 40GHz spectrometer on GBT (Harris et al. 2007) . . . 65, 90

Z-Spec A broadband $185 - 305$ GHz spectrometer on CSO (Glenn et al. 2007) 65

References

Bibliography

Abel, N. P., 2006, MNRAS, 368, 1949–1958 . . . . . 133, 147

Abel, N. P., Dudley, C., Fischer, J., Satyapal, S., and van Hoof, P. A. M., 2009, ApJ, 701, 1147–1160 . . . . . 98, 141

Abel, N. P., Ferland, G. J., Shaw, G., and van Hoof, P. A. M., 2005, ApJS, 161, 65–95 . . . 16, 18, 139, 144

Acero, F. et al., 2009, Science, 326, 1080– 144

Alaghband-Zadeh, S. et al., 2012, MNRAS, 424, 2232–2248 44

Alberts, S. et al., 2013, MNRAS, 431, 194–209 36

Alexander, D. M. et al., 2005, ApJ, 632, 736–750 46

Alexander, D. M. et al., 2008, AJ, 135, 1968–1981 . . . . . 45, 46, 49

Aliev, A. N. and Özdemir, N., 2002, MNRAS, 336, 241–248 45

Allevato, V. et al., 2011, ApJ, 736, 99 50

ALMA Partnership et al., 2015, ApJL, 808, L4 . . . . . 117, 129

Almeida, C., Baugh, C. M., and Lacey, C. G., 2011, MNRAS, 417, 2057–2071 51

Amblard, A. et al., 2010, A&A, 518, L9 . . . . . 37, 47, 116

Assef, R. J. et al., 2011, ApJ, 728, 56 49

Baldwin, J. A., Phillips, M. M., and Terlevich, R., 1981, PASP, 93, 5–19 . . . . . 17, 154

Banerji, M. et al., 2011, MNRAS, 418, 1071–1088 . . . . . 47, 101, 109

Barger, A. J. et al., 1998, Nature, 394, 248–251 30

Barger, A. J. et al., 1999, AJ, 117, 2656–2665 47

Barger, A. J. et al., 2012, ApJ, 761, 89 . . . . . 45, 96

Barker, S., de Grijs, R., and Cerviño, M., 2008, A&A, 484, 711–720 26

Barlow, M. J. et al., 2010, A&A, 518, L138 13

Bastian, N., Covey, K. R., and Meyer, M. R., 2010, ARA&A, 48, 339–389 21

Bate, M. R., 2009, MNRAS, 392, 1363–1380 21

Bate, M. R. and Bonnell, I. A., 2005, MNRAS, 356, 1201–1221 21

Baugh, C. M. et al., 2005, MNRAS, 356, 1191–1200 21

Bayliss, M. B. et al., 2011, ApJL, 727, L26 58

Behroozi, P. S., Wechsler, R. H., and Conroy, C., 2013, ApJ, 770, 57 29

Bell, E. F., 2003, ApJ, 586, 794–813 96

Bell, E. F. et al., 2012, ApJ, 753, 167 50

Belli, S., Newman, A. B., and Ellis, R. S., 2014, ApJ, 783, 117 50
Bendo, G. J. et al., 2013, MNRAS, 433, 3062–3078 . . . . . 63, 117
Bernardi, M. et al., 2010, MNRAS, 404, 2087–2122 7
Berta, S. et al., 2011, A&A, 532, A49 28
Bertone, G., Hooper, D., and Silk, J., 2005, Phys. Rep., 405, 279–390 6
Béthermin, M., Dole, H., Lagache, G., Le Borgne, D., and Penin, A., 2011, A&A, 529, A4 47
Bianchi, S., Davies, J. I., and Alton, P. B., 1999, A&A, 344, L1–L4 14
Biggs, A. D. and Ivison, R. J., 2008, MNRAS, 385, 893–904 . . . . . 43, 106
Blain, A. W., 1996, MNRAS, 283, 1340–1348 . . . . . 56, 60
Blain, A. W., Barnard, V. E., and Chapman, S. C., 2003, MNRAS, 338, 733–744 31
Blain, A. W., Ivison, R. J., and Smail, I., 1998, MNRAS, 296, L29 58
Blain, A. W., Kneib, J. -P., Ivison, R. J., and Smail, I., 1999, ApJL, 512, L87–L90 58
Blain, A. W., Smail, I., Ivison, R. J., Kneib, J. -P., and Frayer, D. T., 2002, Phys. Rep., 369, 111–176 30
Bland, J. and Tully, B., 1988, Nature, 334, 43–45 23
Bolatto, A. D., Wolfire, M., and Leroy, A. K., 2013, ARA&A, 51, 207–268 . . . . . 41, 98
Borne, K. D., Bushouse, H., Lucas, R. A., and Colina, L., 2000, ApJL, 529, L77–L80 . . . 26
Borys, C. et al., 2005, ApJ, 635, 853–863 40
Borys, C. et al., 2006, ApJ, 636, 134–139 . . . . . 57, 63, 132
Bothwell, M. S. et al., 2010, MNRAS, 405, 219–233 43
Bothwell, M. S. et al., 2013, MNRAS, 429, 3047–3067 . . . . . 41, 42, 98, 112, 120, 134
Bournaud, F. et al., 2011, ApJ, 730 7
Bournaud, F. et al., 2014, ApJ, 780, 57 43
Bourne, N. et al., 2012, MNRAS, 421, 3027–3059 37
Bouwens, R. J. et al., 2014, ApJ, 795, 126 7
Bradač, M. et al., 2008, ApJ, 687, 959–967 4
Brauher, J. R., Dale, D. A., and Helou, G., 2008, ApJS, 178, 280–301 . . . . . 104, 105, 134
Briceño, C., Luhman, K. L., Hartmann, L., Stauffer, J. R., and Kirkpatrick, J. D., 2002, ApJ, 580, 317–335 21
Brinchmann, J. et al., 2004, MNRAS, 351, 1151–1179 24
Broadhurst, T. and Lehar, J., 1995, ApJL, 450, L41 30
Bromm, V. and Larson, R. B., 2004, ARA&A, 42, 79–118 7
Brown, R. L. and Vanden Bout, P. A., 1991, AJ, 102, 1956–1959 30
Buat, V. et al., 2010, MNRAS, 409, L1–L6 29
Burgarella, D. et al., 2013, A&A, 554, A70 39
Burgasser, A. J., 2007, ApJ, 659, 655–674 21
Bussmann, R. S. et al., 2012, ApJ, 744, 150 50
Bussmann, R. S. et al., 2013, ApJ, 779, 25 . . . . . 43, 57, 66, 67, 100, 117, 118, 120–123, 129, 131, 135, 136
Calanog, J. A. et al., 2014, ApJ, 797, 138 . . . . . 100, 120, 130

Cantalupo, C. M., Borrill, J. D., Jaffe, A. H., Kisner, T. S., and Stompor, R., 2010, ApJS, 187, 212–227 85
Capak, P. L. et al., 2011, Nature, 470, 233–235 50
Carilli, C. L. and Walter, F., 2013, ARA&A, 51, 105–161 40
Carlberg, R. G. et al., 2000, ApJ, 542, 57–67 50
Carlstrom, J. E. et al., 2011, PASP, 123, 568–581 . . . . . 1, 32, 163
Casey, C. M., Narayanan, D., and Cooray, A., 2014, Phys. Rep., 541, 45–161 . . . 31–33, 38, 44, 47
Casey, C. M. et al., 2012, ApJ, 761, 140 . . . . . 37, 47
Cattaneo, A., Mamon, G. A., Warnick, K., and Knebe, A., 2011, A&A, 533, A5 7
Cen, R., 2012, ApJ, 753, 17 4
Cen, R. and Ostriker, J. P., 1999, ApJ, 514, 1–6 4
Chabrier, G., 2003, PASP, 115, 763–795 . . . . . 21, 40
Chapin, E. L. et al., 2011, MNRAS, 411, 505–549 . . . . . 37, 47
Chapman, S. C., Blain, A. W., Ivison, R. J., and Smail, I. R., 2003, Nature, 422, 695–698 . . . 36, 47
Chapman, S. C., Blain, A. W., Smail, I., and Ivison, R. J., 2005, ApJ, 622, 772–796 . . . . . 36, 47–49
Chapman, S. C., Scott, D., Borys, C., and Fahlman, G. G., 2002, MNRAS, 330, 92–104 . . . 58
Chapman, S. C., Smail, I., Windhorst, R., Muxlow, T., and Ivison, R. J., 2004, ApJ, 611, 732–738 44
Charlot, S. and Fall, S. M., 2000, ApJ, 539, 718–731 13
Chary, R. and Elbaz, D., 2001, ApJ, 556, 562–581 37
Chen, Y. -M. et al., 2010, AJ, 140, 445–461 108
Chomiuk, L. and Povich, M. S., 2011, AJ, 142, 197 29
Cicone, C. et al., 2014, A&A, 562, A21 . . . . . 23, 109
Clark, P. C., Glover, S. C. O., Klessen, R. S., and Bonnell, I. A., 2012, MNRAS, 424, 2599–2613 19
Clavel, J. et al., 2000, A&A, 357, 839–849 45
Clemens, M. S. et al., 2010, A&A, 518, L50 13
Clements, D. L., Isaak, K. G., Madden, S. C., and Pearson, C., 2007, A&A, 465, 125–128 99
Clements, D. L., Rowan-Robinson, M., Lawrence, A., Broadhurst, T., and McMahon, R., 1992, MNRAS, 256, 35P–37P 30
Clements, D. L. et al., 2010, A&A, 518, L8 . . . . . 34, 58
Coc, A., Vangioni-Flam, E., Descouvemont, P., Adahchour, A., and Angulo, C., 2004, ApJ, 600, 544–552 3
Cole, S. et al., 2001, MNRAS, 326, 255–273 4
Conroy, C., 2013, ARA&A, 51, 393–455 22
Contursi, A. et al., 2013, A&A, 549, A118 53
Cowie, L. L., Barger, A. J., and Kneib, J. -P., 2002, AJ, 123, 2197–2205 58

Cox, P. et al., 2011, ApJ, 740, 63 . . . . . 48, 98, 134
Cucciati, O. et al., 2012, A&A, 539, A31 29
da Cunha, E., Charlot, S., and Elbaz, D., 2008, MNRAS, 388, 1595–1617 . . . . . 13, 37, 39
da Cunha, E. et al., 2010, A&A, 523, A78 . . . . . 26, 39
Daddi, E. et al., 2007, ApJ, 670, 156–172 . . . . . 24, 29
Daddi, E. et al., 2010, ApJ, 713, 686–707 42
Daddi, E. et al., 2010, ApJL, 714, L118–L122 39
Dale, D. A. and Helou, G., 2002, ApJ, 576, 159–168 37
Dale, D. A., Helou, G., Contursi, A., Silbermann, N. A., and Kolhatkar, S., 2001, ApJ, 549, 215–227 37
Danforth, C. W. and Shull, J. M., 2008, ApJ, 679, 194–219 4
Danforth, C. W., Stocke, J. T., and Shull, J. M., 2010, ApJ, 710, 613–633 4
Danielson, A. L. R. et al., 2011, MNRAS, 410, 1687–1702 . . . . . 58, 59, 102, 104–106
Danielson, A. L. R. et al., 2013, MNRAS, 436, 2793–2809 . . . 10, 18, 58, 59, 102–104, 106, 107, 111, 112, 120, 132
Davé, R., 2008, MNRAS, 385, 147–160 21
Davé, R. et al., 2001, ApJ, 552, 473–483 4
Davé, R. et al., 2010, MNRAS, 404, 1355–1368 . . . . . 48, 51
Davies, R. I. et al., 2007, ApJ, 671, 1388–1412 27
Davis, M. and Peebles, P. J. E., 1983, ApJ, 267, 465–482 50
Dawson, K. S. et al., 2013, AJ, 145, 10 . . . . . 1, 154
De Breuck, C. et al., 2011, A&A, 530, L8 98
De Breuck, C. et al., 2014, A&A, 565, A59 134
De Looze, I., Baes, M., Bendo, G. J., Cortese, L., and Fritz, J., 2011, MNRAS, 416, 2712–2724 135
De Looze, I. et al., 2014, A&A, 568, A62 135
Decarli, R. et al., 2014, ApJL, 782, L17 106
Del Moro, A. et al., 2013, A&A, 549, A59 106
Devlin, M. J. et al., 2009, Nature, 458, 737–739 28
Dey, A. et al., 2008, ApJ, 677, 943–956 . . . . . 34, 49
Díaz-Santos, T. et al., 2013, ApJ, 774, 68 . . . . . 133, 134, 136
Díaz-Santos, T. et al., 2014, ApJL, 788, L17 . . . . . 133, 136
Donley, J. L., Rieke, G. H., Rigby, J. R., and Pérez-González, P. G., 2005, ApJ, 634, 169–182 97
Dopita, M. A. et al., 2005, ApJ, 619, 755–778 37
Dowell, C. D. et al., "Sharc ii: a caltech submillimeter observatory facility camera with 384 pixels", in Millimeter and submillimeter detectors for astronomy, Vol. 4855, edited by Phillips, T. G. and Zmuidzinas, J., Society of Photo-Optical Instrumentation Engineers (SPIE) Conference Series (), pp. 73–87 162
Downes, A. J. B., Peacock, J. A., Savage, A., and Carrie, D. R., 1986, MNRAS, 218, 31–62 37

Downes, D. and Solomon, P. M., 1998, ApJ, 507, 615–654 27
Draine, B. T., 2003, ARA&A, 41, 241–289 ..... 13, 39
Draine, B. T. et al., 2007, ApJ, 663, 866–894 42
Driver, S. P. et al., 2009, Astronomy and Geophysics, 50, 12–5 ..... 62, 156
Duncan, W. D., Robson, E. I., Ade, P. A. R., Sandell, G., and Griffin, M. J., 1990, MNRAS, 243, 126–132 30
Dunne, L., Eales, S. A., and Edmunds, M. G., 2003, MNRAS, 341, 589–598 ..... 13, 14
Dunne, L. et al., 2000, MNRAS, 315, 115–139 14
Dunne, L. et al., 2009, MNRAS, 394, 1307–1316 13
Dwek, E. et al., 1998, ApJ, 508, 106–122 27
Dye, S. et al., 2008, MNRAS, 386, 1107–1130 ..... 36, 40
Dye, S. et al., 2014, MNRAS, 440, 2013–2025 ..... 66, 67, 120
Dye, S. et al., 2015, MNRAS, 452, 2258–2268 ..... 120, 121, 129, 135
Eales, S. et al., 2010, PASP, 122, 499–515 ..... 33, 89, 157
Eales, S. et al., 2012, ApJ, 761, 168 42
Egami, E. et al., 2004, ApJS, 154, 130–136 36
Ekström, S. et al., 2012, A&A, 537, A146 141
Elbaz, D. et al., 2007, A&A, 468, 33–48 24
Elmegreen, B. G., 1999, ApJ, 517, 103–107 40
Engel, H. et al., 2010, ApJ, 724, 233–243 ..... 43, 44, 48, 94
Engel, H. et al., 2011, ApJ, 729, 58 26
Fakhouri, O., Ma, C. -P., and Boylan-Kolchin, M., 2010, MNRAS, 406, 2267–2278 .... 5, 6
Farrah, D. et al., 2013, ApJ, 776, 38 ..... 104, 105, 108, 134
Ferkinhoff, C. et al., 2011, ApJL, 740, L29 ..... 12, 104, 106
Ferkinhoff, C. et al., 2014, ApJ, 780, 142 ..... 129, 145, 164
Ferland, G. J. et al., 2013, RMxAA, 49, 137–163 ..... 139, 154
Ferrarotti, A. S. and Gail, H. -P., 2006, A&A, 447, 553–576 13
Feruglio, C. et al., 2010, A&A, 518, L155 ..... 23, 109
Fiore, F. et al., 2008, ApJ, 672, 94–101 34
Fischer, J. et al., 2010, A&A, 518, L41 ..... 23, 27, 53
Fischer, J. et al., 2014, ApJ, 795, 117 141
Fixsen, D. J., Dwek, E., Mather, J. C., Bennett, C. L., and Shafer, R. A., 1998, ApJ, 508, 123–128 27
Fomalont, E. B. et al., 2006, ApJS, 167, 103–160 47
Fragos, T. et al., 2013, ApJ, 764, 41 29
Franx, M. et al., 2003, ApJL, 587, L79–L82 50
Frayer, D. T. et al., 1998, ApJL, 506, L7–L10 42
Frayer, D. T. et al., 2011, ApJL, 726, L22 ..... 63, 120
Fruchter, A. S. and Hook, R. N., 2002, PASP, 114, 144–152 86
Fu, H. et al., 2012, ApJ, 753, 134 ..... 63, 66, 90, 99, 120, 121, 130
Fukugita, M. and Peebles, P. J. E., 2004, ApJ, 616, 643–668 4

Fulton, T. R. et al., "The data processing pipelines for the herschel/spire imaging fourier transform spectrometer", in Society of photo-optical instrumentation engineers (spie) conference series, Vol. 7731, Society of Photo-Optical Instrumentation Engineers (SPIE) Conference Series (), p. 34 . . . . . 77, 91, 102
Gavazzi, R. et al., 2011, ApJ, 738, 125 66
Geach, J. E. et al., 2011, ApJL, 730, L19 42
Geach, J. E. et al., 2014, Nature, 516, 68–70 113
Gehrz, R., "Sources of stardust in the galaxy", in Interstellar dust, Vol. 135, edited by Allamandola, L. J. and Tielens, A. G. G. M., IAU Symposium (), p. 445 13
Genel, S. et al., 2014, MNRAS, 445, 175–200 8
Genzel, R. et al., 2011, ApJ, 733, 101 42
George, R. D. et al., 2013, MNRAS, 436, L99–L103 . . . . . i, 73, 89, 102
George, R. D. et al., 2014, MNRAS, 442, 1877–1883 . . . . . i, 76, 101
Gladders, M. D., Hoekstra, H., Yee, H. K. C., Hall, P. B., and Barrientos, L. F., 2003, ApJ, 593, 48–55 . . . . . 58, 90, 91
Gladders, M. D. and Yee, H. K. C., 2005, ApJS, 157, 1–29 91
Glenn, J. et al., "Z-spec: a dispersive millimeter-wave spectrometer", in From z-machines to alma: (sub)millimeter spectroscopy of galaxies, Vol. 375, edited by Baker, A. J., Glenn, J., Harris, A. I., Mangum, J. G., and Yun, M. S., Astronomical Society of the Pacific Conference Series (), p. 63 . . . . . 65, 164
Goicoechea, J. R. and Cernicharo, J., 2002, ApJL, 576, L77–L81 111
González, J. E., Lacey, C. G., Baugh, C. M., and Frenk, C. S., 2011, MNRAS, 413, 749–762 29
González-Alfonso, E. et al., 2012, A&A, 541, A4 24
González-Alfonso, E. et al., 2014, A&A, 561, A27 . . . . . 27, 107, 109
González-Alfonso, E. et al., 2015, ApJ, 800, 69 134
Gott III, J. R. et al., 2005, ApJ, 624, 463–484 5
Graciá-Carpio, J. et al., 2011, ApJL, 728, L7 . . . . . 134, 135
Greene, J. E. and Ho, L. C., 2005, ApJ, 630, 122–129 45
Greve, T. R., Ivison, R. J., and Papadopoulos, P. P., 2003, ApJ, 599, 839–846 49
Greve, T. R. et al., 2005, MNRAS, 359, 1165–1183 . . . . . 42, 94, 99
Griffin, M. J. et al., 2010, A&A, 518, L3 . . . . . v, 69, 89, 102
Gruppioni, C. et al., 2013, MNRAS, 432, 23–52 38
Guhathakurta, P. and Draine, B. T., 1989, ApJ, 345, 230–244 147
Gullberg, B. et al., 2015, MNRAS, 449, 2883–2900 . . . . . 129, 133, 134
Guo, Q. and White, S. D. M., 2008, MNRAS, 384, 2–10 7
Güsten, R. et al., 2006, A&A, 454, L13–L16 . . . . . 34, 153
Guth, A. H., 1981, PhRvD, 23, 347–356 1
Habing, H. J., 1968, Bull. Astr. Inst. Netherlands, 19, 421 17
Hailey-Dunsheath, S. et al., 2010, ApJL, 714, L162–L166 . . . . . 57, 98, 132
Hainline, L. J. et al., 2009, ApJ, 699, 1610–1632 106

Hainline, L. J. et al., 2011, ApJ, 740, 96 40
Hamilton, D. and Keel, W. C., 1987, ApJ, 321, 211–224 23
Hargrave, P., Waskett, T., Lim, T., and Swinyard, B., "Performance of flight-model on-board calibration sources on herschel-spire", in Society of photo-optical instrumentation engineers (spie) conference series, Vol. 6275, Society of Photo-Optical Instrumentation Engineers (SPIE) Conference Series (), p. 14 70
Harper Jr., D. A. and Low, F. J., 1973, ApJL, 182, L89 24
Harris, A. I. et al., "The zpectrometer: an ultra-wideband spectrometer for the green bank telescope", in From z-machines to alma: (sub)millimeter spectroscopy of galaxies, Vol. 375, edited by Baker, A. J., Glenn, J., Harris, A. I., Mangum, J. G., and Yun, M. S., Astronomical Society of the Pacific Conference Series (), p. 82 . . . . . 65, 90, 164
Harris, A. I. et al., 2012, ApJ, 752, 152 . . . 63, 65, 66, 68, 89, 90, 98, 117, 120, 122, 130, 131
Hayward, C. C. et al., 2011, ApJ, 743, 159 45
Hayward, C. C. et al., 2013, MNRAS, 434, 2572–2581 . . . . . 45, 48
Helou, G., Soifer, B. T., and Rowan-Robinson, M., 1985, ApJL, 298, L7–L11 . . . . 35, 96, 97
Herrera-Camus, R. et al., 2015, ApJ, 800 135
Heyminck, S., Kasemann, C., Güsten, R., de Lange, G., and Graf, U. U., 2006, A&A, 454, L21–L24 156
Hezaveh, Y. D., Marrone, D. P., and Holder, G. P., 2012, ApJ, 761, 20 . . . . . 56, 57
Hezaveh, Y. D. et al., 2013, ApJ, 767, 132 66
Hickox, R. C. et al., 2012, MNRAS, 421, 284–295 . . . . . 43, 49–51, 112
Hillier, D. J. and Miller, D. L., 1998, ApJ, 496, 407–427 141
Hodge, J. A. et al., 2013, ApJ, 768, 91 . . . . . 35, 44
Holland, W. S. et al., 1999, MNRAS, 303, 659–672 . . . . . 30, 161
Holland, W. S. et al., 2013, MNRAS, 430, 2513–2533 . . . . . 30, 162
Hopkins, P. F. et al., 2013, MNRAS, 430, 1901–1927 23
Hopkins, P. F. et al., 2013, MNRAS, 433, 78–97 109
Hopwood, R. et al., 2015, MNRAS, 449, 2274–2303 80
Hubble, E. and Humason, M. L., 1931, ApJ, 74, 43 1
Hughes, D. H., Dunlop, J. S., and Rawlings, S., 1997, MNRAS, 289, 766–782 30
Hughes, D. H. et al., 1998, Nature, 394, 241–247 . . . . . 21, 30, 58
Ibar, E. et al., 2010, MNRAS, 401, L53–L57 96
Ibar, E. et al., 2010, MNRAS, 409, 38–47 . . . . . 34, 62, 89
Ibar, E. et al., 2015, MNRAS, 449, 2498–2513 134
Ikarashi, S. et al., 2011, MNRAS, 415, 3081–3096 . . . . . 62, 132
Ikarashi, S. et al., 2014, arXiv, ... 43, 48, 50
Ilbert, O. et al., 2009, ApJ, 690, 1236–1249 47
Iono, D. et al., 2006, PASJ, 58, 957–963 . . . . . 57, 120
Iono, D. et al., 2012, PASJ, 64, L2 . . . . . 120, 132
Irwin, M. J., Ibata, R. A., Lewis, G. F., and Totten, E. J., 1998, ApJ, 505, 529–535 29
Isaak, K. G., McMahon, R. G., Hills, R. E., and Withington, S., 1994, MNRAS, 269, L28 . . . 30

ISS Science Officer Don Pettit, *The smell of space*, http://spaceflight.nasa.gov/station/crew/exp6/spacechronicles4.html (visited on 05/31/2015) 11
Ivison, R. J. et al., 1998, MNRAS, 298, 583–593 . . . . . 35, 44, 47
Ivison, R. J. et al., 2000, MNRAS, 315, 209–222 44
Ivison, R. J. et al., 2002, MNRAS, 337, 1–25 . . . . . 35, 37, 44, 47
Ivison, R. J. et al., 2004, ApJS, 154, 124–129 36
Ivison, R. J. et al., 2007, MNRAS, 380, 199–228 44
Ivison, R. J. et al., 2010, MNRAS, 402, 245–258 . . . . . 46, 96, 97
Ivison, R. J. et al., 2010, MNRAS, 404, 198–205 44
Ivison, R. J. et al., 2010, A&A, 518, L35 . . . . . 53, 54, 58, 62, 81, 92, 98, 102, 103, 105, 112, 116, 132
Ivison, R. J. et al., 2010, A&A, 518, L31 . . . . . 46, 96
Ivison, R. J. et al., 2011, MNRAS, 412, 1913–1925 . . . . . 41, 43, 98, 106
Ivison, R. J. et al., 2013, ApJ, 772, 137 . . . . . 39, 44, 50, 63, 66, 70, 94, 120, 130
Jaffe, W. et al., 2004, Nature, 429, 47–49 26
James, A., Dunne, L., Eales, S., and Edmunds, M. G., 2002, MNRAS, 335, 753–761 14
Jauzac, M. et al., 2011, A&A, 525, A52 28
Jeans, J. H., 1902, Royal Society of London Philosophical Transactions Series A, 199, 1–53 20
Jenkins, A. et al., 2001, MNRAS, 321, 372–384 6
Jones, A. P., Tielens, A. G. G. M., Hollenbach, D. J., and McKee, C. F., 1994, ApJ, 433, 797–810 13
Jones, D. H. et al., 2004, MNRAS, 355, 747–763 153
Jørgensen, J. K., Johnstone, D., Kirk, H., and Myers, P. C., 2007, ApJ, 656, 293–305 22
Kajisawa, M. et al., 2010, ApJ, 723, 129–145 29
Karim, A. et al., 2011, ApJ, 730, 61 24
Kartaltepe, J. S. et al., 2010, ApJ, 721, 98–123 27
Kaufman, M. J., Wolfire, M. G., and Hollenbach, D. J., 2006, ApJ, 644, 283–299 . . . 105, 106
Kaufman, M. J., Wolfire, M. G., Hollenbach, D. J., and Luhman, M. L., 1999, ApJ, 527, 795–813 . . . . . 17, 18, 144, 146, 148
Keeton, C. R. and Kochanek, C. S., 1998, ApJ, 495, 157–169 56
Kennicutt, R. C. and Evans, N. J., 2012, ARA&A, 50, 531–608 . . . . . 39, 129
Kewley, L. J. et al., 2013, ApJ, 774, 100 17
Kleinmann, D. E. and Low, F. J., 1970, ApJL, 159, L165 24
Knapp, G. R., Sandell, G., and Robson, E. I., 1993, ApJS, 88, 173–197 14
Kneib, J. -P., PhD thesis, Ph. D. thesis, Université Paul Sabatier, Toulouse, (1993) 55
Kneib, J. -P. et al., 2004, MNRAS, 349, 1211–1217 58
Knudsen, K. K., Neri, R., Kneib, J. -P., and van der Werf, P. P., 2009, A&A, 496, 45–50 . . . 58
Knudsen, K. K., van der Werf, P. P., and Jaffe, W., 2003, A&A, 411, 343–350 . . . . . 46, 58
Komatsu, E. et al., 2003, ApJS, 148, 119–134 5
Komatsu, E. et al., 2011, ApJS, 192, 18 89

Kornei, K. A. et al., 2012, ApJ, 758, 135 . . . . . 23, 108, 109
Kovács, A. et al., 2010, ApJ, 717, 29–39 . . . . . 14, 37, 94, 95, 97, 118, 119
Kroupa, P., 2001, MNRAS, 322, 231–246 . . . . . 21, 40, 141
Krumholz, M. R., McKee, C. F., and Tumlinson, J., 2009, ApJ, 693, 216–235 . . . . . 40, 42
Lada, C. J. and Kylafis, N. D., eds. (1991), *The physics of star formation and early stellar evolution*, Vol. 342, NATO Advanced Science Institutes (ASI) Series C () 19
Lagache, G., Puget, J. -L., and Dole, H., 2005, ARA&A, 43, 727–768 47
Le Borgne, D., Elbaz, D., Ocvirk, P., and Pichon, C., 2009, A&A, 504, 727–740 28
Le Floc'h, E. et al., 2005, ApJ, 632, 169–190 34
Leger, A. and Puget, J. L., 1984, A&A, 137, L5–L8 11
Lehner, N. et al., 2007, ApJ, 658, 680–709 4
Leitherer, C. et al., 1999, ApJS, 123, 3–40 141
Lejeune, T., Cuisinier, F., and Buser, R., 1997, A&AS, 125, 229–246 141
Lewis, G. F., Chapman, S. C., and Helou, G., 2005, ApJ, 621, 32–40 47
Liddle, A. R. and Lyth, D. H., *Cosmological inflation and large-scale structure* () 1
Lilly, S. J. et al., 1999, ApJ, 518, 641–655 47
Linde, A. D., 1982, Physics Letters B, 108, 389–393 1
López-Sanjuan, C. et al., 2012, A&A, 548, A7 8
Luhman, M. L. et al., 2003, ApJ, 594, 758–775 . . . . . 104, 133
Lupu, R. E. et al., 2012, ApJ, 757, 135 . . . . . 63, 65, 120
Lutz, D., 2014, ARA&A, 52, 373–414 33
Lutz, D. et al., 2011, A&A, 532, A90 . . . . . 28, 161
Ma, B. et al., 2015, arXiv, 1504, 5254 121
MacFadyen, A. I. and Woosley, S. E., 1999, ApJ, 524, 262–289 21
Mach, L., 1892, Zeitschrift fü Instrumentenkunde, 12, 89–93 69
Madau, P. and Dickinson, M., 2014, ARA&A, 52, 415–486 . . . . . 28, 29
Magdis, G. E. et al., 2014, ApJ, 796, 63 . . . . . 129, 134
Magnelli, B. et al., 2012, A&A, 539, A155 . . . . . 37, 39, 66, 94, 118
Magnelli, B. et al., 2015, A&A, 573, A45 96
Malhotra, S. et al., 1997, ApJL, 491, L27–L30 133
Martin, C. L., 2005, ApJ, 621, 227–245 . . . . . 23, 108
Martin, C. L. et al., 2012, ApJ, 760, 127 . . . . . 23, 101, 109
Martínez-Delgado, D. et al., 2010, AJ, 140, 962–967 7
Mason, B. D., Hartkopf, W. I., Gies, D. R., Henry, T. J., and Helsel, J. W., 2009, AJ, 137, 3358–3377 21
Matute, I. et al., 2006, A&A, 451, 443–456 28
McCracken, H. J. et al., 2001, A&A, 376, 756–774 50
McDowell, R. S., 1988, The Journal of Chemical Physics, 88, 356–361 111
McLure, R. J. et al., 2013, MNRAS, 428, 1088–1106 8
McMillan, P. J., 2011, MNRAS, 414, 2446–2457 27
Meier, D. S. et al., 2010, AJ, 140, 1294–1305 26

Meijerink, R., Spaans, M., and Israel, F. P., 2007, A&A, 461, 793–811 144
Meijerink, R., Spaans, M., Loenen, A. F., and van der Werf, P. P., 2011, A&A, 525, A119 145
Menéndez-Delmestre, K. et al., 2007, ApJL, 655, L65–L68 45
Menéndez-Delmestre, K. et al., 2009, ApJ, 699, 667–685 . . . . . 36, 46, 106
Mennella, V. et al., 1998, ApJ, 496, 1058–1066 14
Messias, H. et al., 2014, A&A, 568, A92 . . . . . 63, 117, 120, 130, 131
Michałowski, M. J. et al., 2012, A&A, 541, A85 40
Michałowski, M., Hjorth, J., and Watson, D., 2010, A&A, 514, A67 40
Möller, O., Kitzbichler, M., and Natarajan, P., 2007, MNRAS, 379, 1195–1208 56
Moster, B. P. et al., 2010, ApJ, 710, 903–923 112
Mullaney, J. R., Alexander, D. M., Goulding, A. D., and Hickox, R. C., 2011, MNRAS, 414, 1082–1110 106
Murphy, E. J., Helou, G., Kenney, J. D. P., Armus, L., and Braun, R., 2008, ApJ, 678, 828–850 35
Murphy, E. J. et al., 2011, ApJ, 732, 126 129
Murphy, E. J. et al., 2011, ApJ, 737, 67 . . . . . 26, 39, 97, 112, 120
Murray, N., Ménard, B., and Thompson, T. A., 2011, ApJ, 735, 66 22
Murray, N., Quataert, E., and Thompson, T. A., 2005, ApJ, 618, 569–585 22
Murray, N., Quataert, E., and Thompson, T. A., 2010, ApJ, 709, 191–209 22
Myers, P. C., 2009, ApJ, 700, 1609–1625 20
Myers, P. C., 2009, ApJ, 706, 1341–1352 21
Naab, T., Johansson, P. H., and Ostriker, J. P., 2009, ApJL, 699, L178–L182 50
Nagao, T. et al., 2012, A&A, 542, L34 143
Narayanan, D. et al., 2010, MNRAS, 401, 1613–1619 . . . . . 7, 43, 44, 49
Navarro, J. F., Frenk, C. S., and White, S. D. M., 1997, ApJ, 490, 493 . . . . . 6, 112
Negrello, M. et al., 2007, MNRAS, 377, 1557–1568 . . . . . 47, 60, 61, 115, 116
Negrello, M. et al., 2010, Science, 330, 800– 60, 67, 90, 123
Negrello, M. et al., 2014, MNRAS, 440, 1999–2012 . . . . . 37, 61, 66, 67, 121, 123, 129, 135
Neugebauer, G., Becklin, E. E., Oke, J. B., and Searle, L., 1976, ApJ, 205, 29–43 24
Neugebauer, G. et al., 1984, ApJL, 278, L1–L6 . . . . . 24, 158
Newman, S. F. et al., 2012, ApJ, 761, 43 . . . . . 101, 108, 109
Nguyen, H. T. et al., 2010, A&A, 518, L5 58
Noeske, K. G. et al., 2007, ApJL, 660, L43–L46 24
Norberg, P. et al., 2002, MNRAS, 332, 827–838 50
Noterdaeme, P., Petitjean, P., Ledoux, C., and Srianand, R., 2009, A&A, 505, 1087–1098 . . . 4
Oesch, P. A. et al., 2014, ApJ, 786, 108 7
Oke, J. B. et al., 1995, PASP, 107, 375 . . . . . 47, 159
Oliver, S. J. et al., 2012, MNRAS, 424, 1614–1635 . . . . . 34, 157
Omont, A. et al., 2013, A&A, 551, A115 90
Ostriker, E. C., Stone, J. M., and Gammie, C. F., 2001, ApJ, 546, 980–1005 19

Ota, K. et al., 2014, ApJ, 792, 34 10
Ott, S., "The herschel data processing system — hipe and pipelines — up and running since the start of the mission", in Astronomical data analysis software and systems xix, Vol. 434, edited by Mizumoto, Y., Morita, K.-I., and Ohishi, M., Astronomical Society of the Pacific Conference Series (), p. 139 . . . . . 76, 157
Padoan, P. and Nordlund, Å., 2002, ApJ, 576, 870–879 21
Pan, L. and Padoan, P., 2009, ApJ, 692, 594–607 20
Panuzzo, P. et al., 2010, A&A, 518, L37 53
Papadopoulos, P. P., 2010, ApJ, 720, 226–232 144
Papadopoulos, P. P., Isaak, K. G., and van der Werf, P. P., 2007, ApJ, 668, 815–825 147
Papadopoulos, P. P., van der Werf, P., Isaak, K., and Xilouris, E. M., 2010, ApJ, 715, 775–792 10
Papadopoulos, P. P., van der Werf, P., Xilouris, E., Isaak, K. G., and Gao, Y., 2012, ApJ, 751, 10 42
Papadopoulos, P. P. et al., 2012, MNRAS, 426, 2601–2629 10
Pascale, E. et al., 2008, ApJ, 681, 400–414 . . . . . 33, 154
Pascale, E. et al., 2011, MNRAS, 415, 911–917 . . . . . 34, 89
Pauldrach, A. W. A., Hoffmann, T. L., and Lennon, M., 2001, A&A, 375, 161–195 141
Pérez-González, P. G. et al., 2008, ApJ, 675, 234–261 29
Perrotta, F., Baccigalupi, C., Bartelmann, M., De Zotti, G., and Granato, G. L., 2002, MNRAS, 329, 445–455 60
Perrotta, F. et al., 2003, MNRAS, 338, 623–636 60
Persic, M., Salucci, P., and Stel, F., 1996, MNRAS, 281, 27–47 3
Pilbratt, G. L. et al., 2010, A&A, 518, L1 . . . . . v, 70, 89, 102, 157
Planck Collaboration et al., 2011, A&A, 536, A1 161
Planck Collaboration et al., 2011, A&A, 536, A21 14
Planck Collaboration et al., 2014, A&A, 571, A15 3
Planck Collaboration et al., 2014, A&A, 571, A16 . . . . . 1, 3, 4, 102
Poglitsch, A. et al., 2010, A&A, 518, L2 . . . . . 89, 107
Pope, A. et al., 2006, MNRAS, 370, 1185–1207 36
Pope, A. et al., 2008, ApJ, 675, 1171–1193 . . . . . 32, 36, 46
Popesso, P. et al., 2012, arXiv, 1211, 4257 87
Prochaska, J. X. and Tumlinson, J., "Baryons: what,when and where?", in *Astrophysics in the next decade*, edited by Thronson, H. A., Stiavelli, M., and Tielens, A. (), p. 419 4
Puget, J. -L. et al., 1996, A&A, 308, L5 27
Rangwala, N. et al., 2011, ApJ, 743, 94 53
Rauch, M., 1998, ARA&A, 36, 267–316 4
Rauch, M. et al., 1997, ApJ, 489, 7–20 4
Rawle, T. D. et al., 2014, ApJ, 783, 59 134
Raymond, G., Isaak, K. G., Clements, D., Rykala, A., and Pearson, C., 2010, PASJ, 62, 697– 99

Reddy, N. et al., 2012, ApJ, 744, 154 24
Rees, M. J., Silk, J. I., Werner, M. W., and Wickramasinghe, N. C., 1969, Nature, 223, 788–791 24
Rémy-Ruyer, A. et al., 2014, A&A, 563, A31 42
Rho, J. et al., 2008, ApJ, 673, 271–282 13
Richards, E. A., 2000, ApJ, 533, 611–630 47
Richards, G. T. et al., 2006, AJ, 131, 2766–2787 49
Riechers, D. A. et al., 2013, Nature, 496, 329–333 . . . . . 39, 48, 66, 98, 134
Riechers, D. A. et al., 2014, ApJ, 786, 31 46
Riechers, D. A. et al., 2014, ApJ, 796, 84 . . . . . 10, 53, 134, 138
Rieke, G. H. and Lebofsky, M. J., 1978, ApJL, 220, L37–L41 24
Rieke, G. H. and Low, F. J., 1972, ApJL, 176, L95 24
Rieke, G. H. et al., 2009, ApJ, 692, 556–573 37
Rigby, E. E. et al., 2011, MNRAS, 415, 2336–2348 . . . . . 34, 89
Riotto, A. and Trodden, M., 1999, Annual Review of Nuclear and Particle Science, 49, 35–75 3
Robitaille, T. P. and Whitney, B. A., 2010, ApJL, 710, L11–L15 29
Rodighiero, G. et al., 2011, ApJL, 739, L40 29
Rodighiero, G. et al., 2014, MNRAS, 443, 19–30 39
Rodríguez Zaurín, J., Tadhunter, C. N., and González Delgado, R. M., 2010, MNRAS, 403, 1317–1330 26
Roseboom, I. G. et al., 2010, MNRAS, 409, 48–65 36
Rosenberg, M. J. F. et al., 2015, ApJ, 801, 72 134
Rowan-Robinson, M. et al., 1991, Nature, 351, 719–721 29
Rupke, D. S., Veilleux, S., and Sanders, D. B., 2005, ApJ, 632, 751–780 . . . . . 23, 107, 109
Sakamoto, K. et al., 2008, ApJ, 684, 957–977 26
Sakamoto, K. et al., 2009, ApJL, 700, L104–L108 23
Salpeter, E. E., 1955, ApJ, 121, 161 . . . . . 21, 40
Salucci, P. and Persic, M., 1999, MNRAS, 309, 923–928 4
Sanders, D. B., Mazzarella, J. M., Kim, D. -C., Surace, J. A., and Soifer, B. T., 2003, AJ, 126, 1607–1664 . . . . . 38, 161
Sanders, D. B. and Mirabel, I. F., 1996, ARA&A, 34, 749 26
Sanders, D. B. et al., 1988, ApJ, 325, 74–91 . . . . . 27, 48, 51
Sandstrom, K. M. et al., 2013, ApJ, 777 . . . . . 13, 42, 98
Sargent, B. A. et al., 2010, ApJ, 716, 878–890 13
Sargent, M. T. et al., 2010, ApJL, 714, L190–L195 96
Sargsyan, L. et al., 2014, ApJ, 790, 15 . . . . . 134, 135
Schawinski, K., Simmons, B. D., Urry, C. M., Treister, E., and Glikman, E., 2012, MNRAS, 425, L61–L65 34
Schaye, J. et al., 2015, MNRAS, 446, 521–554 8
Schleicher, D. R. G. and Beck, R., 2013, A&A, 556, A142 36

Scoville, N. Z., "Evolution of star formation and gas", in *Secular evolution of galaxies*, edited by Falcón-Barroso, J. and Knapen, J. H. (), p. 491 39
Scoville, N. et al., 2014, ApJ, 783, 84 42
Serjeant, S., 2012, MNRAS, 424, 2429–2441 . . . . . 56, 99
Shu, F. H., Adams, F. C., and Lizano, S., 1987, ARA&A, 25, 23–81 20
Shull, J. M., Smith, B. D., and Danforth, C. W., 2012, ApJ, 759, 23 4
Silva, L., Granato, G. L., Bressan, A., and Danese, L., 1998, ApJ, 509, 103–117 . . . . . 35, 37
Simpson, J. M. et al., 2014, ApJ, 788, 125 . . . . . 47, 48
Simpson, J. M. et al., 2015, ApJ, 799, 81 . . . . . 35, 43
Siringo, G. et al., 2009, A&A, 497, 945–962 . . . . . 50, 158
Smail, I., Ivison, R. J., and Blain, A. W., 1997, ApJL, 490, L5 . . . . . 21, 30, 58
Smail, I., Ivison, R. J., Blain, A. W., and Kneib, J. -P., 2002, MNRAS, 331, 495–520 58
Smail, I., Ivison, R. J., Owen, F. N., Blain, A. W., and Kneib, J. -P., 2000, ApJ, 528, 612–616 35
Smith, B. D., Hallman, E. J., Shull, J. M., and O'Shea, B. W., 2011, ApJ, 731 4
Solomon, P. M., Downes, D., Radford, S. J. E., and Barrett, J. W., 1997, ApJ, 478, 144 . . . 27, 42
Solomon, P. M., Rivolo, A. R., Barrett, J., and Yahil, A., 1987, ApJ, 319, 730–741 41
Sparre, M. et al., 2015, MNRAS, 447, 3548–3563 25
Spitzer, L., *Physical processes in the interstellar medium* () 13
Spoon, H. W. W. et al., 2013, ApJ, 775, 127 . . . . . 23, 27, 107–109
Springel, V. et al., 2005, Nature, 435, 629–636 5
Stacey, G. J. et al., 1991, ApJ, 373, 423–444 . . . . . 9, 17, 92
Stacey, G. J. et al., "Zeus: the redshift (z) and early universe spectrometer", in From z-machines to alma: (sub)millimeter spectroscopy of galaxies, Vol. 375, edited by Baker, A. J., Glenn, J., Harris, A. I., Mangum, J. G., and Yun, M. S., Astronomical Society of the Pacific Conference Series (), p. 52 . . . . . 132, 164
Stacey, G. J. et al., 2010, ApJ, 724, 957–974 . . . . . 133, 134
Staguhn, J. et al., 2008, Journal of Low Temperature Physics, 151, 709–714 . . . . . 30, 156
Steidel, C. C. et al., 2010, ApJ, 717, 289–322 101
Stewart, K. R. et al., 2011, ApJL, 735, L1 7
Storey, J. W. V., Watson, D. M., and Townes, C. H., 1981, ApJL, 244, L27–L30 23
Strickland, D. K. and Heckman, T. M., 2009, ApJ, 697, 2030–2056 22
Sturm, E. et al., 2010, A&A, 518, L36 . . . . . 57, 132
Sturm, E. et al., 2011, ApJL, 733, L16 23
Sutherland, W. and Saunders, W., 1992, MNRAS, 259, 413–420 37
Swetz, D. S. et al., 2011, ApJS, 194, 41 . . . . . 1, 153
Swinbank, A. M. et al., 2006, MNRAS, 371, 465–476 . . . . . 57, 132
Swinbank, A. M. et al., 2010, MNRAS, 405, 234–244 43
Swinbank, A. M. et al., 2010, Nature, 464, 733–736 . . . 53, 58, 63, 65, 101, 112, 117, 132, 133

Swinbank, A. M. et al., 2011, ApJ, 742, 11 .... 42, 58, 59, 66, 102–104, 106, 107, 109, 111, 112, 117, 132
Swinbank, A. M. et al., 2012, MNRAS, 427, 1066–1074 ..... 10, 53, 134
Swinbank, A. M. et al., 2014, MNRAS, 438, 1267–1287 ..... 30, 35, 39, 66
Swinyard, B. M. et al., 2010, A&A, 518, L4 ..... 63, 70, 117
Swinyard, B. M. et al., 2014, MNRAS, 440, 3658–3674 103
Swinyard, B. et al., 2009, Experimental Astronomy, 23, 193–219 ..... 13, 89, 99
Symeonidis, M. et al., 2013, MNRAS, 431, 2317–2340 37
Tacconi, L. J. et al., 2006, ApJ, 640, 228–240 42–44
Tacconi, L. J. et al., 2008, ApJ, 680, 246–262 ..... 44, 49
Tacconi, L. J. et al., 2010, Nature, 463, 781–784 42
Targett, T. A. et al., 2011, MNRAS, 412, 295–317 44
Targett, T. A. et al., 2013, MNRAS, 432, 2012–2042 ..... 43, 44
Telesco, C. M. and Harper, D. A., 1980, ApJ, 235, 392–404 24
Thomas, D., Maraston, C., Bender, R., and Mendes de Oliveira, C., 2005, ApJ, 621, 673–694 29
Thomas, D., Maraston, C., Schawinski, K., Sarzi, M., and Silk, J., 2010, MNRAS, 404, 1775–1789 8
Thomson, A. P. et al., 2012, MNRAS, 425, 2203–2211 39
Tielens, A. G. G. M., *The physics and chemistry of the interstellar medium* () ... 8, 10–12, 15, 19
Tielens, A. G. G. M. and Hollenbach, D., 1985, ApJ, 291, 722–754 17
Tilton, E. M., Danforth, C. W., Shull, J. M., and Ross, T. L., 2012, ApJ, 759, 112 4
Tisserand, P. et al., 2007, A&A, 469, 387–404 6
Toft, S. et al., 2014, ApJ, 782, 68 50
Toomre, A., 1964, ApJ, 139, 1217–1238 42
Treu, T. et al., 2010, ApJ, 709, 1195–1202 21
Trujillo, I. et al., 2006, MNRAS, 373, L36–L40 50
Uhlig, M. et al., 2012, MNRAS, 423, 2374–2396 22
Valtchanov, I. et al., 2011, MNRAS, 415, 3473–3484 ..... 18, 53, 54, 69, 70, 72, 81, 97, 98, 102, 104, 129
van der Wel, A., Rix, H. -W., Holden, B. P., Bell, E. F., and Robaina, A. R., 2009, ApJL, 706, L120–L123 7
van der Werf, P. P., Goss, W. M., and O'Dell, C. R., 2013, ApJ, 762, 101 17
van der Werf, P. P., Stutzki, J., Sternberg, A., and Krabbe, A., 1996, A&A, 313, 633–648 ... 20
van der Werf, P. P. et al., 2010, A&A, 518, L42 ..... 10, 53
van der Werf, P. P. et al., 2011, ApJL, 741, L38 20
van Dokkum, P. G. and Conroy, C., 2010, Nature, 468, 940–942 21
van Dokkum, P. G. and Franx, M., 2001, ApJ, 553, 90–102 50
van Dokkum, P. G. et al., 2008, ApJL, 677, L5–L8 50
van Dokkum, P. G. et al., 2010, ApJ, 709, 1018–1041 50

van Starkenburg, L. et al., 2008, A&A, 488, 99–112 42
Veilleux, S. and Osterbrock, D. E., 1987, ApJS, 63, 295–310 16
Veilleux, S. et al., 2009, ApJS, 182, 628–666 46
Veilleux, S. et al., 2013, ApJ, 776, 27 . . . . . 23, 27, 108, 109
Vieira, J. D. et al., 2010, ApJ, 719, 763–783 . . . . . 32, 61
Vieira, J. D. et al., 2013, Nature, 495, 344–347 61
Viero, M. P. et al., 2009, ApJ, 707, 1766–1778 50
Viero, M. P. et al., 2013, ApJ, 779, 32 28
Vogelsberger, M. et al., 2014, Nature, 509, 177–182 8
Wagg, J. et al., 2012, ApJL, 752, L30 . . . . . 10, 98, 134
Wall, J. V., Jackson, C. A., Shaver, P. A., Hook, I. M., and Kellermann, K. I., 2005, A&A, 434, 133–148 46
Walter, F., Weiss, A., and Scoville, N., 2002, ApJL, 580, L21–L25 23
Walter, F. et al., 2012, Nature, 486, 233–236 . . . . . 48, 50, 98
Wang, S. X. et al., 2013, ApJ, 778, 179 46
Wardlow, J. L. et al., 2011, MNRAS, 415, 1479–1508 . . . . . 47, 48
Wardlow, J. L. et al., 2013, ApJ, 762, 59 . . . . . 60, 64, 66
Weiner, B. J. et al., 2009, ApJ, 692, 187–211 101
Weingartner, J. C. and Draine, B. T., 2001, ApJ, 548, 296–309 13
Weiß, A. et al., 2009, ApJL, 705, L45–L47 65
Weiß, A. et al., 2009, ApJ, 707, 1201–1216 . . . . . 35, 158
Weiß, A. et al., 2013, ApJ, 767, 88 . . . . . 56, 57, 89
Wellons, S. et al., 2015, MNRAS, 449, 361–372 50
Whitaker, K. E. et al., 2013, ApJL, 770, L39 50
Wieprecht, E. et al., "The herschel/pacs photometer pipeline", in Astronomical data analysis software and systems xviii, Vol. 411, edited by Bohlender, D. A., Durand, D., and Dowler, P., Astronomical Society of the Pacific Conference Series (), p. 531 85
Wild, V. et al., 2007, MNRAS, 381, 543–572 13
Willmer, C. N. A., da Costa, L. N., and Pellegrini, P. S., 1998, AJ, 115, 869–884 50
Wilson, G. W. et al., 2008, MNRAS, 386, 807–818 . . . . . 30, 153
Wuyts, S. et al., 2010, ApJ, 722, 1666–1684 50
Yang, M. and Phillips, T., 2007, ApJ, 662, 284–293 14
Yao, Y., Shull, J. M., Wang, Q. D., and Cash, W., 2012, ApJ, 746, 166 4
Younger, J. D. et al., 2008, ApJ, 688, 59–66 43
Yun, M. S. and Carilli, C. L., 2002, ApJ, 568, 88–98 35
Yun, M. S., Reddy, N. A., and Condon, J. J., 2001, ApJ, 554, 803–822 96
Zehnder, L., 1891, Zeitschrift fü Instrumentenkunde, 11, 275–285 69
Zinnecker, H. and Yorke, H. W., 2007, ARA&A, 45, 481–563 21

Publications

Far-infrared spectroscopy of a lensed starburst: a blind redshift from Herschel
George, R. D., Ivison, R. J., Hopwood, R., Riechers, D. A., Bussmann, R. S., Cox, P., Dye, S., Krips, M., Negrello, M., Neri, R., Serjeant, S., Valtchanov, I., Baes, M., Bourne, N., Clements, D. L., De Zotti, G., Dunne, L., Eales, S. A., Ibar, E., Maddox, S., Smith, M. W. L., Valiante, E., and van der Werf, P., 2013, MNRAS, 436, L99–L103

Herschel reveals a molecular outflow in a $z = 2.3$ ULIRG
George, R. D., Ivison, R. J., Smail, I., Swinbank, A. M., Hopwood, R., Stanley, F., Swinyard, B. M., Valtchanov, I., and van der Werf, P. P., 2014, MNRAS, 442, 1877–1883

Herschel-ATLAS: A Binary HyLIRG Pinpointing a Cluster of Starbursting Protoellipticals
Ivison, R. J., Swinbank, A. M., Smail, I., Harris, A. I., Bussmann, R. S., Cooray, A., Cox, P., Fu, H., Kovács, A., Krips, M., Narayanan, D., Negrello, M., Neri, R., Peñarrubia, J., Richard, J., Riechers, D. A., Rowlands, K., Staguhn, J. G., Targett, T. A., Amber, S., Baker, A. J., Bourne, N., Bertoldi, F., Bremer, M., Calanog, J. A., Clements, D. L., Dannerbauer, H., Dariush, A., De Zotti, G., Dunne, L., Eales, S. A., Farrah, D., Fleuren, S., Franceschini, A., Geach, J. E., **George, R. D.**, Helly, J. C., Hopwood, R., Ibar, E., Jarvis, M. J., Kneib, J. -P., Maddox, S., Omont, A., Scott, D., Serjeant, S., Smith, M. W. L., Thompson, M. A., Valiante, E., Valtchanov, I., Vieira, J., and van der Werf, P., 2013 ApJ, 772, 137

George, R. D, Ivison, R. J., Hopwood, R., Valtchanov, I. et al., 2015, MNRAS, in preparation